Synthesis, Characterization, and Reactivity of Metal-Metal Bonded Complexes with Cobalt, Iron, and Manganese

A DISSERTATION
SUBMITTED TO THE FACULTY OF
UNIVERSITY OF MINNESOTA
BY

Stephen J. Tereniak

IN PARTIAL FULFILLMENT OF THE REQUIREMENTS
FOR THE DEGREE OF
DOCTOR OF PHILOSOPHY

Connie C. Lu, Adviser

November, 2014

Acknowledgements

Thanks to all who have been a part of my life here at the University of Minnesota. Connie, thanks for bringing me aboard five years ago and guiding me through the Ph.D. Thanks to the older Lu lab members – Elodie, Keying, Deanna, Kit, and Aubrey – for providing invaluable advice in the beginning. Thanks to Reed, Randy, Laura C., and Ryan for keeping me sane towards the end. Thanks to our Lu lab collaborators for being a great team to work with – Laura G., Becky, Christine K., Vic, Yu-Sheng, Eckhard, Bernd, Andreas, Larry, and Andy J. Thanks to my fellow users, past and present, of the 409 South Box – Keying, Elodie, Kit, Ryan, and Dave – for providing endless amusement during all hours. Thanks to the Ph.D. committee for advising me along the way. It's been a privilege and a pleasure to work with all of you. And finally, thanks to my parents and my sister for being a rock of support despite being a thousand miles away.

Table of Contents

List of Tables

List of Figures

List of Schemes

List of Symbols and Abbreviations

°	degree
12-crown-4	1,4,7,10-butaoxacyclododecane
18-crown-6	1,4,7,10,13,16-hexaoxacyclooctadecane
Å	angstrom
Ad	adamantyl
ap	apical
avg	average
ax	axial
B	magnetic field
Bn	benzyl
br	broad
C	celsius
C_6D_6	deuterated benzene
C_6H_6	benzene
CASPT2	complete active space second order perturbation theory
CASSCF	complete active space self consistent field
CCD	charge coupled device
$CDCl_3$	deuterated chloroform
$CHCl_3$	chloroform
CH_3CN	acetonitrile
CD_2Cl_2	deuterated dichloromethane
CH_2Cl_2	dichloromethane
CD_3CN	deuterated acetonitrile
cm	centimeter
cm^{-1}	wavenumber
COSY	correlation spectroscopy
Cp	cyclopentadienyl
Cp*	pentamethylcyclopentadienyl
Cpd.	compound
CSD	Cambridge Structural Database
CV	cyclic voltammetry
Cy	cyclohexyl
d	doublet
dd	doublet of doublets
ddd	doublet of doublets of doublets
D	zero-field splitting
dc	direct current
DCM	dichloromethane
DG	D-glucuronate
DH_{298}	bond dissociation enthalpy

DMF	dimethylformamide
DMSO	dimethyl sulfoxide
dpa	*N*,*N*-bis(2-pyridyl)amide
DPhBz	diphenylbenzamidinate
DPhF	diphenylformamidinate
dt	doublet of triplets
DTolTA	*N*,*N*'-bis(4-tolyl)triazenate
E/*D*	rhombicity
$E°$	standard electrode potential
E_{pa}	peak anodic current
E_{pc}	peak cathodic current
EBO	effective bond order
EMAC	extended metal atom chain
EPR	electron paramagnetic resonance
eq	equatorial
eq	equivalent
ESI-MS	electrospray ionization-mass spectrometry
Et	ethyl
Et_2O	diethyl ether
EtOAc	ethyl acetate
FBO	formal bond order
Fc	ferrocene
FcA	ferrocenylacetylide
FWHM	full width at half maximum
g	gram
g	anisotropic *g* factor
G	Gauss
GBq	gigabecquerel
GHz	gigahertz
giso	$ArNC(NCy_2)CNAr^{-}$, Ar = 2,6-$^{i}Pr_2C_6H_3$
HCl	hydrochloric acid
hrs	hours
I	nuclear spin quantum number
i_{pa}/i_{pc}	ratio of peak anodic current to peak cathodic current
ICP-OES	inductively coupled plasma-optical emission spectroscopy
^{i}Pr	isopropyl
J	coupling constant
K	Kelvin
kcal	kilocalorie
KBn	benzylpotassium
KC_8	potassium graphite
LMCT	ligand-to-metal charge transfer
L^{Ph}	tris(2-(*N*-phenylbenzamidinato)ethyl)amine
m	multiplet

M	molarity
m/*z*	mass-to-charge ratio
Me	methyl
MeOH	methanol
Mes	mesityl
mg	milligram
MHz	megahertz
min	minute
mL	milliliter
MLCT	metal-to-ligand charge transfer
mm	millimeter
mM	millimolar
MMCT	metal-to-metal charge transfer
mmol	millimole
M_{mol}	molar magnetization
MO	molecular orbital
mol	mole
m_s	electron spin quantum number
mV	millivolts
mT	millitesla
MI	*myo*-inositol
NHE	normal hydrogen electrode
Ni-L	light induced state of nickel iron hydrogenase
NIR	near infrared
nm	nanometers
NBS	*N*-bromosuccinimide
NMR	nuclear magnetic resonance
Ph	phenyl
pipiso	ArNC(N(*cis*-2,6-$Me_2C_5H_8$)CNAr$^-$, Ar = 2,6-$^i Pr_2C_6H_3$
piso	ArNC(^{t}Bu)CNAr$^-$, Ar = 2,6-$^i Pr_2C_6H_3$
pKa	pK for association
ppm	parts per million
py	pyridine
py_3tren	*N*,*N*,*N*-tris(2-(2-pyridylamino)ethyl)amine
q	quartet
r	the formal shortness ratio
RASSCF	restricted active space self consistent field
reflns	reflections
RNR	ribonucleotide reductase
rt	room temperature
s	singlet
s	second
S	spin state
s^{-1}	frequency

SCF-Xα-SW	self consistent field-Xα-scattered wave
SQUID	superconducting quantum interference device
sMMO	soluble methane monooxygenase
Su	succinimide
T	temperature
t	triplet
^{t}Bu	*tert*-butyl
T	Tesla
T_1	spin-lattice relaxation time
tacn	triazacyclononane
$TBAPF_6$	tetrabutylammonium hexafluorophosphate
TEMPO	(2,2,6,6-tetramethylpiperidin-1-yl)oxy
THF	tetrahydrofuran
TPA	*N*,*N*,*N*-tris((2-pyridyl)methyl)amine
d_8-THF	deuterated tetrahydrofuran
d_8-tol	deuterated toluene
tren	tris(2-aminoethyl)amine
UV	ultraviolet
V	volts
V	volume
vis	visible
vs.	versus
W	width
Y	tyrosine
Z	number of independent structures in unit cell
*	antibonding
δ	chemical shift
δ	isomer shift
δ	delta
ΔE_Q	quadrupole splitting
Δf'	real component of the anomalous scattering factor
Δf''	imaginary component of the anomalous scattering factor
ΔG°	Gibbs free energy
ε	Molar absorptivity
θ	degrees of data collection
θ_w	Weiss temperature
η	hapticity
χ	magnetic susceptibility
λ	wavelength
λ_{max}	maximum absorbance wavelength
λ_{edge}	K edge energy
μ	bridging
μ	absorption coefficient
μ_B	Bohr magnetons

μ_{eff}	effective magnetic moment
μL	microliter
μM	micromolar
π	pi
σ	sigma

Chapter 1

Introduction

In part from:

Tereniak, S. J.; Lu, C. C. "Group 8 Metal-Metal Bonds." In Molecular Metal-Metal Bonds. Compounds, Synthesis, Properties. ed. S. Liddle, Wiley. In press.

1.1 Small-Molecule Activation in Metalloenzymes of Relevance to Renewable Energy: Metal-Metal Bonds as a Bioinspired Strategy Towards Designing Synthetic Compounds

Over the last century, the human population has exploded. Some of this growth is attributable to the Haber-Bosch process, in which N_2 and H_2 are converted into NH_3 with a heterogeneous catalyst based on iron. Approximately half the global need of fixed nitrogen is met by the Haber-Bosch process, and it generates 500 million tons of nitrogen fertilizer annually.[1,2] As the world's population continues to increase, and as nonrenewable energy sources are depleted, new methods of energy generation are needed. As one example, methane is the main component in natural gas and is used as a fuel. However, due to its being a gas, it is difficult to capture and transport, and is also deleterious towards the atmosphere as it is a greenhouse gas.[3] If one could convert methane to methanol on the drilling site, the transportation problem associated with methane would be avoided as methanol is a liquid at room temperature and a potentially useful fuel in its own right.[4]

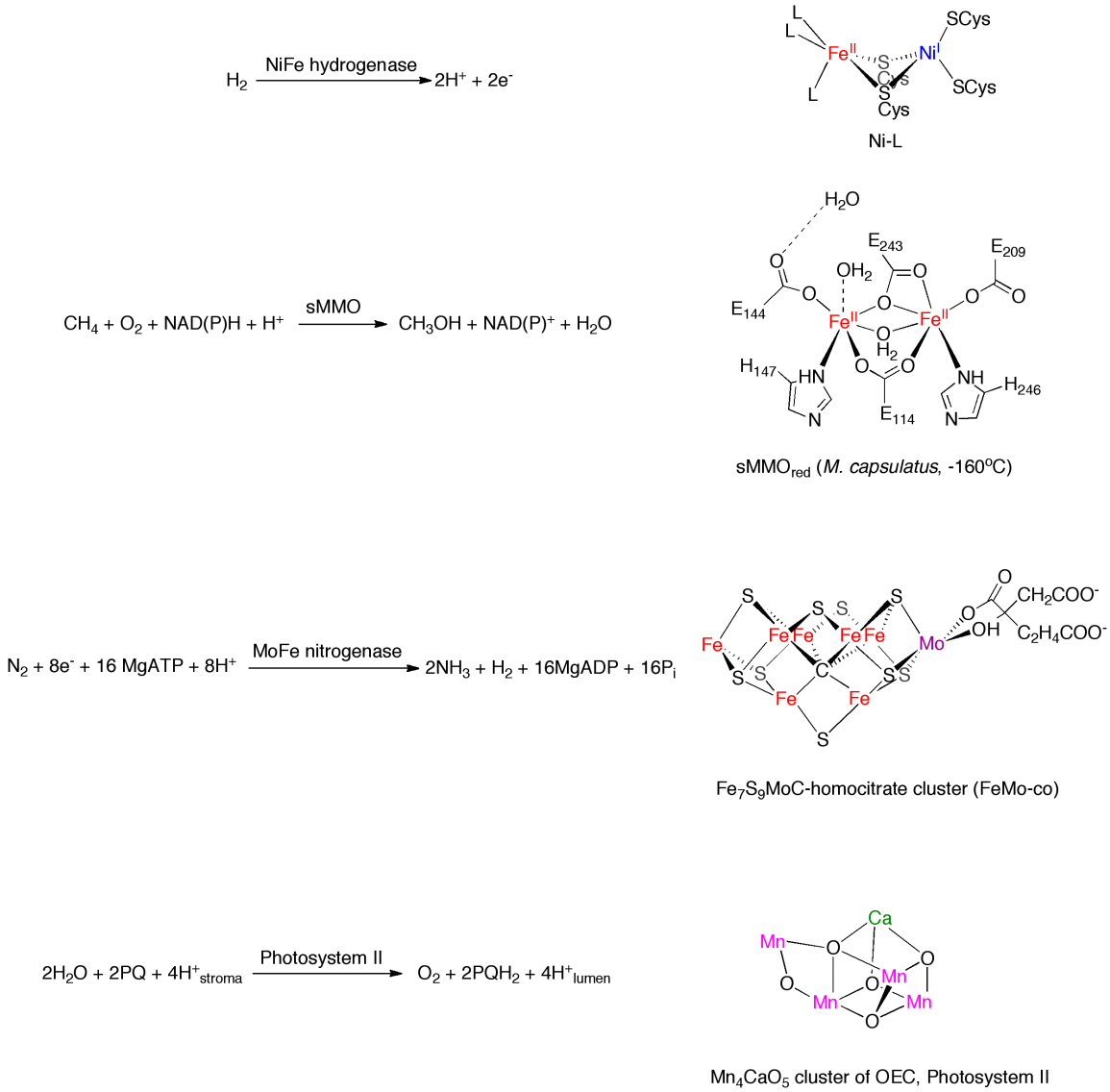

Scheme 1.1. (Left) Reactions catalyzed by metalloenzymes, and (right) the metal-containing cofactors of the enzymes. For the NiFe hydrogenase, the three L donors are 2 CO and 1 CN^-, but the exact positions in which they are located are unknown. It is proposed that one of the two cysteines binding Ni terminally accept the proton that was bridging the metals as a hydride in the Ni-C state. In the Photosystem II catalysis, PQ is plastoquinone, and PQH_2 is plastoquinol.[5-10]

Nature has developed exquisite solutions to these and other challenging chemical problems of relevance to energy management and conversion by utilizing metalloenzymes, including: nitrogenase, which converts N_2 into NH_3; soluble methane

monooxygenase (sMMO), which selectively oxidizes CH_4 to CH_3OH; photosystem II, in which H_2O is oxidized to O_2; and hydrogenases, which reversibly convert protons and electrons to H_2 (Scheme 1.1). The common theme in all of these metalloenzymes is the presence of two or more metals in an active site surrounded by a protein scaffold (Scheme 1.1). The interplay of the metals and the protein residues creates an environment that enables the chemical reactions to be kinetically feasible. The choice of metals and the ligand environment affects properties such as the redox potential of the cofactor. It has recently been suggested that the role of the calcium ion in the Mn_5Ca cluster of photosystem II is to tune the redox potential of the cluster such that water oxidation is thermodynamically favorable.[11]

One strategy towards developing synthetic catalysts for challenging transformations such as those discussed above involves mimicking certain features of metalloenzyme active sites.[12] These may include the same choice of metals, using a ligand with the same or similar donor atoms as the protein residues in the cofactor, and targeting the same geometry at the metal center as found in the enzyme. The field of bioinorganic chemistry, which uses these types of strategies, has been an area of intense focus for a number of years, and has allowed much to be learned about how the enzymes function.[13,67]

Inspiration for a new strategy comes from recent studies into the nickel-iron cofactor of the NiFe hydrogenase. It has been suggested that there exists a Ni-Fe bond in the NiFe hydrogenase Ni-L state and in intermediates that have a vacant bridging site.[14] Considering the variety of first-row transition metals found in metalloenzyme active sites,

an attractive approach involves the synthesis and study of compounds exhibiting direct bonds between two first-row transition metals. Metal-metal bonded complexes of first-row transition metals, due to overlap among the 3*d* orbitals between each metal, will exhibit different properties than the component transition metals (e.g. redox events, oxidation states, and spin states) on their own.

Interest in mid-to-late (Mn to Co), first-row metal-metal bonded complexes stems from their analogy to bimetallic enzyme active sites such as sMMO and ribonucleotide reductases (RNRs), the variety of electronic structures that they can have, and their potential for multielectron reactivity. In particular, remarkable small molecule activation reactions have recently been uncovered for triiron complexes.[15,16] Synthetic examples of metal-metal bonds involving mid-to-late first-row transition metals, especially heterometallic examples, until recently, were uncommon. The reason is that suitable synthetic procedures and supporting ligands, particularly for modular syntheses of metal-metal bonded complexes to give families of compounds, were limited. In particular, the lability of high-spin mid-to-late first-row transition metals makes the selective synthesis of heterobimetallics a challenge, as metal scrambling is an issue that must be addressed.

1.2. Mid-to-Late First-Row Metal-Metal Bonded Complexes: Synthesis and Electronic Structure

Given the paucity of mid-to-late first-row (Co, Fe, Mn) transition metal-metal bonded complexes, some of the interest in these compounds stems from their electronic structures and magnetic properties. Some (though not usually all) of the 3*d* orbitals in these compounds combine maximally between two metals to give bonding and

antibonding orbitals (σ, π, and δ). Different spin states (*S*) may be obtained depending on the metal choices and the supporting ligand, including a number of compounds with high-spin states, which is quite unusual in comparison to many second- and third-row metal-metal bonded complexes. Hence, in this section, the metal-metal bonded complexes will be discussed in terms of the supporting ligand, and molecular orbital diagrams with the dominant electronic configuration will be shown. Since much of the focus of this field has been on rationally synthesizing families of compounds with an appropriate supporting ligand, the discussion will focus on metal-metal bonded complexes with three-atom bridging ligands, two-atom bridging ligands, or polynucleating hexaamide ligands. The important parameters for comparing these complexes are their geometries, metal-metal distances, oxidation states, and spin states (*S*), as these qualities all affect the electronic structure of the compounds.

The overall picture emerging from the metal-metal bonded complexes outlined in this section can be summarized as follows. Generally speaking, diiron or triiron-containing complexes are more likely to attain a high-spin configuration than dicobalt or tricobalt complexes, though high-spin cobalt complexes (e.g. $Co_2(DPhF)_3$[21,29,30]) are known. The spin states and iron-iron distances of triiron compounds are highly variable and especially dependent on the steric bulk and ligand field strengh of supporting ligands. Dimanganese and trimanganese complexes show antiferromagnetic coupling among Mn centers, most of which do not have a Mn-Mn bond; to date, there is one example of a $Mn^{1.5}Mn^{1.5}$ complex with a formal bond order of 0.5 supported by three-atom bridging ligands, though unsupported Mn-Mn bonds are known.[17-20] Only *one* example of a

heterobimetallic metal-metal bonded complex (CoFe, CoMn, or FeMn) was known prior to this thesis work.[21] Heterotrimetallic compounds have been prepared in unbiased ligand platforms either by "knocking out" a metal from a homotrimetallic with a different metal or by the addition of a heterometal to a homobimetallic precursor.[22,23] The ligand framework plays a significant role in dictating the properties of these compounds, and significantly, among these literature examples, there is a lack of an *isostructural* family of both homo- and heterometallic compounds prepared by modular routes – with all of the combinations among CoFe, CoMn, and FeMn – displaying metal-metal bonding.

1.2.1. Complexes with Three-Atom Bridging Ligands

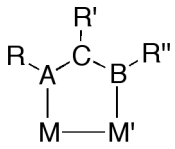

Scheme 1.2. A generic three-atom bridging ligand containing donor atoms A and B linked by atom C with arbitrary substituents R, R', and R" supporting a bond between metals M and M'.

The most common type of bridging ligand found in mid-to-late first-row transition metal-metal bonded complexes has two donor atoms and a third atom linking the two donors (Scheme 1.2). This is likely due to the favorable geometry of the central bridging atom; with sp^2 hybridization of the central atom, the three-atom bridging ligand motif is ideal for bridging transition metals. Substituents on each donor atom as well as the bridging atom can be varied, tuning the electronic properties of the ligand. In practice, nitrogen donors are found most often in this group. These ligands support metal geometries ranging from tetragonal (four bridging ligands) to trigonal (three bridging ligands) to even planar or T-shaped (two bridging ligands).

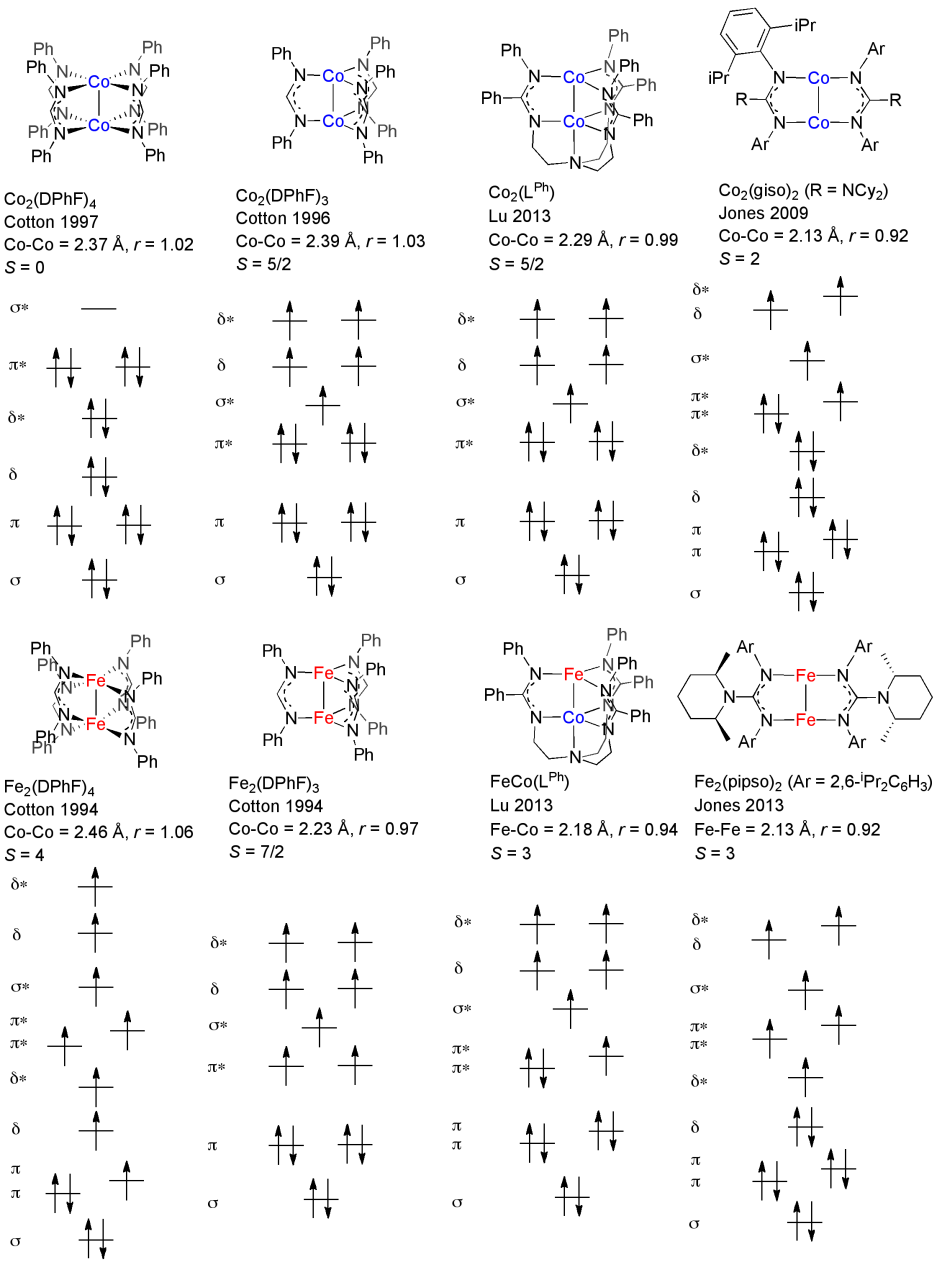

Scheme 1.3. Dicobalt, diiron, and cobalt-iron metal-metal bonded complexes with three-atom bridging ligands.

Complexes with this three-atom bridging motif are shown in Scheme 1.3 along with qualitative molecular orbital diagrams. Most of these complexes, with the exception of $Co_2(DPhF)_4$, adopt high-spin states. It should be noted that the qualitative molecular orbital diagrams represent the dominant configuration of the given spin state and do not

include other, more minor configurations as determined by quantum chemical multiconfigurational calculations. Because all the molecules in Scheme 1.3 are neutral and have monoanionic ligands (or monoanionic ligand "arms" in the case of the heptapodal ligand L^{Ph} prepared by Zall and Lu), the total oxidation state of the bimetallic core is the same as the number of ligands. The compounds will be discussed in order of decreasing donor atom number at a given metal, or generally left to right in Scheme 1.3. The parameter "*r*," which will be frequently cited herein, is defined as the ratio of the distance between the metals in the crystal structure divided by the sum of the single-bond radii of the metals.[24] An *r* value of 1 formally corresponds to a single bond, while values less than 1 may indicate a degree of multiple bonding, and values greater than 1 suggest that the bond is weaker than a single bond. The *r* values do not constitute a rigorous proof of bond order or bond strength, but are best used as a starting point for understanding the bonding situation between two metals.

Cotton and coworkers prepared $Co_2(DPhF)_4$ (DPhF = diphenylformamidinate) by addition of two equivalents of MeLi to $CoCl_2(HDPhF)_2$ (Scheme 1.4).[25] The crystal structure of $Co_2(DPhF)_4$ revealed a Co-Co distance of 2.3735(9) Å (*r* = 1.03, Scheme 1.3). The Co-Co distance is longer than that seen in $Co_2(DPhBz)_4$ (2.302(1) Å, *r* = 0.99, DPhBz = diphenylbenzamidinate) or $Co_2(DTolTA)_4$ (2.265(2) Å, *r* = 0.98, DTolTA = di(*p*-tolyl)triazenate).[26] The decrease in the Co-Co bond length from $Co_2(DPhF)_4$ to $Co_2(DPhBz)_4$ to $Co_2(DTolTA)_4$ was suggested to be likely due to geometric constraints of the ligands. Ab initio configuration interaction (CI) calculations for these three molecules are consistent with an electronic configuration of $(\sigma)^2(\pi)^4(\delta)^2(\delta^*)^2(\pi^*)^4(\sigma^*)^0$ for the $S = 0$

ground state. Formally, these tetragonal cobalt lantern complexes can be described as having a σ bond. The addition of $AgPF_6$ to $Co_2(DPhBz)_4$ gave $[Co_2(DPhBz)_4](PF_6)$, a $Co^{II}Co^{III}$ species. The Co-Co bond length of the crystal structure is 2.322(2) Å (r = 1.00), or nearly the same as $Co_2(DPhBz)_4$, which is not a surprise as an electron is removed from a π* orbital, which only has a small effect on the Co-Co distance.

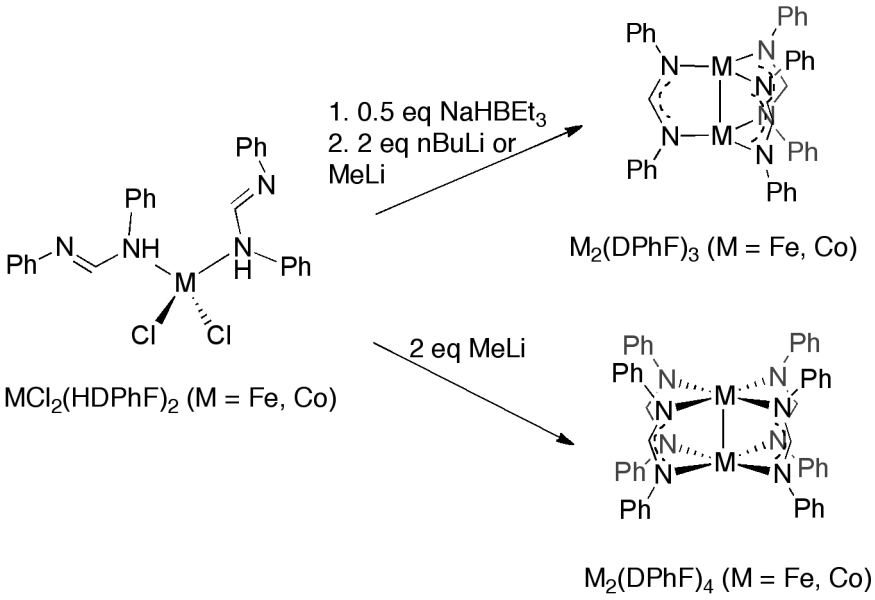

Scheme 1.4. Syntheses of $M_2(DPhF)_3$ or $M_2(DPhF)_4$ (M = Fe, Co)by Cotton and coworkers.

Addition of MeLi to $FeCl_2(HDPhF)_2$ gave the compound $Fe_2(DPhF)_4$, as described by Cotton and coworkers (Scheme 1.4).[27] The solid state structure displays differences from that of $Co_2(DPhF)_4$: pairs of amidinate ligands across from each other in the coordination sphere distort along the Fe-Fe axis. The two pairs of ligands distort in alternating fashions such as to reduce the symmetry from idealized D_{4h} to D_{2d}. The Fe-Fe distance is 2.462(2) Å (r = 1.07, Scheme 1.3). An Evans' method measurement gave 8.8 μ_B, consistent with S = 4. This is in contrast to $Co_2(DPhF)_4$, which has a ground state of S

= 0 and a geometry approximately consistent with D_{4h} symmetry. The high-spin state and distortion of $Fe_2(DPhF)_4$ remained unexplained until recently. Timmer and Berry performed density functional theory (DFT) calculations on $Fe_2(DPhF)_4$ and found that the electronic configuration $(\sigma)^2(\pi)^3(\delta)^1(\delta^*)^1(\pi^*)^2(\sigma^*)^1(d_{x2-y2(1)})^1(d_{x2-y2(2)})^1$ was unstable to a Jahn-Teller distortion.[28] Reduction of the symmetry from D_{4h} to D_{2d} transforms the $(2\pi)^3$ configuration into $(\pi)^2(\pi)^1$. This distortion also has the effect of lowering the energies of the d_{x2-y2} orbitals (they are too high in energy in $Co_2(DPhF)_4$ to be available for metal-metal bonding due to strong metal-ligand antibonding interactions), resulting in a second pair of half-filled δ and δ* orbitals. Hence, the electronic configuration of $Fe_2(DPhF)_4$ is $(\sigma)^2(\pi)^2(\pi)^1(\delta)^1(\delta^*)^1(\pi^*)^1(\pi^*)^1(\sigma^*)^1(\delta)^1(\delta^*)^1$. Formally, the molecule has a bond order of 1 due to the presence of a half σ bond and a half π bond, though since the overlap of a π orbital is less than that of a σ orbital, the Fe-Fe distance is less than the Co-Co distance in $Co_2(DPhF)_4$, which has a single bond due to a full σ bond.

The complex $Co_2(DPhF)_3$ was prepared by Cotton and coworkers by treating $CoCl_2(HDPhF)_2$ with a half equivalent of $NaHBEt_3$, then deprotonating with nBuLi (Scheme 1.4).[29,30] It has a Co-Co distance of 2.385(1) Å (r = 1.03, Scheme 1.3). The related compound $Co_2(DPhBz)_3$ was prepared in the same manner as $Co_2(DPhF)_3$; its Co-Co distance is 2.3201(9) Å (r = 1.00), ~0.06 Å shorter than that of $Co_2(DPhF)_3$. The reason suggested by the authors for this shortening relates to steric factors: the central phenyl ring in DPhBn pushes the N-bonded phenyl rings out, which compresses the bite angle of the ligand and forces the cobalts closer together. The room temperature magnetic susceptibilities of both $Co_2(DPhF)_3$ and $Co_2(DPhBz)_3$ were measured to be 5.2 μ_B. While

Evans' method measurements of the magnetic susceptibility of $Co_2(DPhF)_3$ and $Co_2(DPhBz)_3$ gave intermediate values between those corresponding to $S = 3/2$ and $S = 5/2$ electronic states, an electron paramagnetic resonance (EPR) spectrum of $Co_2(DPhF)_3$ collected by Zall and Lu was consistent with an energetically well isolated $S = 5/2$ ground state.[21] The electronic structures of $Co_2(DPhF)_3$ and $Co_2(DPhBz)_3$ are consistent with a Co_2^{3+} oxidation state of the core, or a fully delocalized mixed-valence $Co^{1.5}Co^{1.5}$ oxidation state. The electronic population, then, of the dominant electronic configuration of the ground state of $Co_2(DPhF)_3$ is $(\sigma)^2(\pi)^4(\pi^*)^4(\sigma^*)^1(\delta)^2(\delta^*)^2$, which is consistent with a formal bond order of 0.5.

The diiron analogue of $Co_2(DPhF)_3$, $Fe_2(DPhF)_3$, was prepared by Cotton and coworkers by the addition of a half equivalent of $NaHBEt_3$, then 2 equivalents of MeLi (Scheme 1.4).[31,32] The compound $Fe_2(DPhBz)_3$ could be prepared analogously to $Fe_2(DPhF)_3$. The Fe-Fe bond lengths are 2.2318(8) Å ($r = 0.97$) for $Fe_2(DPhF)_3$ and 2.198(2) Å ($r = 0.95$) for $Fe_2(DPhBz)_3$ (Scheme 1.3). These lengths are significantly shorter than those of the dicobalt analogues $Co_2(DPhF)_3$ and $Co_2(DPhBz)_3$. This discrepancy can be understood simply by the removal of two antibonding electrons upon going from the dicobalt molecules (15 total electrons) to the diiron molecules (13 total electrons). $Fe_2(DPhF)_3$ has been characterized by various physical and spectroscopic methods, most of which were collected recently by Zall and Lu and coworkers.[33] The electron paramagnetic resonance (EPR) spectrum and SQUID magnetometry data were consistent with a well isolated $S = 7/2$ ground state, the highest possible spin for Fe_2^{3+}. Variable-field, variable-temperature (VTVH) Mössbauer spectra were globally fitted with

an isomer shift (δ) of 0.65 mm s^{-1}, quadrupole splitting (ΔE_Q) = 0.32 mm s^{-1}, and a zero-field splitting ($D_{7/2}$) of 8.2 cm^{-1}. As the fitting required only one unique iron, the Fe_2^{3+} core must be fully delocalized, or $Fe^{1.5}Fe^{1.5}$, on the Mössbauer timescale.

Theoretical calculations were performed, initially with SCF-Xα-SW methods on a truncated model, and later with the complete active space self-consistent field (CASSCF) and multiconfigurational second-order perturbation theory (CASPT2) methods on the full molecule.[33,34] The electronic structures from the two calculations were remarkably similar. The CASSCF/PT2 calculations predicted a single, dominant configuration (73%) with $(\sigma)^2(\pi)^4(\pi^*)^2(\sigma^*)^1(\delta)^2(\delta^*)^2$. Although the formal bond order is 1.5 (a half σ bond and a full π bond), the effective bond order, which considers minor configurations that contribute to the ground-state wavefunction, is lower at 1.15.

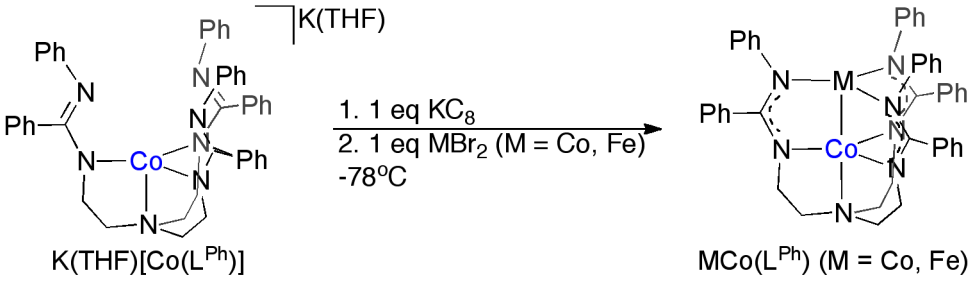

Scheme 1.5. Modular synthesis of $MCo(L^{Ph})$ (M = Co, Fe) by Zall and Lu.

A recent advance in the synthesis of mid-to-late first-row transition metal-metal bonded complexes was the inclusion of a tertiary amine that binds apically to the metal-metal bond. This amine ties three ligand arms together to form a heptadentate tris(amidinato)amine ligand, tris(2-(*N*-phenylbenzamidinato)ethyl)amine (H_3L^{Ph}). Two cobalt-containing bimetallics were prepared using L^{Ph}: a dicobalt compound, $Co_2(L^{Ph})$, and a heterobimetallic, $FeCo(L^{Ph})$ (Scheme 1.5).[21] In the synthesis of the L^{Ph} bimetallics, H_3L^{Ph} was deprotonated with three equivalents of benzylpotassium, then $CoCl_2$ was added, from which the monocobalt species $K(THF)[Co(L^{Ph})]$ could be isolated. For the addition of the second metal, the reductant KC_8 was added to the monocobalt precursor at -78ºC, then MBr_2 (M = Co or Fe) was added to the reaction mixture cold. For the FeCo heterobimetallic, the addition must be conducted at low temperatures to impede metal scrambling. Crystal structures showed Co-M distances of 2.2944(7) Å (r = 0.99) for $Co_2(L^{Ph})$ and 2.1846(4) Å (r = 0.94) for $FeCo(L^{Ph})$ (Scheme 1.3). $Co_2(L^{Ph})$ has a significantly shorter Co-Co distance than $Co_2(DPhF)_3$, though it is close to that of $Co_2(DPhBz)_3$, which also has a phenyl ring on the bridgehead position. As was seen earlier with the tetragonal dicobalt lantern compounds, the cobalt-cobalt separation can

depend on the substituents of the bridging ligand. Fe and Co atoms have similar sizes, and so they cannot be distinguished in FeCo(L^{Ph}) by conventional X-ray crystallographic methods. However, anomalous diffraction experiments were performed on FeCo(L^{Ph}). Anomalous diffraction is a technique that takes advantage of the fact that anomalous dispersion contributions to scattering factors for a given element will drop significantly around the element's K-edge. Different elements have significantly different K-edge energies. Therefore, by carrying out multiple X-ray diffraction experiments on FeCo(L^{Ph}) at different X-ray energies around the Fe and the Co K edges, and then performing a least-squares refinement of all the anomalous scattering experiment data collected at different energies simultaneously, the Fe/Co ratios at the two sites were determined. Assuming statistical mixing of the metals at each site, the percentage of FeCo(L^{Ph}) in the sample was 89%. The location of Fe and Co found by anomalous diffraction was as expected based on the synthetic protocol. The initial report with this FeCo bimetallic was a watershed moment in the first-row transition metal heterobimetallic field, because it demonstrated that design of the appropriate ligand framework could allow the sequential addition of two labile transition metals to generate heterobimetallic metal-metal bonded complexes with high site-specific purity.

EPR spectroscopy and SQUID magnetometry on $Co_2(L^{Ph})$ were both consistent with an $S = 5/2$ ground state. CASSCF/PT2 calculations found a dominant electronic configuration of $(\sigma)^2(\text{Co1 } d_{xz},d_{yz})^4(\text{Co2 } d_{xz},d_{yz})^4(\sigma^*)^1(\delta)^2(\delta^*)^2$, where the formal bond order is 0.5 (0.5 σ). The EBO is as expected at 0.51. FeCo(L^{Ph}) was characterized by SQUID magnetometry, revealing a high-spin, $S = 3$ ground state. CASSCF/PT2

calculations revealed the main electronic configuration to be $(\sigma)^2(\pi)^4(\pi^*)^3(\sigma^*)^1$(Co $d_{xy},d_{x2-y2})^2$(Fe $d_{xy},d_{x2-y2})^2$, where the formal bond order is 1 (0.5 σ + 0.5 π). The EBO is only slightly lower at 0.95. The increase in EBO upon going from the 15 *d* electrons of $Co_2(L^{Ph})$ to the 14 *d* electrons of $FeCo(L^{Ph})$ can be attributed to the removal of an electron from an orbital of π* symmetry, which had been localized in $Co_2(L^{Ph})$ but is delocalized in $FeCo(L^{Ph})$. The Mössbauer isomer shift (δ) for this complex is 0.65 mm/s, whereas the quadrupole splitting (ΔE_Q) is 0.64 mm/s. The δ value is exactly the same as that in the mixed-valent diiron complex, $Fe_2(DPhF)_3$, which has a fully delocalized $Fe^{1.5}Fe^{1.5}$ core. Thus, by analogy, a delocalized $(FeCo)^{3+}$ core was proposed for $FeCo(L^{Ph})$.

With appropriately bulky ligands, planar (or I-shaped) complexes with the formulation $M_2(L)_2$ have been isolated. These have the shortest crystallographically characterized M-M bond distances to date for the given metal; in these complexes, the metals are in the monovalent oxidation state. Jones and coworkers isolated $Co_2(piso)_2$ (piso = $ArNC(^tBu)CNAr^-$, Ar = 2,6-$^i Pr_2C_6H_3$) and $Co_2(giso)_2$ (giso = $ArNC(NCy_2)CNAr^-$, Ar = 2,6-$^i Pr_2C_6H_3$) from reduction of $[Co(L)]_2(\mu\text{-}X)_2$ (X = Br or I) with potassium in cyclohexane.[35] These complexes have extremely short Co-Co bond distances of 2.1404(1) Å (*r* = 0.92) for $Co_2(piso)_2$ and 2.1345(7) Å (*r* = 0.92) for $Co_2(giso)_2$ (Scheme 1.3). SQUID magnetometry data and an Evans' method measurement were consistent with a high-spin, *S* = 2 ground state. CASSCF/PT2 calculations on truncated models of $Co_2(piso)_2$ and $Co_2(giso)_2$ were consistent with *S* = 2 ground states. The dominant configuration of the *S* = 2 state for both of the truncated models is

$(\sigma)^2(\pi)^2(\pi)^2(\delta)^2(\delta^*)^2(\pi^*)^2(\pi^*)^1(\sigma^*)^1(\delta)^1(\delta^*)^1$. The formal bond order of these complexes is 1 (0.5 σ and 0.5 π). The effective bond order of these complexes is 0.76 for the $Co_2(piso)_2$ truncated model and 0.40 for the $Co_2(giso)_2$ truncated model. The FBO and EBOs of these compounds are much lower than what would be expected from the crystallographic bond distances.

Jones and coworkers prepared $Fe_2(pipiso)_2$ (pipiso = ArNC(N(*cis*-2,6-$Me_2C_5H_8$)CNAr$^-$, Ar = 2,6-^{i}Pr$_2$C$_6$H$_3$) from the reduction of [(Fe(pipiso)$_2$](μ-Br)$_2$ with one equivalent of {(^{Mes}nacnac)Mg}$_2$ (Mes = 2,4,6-$Me_3C_6H_2$) (Scheme 1.3). The crystal structure revealed a quite short Fe-Fe bond of 2.1270(7) Å (r = 0.92). The CASSCF/PT2 calculations predict the ground spin state to be high spin, or S = 3. The dominant electronic configuration of $(\sigma)^2(\pi)^2(\pi)^2(\delta)^2(\delta^*)^1(\pi^*)^1(\pi^*)^1(\sigma^*)^1(\delta)^1(\delta^*)^1$ is consistent with a FBO of 2, or a double bond (0.5 σ, 1 π, and 0.5 δ). The calculations yield an EBO of 1.19, suggesting a modest amount of multiple bonding despite the experimentally short Fe-Fe bond.

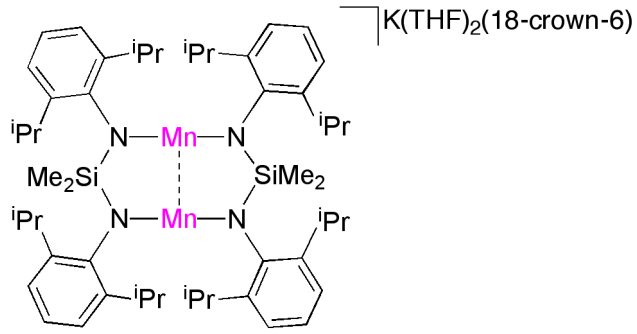

[Mn_2(Me_2Si(N(2,6-^{i}Pr$_2$C$_6$H$_3$)$_2$)$_2$][K(THF)$_2$(18-crown-6)]
Tsai 2011
Mn-Mn = 2.68 Å, r = 1.15

Scheme 1.6. [(THF)$_2$K(18-crown-6)][Mn_2(Me_2Si(NAr)$_2$)$_2$] (Ar = 2,6-^{i}Pr$_2$C$_6$H$_3$), prepared by Tsai and coworkers.

Tsai and coworkers crystallographically characterized $[(THF)_2K(18\text{-crown-}6)][Mn_2(Me_2Si(NAr)_2)_2]$, with Ar = 2,6-$^{i}Pr_2C_6H_3$ and Mn-Mn = 2.6848(8) Å/*r* = 1.15) (Scheme 1.6). This formally mixed-valent $Mn^{II}Mn^{I}$ monoanionic complex has no major structural differences at each Mn center of the crystal structure, suggesting a fully delocalized $Mn^{1.5}Mn^{1.5}$ core. The room-temperature magnetic moment measured by SQUID magnetometry was 6.10 μ_B, and the magnetism gradually decreased to approximately 4.10 μ_B at the lowest temperature measured (below 10 K). The authors postulated an antiferromagnetic interaction between the Mn centers and suggested only a bond order of 0.5, but the data were not modeled, and the electronic structure of the molecule was not studied by computations.

1.2.2. Complexes with Two-Atom Bridging Ligands

Unlike the three-atom bridging ligands, two-atom bridging ligands show diversity in the types of donor atoms that have been proven to support metal-metal bonds with mid-to-late first-row transition metals. Both phosphinoamides (PN donors) and iminoacyl ligands (CN donors) have been proven to form complexes with short metal-metal distances consistent with metal-metal bonding.

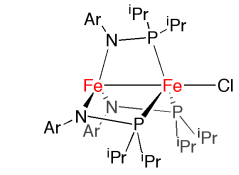

Fe(MesNP^{i}Pr$_2$)$_3$FeCl
Thomas 2012
Fe-Fe = 2.59 Å, r = 1.12
S = 4

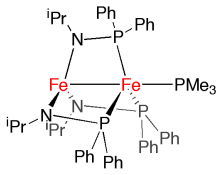

Fe(^{i}PrNPPh$_2$)$_3$Fe(PMe$_3$)
Thomas 2013
Fe-Fe = 2.45 Å, r = 1.06
S = 7/2

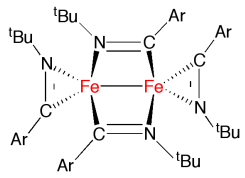

(^{t}BuN=CMes)$_2$Fe$_2$(μ^2-^{t}BuN=CMes)$_2$
Floriani 1994
Fe-Fe = 2.37 Å, r = 1.03
S = 0

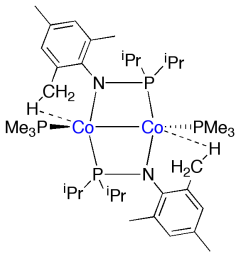

(PMe$_3$)Co(MesNP^{i}Pr$_2$)$_2$Co(PMe$_3$)
Thomas 2013
Co-Co = 2.55 Å, r = 1.10
S = 1

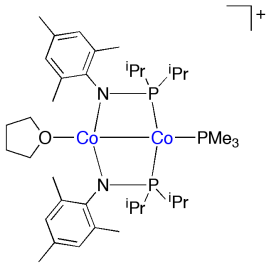

[(THF)Co(MesNP^{i}Pr$_2$)$_2$Co(PMe$_3$)](PF$_6$)
Thomas 2013
Co-Co = 2.49 Å, r = 1.08
S = 1/2

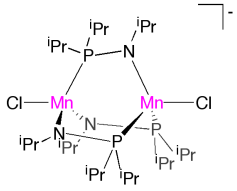

[Li(THF)$_3$][ClMn(^{i}PrNP^{i}Pr$_2$)(^{i}Pr$_2$PN^{i}Pr)MnCl]
Thomas 2012
Mn-Mn = 3.25 Å, r = 1.39
S = 0

Scheme 1.7. Selected examples of bimetallics containing Mn, Fe, and Co ligated by two-atom bridging ligands.

Thomas and coworkers prepared the symmetric $Co^{I}Co^{I}$ complex (Me$_3$P)Co(MesNP^{i}Pr$_2$)$_2$Co(PMe$_3$) by reduction of (THF)Co(MesNP^{i}Pr$_2$)$_2$(μ-I)CoI with excess Na/Hg amalgam in the presence of excess PMe$_3$ in THF.[36] The Co-Co distance is 2.5536(3) Å (r = 1.10), substantially longer than the planar $Co^{I}Co^{I}$ complexes Co$_2$(piso)$_2$ and Co$_2$(giso)$_2$ mentioned above (Scheme 1.7). Some of this effect is surely due to the presence of two PMe$_3$ ligands apical to the Co-Co bond. It should be noted that the PMe$_3$ ligands are 0.93 Å out of the Co$_2$N$_2$P$_2$ plane created by the phosphinoamide ligands, and that there is a weak agostic interaction between the Co and one of the hydrogens of one of the methyl groups of the mesityl substituent of the phosphinoamide ligand. The authors proposed that the PMe$_3$ out-of-plane distortion arises from this agostic interaction. The solution magnetic moment of (Me$_3$P)Co(MesNP^{i}Pr$_2$)$_2$Co(PMe$_3$) was

consistent with an $S = 1$ ground state. $(PMe_3)Co(MesNP^iPr_2)_2Co(PMe_3)$ was oxidized with $FcPF_6$ to provide the planar mixed-valent $Co^{II}Co^{I}$ compound $[(THF)Co(MesNP^iPr_2)_2Co(PMe_3)](PF_6)$. Interestingly, one of the two phosphinoamide ligands rearranged so that one cobalt bound both phosphines of the phosphinoamides ($(P_3)Co$ coordination environment) and the other cobalt bound both amides of the phosphinoamides ($(N_2O)Co$ coordination environment). The Co-Co distance in the crystal structure is 2.4864(6) Å ($r = 1.08$) (Scheme 1.7). This shortening is consistent with removal of an antibonding electron upon oxidation. DFT calculations suggest that the Co^{II} is the amide-ligated Co. The rearrangement of one of the phosphinoamides was suggested to occur because the π-donating amide preferred to bind to Co^{II} rather than Co^{I}. EPR spectroscopy on $[(THF)Co(MesNP^iPr_2)_2Co(PMe_3)](PF_6)$ was consistent with an $S =$ ½ ground state.

Thomas and co-workers have also used phosphinoamides to isolate trigonal $Fe^{II}Fe^{II}$ and mixed-valent Fe_2^{3+} complexes. Typically, the $Fe^{II}Fe^{II}$ compounds are prepared by deprotonating three equivalents of a phosphinoamine with an appropriate base (e.g. KH or *n*BuLi) and mixing with $FeCl_2$ in THF. The $Fe^{II}Fe^{II}$ complexes include $Fe(ArNP^iPr_2)_3FeCl$ (where Ar = 2,4,6-$Me_3(C_6H_2)$) and $Fe(^iPrNP^iPr_2)_2(^iPr_2PN^iPr)FeCl$, with Fe-Fe bond distances of 2.5855(4) Å ($r = 1.11$) and 2.6112(7) Å ($r = 1.12$), respectively (Scheme 1.7).[37] In $Fe(ArNP^iPr_2)_3FeCl$, all three phospinoamide ligands are oriented in the same direction, giving a triamido iron and a triphosphine iron, which also binds to chloride. In $Fe(^iPrNP^iPr_2)_2(^iPr_2PN^iPr)FeCl$, one of the phosphinoamides is oriented in the opposite direction as the other two, creating two new coordination

environments, $(N_2P)Fe$ and $(NP_2)FeCl$. Evans' method measurements suggest a high-spin ground state of $S = 4$ for these $Fe^{II}Fe^{II}$ cores. Wiberg bond indices were calculated by DFT to be 0.42 and 0.43, consistent with weak Fe-Fe bonding.

Using a less electron-rich phosphinoamide, $(^{i}PrNPPh_2)^{-}$, Thomas and coworkers prepared Fe_2^{3+} complexes, $Fe_2(^{i}PrNPPh_2)_3L$, featuring axial phosphines, L = PMe_3 and $PPh_2NH^{i}Pr$.[38] The Fe_2^{3+} $PPh_2NH^{i}Pr$-adduct was isolated directly from the reduction of the Fe_2^{4+} precursor, $Fe(^{i}PrNPPh_2)_3Fe(\eta^2\text{-}^{i}PrNPPh_2)$ with 1.5 equiv. sodium amalgam. Adding excess PMe_3 to $Fe(\mu\text{-}^{i}PrNPPh_2)_3Fe(PPh_2NH^{i}Pr)$ then formed the Fe_2^{3+} PMe_3-adduct. While the Fe_2^{4+} precursor has a negligible metal-metal interaction (Fe-Fe distance is 2.87 Å, $r = 1.24$), both Fe_2^{3+} complexes have considerably contracted Fe-Fe distances of 2.4545(5) Å ($r = 1.05$, L = PMe_3) and 2.4694(3) Å ($r = 1.06$, L = $PPh_2NH^{i}Pr$) (Scheme 1.7). The reduction is primarily localized at the $(P_4)Fe$ site, as the Fe-P bond distances contract significantly from 2.49 Å in the Fe_2^{4+} precursor to 2.345−2.385 Å due to Fe-P backbonding. The Fe-Fe distance is noticeably longer than that of $Fe_2(DPhF)_3$, likely because (1) the different ligand environments of the two Fe centers ($(N_3)Fe$ and $(P_4)Fe$) result in mismatched orbital energies, and (2) a phosphine ligand apical to the Fe-Fe bond is present. SQUID magnetometry on $Fe_2(^{i}PrNPPh_2)_3(PMe_3)$ was consistent with a well-isolated $S = 7/2$ ground state, like $Fe_2(DPhF)_3$. DFT calculations on $Fe_2(^{i}PrNPPh_2)_3(PMe_3)$ show polarized σ overlap and relatively poor π and δ overlap, the latter as a result of mismatched orbital energies.[38] The calculations on $Fe_2(^{i}PrNPPh_2)_3(PMe_3)$ support it as having a polar covalent Fe-Fe bond, in contrast to the

nonpolar covalent Fe-Fe bond of $Fe_2(DPhF)_3$, which is what is expected based on the donor sets of the two compounds.

Phosphinoamide supported $Mn^{II}Mn^{II}$ complexes will be discussed briefly since they do not have a metal-metal bond. The complex $[Li(THF)_3][ClMn(^{i}PrNP^{i}Pr_2)_2(^{i}Pr_2PN^{i}Pr)MnCl]$ has three bridging phosphinoamides that are coordinated unsymmetrically, creating a $(ClNP_2)Mn$ coordination environment and a $(ClN_2P)Mn$ coordination environment.[37] The $Li(THF)_3^+$ cation interacts with the Cl at the $(ClN_2P)Mn$ site. The Mn-Mn distance of 3.2464(9) Å (*r* = 1.39, Scheme 1.7) indicates the two Mn centers do not bond with each other. A qualitative analysis of SQUID magnetometry data of $[Li(THF)_3][ClMn(^{i}PrNP^{i}Pr_2)_2(^{i}Pr_2PN^{i}Pr)MnCl]$ is consistent with two Mn^{II} centers weakly antiferromagnetically coupling to give an $S = 0$ ground state. It is proposed that the antiferromagnetic exchange occurs through the phosphinoamide ligand. Note that this is different from the phosphinoamide-supported $Fe^{II}Fe^{II}$ complexes, which *ferromagnetically* couple through their Fe-Fe bond to give an $S = 4$ ground state.

An iminoacyl-supported $Fe^{II}Fe^{II}$ complex, $(\eta^2\text{-MesC=N}^{t}\text{Bu})Fe(\mu^2\text{-MesC=N}^{t}\text{Bu})^2Fe(\eta^2\text{-MesC=N}^{t}\text{Bu})$, was prepared by adding $C{\equiv}N^{t}Bu$ to $Fe_2(Mes)_4$ at 0°C in THF.[39] Two of the iminoacyl ligands bind each Fe center terminally while the other two iminoacyl ligands bridge the Fe centers. The Fe-Fe bond distance is 2.371(4) Å (*r* = 1.02, Scheme 1.7). SQUID magnetometry data were fit to an $S = 0$ ground state. A single Fe-Fe bond was deduced, as the strong coupling of only one unpaired electron per Fe(II) would be consistent with the magnetic data.

Prior to this thesis work, there was only one example of a heterobimetallic (CoFe, CoMn, or FeMn) complex with metal-metal bonding: the earlier described FeCo(L^{Ph}).[21] This is understandable given that many of the ligands in this section are symmetric, which means that the labile metals can scramble easily in a bimetallic synthesis. In other cases, even though the ligands are not symmetric (e.g., the two-atom donor ligands such as the phosphinoamides), the syntheses are done with a one-pot procedure, and/or the two metals are added at the same time. In this context, a major advancement contained in this thesis work was the synthesis of an *isostructural* family of homobimetallic and heterobimetallic metal-metal bonded complexes with the elements Co, Fe, and Mn by a modular procedure.

1.2.3. Polynuclear (L)M_3 and (L)$_2M_6$ Clusters

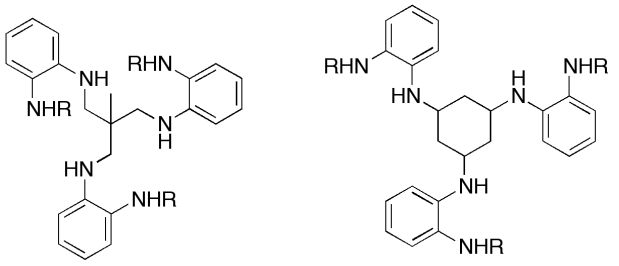

R = H, ^{H}L
R = Ph, ^{Ph}L
R = Mes, ^{Mes}L

R = H, ^{H,Cy}L
R = $SiMe_2{}^tBu$, ^{tbs}L

Scheme 1.8. Trinucleating ligands designed by Betley.

Betley and coworkers have designed hexaamide ligands that support clusters with a triangular arrangement of metals (Scheme 1.8). Both homometallic and heterometallic clusters of Co, Fe, and Mn have been prepared. Extensive spectroscopic studies have revealed insights into the electronic structure of the compounds. While there are detailed

differences among clusters with characteristics such as the binding mode of the dianilide arms of the supporting ligand, these details will not be discussed because they do not affect the spin states of the Co and Mn clusters, and while different binding modes of the Fe clusters correlate with different cluster spin states, they are consequences of the steric bulk of the anilide substituents. In homometallic complexes that do not feature threefold symmetry, the metal-metal distances will be averaged except where otherwise noted. The Co_3^{n+} (n = 6, 7) and Mn_3^{6+} clusters prepared by Betley and coworkers are low-spin and will be discussed first. The Fe_3^{n+} (n = 6, 7) clusters show greater diversity in spin states and bonding and will be discussed next. The discussion of Betley's compounds within this synthesis and electronic structure section will conclude with heterometallic Fe_2Co^{7+}, $FeCo_2^{7+}$, and Fe_2Mn^{6+} examples.

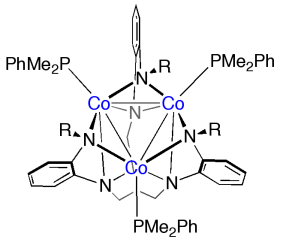

(^{R}L)Co$_3$(L')$_3$, Co$_3^{6+}$
Betley 2013
Co-Co (averages):
R = H: 2.39 Å, *r* = 1.03, *S* = 1/2
R = Ph: 2.43 Å, *r* = 1.05, *S* = 1/2

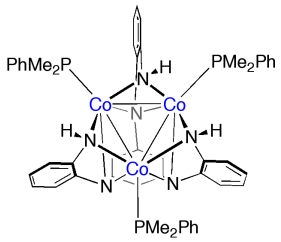

(^{H,Cy}L)Co$_3$(PMe$_2$Ph)$_3$, Co$_3^{6+}$
Betley 2013
Co-Co (average): 2.39 Å, *r* = 1.03, *S* = 1/2

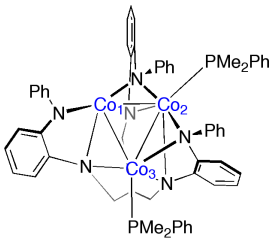

(^{Ph}L)Co$_3$(PMe$_2$Ph)$_2$, Co$_3^{6+}$
Betley 2013
Co-Co:
Co$_1$-Co$_2$: 2.34 Å, *r* = 1.01
Co$_3$-Co$_{1,2}$ (average): 2.44 Å, *r* = 1.05
S = 1/2

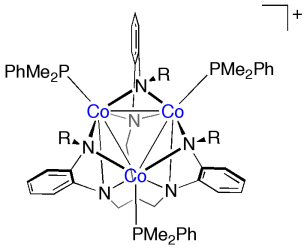

[(^{R}L)Co$_3$(L')$_3$](PF$_6$), Co$_3^{7+}$
Betley 2013
Co-Co (averages):
R = H: 2.34 Å, *r* = 1.01, *S* = 0
R = Ph: 2.39 Å, *r* = 1.03, *S* = 0

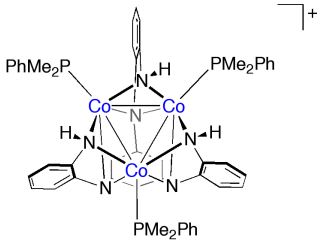

[(^{H,Cy}L)Co$_3$(PMe$_2$Ph)$_3$](PF$_6$), Co$_3^{7+}$
Betley 2013
Co-Co (average): 2.35 Å, *r* = 1.01, *S* = 0

Scheme 1.9. Co$_3^{n+}$ (n = 6 or 7) clusters crystallographically characterized by Betley and coworkers.

Co$_3^{6+}$ complexes have been prepared by the addition of 1.5 equivalents of Co$_2$(N(SiMe$_3$)$_2$)$_4$ to ^{R}LH$_6$ (R = H, Ph, Mes with a 1,1,1-(trimethyl)-substituted ethyl backbone, or R = H with a 1,3,5-substituted cyclohexyl backbone) in the presence of three equivalents of a phosphine (PMe$_3$ or PMe$_2$Ph).[40] These afforded complexes (^{R}L)Co$_3$(PMe$_2$R')$_3$ in good yields. The PMe$_2$Ph-ligated complexes have been characterized by X-ray crystallography; these approximately C_3 symmetric compounds have average Co-Co distances of 2.3860 Å (*r* = 1.03) for (^{H}L)Co$_3$(PMe$_2$Ph)$_3$, 2.3855 Å (*r* = 1.03) for (^{H,Cy}L)Co$_3$(PMe$_2$Ph)$_3$, and 2.4270 Å (*r* = 1.05) for (^{Ph}L)Co$_3$(PMe$_2$Ph)$_3$ (Scheme 1.9). All of these complexes have distorted square pyramidal (N$_4$P)Co

coordination environments. A fourth Co_3^{6+} cluster was prepared by the addition of only two equivalents of PMe_2Ph in the same manner as described above to afford $(^{Ph}L)Co_3(PMe_2Ph)_2$. This latter complex has a short Co-Co distance (2.3368(7) Å, r = 1.01) and two long Co-Co distances (average 2.4382 Å, r = 1.05) (Scheme 1.9). In terms of the Co-Co distances, there are two Co that interact slightly more strongly with each other than with the third, unique Co. One might expect that the unique Co would not have PMe_2Ph bound to it; however, this is not the case: the Co that does not have a phosphine bound to it is involved in the strong Co-Co interaction with a separation of 2.3368(7) Å. Hence, this cluster has C_1 symmetry. Evans' method measurements at room temperature and EPR spectroscopy at 3.3 K of these clusters are all consistent with S = ½ ground states. That the magnetic moment does not vary with temperature would imply very strong antiferromagnetic coupling, and the authors proposed that this arises from cobalt-cobalt bonding within the core of these clusters.

Cyclic voltammetry on the cluster $(^{H}L)Co_3(PMe_3)_3$ revealed a reversible oxidation at -1.75 V (vs. Fc/Fc^+).[40] Indeed, chemical oxidation of the clusters could be accomplished with $FcPF_6$. Three of these Co_3^{7+} clusters were crystallographically characterized: $[(^{H}L)Co_3(PMe_2Ph)_3](PF_6)$, with an average Co-Co distance of 2.344 Å (r = 1.01), $[(^{H,Cy}L)Co_3(PMe_2Ph)_3](PF_6)$, with a Co-Co distance of 2.3477(6) Å (r = 1.01), and $[(^{Ph}L)Co_3(PMe_2Ph)_3](PF_6)$, with a Co-Co distance of 2.3907(5) Å (r = 1.03) (Scheme 1.9). All of these cationic clusters are either approximately or crystallographically C_3 symmetric and are diamagnetic at room temperature. DFT calculations revealed that, upon oxidation of the Co_3^{6+} clusters, an electron is removed from an orbital that has Co-

Co π* symmetry, which explains the *ca* 0.04 Å contraction of the Co-Co distances of the Co_3^{7+} clusters compared to the Co_3^{6+} clusters.

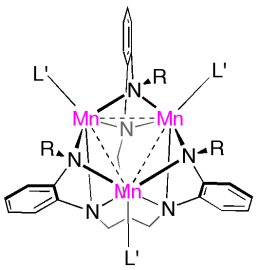

$(^{R}L)Mn_3(L')_3$, Mn_3^{6+}
Betley 2011, 2013
Mn-Mn (averages):
R = H, L' = THF: 2.82 Å, *r* = 1.21, *S* = 1/2
R = H, L' = py: 2.86 Å, *r* = 1.22, *S* = 1/2
R = Ph, L' = py: 2.82 Å, *r* = 1.21, *S* = 1/2
R = Mes, L' = py: 3.13 Å, *r* = 1.34, *S* = 1/2

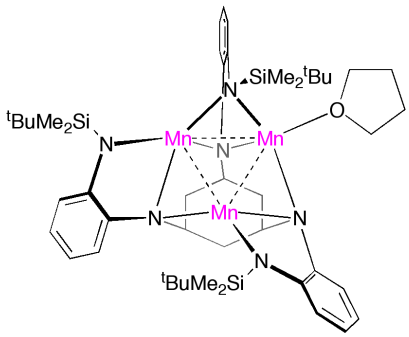

$(^{tbs}L)Mn_3(THF)$, Mn_3^{6+}
Betley 2013
Mn-Mn (average): 3.07 Å, *r* = 1.34, *S* = 1/2

Scheme 1.10. Mn_3^{6+} clusters crystallographically characterized by Betley and coworkers.

Mn_3^{6+} clusters prepared by Betley and coworkers have low-spin states like their Co_3^{6+} complexes, though the spin arises by a different kind of metal-metal interaction, as this discussion will show. Mixing the ^{R}L ligand with 1.5 equivalents of $Mn_2(N(SiMe_3)_2)_4$ in THF gave the cluster $(^{H}L)Mn_3(THF)_3$ for R = H; performing a workup in which three drops of pyridine was added afforded the clusters $(^{R}L)Mn_3(py)_3$ in good yields.[40,41] Another Mn_3^{6+} cluster, $(^{tbs}L)Mn_3(THF)$, was prepared by mixing 1 equivalent of $Mn_3(Mes)_6$ with $^{tbs}LH_6$.[23] Five of these clusters have been crystallized: $(^{H}L)Mn_3(THF)_3$, with an average Mn-Mn distance of 2.816 Å (*r* = 1.21); $(^{H}L)Mn_3(py)_3$, with an average Mn-Mn distance of 2.8550 Å (*r* = 1.22); $(^{Ph}L)Mn_3(py)_3$, with an average Mn-Mn distance of 2.8201 Å (*r* = 1.21); $(^{Mes}L)Mn_3(py)_3$, with an average Mn-Mn distance of 3.1260 Å (*r* = 1.34); and $(^{tbs}L)Mn_3(THF)$, with an average Mn-Mn distance of 3.0730 Å (*r* = 1.34)

(Scheme 1.10). These clusters have approximate C_3 symmetry by crystallography. SQUID magnetometry and EPR spectroscopy data are consistent with $S = ½$ ground states for these clusters. The $(^{Mes}L)Mn_3(py)_3$ cluster shows an absorption signal at $g = 4.6$ in the EPR spectrum, unlike the other two pyridine ligated clusters, which may be a signal associated with the $S = 3/2$ excited state.[40] This would make sense given that the Mn-Mn distances in the mesityl-substituted cluster are much bigger than those of the other two pyridine-ligated clusters, and indeed, fits to the SQUID magnetometry data showed that the antiferromagnetic exchange coupling values are smallest in magnitude for the mesityl cluster. Taken together, the data suggest the $S = 5/2$ Mn centers of the Mn_3^{6+} clusters antiferromagnetically couple through the supporting hexaamide ligand rather than by metal-metal bonding, unlike the Co_3^{6+} clusters, and that the strength of the antiferromagnetic coupling is dependent on the Mn-Mn separation, which is affected by the steric bulk of the anilide substituents. In terms of the nature of the Mn-Mn interactions, these Mn_3^{6+} clusters are akin to the Mn_2^{4+} bimetallics prepared by Thomas and coworkers.

As the following discussion will elaborate, the Fe_3^{6+} clusters display a greater variety of Fe-Fe separations and spin states that depend on both the substituents of the supporting hexaamide ligand as well as the capping ligand. A typical metallation involves mixing the neutral ligand ($^RLH_6$) with 1.5 equivalents of $Fe_2(N(SiMe_3)_2)_4$. For the less bulky ligands, an additional capping ligand (L′) is needed to isolate the Fe_3^{6+} product, $(^RL)Fe_3(L')_3$, where L′ can be a phosphine, pyridine, or simply the THF solvent.[42-44] For the bulky ligand, $(^{tbs}L)^{6-}$ (where tbs = tertbutyldimethylsilyl), the metallation involved

heating the neutral ligand and $Fe_2(Mes)_4$ in benzene to afford (^{tbs}L)Fe_3(THF), with only one capping ligand.[15] Generally, the bulkier the substituent on the hexaamide ligand, the greater the spin of the complex.

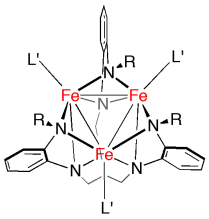

(^{R}L)Fe_3(L')$_3$, Fe_3^{6+}
Betley 2011-12
Fe-Fe (averages):
R = H, L' = PMe_3 or PMe_2Ph: 2.30 Å, *r* = 0.99, *S* = 1
R = Ph, L' = THF: 2.49 Å, *r* = 1.08, *S* = 6
R = Ph, L' = py: 2.58 Å, *r* = 1.12, *S* = 2 to 4
R = Ph, L' = $PMePh_2$: 2.59 Å, *r* = 1.12, *S* = 2 to 4

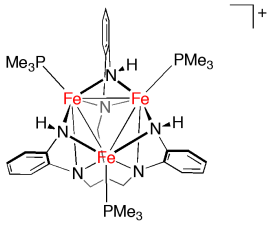

[(^{H}L)$Fe_3(PMe_3)_3$](PF_6), Fe_3^{7+}
Betley 2011
Fe-Fe (average): 2.27 Å, *r* = 0.98, *S* = 3/2

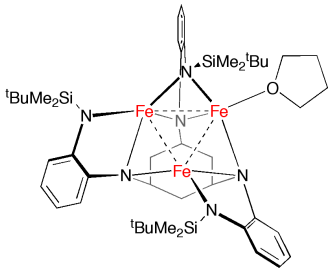

(^{tbs}L)Fe_3(THF), Fe_3^{6+}
Betley 2011
Fe-Fe (average): 2.58 Å, *r* = 1.12, *S* = 6

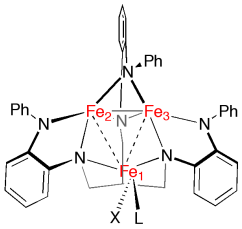

(^{Ph}L)Fe_3XL, Fe_3^{7+}
Betley 2013
Fe-Fe:
X = Cl, L = py: Fe_2-Fe_3 = 2.30 Å, *r* = 1.00
Fe_1-$Fe_{2,3}$ (avg) = 2.69, *r* = 1.17
X = Br, L = THF: Fe_2-Fe_3 = 2.30 Å, *r* = 1.00
Fe_1-$Fe_{2,3}$ (avg) = 2.71, *r* = 1.17
X = I, L = THF: Fe_2-Fe_3 = 2.31 Å, *r* = 1.00
Fe_1-$Fe_{2,3}$ (avg) = 2.65, *r* = 1.15
S = 7/2

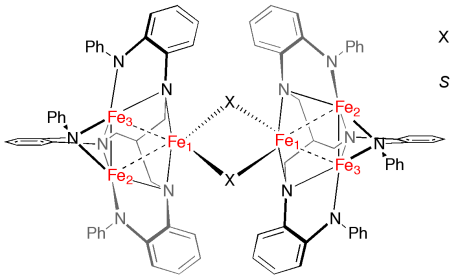

[(^{Ph}L)Fe_3(μ-X)]$_2$, Fe_6^{14+}
Betley 2013
Fe-Fe:
X = Br: Fe_2-Fe_3 = 2.35 Å, *r* = 1.02
Fe_1-$Fe_{2,3}$ (avg) = 2.59, *r* = 1.12
X = Cl: Fe_2-Fe_3 = 2.34 Å, *r* = 1.01
Fe_1-$Fe_{2,3}$ (avg) = 2.58, *r* = 1.12

Scheme 1.11. Fe_3^{6+}, Fe_3^{7+}, and Fe_6^{14+} clusters crystallographically characterized by Betley and coworkers.

The $(^{H}L)Fe_3(PMe_2R')_3$ complexes (where R' = Me or Ph) have an $S = 1$ ground state with short Fe-Fe bond distances at 2.299 Å ($r = 0.99$) (Scheme 1.11).[44] The Mössbauer spectra of these compounds contain only one signal with similar δ (0.38 and 0.39 mm s^{-1}) and ΔE_Q values (1.03 and 0.96 mm s^{-1}) for R= Me and Ph, respectively. This indicates that the Fe centers are equivalent on the Mössbauer time scale (~10^{-8} s). While higher spin states were observed for the $(^{Ph}L)Fe_3(L')_3$ complexes (where L′ = THF, py, $PMePh_2$), the exact spin depended on L'.[42] For L' = THF, the SQUID magnetometry were fit to an $S = 6$ ground state. In contrast, for L' = py or $PMePh_2$, the SQUID magnetometry data were fit to an equilibrium between an $S = 2$ ground state and a thermally accessible $S = 4$ excited state, with a higher transition temperature for the phosphine-ligated compound than the pyridine-ligated compound. The differences in these spin states and transition temperatures are consistent with what is expected from the ligand field strengths of the capping ligand L'. The average Fe-Fe bond distances, which increase according to L' = THF < py < $PMePh_2$, are 2.49 to 2.59 Å (r = 1.07-1.11, Scheme 1.7), which are elongated compared to $(^{H}L)Fe_3(PMe_2R')_3$. Finally, the solid-state structure of $(^{tbs}L)Fe_3(THF)$ revealed a unique coordination, with only one bridging silylamide group and one capping ligand.[15] The average Fe-Fe bond distance was 2.58 Å (r = 1.11, Scheme 1.11). The room temperature solution state magnetic moment of $(^{tbs}L)Fe_3(THF)$ was consistent with an $S = 6$ ground state, akin to $(^{Ph}L)Fe_3(THF)_3$.

Some of the Fe_3^{6+} clusters have been chemically oxidized. The CV of $(^{H}L)Fe_3(PMe_3)_3$ showed two quasi-reversible, one-electron oxidations at −1.59 and −1.04 V (vs. Fc/Fc^+).[44] Chemical oxidation with $FcPF_6$ afforded the Fe_3^{7+} complex,

$[(^{H}L)Fe_3(PMe_3)_3](PF_6)$. The average Fe-Fe bond length contracted to 2.27 Å (r = 0.97), a shortening by 0.03 Å relative to the Fe_3^{6+} analogue (Scheme 1.11). The Mössbauer isomer shift decreased to 0.28 mm s^{-1} (from 0.38 mm s^{-1}) with ΔE_Q = 0.78 mm s^{-1}, which is consistent with a delocalized oxidation of all three iron centers. Chemical oxidation was also performed on $(^{Ph}L)Fe_3(THF)_3$ with 1 equiv. Ph_3CX (X = Cl, Br) or 0.5 equiv. I_2, affording either halide-bridged hexairon clusters $[(^{Ph}L)Fe_3(\mu\text{-}X)]_2$ (X = Cl or Br) or triiron clusters $(^{Ph}L)Fe_3X(L')$ (X = Cl, L' = py; X = Br, L' = THF; X = I, L' = THF).[22] In the latter Fe_3^{7+} complexes, the halide and capping ligand are bound to the same iron center, leaving the other two iron centers to form a short bond of 2.308(1) Å (r = 0.99, Scheme 1.11). The oxidation was proposed to be localized on the diiron unit, and further, that the S = 3/2 Fe_2^{5+} unit coupled ferromagnetically to the S = 2 Fe^{II} center. The different extent of delocalization upon oxidation, as observed in these two systems, was attributed to their different spin preferences, i.e. low-spin $(^{H}L)Fe_3(PMe_3)_3$ versus high-spin $(^{Ph}L)Fe_3(THF)_3$.

For the least bulky ligand, $^{H}L^{6-}$, Betley and co-workers have also generated octahedral Fe_6 clusters. Formation of the Fe_6 clusters was favored over formation of the Fe_3 clusters by metalating the ligand $^{H}LH_6$ with $Fe_2(Mes)_4$ in a mixture of benzene and pyridine, yielding the all ferrous Fe_6^{12+} cluster, $(^{H}L)_2Fe_6$.[43] The average Fe-Fe bond length was 2.597(2) Å (r = 1.11). The CV of this complex was incredibly rich with five reversible redox events, including one reduction at −2.04 V (vs. Fc/Fc^+), and five oxidations between −1.55 V to −0.72 V. In total, a six-membered redox series was isolated, containing Fe_6^{n+} cores with n ranging from 11 (5Fe(II)Fe(I)) to 16

(4Fe(III)2Fe(II)). Even the hexacationic, nominally all-ferric cluster (n = 18, Fe(III)) could be observed by ^{1}H NMR spectroscopy and Mössbauer spectroscopy upon oxidation of the Fe_6^{16+} cluster with two equivalents of [NO](PF$_6$), although it decayed within hours in solution at room temperature. For the Fe_6^{11+} cluster, $[(^{H}L)_2Fe_6]^{-}$, the average Fe-Fe bond lengths slightly contracted to 2.580(1) Å (r = 1.11). As the clusters were increasingly oxidized, the acetonitrile solvent bound as capping ligands, as observed by X-ray crystallography. The number of acetonitrile ligands varied with the oxidation state: two in $[(^{H}L)_2Fe_6(CH_3CN)_2]^{+}$, four in $[(^{H}L)_2Fe_6(CH_3CN)_4]^{2+}$, and a maximum of six, 1 per Fe, in $[(^{H}L)_2Fe_6(CH_3CN)_6]^{3+/4+}$. A qualitative trend was that the average Fe-Fe bond lengths increase with increasing positive charge, reaching upwards of 2.69-2.70 Å (r = 1.15-1.16).

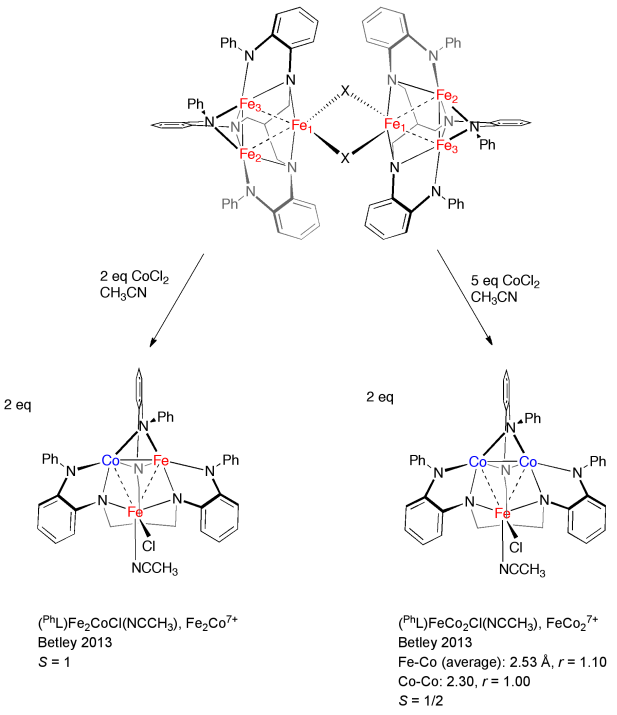

Scheme 1.12. Syntheses of $Fe_nCo_{(3-n)}^{7+}$ (n = 1, 2) clusters by Betley and coworkers.

Another advancement by Betley and coworkers has been the discovery of methods of preparing heterotrimetallics with mid-to-late first-row transition metals. Iron-cobalt bonds have been studied within Fe-Co heterotrimetallics featuring Fe_2Co^{7+} and $FeCo_2^{7+}$ cores. The mixed-metal clusters were synthesized using a novel strategy of metal atom substitution (Co) into a pre-exisiting Fe_3^{7+} core, $[(^{Ph}L)Fe_3(\mu\text{-Cl})]_2$. Addition of two and five equiv. of $CoCl_2$ effected the replacement of one and two iron centers in the triiron core with cobalt to generate $(^{Ph}L)CoFe_2Cl(CH_3CN)$ and $(^{Ph}L)Co_2FeCl(CH_3CN)$, respectively (Scheme 1.12).[22] The reaction was performed in THF at room temperature for 3 hours, and dissolution of the reaction crude into acetonitrile resulted in precipitation of the acetonitrile-cluster adducts as a crystalline material. Notably, no metal atom substitution occurs at the unique iron site, where chloride is bound.

Magnetic susceptibility of the Fe_2Co^{7+} and $FeCo_2^{7+}$ heterometallics were measured to gauge the effect of Co substitution on the overall magnetic properties of the cluster. The most dramatic change is the decrease in spin state, from S = 7/2 for the Fe_3^{7+} unit in $[(^{Ph}L)Fe_3(\mu\text{-Cl})]_2$ to $S = 1$ and ½ for the Fe_2Co^{7+} and $FeCo_2^{7+}$ clusters, respectively.[22] SQUID magnetometry data on the heterometallic clusters were modeled as a two spin system comprising an $S = 2$ Fe^{II} center and a bimetallic $S = 1$ $(FeCo)^{5+}$ or $S =$ ½ Co_2^{5+} unit that are weakly coupled ($J = -4.25$ and -6.25 cm^{-1}). The Mössbauer spectra of the Fe_2Co^{7+} complex showed three doublets, indicating that Co substitution occurs indiscriminately into two of the three iron sites. On the other hand, the $FeCo_2^{7+}$ cluster exhibited a single doublet with $\delta = 0.69$ mm/s and $\Delta E_Q = 1.38$ mm/s, which corresponds to the unique Fe-Cl site. The shortest metal-metal bond in the trimetallic core is the Co-

Co bond at 2.286(1) Å (r = 0.98). The two Fe-Co bonds are longer, ranging from 2.50 to 2.53 Å (r = 1.08-1.09).

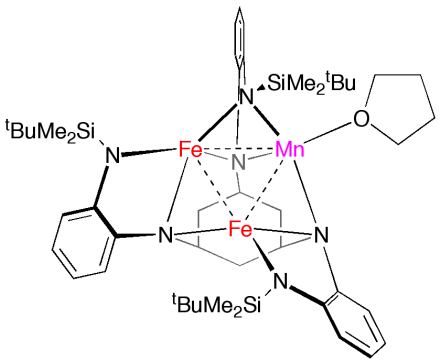

(^{tbs}L)Fe$_2$Mn(THF), Fe$_2$Mn^{6+}
Betley 2013
Fe-Mn (average): 2.74 Å, r = 1.18
Fe-Fe: 2.87, r = 1.24
S = not determined

Scheme 1.13. The Fe$_2$Mn^{6+} cluster (^{tbs}L)Fe$_2$Mn(THF) crystallographically characterized by Betley and coworkers.

A stepwise metallation strategy was used to successfully form a trinuclear heterometallic cluster featuring Fe-Mn interactions. The trigonal Fe$_2$Mn^{6+} core in (^{tbs}L)Fe$_2$Mn(THF) was assembled by heating the diiron intermediate (^{tbs}LH$_2$)Fe$_2$ and 0.5 equiv. Mn$_2$(N(SiMe$_3$)$_2$)$_4$ at 75°C in THF.[23] The solid-state structure showed Fe-Mn distances of 2.7247(5) and 2.7485(5) Å (average r = 1.18), which are consistent with weak interactions (Scheme 1.13). The paramagnetic ^{1}H NMR spectrum established C_1 symmetry for the complex, as expected based on the crystal structure. Consistent with the lack of symmetry elements in the cluster, Mössbauer spectroscopy showed two doublets with δ = 0.35 mm s^{-1}/ΔE_Q = 1.77 mm s^{-1} and 0.58 mm s^{-1}/ΔE_Q = 1.30 mm s^{-1}. X-ray anomalous scattering measurements showed that Mn was located at the metal site that coordinates THF.

1.3. Small-Molecule Activation with Mid-to-Late First-Row Metal-Metal Bonded Complexes

Interest in metal-metal bonded complexes with mid-to-late first-row transition metals stems not only from their electronic structures, but especially, their potential for small-molecule activation. The capability of these multimetallic clusters to activate small molecules is reminiscent of the biological cofactors of metalloenzymes, which activate small molecules such as H_2, O_2, N_2, and H_2O, as mentioned earlier. As the following discussion will make clear, much of the demonstrated first-row metal-metal bonded multimetallic small-molecule activation has been demonstrated with *high-spin* complexes. Hence, these molecules offer an interesting contrast to many reactive second- and third-row metal-metal bonded complexes such as dirhodium(II) tetragonal lantern $Rh_2(L)_4$ (e.g., L = carboxylate or caroboxamidate) complexes, which feature *low-spin* electronic configurations.[45-47]

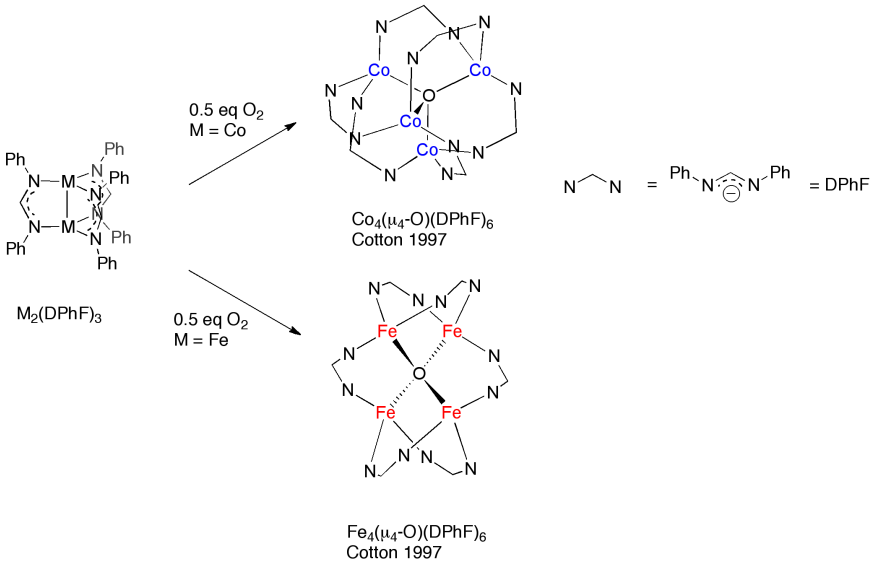

Scheme 1.14. Syntheses of $M_4(\mu_4\text{-O})(DPhF)_6$ clusters by Cotton and coworkers.

Cotton and coworkers observed decomposition of the trigonal lantern M_2^{3+} complexes $M_2(DPhF)_3$ (M = Fe, Co) with trace amounts of oxygen to give compounds with the formulation $M_4(\mu_4\text{-}O)(DPhF)_6$ (Scheme 1.14). Formally, the reaction can be balanced with a half equivalent of O_2 per $M_2(DPhF)_3$ unit, meaning that each bimetallic unit oxidized by one electron to give cores in which all the metals are divalent. Both the Fe and the Co products have a distorted tetrahedral arrangement of M^{II} centers around each of the O atoms, but the arrangement of DPhF ligands depends on the metal. For $Co_4(\mu_4\text{-}O)(DPhF)_6$, the cluster has approximate C_3 symmetry. One of the four Co centers is coordinated by three N donors from three planar DPhF ligands, with each ligand coordinated to one of the other three Co. The other three Co centers are each coordinated to an N donor from one planar DPhF ligand and two N donors from "twisted" DPhF ligands. The cluster $Fe_4(\mu_4\text{-}O)(DPhF)_6$ has approximate C_2 symmetry. Two of the six possible Fe-Fe pairings in the core are bridged by two DPhF ligands each, another two pairs of Fe-Fe pairings are bridged by one DPhF ligand each, and the other two Fe-Fe pairings are not bridged by any DPhF ligands. In neither of these clusters are metal-metal bonds present, as the shortest M-M distance in either cluster is 2.85 Å.

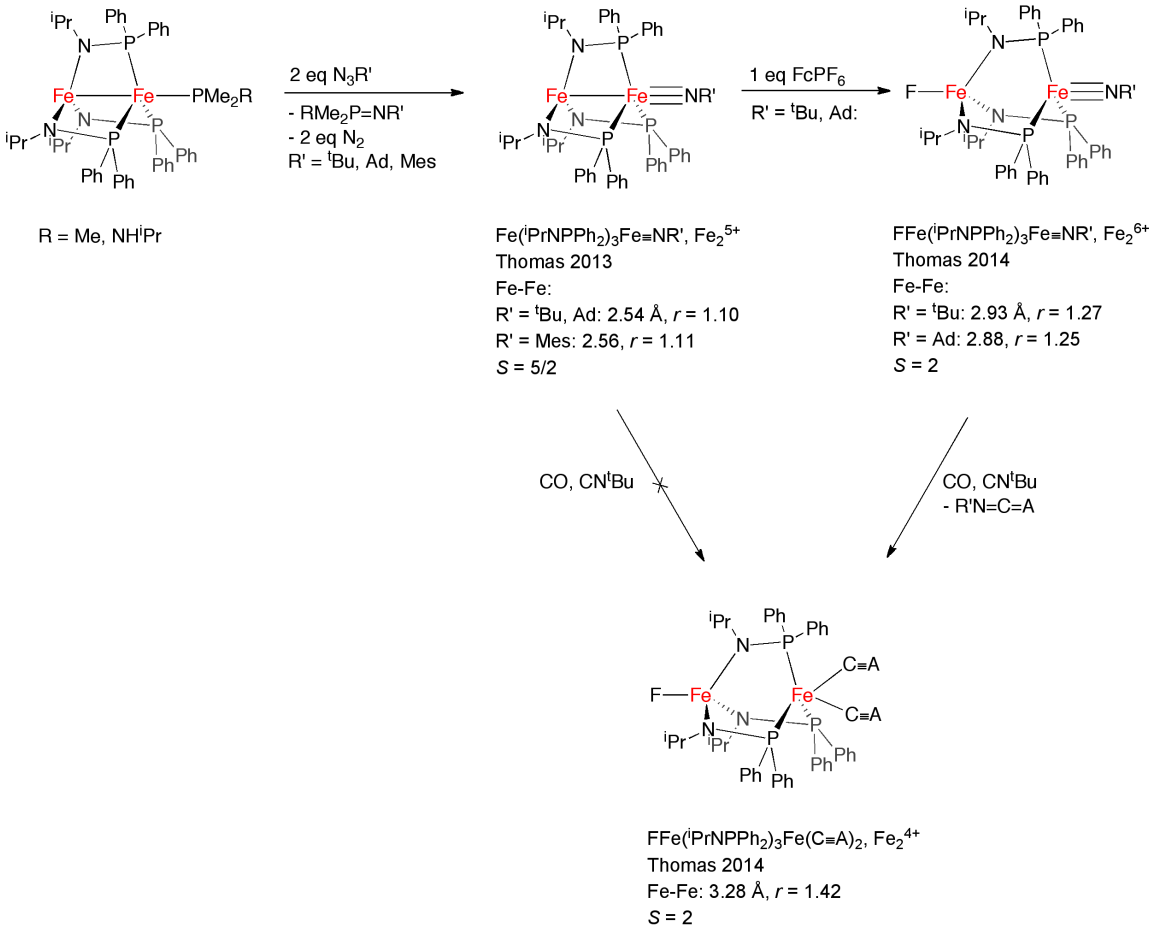

Scheme 1.15. Organic azide decomposition and imide transfer by diiron complexes.

Thomas and coworkers have demonstrated the decomposition of organic azides via oxidative group transfer to $S = 7/2$ Fe_2^{3+} molecules to give Fe_2^{5+} imides (Scheme 1.15). Addition of two equiv. N_3R (where R = ^{t}Bu, Ad, 2,4,6-$Me_3C_6H_2$) to $Fe_2(^i PrNPPh_2)_3L$ (L = PMe_3, $^i PrNHPPh_2$) affords $Fe(^i PrNPPh_2)_3Fe{\equiv}NR$, two equiv. N_2, and the corresponding phosphinoimide, L=NR.[38] The Fe_2^{5+} imides have reasonably short Fe-Fe distances of 2.54-2.56 Å (r = 1.09-1.10). The Fe-N(imide) bond lengths of 1.64-1.67 Å are consistent with other C_3-symmetric Fe-imide bonds in the literature. A Mössbauer spectrum of $Fe(^i PrNPPh_2)_3Fe{\equiv}N^t Bu$ showed a single doublet with $\delta = -0.06$

mm s^{-1} and ΔE_Q = 0.54 mm s^{-1}, which was similar to the S = ½ Fe(III) imide, $PhB(MesIm)_3Fe{\equiv}NAd$.[48] Hence, the Fe_2^{5+}-imide core was proposed to be $Fe^{II}Fe^{III}{\equiv}NR$. An Evans' method measurement led to the proposal of an S = 5/2 ground state which arises from ferromagnetic coupling of high-spin Fe(II) and low-spin Fe(III).

These are the first examples of metal-ligand multiple bonds that are *trans* to a M-M interaction involving *first-row* metals.[38] Hence, it was of interest to investigate the bonding in the $Fe^{II}Fe^{III}{\equiv}NR$ core by DFT. The DFT calculations support the S = 5/2 ground state. Overall, the *d* electrons are highly localized, and M-M bonding interactions are evident only in the σ(Fe-Fe) and the three-centered σ*(Fe-Fe-N) orbitals. The Fe-Fe bond order is predicted to be low at 0.5, which is consistent with a weak Fe-Fe interaction.

Addition of $FcPF_6$ to the $Fe^{II}Fe^{III}{\equiv}NR$ (R = ^{t}Bu, Ad) complexes in THF resulted in one-electron oxidation and fluoride abstraction to give $FFe^{III}(^i PrNPPh_2)_3Fe^{III}{\equiv}NR$ (Scheme 1.15).[49] Solution-state magnetic moments were measured to be 4.83 μ_B for R=^{t}Bu and 4.62 μ_B for R=Ad. These values are consistent with overall S = 2 ground states. SQUID magnetometry of $FFe^{III}(^i PrNPPh_2)_3Fe^{III}{\equiv}N^tBu$ was fit to antiferromagnetically coupled S = 1/2 Fe^{III} (the imide-ligated Fe center) and S = 5/2 Fe^{III} (the F-ligated Fe center). The Fe-Fe distances elongate substantially relative to the starting materials at 2.9330(3) Å (r = 1.27) for R=^{t}Bu and 2.8796(4) Å for R=Ad, consistent with scission of the Fe-Fe bonding interaction with concomitant alteration of the geometry at the amide-ligated Fe from distorted trigonal pyramidal in the starting material to tetrahedral in the product. Mössbauer spectroscopy of

$FFe^{III}(^{i}PrNPPh_2)_3Fe^{III}{\equiv}N^{t}Bu$ showed two signals with $\delta = 0.26$ mm s^{-1}/ $\Delta E_Q = 1.28$ mm s^{-1} and $\delta = -0.12$ mm s^{-1}/ $\Delta E_Q = 2.70$ mm s^{-1}. The former signal was assigned to the S = 5/2 Fe^{III} center while the latter signal was assigned to the S = ½ nitrene-bound Fe^{III} center.

From a reactivity standpoint, it is interesting to compare $Fe^{II}(^{i}PrNPPh_2)_3Fe^{III}{\equiv}NR$ to its one-electron oxidized congener $FFe^{III}(^{i}PrNPPh_2)_3Fe^{III}{\equiv}NR$, as the former has a Fe-Fe bonding interaction, whereas the latter does not. It is found that the $Fe^{II}Fe^{III}{\equiv}NR$ complexes are unreactive towards nitrene transfer, whereas the $Fe^{III}Fe^{III}{\equiv}NR$ complexes transfer nitrene to either CO or $C{\equiv}N^{t}Bu$ to give $FFe^{III}(^{i}PrNPPh_2)_3Fe^{I}(L)_2$ (L = CO, $C{\equiv}N^{t}Bu$) and either $O{=}C{=}NR$ or $^{t}BuN{=}C{=}N^{t}Bu$ (Scheme 1.15).[49] The $Fe^{III}Fe^{I}$ bimetallics were crystallographically characterized, showing Fe-Fe distances of ~3.28 Å (r = 1.42), indicating the lack of a Fe-Fe bonding interaction. An S = 2 ground state, generated by antiferromagnetic coupling of S = 5/2 Fe^{III} and S = 1/2 Fe^{I}, was characterized by both SQUID magnetometry and Evans' method. The low-spin nature of the Fe^{I} center is as expected based on the presence of strong-field carbonyl or isocyanide ligands. Overall, the enhanced reactivity of the $Fe^{III}Fe^{III}{\equiv}NR$ complexes towards nitrene transfer was attributed to the greater nucleophilicity of the $Fe^{III}{\equiv}NR$ fragment in $Fe^{III}Fe^{III}{\equiv}NR$ compared to the $Fe^{III}{\equiv}NR$ moieties of the $Fe^{II}Fe^{III}{\equiv}NR$ molecules due to the delocalization of electron density into the Fe-Fe bonding interaction of the latter.

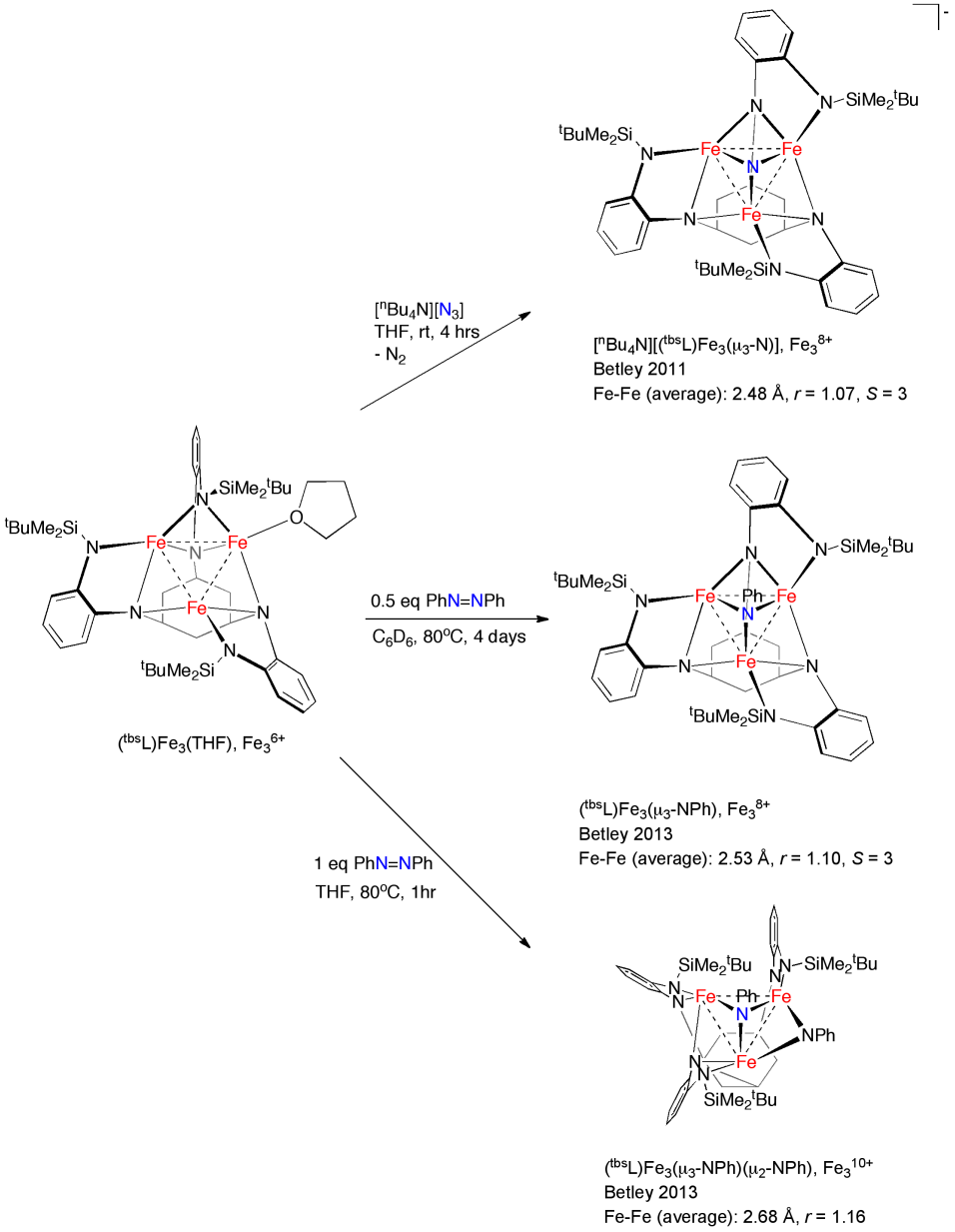

Scheme 1.16. Select multielectron reactivity of (^{tbs}L)Fe$_3$(THF).

The bulkier (^{tbs}L)Fe$_3$(THF) system mediated a number of multi-electron processes that are potentially relevant to N_2 activation. A triiron core with a μ^3-capping nitride, [(^{tbs}L)Fe$_3$(μ^3-N)](Bu$_4$N), with a formal Fe$_3^{8+}$ core, was generated by adding 1 equiv. (Bu$_4$N)(N$_3$) to (^{tbs}L)Fe$_3$(THF) (Scheme 1.16).[15] This transformation was unusually facile

at room temperature and did not require photolysis or heating, which are typically needed to extrude N_2 from a metal-azide intermediate. Functionalization of the capping nitride was performed with either MeI or lutidinium tetraphenylborate to give the Fe_3^{8+} μ^3-imide complex, (^{tbs}L)Fe_3(μ^3-NR), where R = Me or H. The Fe-Fe distance in both the Fe_3 nitride and the Fe_3 methylimide complexes is 2.48 Å (r = 1.06), which is shorter than the average of 2.58 Å in (^{tbs}L)Fe_3(THF). The average Fe-N bond length elongates slightly from 1.871(3) in the Fe_3 nitride to 1.892(3) Å in the Fe_3 methylimide. The ground states of the Fe_3^{8+} cores in the nitride and imide complexes were S = 3 and 2, respectively, much lower than the S = 6 Fe_3^{6+} starting material.

The (^{tbs}L)Fe_3(THF) complex was found to cleave both N-N and N=N bonds. Hydrazine substrates, H_2NNHR (R = H, Ph), are reduced by (^{tbs}L)Fe_3(THF) to form the Fe_3^{8+} μ^3-imide, (^{tbs}L)Fe_3(μ^3-NH) and an amine byproduct, NH_2R (R = H, Ph).[16] The use of the disubstituted hydrazine, HPhNNHPh, generates the phenyl imide, (^{tbs}L)Fe_3(μ^3-NPh) and aniline. Finally, adding a half equivalent or one equivalent of azobenzene to (^{tbs}L)Fe_3(THF) generates the capping imide, (^{tbs}L)Fe_3(μ^3-NPh), or the bis(imide) complex, (^{tbs}L)Fe_3(μ^3-NPh)(μ^2-NPh), respectively (Scheme 1.16). In both reactions, the N=N bond is fully cleaved, a rare feat for iron. Of interest, the latter reaction is formally a four-electron oxidation from Fe_3^{6+} (3Fe(II)) to Fe_3^{10+} (2Fe(III)Fe(IV)). The reactivity of the (^{tbs}L)Fe_3 system has thus far demonstrated metal cooperativity, redox flexibility, as well as ligand flexibility for potential applications in small-molecule activation.

Reactivity between (^{H}L)$_2Fe_6$ and nitrite was reported. The S = 6 Fe_6^{12+} cluster reduced 6 equivalents of nitrite in the presence of protons (12 equivalents of benzoic

acid) to generate the hexanitrosyl cluster, $(^{H}L)_2Fe_6(NO)_6$, in which the long Fe-Fe distances of 3.217(3) Å (r = 1.38) suggest no Fe-Fe interactions.[50] Interestingly, the nitro-ligated intermediate, $[(^{H}L)_2Fe_6(NO_2)_6]^{2-}$ was isolated by adding 6 equivalents of nitrite to the oxidized Fe_6^{16+} cluster, $[(^{H}L)_2Fe_6(CH_3CN)_6]^{4+}$. In the nitro intermediate, the average Fe-Fe bond distance of 2.727(4) Å (r = 1.17) indicates weak Fe-Fe interactions. The lone quadrupole doublet in the Mössbauer spectrum (δ = 0.38 mm s^{-1}, ΔE_Q = 2.38 mm s^{-1}) is consistent with fully delocalized *d* electrons over the six iron centers.

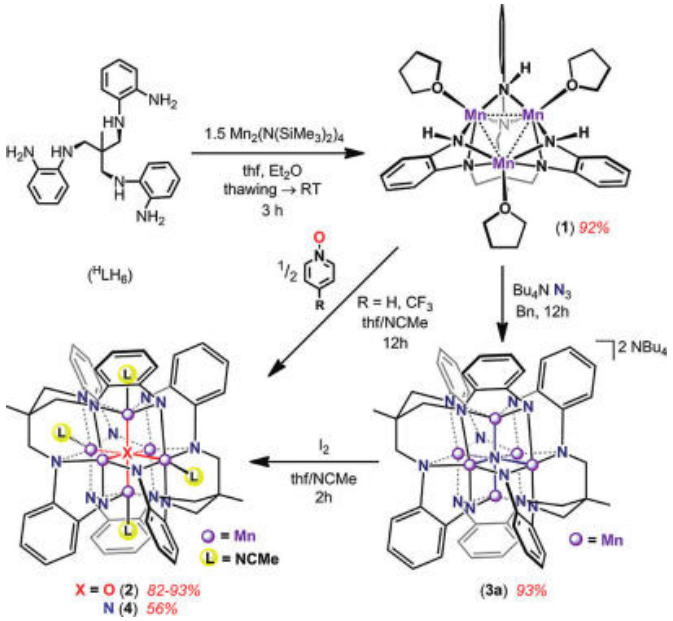

Scheme 1.17. Reactivity of $(^{H}L)Mn_3(THF)_3$. Taken from reference 41.

The Mn_3^{6+} cluster $(^{H}L)Mn_3(THF)_3$ reacted with 1 equivalent of $[nBu_4](N_3)$ to give the dianionic Mn_6^{13+} cluster $(nBu_4)_2[(^{H}L)_2Mn_6(\mu_6\text{-}N)]$ (Scheme 1.17).[41] Though 1 equivalent of azide was added, only 0.5 equivalents of nitride were transferred per equivalent of Mn_3^{6+} starting material. The oxidation state of the cluster, then is 5Mn(II)Mn(III), or an overall one-electron oxidation of two clusters. A half equivalent of iodosobenzene, pyridine *N*-oxide, or 4-trifluoromethylpyridine *N*-oxide added to

(^{H}L)Mn_3(THF)$_3$ afforded [(^{H}L)$_2Mn_6$(μ_6-O)]. In this case, a two-electron oxidation of two clusters produced a 4Mn(II)2Mn(III) core.

It is worth comparing this Mn_3^{6+} reactivity to the Fe_3^{6+} reactivity discussed earlier. In the Mn_3^{6+} atom transfer reactions, the clusters were oxidized by one-half or 1 electron. This is in sharp contrast to the (^{tbs}L)Fe_3(THF) and (^{H}L)$_2Fe_6$ reactivity, in which 2-electron, 3-electron, and even 4-electron oxidations (per three Fe centers) of the core were achieved. As a reminder, the ground state of the Mn_3^{6+} cluster is S = ½, which is the result of the Mn centers engaging in superexchange through the bridging anilide ligands without Mn-Mn bonding interactions. On the other hand, the (^{tbs}L)Fe_3(THF) cluster has a high-spin S = 6 ground state, and the Fe centers have direct Fe-Fe bonding. It is the combination of the high spin state and metal-metal bonding of (^{tbs}L)Fe_3(THF) compared to (^{H}L)Mn_3(THF)$_3$ that enhances its capability for small-molecule activation such that transformations like cleaving the N=N bond of azobenzene can be accomplished.

1.4. Organometallic Motifs and Reactivity with Metal-Metal Bonded Complexes Containing Mid-to-Late First-Row Transition Metals

While the last few years have seen progress in small molecule activation with metal-metal bonded complexes containing two mid-to-late first-row transition metals, these transformations have not yet been implemented in a catalytic cycle. One general class of catalysis that is of great interest is C-C and/or C-X bond formation. In order to design such catalysts, observing the fundamental steps, i.e. C-C and C-X bond forming and bond breaking reactions, is important. Intermediates in such transformations may include M-C bonds. In this section, motifs including a metal-metal bond with a mid-to-

late first-row transition metal and an organometallic ligand will be outlined, and examples of reactivity which involve M-C, C-C, or C-X bond forming or bond breaking reactions will be included. Again, as with the previous discussion, carbonyl- and isocyanide-rich reactive precursors are not included here, as the overarching themes involve the design of well-defined catalysts with predictable coordination chemistry.

1.4.1. Cobalt Extended Metal Atom Chains (EMACs) with Organometallic Ligands

EMACs, which are compounds with a string of three or more metals, have been a well-studied class of compounds because of their potential as nanoscale electronic devices.[51] A molecular wire requires the electronic communication of metal atoms; in an EMAC, electronic communication can be accomplished by direct metal-metal bonding or the coupling of metals in close proximity. The chemical, electrochemical, and magnetic properties of EMACs can be modified by substitution of ligands axially bound to the terminal metals. A number of cobalt EMACs with organometallic axial ligands have been prepared which show rich electrochemical redox reactivity. These compounds are shown in Scheme 1.18.

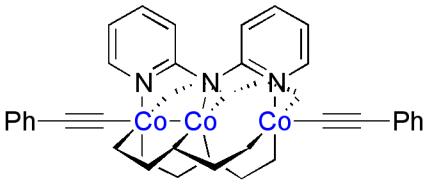

Cotton 2004
$Co_3(dpa)_4(CCPh)_2$, Co_3^{6+}
Co-Co: 2.34 Å, r = 1.01
2.40 Å, r = 1.04
S = 1/2 to 3/2

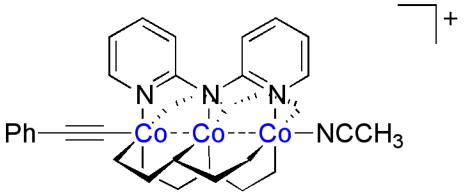

Cotton 2004
$[Co_3(dpa)_4(CCPh)(NCCH_3)](PF_6)$, Co_3^{6+}
Co-Co: 2.33 Å, r = 1.01

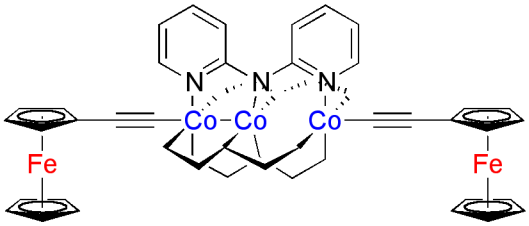

Cotton 2004
$Co_3(dpa)_4(FcA)_2$, Co_3^{6+}
Co-Co: 2.31 Å, r = 1.00
2.52 Å, r = 1.09

Scheme 1.18. Co_3^{6+} EMACs prepared by Cotton and coworkers.

The Co_3^{6+} molecule $[Co_3(dpa)_4(NCCH_3)(C{\equiv}CPh)](PF_6)$ features two identical Co-Co bond lengths of 2.328(1) Å (r = 1.01); this indicates that cobalt-cobalt bonding is delocalized over the three Co centers (Scheme 1.18).[51] On the other hand, the Co_3^{6+} molecule $Co_3(dpa)_4(C{\equiv}CPh)_2$ features two significantly different Co-Co distances of 2.344(1) Å (r = 1.01) and 2.401(1) Å (r = 1.04) (Scheme 1.18). The crystal structure data were interpreted such that the short Co-Co distance corresponded to a diamagnetic Co_2^{4+} unit with a single bond (as seen for isolated tetragonal lantern Co_2^{4+} complexes such as $Co_2(DPhF)_4$ described previously), and the long Co distance was a noncovalent interaction between a paramagnetic Co^{II} center and the Co_2^{4+} unit. Analysis of SQUID

magnetometry data indicated that $Co_3(dpa)_4(C{\equiv}CPh)_2$ is a spin crossover compound, undergoing a ground state $S = 1/2$ to $S = 3/2$ transition. Given the crystal structure discussion, it is the lone Co^{II} center that undergoes this spin transition. $Co_3(dpa)_4(C{\equiv}CPh)_2$ also undergoes two reversible metal-based oxidations by cyclic voltammetry at -0.33 V and 0.28 V (vs. Fc/Fc^+), though the oxidized species were not chemically isolable.

The ferrocenylacetylide (FcA) capped EMAC $Co_3(dpa)_4(FcA)_2$ was also analyzed by X-ray crystallography. The difference in the Co-Co separations (2.3098(1) Å/$r = 1.00$ and 2.5208(9) Å/$r = 1.09$) is more pronounced than in $Co_3(dpa)_4(C{\equiv}CPh)_2$; the same bonding picture was proposed: a diamagnetic Co_2^{4+} unit with a single bond interacted noncovalently with a paramagnetic Co^{II} center (Scheme 1.18). The cyclic voltammogram of $Co_3(dpa)_4(FcA)_2$ revealed three reversible oxidations. The first oxidation, at -0.36 V (vs. Fc/Fc^+) was assigned as a Co_3^{6+}/Co_3^{7+} couple, in analogy to the first oxidation of $Co_3(dpa)_4(C{\equiv}CPh)_2$. The second oxidation (0.08 V) had twice as much current as the first oxidation, and so was assigned as the oxidation of the Fe(II) centers in the two FcA ligands. The third oxidation (0.34 V), with the same current as the first oxidation, was assigned as a Co_3^{7+}/Co_3^{8+} couple. The width of the peak at 0.08 V in the differential pulse voltammogram of $Co_3(dpa)_4(FcA)_2$ was broadened, which is expected for a two-electron process, and an analysis showed that the peak was comprised of two one-electron oxidations separated by a potential of 0.07 V, indicating that the two ferrocenyl ligands communicate weakly. Cyanide-capped Co_3^{6+} and Co_5^{10+} EMACs with short Co-Co distances have also been structurally characterized.[52,53]

1.4.2. Phosphinoamide-Supported Stoichiometric ZrCo Organometallic Reactivity

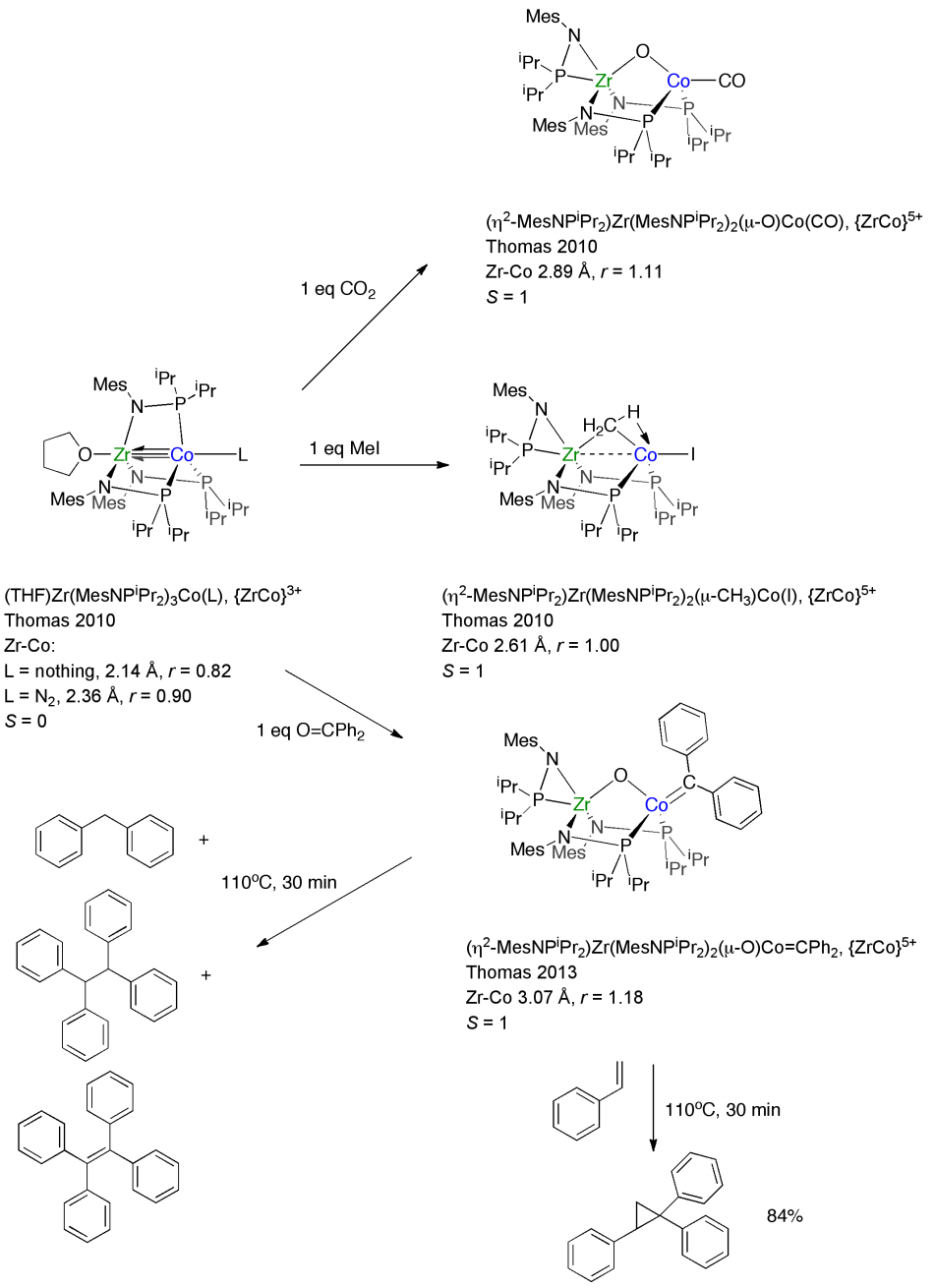

Scheme 1.19. Select reactivity with (THF)Zr(MesNP^{i}Pr$_2$)$_3$Co(N$_2$).

Thomas and coworkers have observed a number of C-X bond breaking reactions with ZrCo bimetallics. The complex (THF)Zr(MesNP^{i}Pr$_2$)$_3$Co(N$_2$), which features Zr-Co

multiple bonding (Zr-Co = 2.36 Å, r = 0.90), oxidatively adds MeI to give the methyl-bridged product (η^2-MesNP^{i}Pr$_2$)Zr(MesNP^{i}Pr$_2$)$_2$(μ-CH$_3$)CoI (Zr-Co = 2.61347(19) Å, r = 1.00) (Scheme 1.19).[54,55] X-ray crystallography revealed the presence of an agostic interaction between the methyl and Co center, while a phosphinoamide was displaced from its original bridging coordination mode to bind exclusively to the Zr center. If the RX reagents ^{i}PrI, EtI, or CyCl were added to (THF)Zr(MesNP^{i}Pr$_2$)$_3$Co(N$_2$), oxidative addition was not observed, but C-H activation of a mesityl methyl group instead occurred to afford (η^3-P^{i}Pr$_2$N{C$_6$Me$_2$H$_2$(CH$_2$)})Zr(MesNP^{i}Pr$_2$)$_2$CoX (X = I or Cl) (Zr-Co = 2.5562(4) Å for X = I, r = 0.98). These crystal structures also feature agostic interactions between the C-H activated methylene group and the Co center. The volatiles of the reaction with CyCl were analyzed by ^{1}H NMR spectroscopy, showing that cyclohexane was the only organic product.

The N$_2$-free congener of the reactive species described above, (THF)Zr(MesNP^{i}Pr$_2$)$_3$Co, reacts with one equivalent of CO$_2$ to break a C=O bond, affording (η^2-MesNP^{i}Pr$_2$)Zr(MesNP^{i}Pr$_2$)$_2$(μ-O)Co(CO) (Scheme 1.15).[56] This is formally an oxidative addition reaction, in analogy to the MeI reaction described previously, and as in that reaction, a phosphinoamide dissociates from its bridging position to bind exclusively to the Zr center. The Zr-Co distance is 2.8865(5) Å (r = 1.11), consistent with Zr-Co bond breaking. In the presence of one equivalent of CO$_2$ and excess Na/Hg, the oxide ligand could be scavenged to give the carbonate (THF)$_4$Na$_2$(κ^2-CO$_3$)Zr(MesNP^{i}Pr$_2$)$_3$Co(CO) (Zr-Co = 2.6111(4) Å, r = 1.00). The Zr center binds the

carbonate ligand in a κ^2 fashion, and each Na center also binds to the carbonate in a κ^2 fashion, as well as to a flanking mesityl ligand in an η^6 fashion.

(THF)Zr(MesNP^{i}Pr$_2$)$_3$Co(N$_2$) reacts with O=CPh$_2$ at room temperature to give a compound with a isobenzopinacol ligand bridging two Zr-Co units *via* the O atoms bound to the Zr centers.[57] Heating this tetrametallic compound at 70°C for 20 minutes resulted in a remarkable reaction. Two products were observed by ^{1}H NMR spectroscopy and crystallographically characterized: (η^2-MesNP^{i}Pr$_2$)Zr(MesNP^{i}Pr$_2$)$_2$(μ-O)Co=CPh$_2$ (80%) (Zr-Co = 3.0667(4) Å, *r* = 1.17) and ((^{i}Pr$_2$P)Ph$_2$CO)Zr(MesNP^{i}Pr$_2$)$_2$(μ-NMes) (20%).[58] The products can be explained by the presence of a ketyl radical intermediate derived from C-C bond breaking of the isobenzopinacol starting material. The former product is the result of the cleavage of the C-O bond of the putative ketyl radical intermediate to give a cobalt carbene and a bridging oxide, while the latter product formed from homolysis of a phosphinoamide ligand, followed by subsequent trapping of the iPr$_2$P radical with the ketyl radical. Evacuating the isobenzopinacol complex prior to thermolysis resulted in clean conversion to (η^2-MesNP^{i}Pr$_2$)Zr(MesNP^{i}Pr$_2$)$_2$(μ-O)Co=CPh$_2$ (Scheme 1.19). Under 5 atmospheres of N$_2$, the thermolysis did not generate any product, meaning that N$_2$ dissociation is necessary for the reaction to occur.

DFT calculations on (η^2-MesNP^{i}Pr$_2$)Zr(MesNP^{i}Pr$_2$)$_2$(μ-O)Co=CPh$_2$ revealed that little spin density was located on the carbene, indicating that the oxidation states are best described as Zr^{IV}Co^I with a neutral singlet carbene.[58] Along these lines, the complex did not react with cyclohexadiene, a source of H atoms that would likely react with an open-shell carbene. Heating (η^2-MesNP^{i}Pr$_2$)Zr(MesNP^{i}Pr$_2$)$_2$(μ-O)Co=CPh$_2$ with styrene at

110°C for 30 minutes resulted in the formation of (1,2-diphenylcyclopropyl)benzene in 84% yield. If the complex was heated at 110°C without styrene, a mixture of tetraphenylethane, tetraphenylethylene, and diphenylmethane was generated, suggesting that the :CPh_2 moiety is released upon heating (Scheme 1.19). Because the rates of reaction with and without styrene were similar, the authors postulated that the formation of the cyclopropane product occurred after the carbene was released. In addition, (η^2-$MesNP^iPr_2$)$Zr(MesNP^iPr_2)_2(\mu$-O)Co=CPh_2 reacted with $PhSiH_3$ to give $(PhH_2SiO)Zr(MesNP^iPr_2)_3Co(N_2)$ and tetraphenylethane. The authors proposed that the tetraphenylethane formed from a cobalt hydride/carbene intermediate, followed by insertion to give a cobalt diphenylmethane intermediate, then homolysis of the Co^I-alkyl bond would give a benzhydryl radical, which would dimerize to give tetraphenylethane.

1.4.3. Dinickel-Mediated Organometallic Reactivity

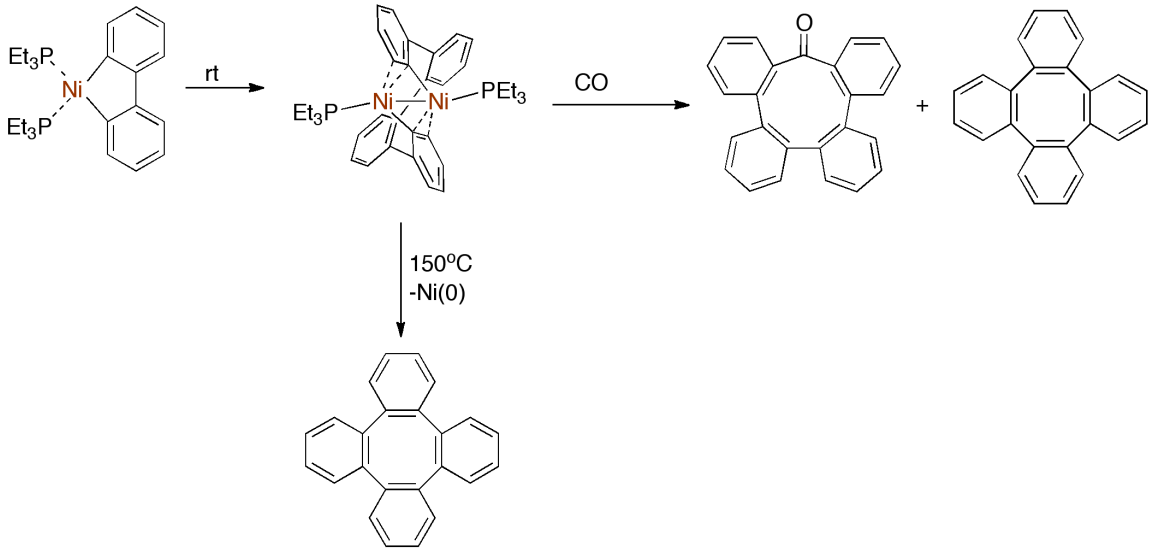

Scheme 1.20. Conversion of a dibenzonickelole into a Ni^INi^I complex, and select reactivity with the latter.

In 1985, Eisch and coworkers isolated a dibenzonickelole from the addition of biphenylene to $Ni(PEt_3)_4$ at 0°C (Scheme 1.20).[59] Upon standing ethereal solvents at room temperature, this dibenzonickelole decomposed into the Ni^INi^I compound $[(PEt_3)Ni]_2[\mu\text{-}\eta^1\text{:}\eta^1\text{-}(C_{12}H_8)]_2$, which features a Ni-Ni single bond of 2.319 Å (r = 1.01). The process corresponds to a C-C reductive elimination from two Ni centers. Above 150°C, the Ni^INi^I complex decomposed into metallic nickel and tetraphenylene, which corresponds to a reductive elimination of C-C bonds from a Ni-Ni bond. Addition of CO to the Ni^INi^I compound resulted in a ~50:50 mixture of tetraphenylene and the cyclic ketone tetrabenzo-2,4,6,8-cyclononatetraenone. Similar reactivity was later reported by Sharp and Ramakrishna from a triphenylene-derived nickelacycle.[60] One new reaction was demonstrated, as the addition of diphenylacetylene or diethylacetylene to the Ni^INi^I complex gave 4,5-disubstituted benzo[*e*]pyrenes (Scheme 1.20). A kinetic study indicated that the reaction was first order in both diphenylacetylene and the Ni^INi^I compound, indicating that the alkyne induced rupture of the C-C bond linking the two halves of the dimer.

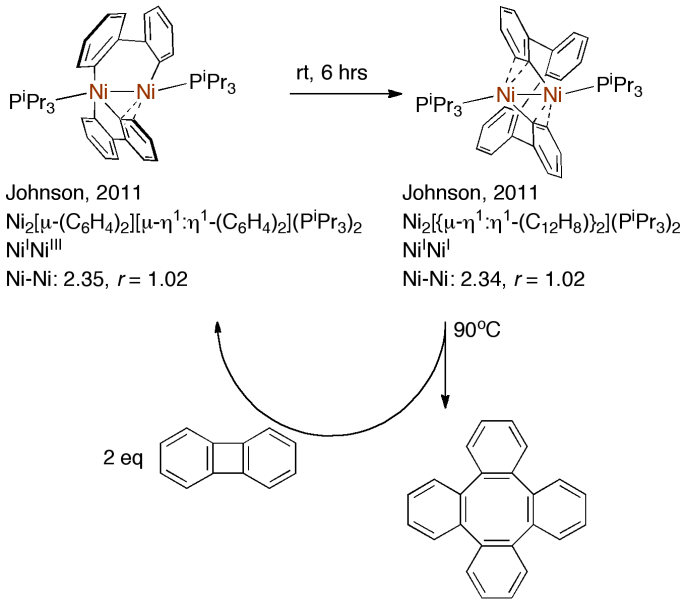

Scheme 1.21. Conversion of a $Ni^{III}Ni^{I}$ complex to a $Ni^{I}Ni^{I}$ complex, formation of tetraphenylene, and regeneration of the $Ni^{III}Ni^{I}$ complex upon addition of biphenylene.

The mechanism of formation of the Eisch dinuclear $Ni^{I}Ni^{I}$ complex was unknown. Using $PiPr_3$ instead of PEt_3, Johnson and coworkers made the analogous biphenyldiyl $Ni^{I}Ni^{I}$ compound $[(P^{i}Pr_3)Ni]_2[\mu\text{-}\eta^1\text{:}\eta^1\text{-}(C_{12}H_8)]_2$ (Ni-Ni = 2.3352(4) Å, r = 1.02) (Scheme 1.21). They identified an intermediate in its synthesis at room temperature and obtained the crystal structure of the intermediate: $[(P^{i}Pr_3)Ni]_2[\mu\text{-}(C_6H_4)_2][\mu\text{-}\eta^1\text{:}\eta^1\text{-}(C_6H_4)_2]$ (Ni-Ni = 2.3521(6) Å, r = 1.02). Formally, this intermediate is a $Ni^{I}Ni^{III}$ complex since one of the two biphenyldiyl ligands makes σ bonds with only one nickel center. The conversion of the $Ni^{I}Ni^{III}$ complex to the $Ni^{I}Ni^{I}$ complex was suggested to proceed by an intramolecular mechanism with an off-pathway mononickel complex. This means that the conversion of the $Ni^{I}Ni^{III}$ intermediate to the $Ni^{I}Ni^{I}$ product occurs by a reductive elimination from the Ni^{III} center. Moreover, $[(P^{i}Pr_3)Ni]_2[\mu\text{-}\eta^1\text{:}\eta^1\text{-}(C_{12}H_8)]_2$ was showed to catalytically convert biphenylene into tetraphenylene.

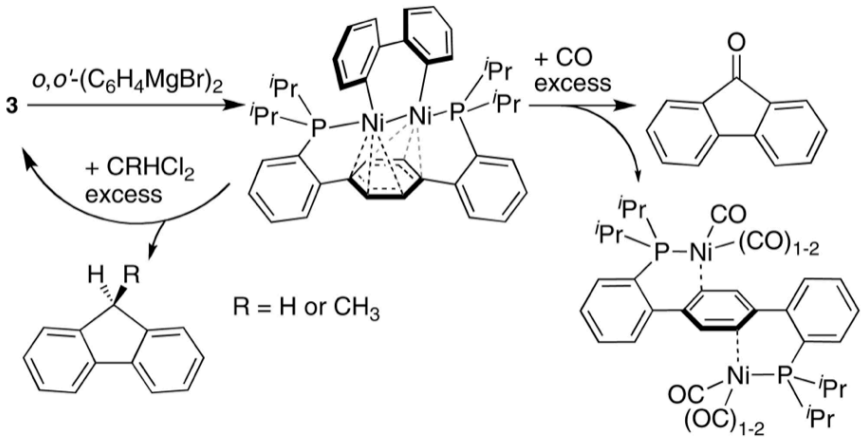

Scheme 1.22. Reactivity of a *p*-terphenyl diphosphine supported $Ni^{I}Ni^{I}$ organometallic complex. Complex 3 is $(L)Ni_2(\mu\text{-}Cl)_2$, where L is the diphosphine ligand. Adapted from reference 61.

Using a *p*-terphenyl diphosphine ligand, Agapie and coworkers synthesized a biphenyldiyl complex $(L)Ni_2[\mu\text{-}(C_6H_4)_2]$, where L is the diphosphine ligand (Scheme 1.22).[61] The crystal structure (Ni-Ni = 2.44266(19) Å, r = 1.06) showed that each nickel interacted with three C atoms in the middle phenyl ring of the diphosphine ligand. Reaction of the biphenyldiyl complex with an atmosphere of CO at room temperature resulted in fluorenone formation and a dinickel(0) product in which the Ni-Ni bond was ruptured. Addition of excess geminal dichloroalkanes resulted in formation of fluorene derivatives and $(L)Ni_2(\mu\text{-}Cl)_2$.

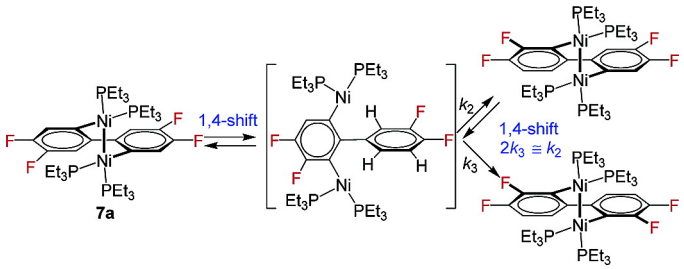

Scheme 1.23. Reversible 1,4-shifts (aromatic C-H bond activations) of $Ni^{I}Ni^{I}$ complexes. From reference 63.

Johnson and coworkers observed that the addition of $Br_2Ni(PEt_3)_2$ and 1% Na/Hg to the aryne complex $(PEt_3)_2Ni(\eta^2\text{-}C_6H_2\text{-}4,5\text{-}F_2)$ gave the $Ni^{I}Ni^{I}$ complex $[(PEt_3)_2Ni]_2[\mu\text{-}\eta^1\text{:}\eta^1\text{-}(C_6H_2\text{-}3,4\text{-}F_2)_2]$ (Ni-Ni = 2.3710(5) Å, r = 1.03), in which the fluorine substituents have isomerized, over 1-2 days.[62] The slow conversion allowed mechanistic work to be conducted, and intermediates were observed by ^{1}H, ^{19}F, and ^{31}P NMR spectroscopies.[63] A mixed PEt_3/PMe_3 analogue of one of these intermediates, $[(PEt_3)(PMe_3)Ni]_2(\mu\text{-}\eta^1\text{:}\eta^1\text{-}3,4\text{-}F_2C_6H_2\text{-}3',4'\text{-}F_2C_6H_2)$ was independently prepared and crystallographically characterized (Ni-Ni = 2.3079(8) Å, r = 1.00). NMR spectroscopy experiments revealed another intermediate, which was assigned as the asymmetric complex $[(PR_3)_2Ni]_2(\mu\text{-}\eta^1\text{:}\eta^1\text{-}3,4\text{-}F_2C_6H_2\text{-}4',5'\text{-}F_2C_6H_2)$. The interconversion of these intermediates and the final product is shown in Scheme 1.23. To summarize, this reaction pathway indicates that the $Ni^{I}Ni^{I}$ complexes reversibly activate aromatic C-H bonds at room temperature. Other systems that undergo 1,4- or 1,5-shifts contain Pd(II), Pt(II), and Rh(I), and so the observation of this chemistry with a first-row metal-metal bonded complex is unique.

The organometallic reactivity displayed by mid-to-late first-row metal-metal bonded bimetallics includes remarkable transformations such as the synthesis of a stable cobalt carbene derived from O=C bond cleavage of benzophenone and the reversible

activation of aromatic C-H bonds. A highly sought challenge is incorporating these stoichiometric reactions into a catalytic cycle. Indeed, propelled by the observation of oxidative addition of methyl iodide at (THF)Zr(MesNP^{i}Pr$_2$)$_3$Co(N$_2$), Thomas and coworkers have utilized zirconium-cobalt bimetallics as catalysts for Kumada couplings of unactivated alkyl halides and alkyl Grignards,[64,65] and Johnson and coworkers found that [(P^{i}Pr$_3$)$_2$Ni]$_2$[μ-η^1:η^1-(C$_6$H$_4$)]$_2$ can catalytically convert biphenylene into tetraphenylene.[66] However, more work towards understanding how the electronic structure affects reactivity could lead to the design of better catalysts. In particular, a better understanding of the role of the metal-metal bond in the reactivity would be desirable. One way to accomplish this would be to design reactivity studies using isostructural organometallic molecules containing metal-metal bonds with different combinations of metals. The third chapter of the thesis deals with these considerations.

1.5. Scope of the Thesis

The purpose of this thesis involves detailing the preparation of a new binucleating ligand, tris-(2-(2-pyridylamino)ethyl)amine (H$_3$py$_3$tren), and studying the synthesis, characterization, and reactivity of py$_3$tren supported bimetallics with managanese, iron, and cobalt. Chapter 2 of this thesis will elucidate the synthesis and characterization of a family of five isostructural bimetallics (cobalt-cobalt, cobalt-iron, cobalt-manganese, iron-iron, and iron-manganese) containing metals in the divalent oxidation state. It will be shown that the diiron bimetallic, which has a much shorter crystallographically characterized metal-metal distance than the other four bimetallics, features an $S = 3$ spin arising from iron-iron bonding due to delocalized orbitals, in contrast to the other four

bimetallic combinations, which feature antiferromagnetic coupling of the metals due to primarily localized orbitals. The third chapter of the thesis compares the metal-metal bonding and reactivity of two isostructural bimetallics with a benzyl ligand – a dicobalt molecule and an aluminum-cobalt molecule. It will be suggested that the dicobalt molecule contains two cobalt(II) centers that antiferromagnetically couple, while the aluminum-cobalt bimetallic contains a cobalt(I) center that datively bonds to an aluminum(III) center. Both complexes react with reagents prone to one-electron chemistry; it is suggested that the aluminum-cobalt complex reacts with some substrates by two-electron chemistry, whereas the dicobalt compound does not. The fourth chapter of this thesis will explain the synthesis and characterization of a redox series of hexairon clusters containing cores with the same solution state structure, as well as detail a crystallographic comparison of two tetrairon clusters. It will be shown that the mixed-valent clusters contain localized valences. In Chapter 5, a preliminary study concerning the reaction of O_2 with a py_3tren supported diiron molecule will be overviewed. Mixed-valent tetrairon and hexairon clusters are intermediates in this reactivity, and the thermodynamic sink of the system is another hexairon cluster.

Chapter 2

Role of the Metal in the Bonding and Properties of Bimetallic Complexes Involving Manganese, Iron, and Cobalt

From:

Tereniak, S. J.; Carlson, R. K.; Clouston, L. J.; Young, V. G., Jr.; Bill, E.; Maurice, R.; Chen, Y.-S.; Kim, H. J.; Gagliardi, L.; Lu, C. C. *J. Am. Chem. Soc.* **2014**, *136*, 1842.

2.1 Overview

A multidentate, ligand platform is introduced that enables the isolation of both homo- and heterobimetallic complexes of divalent first-row transition metal ions such as Mn(II), Fe(II), and Co(II). By using a two-step metallation strategy, five bimetallic coordination complexes were synthesized with the general formula MM'Cl(py_3tren), where py_3tren is the triply deprotonated form of *N*,*N*,*N*-tris(2-(2-pyridylamino)ethyl)amine. The metal-metal pairings include dicobalt (**1**), cobalt-iron (**2**), cobalt-manganese (**3**), diiron (**4**), and iron-manganese (**5**). The bimetallic complexes have been investigated by X-ray diffraction and X-ray anomalous scattering studies, cyclic voltammetry, magnetometry, Mössbauer spectroscopy, UV-Vis-NIR spectroscopy, NMR spectroscopy, combustion analyses, inductively coupled plasma optical emission spectrometry, and *ab initio* quantum chemical methods. Only the diiron complex in this series contains a metal-metal single bond (2.29 Å). The others show weak metal-metal interactions (2.49 to 2.53 Å). The diiron complex is also distinct with a septet ground state, while the other bimetallic species have much lower spin states from $S = 0$ to $S = 1$. We propose that the diiron system has delocalized metal-metal bonding electrons, which correlates with the short metal-metal bond and the higher spin state. Multi-configurational wavefunction calculations reveal that, indeed, the metal-metal bonding orbitals in the diiron complex are much more delocalized compared to the orbitals of the dicobalt analogue.

2.2 Introduction

Heterometallic clusters are used as bioinorganic cofactors to perform diverse chemical reactions. They occur in MoFe and VFe nitrogenases, [NiFe] hydrogenases, purple acid phosphatases, Ni-[3Fe-4S] CO dehydrogenases, and class Ic ribonucleotide reductases (RNRs).[67-70] Many of these heterometallic cofactors pair a mid and late first-row transition metal, e.g. Fe and Ni, to promote the heterolytic activation of small molecules, e.g. H_2 and CO_2.[71] In contrast, Class Ic RNRs uses two *similar* metals, Fe and Mn, to tune the redox properties of the cofactor.[72,73] The heterobimetallic cofactor is unique to this subclass, as most class I RNRs use a classical diiron(II,II) active site with a neighboring tyrosine.[74] When the diiron cofactor reacts with dioxygen, a diiron(III,III)-tyrosyl radical (i.e. 2Fe(III)-Y•) intermediate is formed, where the reactive hole equivalent is located on the amino acid. It is proposed that since Class Ic RNRs lack this tyrosine, an iron site is swapped for manganese to store the oxidizing equivalent as the Fe(III)Mn(IV) intermediate.[75-78] To better understand the different roles of iron versus manganese, Fe-Mn complexes have been targeted, but only a few, biomimetic Fe-Mn complexes have been reported.[79-82] A key challenge is the selective preparation and/or clean isolation of the heterometallic core when the metal centers are so similar.[81]

Beyond their bioinorganic relevance, heterometallic clusters may give rise to unusual magnetic and electronic properties. Indeed, Fe-Mn complexes have been studied for elucidating magnetic exchange interactions.[83-86] Betley and co-workers have shown that the homotrimetallic clusters, Fe_3, Co_3 and Mn_3, exhibit interesting magnetic behavior and are extending their studies to mixed-metal analogues.[22,23,40,42] Also, as in the case of

Class Ic RNRs, swapping of metal sites with similar transition metals could prove a versatile strategy for tuning redox potentials. In related work, Agapie *et al.* have shown that the redox potentials of Mn_3-oxide clusters can be systematically tuned over 800 mV by covalently attaching redox-inactive metal centers of varying Lewis acidities.[11,87] Systematic studies of heterobimetallic species may provide great insight into structure-property relationships, and hold promise for achieving predictable and precise control of cluster properties through metal atom substitution.

Of note, nearly all these examples contain a bridging oxo, phenoxo, or amido ligand, which can greatly attenuate the metal-metal interaction. We have been interested in configuring bonds between first-row transition metals by using ligands that facilitate metal-metal bonding.[88-90] Recently, use of multidentate ligands with two distinct binding sites enabled the synthesis of a rare, iron-cobalt heterobimetallic complex.[21] The same ligand also gave access to a related dicobalt complex. Both the iron-cobalt and dicobalt species have short metal-metal bonds and are high spin. However, attempts to extend the coordination chemistry to other similar metal pairings were unsuccessful.

Herein, we report a new ligand variant where three pyridyl groups are covalently attached to tris(2-aminoethyl)amine, or tren. The ligand, *N*,*N*,*N*-tris(2-(2-pyridylamino)ethyl)amine, or $H_3(py_3tren)$, has enabled the isolation of homo- and heterobimetallic complexes of cobalt, iron, and manganese. Five bimetallic chloride complexes, MM'Cl(py_3tren) (see Figure 1), have been isolated and characterized by a host of physical methods. Since standard X-ray diffraction experiments do not differentiate between similar transition metals, the heterobimetallic species have been

further examined by both X-ray anomalous scattering and inductively coupled plasma optical emission spectrometry (ICP-OES) for analysis of single crystals and the bulk material, respectively. Two of the three heterobimetallic complexes (CoMn **3** and FeMn **5**) showed only a slight degree of metal-site mixing, while CoFe **2** was contaminated by CoCo **1** (8%). The good-to-high purity of these heterobimetallic complexes is remarkable, given the propensity of high-spin Co(II), Fe(II), and Mn(II) ions to undergo ligand exchange and thus effect metal scrambling.

This isostructural bimetallic family presents a unique opportunity to systematically study the effect of the metal identity on metal-metal bonding as well as on their electronic and magnetic properties.[37,38,90-92] We have found that the metal-metal interactions are generally weak with the notable exception of the diiron complex, **4**, which contains a bonafide iron-iron bond. With the exception of **4**, the electrochemical and magnetic properties of the bimetallic family can be rationalized by considering these bimetallic species as individual metal ions, or as localized spins that couple antiferromagnetically, giving lower spin states. In contrast, complex **4**, which has an $S = 3$ ground state, does not fit the localized description. Theoretical studies reveal delocalized metal-metal bonding in **4**, which is correlated with its different magnetic behavior. Finally, the isotropic magnetic couplings for the bimetallics were computed using density functional theory (DFT) with various exchange-correlation functionals.

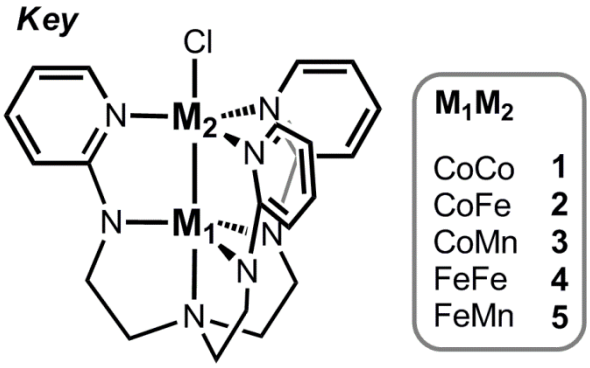

Figure 2.1. Key for the five $M_1M_2Cl(py_3tren)$ bimetallics **1**-**5** discussed in this chapter.

2.3 Results and Discussion

2.3.1 Synthesis

The ligand, *N*,*N*,*N*-tris(2-(2-pyridylamino)ethyl)amine, or $H_3(py_3tren)$, was obtained in one step by heating tren with 2-bromopyridine (3.14 equiv.) and K_2CO_3 in DMSO (180 °C, 3 days). The slight excess of 2-bromopyridine was necessary to facilitate the work up, as the desired product is more easily separated from the tetra-substituted byproduct than from the bis-substituted one. The reaction worked well on a 20 g scale; and, subsequent purification by column chromatography gave a moderate yield (14.2 g, 55 %) of clean $H_3(py_3tren)$ as a tan solid.

A five-membered series of homo- and heterobimetallic complexes featuring cobalt, iron, and/or manganese was then rapidly assembled using the two-step metallation strategy depicted in Scheme 1. Deprotonation of $H_3(py_3tren)$ with 3 equiv. of benzylpotassium (abbreviated as KBn) followed by metathesis with $CoCl_2$ and $FeCl_2$ generated the mononuclear precursors, K[Co(py_3tren)] and K[Fe(py_3tren)], respectively. A crystal structure of K[Co(py_3tren)] shows that the cobalt center is exclusively

coordinated by the tris(amido)amine donors, leaving the pyridine donors free to bind a second metal (Figure A1.7 and Tables A1.1 and A1.2). Indeed, K[Co(py_3tren)] can be reacted with $CoCl_2$, $FeCl_2(THF)_{1.5}$, or $MnCl_2(THF)_2$ to form bimetallic CoCoCl(py_3tren) (**1**), CoFeCl(py_3tren) (**2**), or CoMnCl(py_3tren) (**3**), respectively. Similarly, the mononuclear iron precursor, K[Fe(py_3tren)], can be mixed with $FeCl_2(THF)_{1.5}$ or $MnCl_2(THF)_2$ to produce FeFeCl(py_3tren) (**4**) and FeMnCl(py_3tren) (**5**), respectively. The homobimetallic species **1** and **4** were synthesized at room temperature. On the other hand, the second metallations for the heterobimetallic complexes were conducted at much lower temperatures of −50 °C to impede metal scrambling in the two distinct binding sites (*vide infra*).

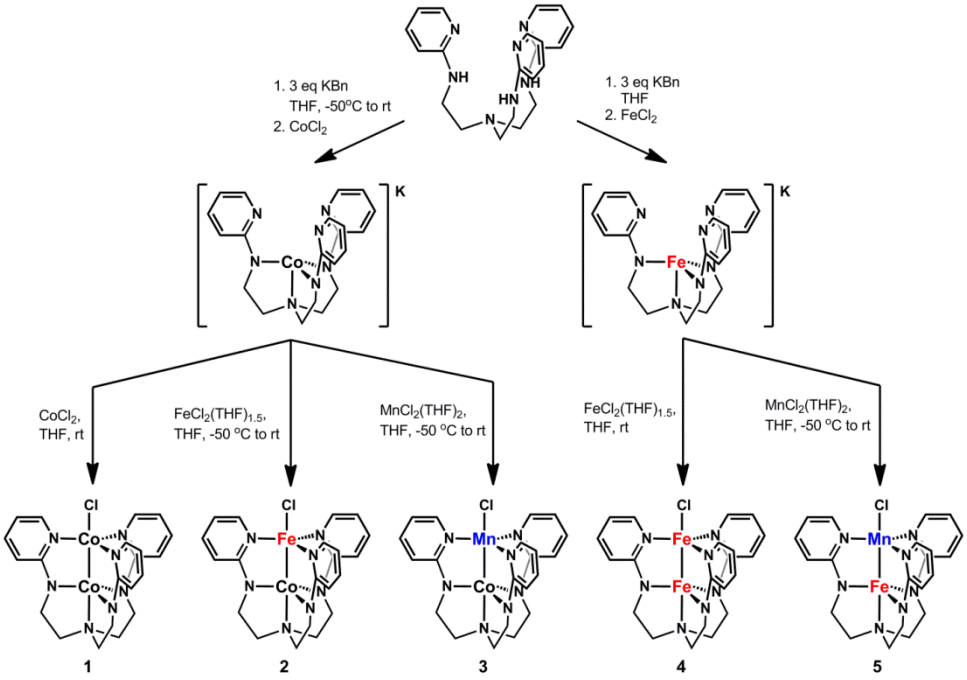

Scheme 2.1. Two-step metallation reactions: (1) synthesis of K[Co(py_3tren)] and K[Fe(py_3tren)]; and (2) synthesis of $M_1M_2Cl(py_3tren)$ complexes **1**−**5**.

Of note, we did observe significant metal scrambling during the attempted synthesis of FeCoCl(py_3tren), which is a structural isomer of **2**. The metallation reaction of mono-iron with $CoCl_2$ gave a mixture of dicobalt **1**, diiron **4**, and cobalt-iron **2** (by ^{1}H NMR). In contrast, the metallation reaction of mono-cobalt with $FeCl_2(THF)_{1.5}$ proceeds quite cleanly to **2**. Based on these results, we believe that complex **2** is the thermodynamically favored isomer, and that attempts to kinetically prepare the higher energy isomer were unsuccessful because of the lability of high-spin M(II) ions in these binding sites.

2.3.2 NMR Spectroscopy

Each of the five bimetallic compounds has been characterized by NMR. Proton NMR spectra for all the bimetallics contain six resonances, which is consistent with C_{3v} symmetry in solution (Figure 2.2). At room temperature, the complexes also appear to be paramagnetic based on the isotropic peak shifts. Interestingly, dicobalt **1** has the smallest range of proton chemical shifts from −1.6 to 21.7 ppm, while diiron **4** has by far the largest range from −15.7 to 168 ppm.

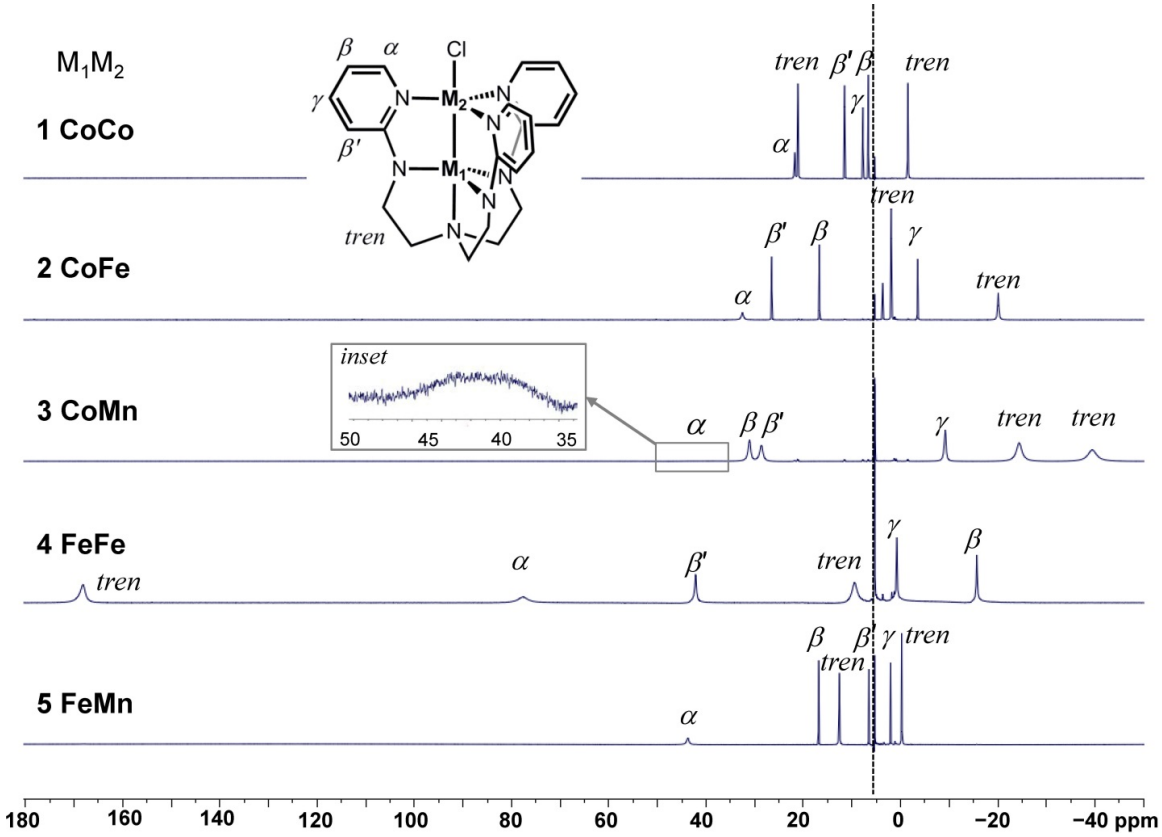

Figure 2.2. Stacked plot of the ^{1}H NMR spectra of 1−5 (500 MHz, CD_2Cl_2). Inset shows a close-up of a broad peak, assigned as the α proton in **3**. The residual solvent peaks are marked by the dotted line.

The protons of the tren backbone can be distinguished from those of the pyridyl ring by the relative peak integrations of 2H and 1H, respectively. The pyridyl protons can be further differentiated by using two-dimensional NMR techniques. Correlation spectroscopy (COSY) of dicobalt **1** showed all the major cross peaks, including $\alpha-\beta$, $\beta-\gamma$, and $\beta'-\gamma$ (Figure A1.5). Unfortunately, the $\alpha-\beta$ cross peak was not observed for cobalt-iron **2** or iron-manganese **5**; and, *no* cross peaks were detected for **3** and **5**.

Since the loss of coupling information often results in paramagnetic peak broadening, we performed inversion recovery experiments to measure the spin-lattice

relaxation times (T_1). The T_1 values and proton assignments are shown in Table 2.1. The α-protons of the pyridyl ring, which gives rise to the most downfield peak (except in the case of diiron **4**), have the shortest T_1 relaxation times of all the proton types. At the other extreme, the γ-protons, which are located farthest from *any* metal center, have the longest T_1 values. The specific assignments of β and β' protons are obvious only in the case of **1** (based on COSY), but they are ambiguous in the other bimetallic complexes. As the β' proton is located closer to M_1 (4.5 to 4.6 Å) than β is to M_2 (~5.0 Å), we assign the resonance with the slightly shorter T_1 to β', which is independently confirmed for **1**. Interesting, the bimetallic complexes can be subdivided into two categories based on their T_1 values: **1**, **2**, and **5** relax more slowly compared to **3** and **4**. Of interest, the faster relaxation times appear to be correlated with the overall spin state, $S_{tot} > ½$ (*vide infra*), rather than the identity of the metal ion(s).

Table 2.1. Proton NMR assignments of **1**−**5** with chemical shifts (ppm) and T_1 (ms).

Cpd.	α (T_1)	β (T_1)	γ (T_1)	β' (T_1)	*tren* (T_1)
1	21.7 (5.6)	6.7 (95)	7.7 (255)	11.5 (80)	20.9 (15), −1.6 (15)
2	32.5 (1.4)	16.8 (69)	−3.6 (105)	26.6 (46)	1.7 (33), −20.3 (29)
3	40.0 (*nd*)[a]	31.1 (1.9)	−9.2 (3.7)	28.6 (1.6)	−24.4 (1.3), −39.4 (1.1)
4	79 (*nd*)[a]	−15.7 (5.1)	0.78 (8.0)	42 (2.5)	168 (0.65), 9.5 (0.67)
5	43.7 (1.0)	16.8 (57)	2.0 (67)	6.5 (30)	−0.3 (16), 12.6 (7.8)

[a] *nd* = not determined because of peak broadness.

2.3.3 UV-Vis-NIR Spectroscopy

All the coordination complexes, both mono- and dinuclear, are colorful. The mononuclear cobalt complex is bright green, and its bimetallic derivatives are green-brown for dicobalt **1**, red for cobalt-iron **2**, and green-yellow for cobalt-manganese **3**. In

the iron series, the mononuclear iron species is yellow, while diiron **4** is dark red, and iron-manganese **5** is orange.

Of interest, all complexes show intense bands in the UV-visible region and weak bands in the near-infrared region (NIR) (Figure 2.3). In the cobalt series, mononuclear cobalt and complexes **1** – **3** have an intense peak at ~315 nm ($\varepsilon > 22{,}000\ M^{-1}cm^{-1}$) with a shoulder at ~350 nm. A second shoulder is discerned in two complexes, the mono-cobalt (386 nm, $\varepsilon = 6{,}700\ M^{-1}cm^{-1}$) and cobalt-manganese (397 nm, $\varepsilon = 6{,}780\ M^{-1}cm^{-1}$). The bimetallics **1** – **3** also have a visible band at ~450 nm ($\varepsilon = 7{,}480$ to $8{,}950\ M^{-1}cm^{-1}$), which is notably absent for mono-cobalt. Of interest, this band undergoes a blue shift from **1** (450 nm) to **2** (448 nm) to **3** (435 nm). This band could correspond to a metal-ligand charge transfer of the top metal (M_2). Related monometallic complexes with a trigonal pyridyl environment are known. For example, $[M(TPA)Cl]^+$ complexes, where TPA is tris(2-pyridylmethyl)amine), have been prepared for Co(II), Fe(II), and Mn(II).[93-95] However, in none of these cases was a peak near 450 nm reported with such high intensity. Alternatively, this band could correspond to a metal-to-metal charge transfer (MMCT), specifically $Co \rightarrow M_2$, since the energy decreases from M_2 = Co to Fe to Mn, which would be consistent with the trend in the electronegativities of the metal ions. While the energy for MMCT may seem atypically high, transitions of *d* electrons from/into the M_1-M_2 σ/σ^* orbital would be expected to need higher energy photons (*vide infra*). Finally, mono-cobalt and complexes **1** – **3** have NIR bands of similar intensities, ε ~100 $M^{-1}cm^{-1}$. The main NIR band shifts to the blue from mono-cobalt to **2** ~ **3** to **1**. The NIR band is thus proposed to arise from intrametal *d-d* transitions, though we cannot

rule out intermetal *d-d* transitions (e.g. MMCT). Further work will be needed to make definitive assignments.

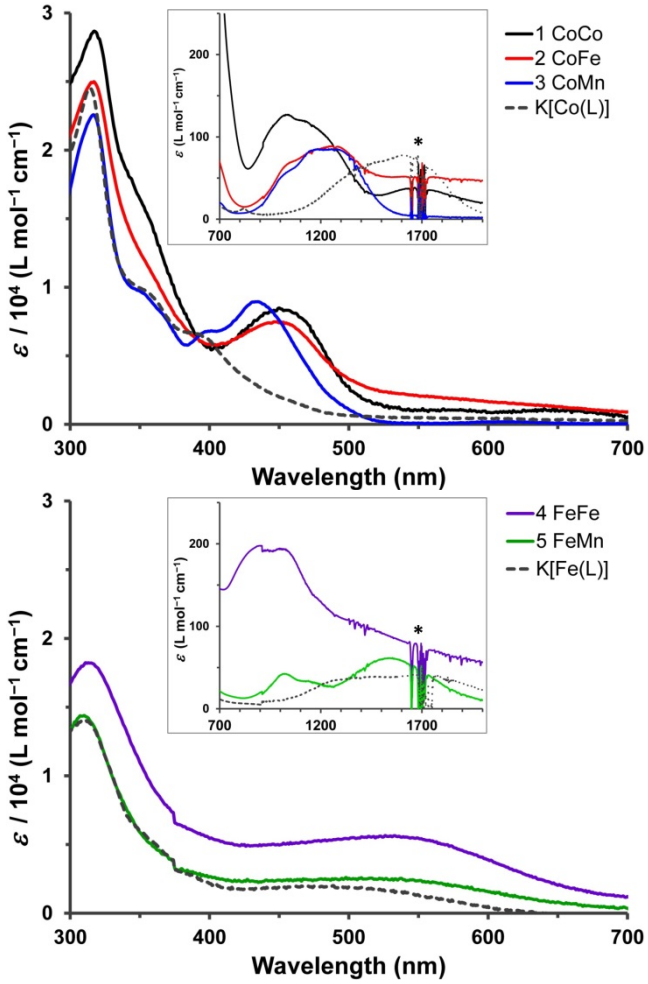

Figure 2.3. Top: UV-Vis plots of K[Co(py_3tren)] and cobalt-containing complexes 1−3. Bottom: UV-Vis plots of K[Fe(py_3tren)] and iron-containing complexes 4 and 5. Insets show the Vis-NIR region. Spectra were collected as solutions in CH_2Cl_2. The asterisk denotes artifacts from solvent subtraction.

In the iron series, the UV-Vis region is remarkably similar for mono-iron and the bimetallic complexes **4** and **5**. Of note, the intensities of the bands in the UV-Vis are practically identical for mono-iron and iron-manganese **5**, but are greater for diiron **4**, which suggests that the doubling of the intensity of the broad visible band may be due to

the presence of two iron centers. The broad, visible band also detectably red-shifts from mono-iron to bimetallic **4** and **5**. Unlike the cobalt series, there is no indication of any unique absorption feature that can be attributed to a metal-metal charge transfer. Like the cobalt series, the NIR bands in iron series also undergo a blue shift from mono-iron to bimetallic **4** and **5**, with the NIR band for the homobimetallic diiron **4** gaining appreciable intensity.

2.3.4 X-ray Diffraction Studies

Single crystals of **1** – **5** were examined by X-ray diffraction. Dicobalt **1** crystallized in the orthorhombic space group $P2_12_12_1$, while complexes **2** – **5** all crystallized in the monoclinic space group $P2_1/n$ with similar unit cells. The coordination geometry at each metal center is trigonal bipyramidal with an axial chloride ligand bound to the pyridine-coordinated metal, i.e. M_2 (Figure 2.4). Unfortunately, standard X-ray data cannot distinguish between metals of similar atomic numbers. To address the complicated issue of metal-site scrambling, we have conducted X-ray anomalous scattering experiments for the heterobimetallic complexes (*vide infra*). Nonetheless, some clear trends are observed in the collective geometrical data that support the metal assignments (Table 2.2). For instance, the cobalt-apical amine (N_{ap}) bond distance remains essentially unchanged at 2.01 to 2.02 Å in the cobalt series, i.e. when M_1 = Co. The iron-N_{ap} bond lengths in **4** and **5** are identical at 2.05 Å, and gratifyingly, they are slightly longer than those for Co-N_{ap}, which is consistent with the larger covalent radius of Fe(II) versus Co(II). Likewise, the bond distances between the bottom metal and the equatorial nitrogen atoms (i.e. M_1−N_{eq}) increase from 1.89 − 1.90 Å for M_1 = Co (in **1** –

3) to 1.93 − 1.94 Å for M_1 = Fe (in **4** and **5**). For the metal-ligand bonds lengths around the top metal center, especially M_2−Cl, no clear trend was readily discerned as M_2 can be Co, Fe or Mn. One notable finding is that when M_2 = Mn (in **3** and **5**), the M_2−N_{py} (where py = pyridine) and M_2−Cl bond distances are essentially identical.

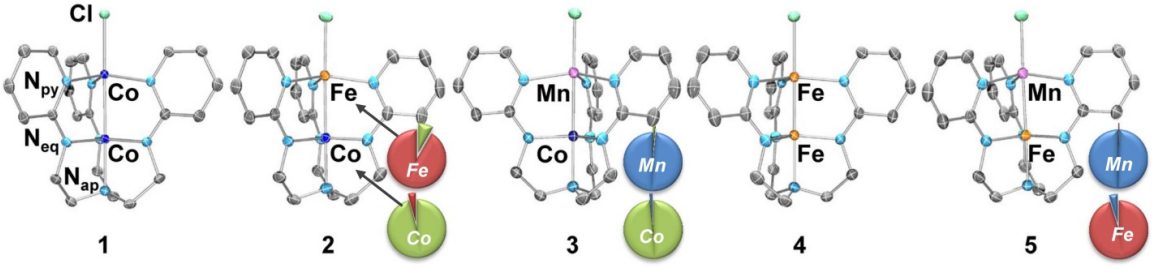

Figure 2.4. Solid-state structures of 1−5. Thermal elliposids are shown at 50% probability. Protons are omitted for clarity. For the heterobimetallic species, the percentages of each metal (Co in green, Fe in red, and Mn in blue) at each binding site (as determined by X-ray anomalous dispersion) are depicted as pie charts.

Table 2.2. Geometrical parameters, including bond lengths (Å) and angle (°) for complexes **1** – **5**.[a]

	1	**2**	**3**	**4**	**5**
M_1−M_2 (Å)	2.4986(4)	2.4913(3)	2.5312(4)	2.2867(5)	2.5283(3)
r[b]	1.08	1.07	1.09	0.98	1.08
M_1−N_{ap} (Å)	2.012(1)	2.010(1)	2.018(2)	2.054(1)	2.053(1)
M_1−N_{eq} (Å)[c]	1.885±0.004	1.894±0.006	1.903±0.005	1.931±0.007	1.940±0.007
M_2−Cl (Å)	2.3487(5)	2.3455(4)	2.361(2)	2.3759(6)	2.3559(5)
M_2−N_{py} (Å)[c]	2.074±0.007	2.107±0.008	2.163±0.008	2.11±0.01	2.179±0.007
M_1−M_2−Cl (°)	177.69(2)	177.36(1)	177.92(2)	178.14(2)	177.26(2)

[a] Estimated standard deviations (esd) are provided in parentheses. [b] r = ratio of M_1−M_2 bond distance to the sum of M_1 and M_2 single-bond radii. [c] M_1−N_{eq} and M_2−N_{py} bond lengths are reported as averages ± standard deviations.

Of central interest, the M_1−M_2 bond lengths would give insight into the nature of the metal-metal bonding in these different metal pairs. The longest M_1−M_2 distances (2.53 Å) are observed in cobalt-manganese **3** and iron-manganese **5**. Intermediate metal-metal bond distances of 2.49 − 2.50 Å are found in dicobalt **1** and cobalt-iron **2**, while the diiron complex **4** has by far the shortest metal-metal bond distance of 2.29 Å in this

series. Because the expected differences in metal covalent radii complicate any absolute comparisons, Cotton *et al.* introduced the formal shortness ratio[96] (denoted as *r* in Table 2.2), where the metal-metal bond lengths are normalized by the sum of the two metals' single-bond radii. With the notable exception of diiron **4**, the *r* values for all the other bimetallic complexes are significantly greater than one (1.07 to 1.09), suggesting that the metal-metal covalent interactions are weak at best. In the case of diiron **4**, the *r* value of 0.98 is near the expected value of 1.0 for a single metal-metal bond. Hence, diiron **4** stands out in this series in that it has a bona fide metal-metal bond. Of interest is the extremely short iron-iron bond of 2.13 Å that is found in a diiron(I,I) bis(guanidinate) complex by Jones *et al*.[20] The authors proposed the iron centers to be multiply bonded and reported a large magnetic moment of 7.95 μ_B.

The heterobimetallic species **2**, **3**, and **5** were investigated by X-ray anomalous scattering to assess the purity of each metal-binding site, and consequently, to determine the selectivity of our metallation strategy. This technique differentiates metals with similar number of electrons by exploiting the differences in the metals' K-edge energies. As the X-ray wavelength approaches the metal's K edge energies, the anomalous terms of the atomic scattering factor change rapidly (Figure 2.10). Using a synchrotron source, a series of anomalous datasets are collected to span the metals K-edges, including the edge energies (λ_{edge}) as well as 50 eV above and below it ($\lambda_{edge} \pm 50$ eV).[97] In addition, an additional dataset is collected at high energy (30 keV) to determine a high-resolution structure. For reasons detailed in the experimental section, the measurements taken at lower energy ($\lambda > \lambda_{edge}$) are more reliable, and so, they were used exclusively in solving

the metal occupancies at each binding site.[98] Recently, Betley *et al.* reported a similar methodology for obtaining anomalous scattering data.[23] A unique aspect of our approach is that we simultaneously analyze the anomalous datasets and perform a least-square refinement[99] to determine metal occupancies.

The high resolution structures of the heterobimetallic complexes are practically identical (within 0.01 Å) to those determined by standard X-ray diffraction (Tables A1.3 and A1.4). The results of the metal occupancies are given in Table 2.3 and graphically portrayed as pie charts in Figure 2.4. Gratifyingly, very little metal-mixing is observed. For compounds **3** and **5**, both metal-binding sites are substitutionally pure (≥ 95%), and thus, we expect these complexes to be highly homogeneous. While the main component is quite clearly the expected product, $M_1M_2Cl(py_3tren)$, other related species may be present as minor impurities, including its constitutional isomer, $M_2M_1Cl(py_3tren)$, and the two homobimetallic species. If we assume statistical mixing of the M_1/M_2 populations at the two independent sites, then the overall purity of the $M_1M_2Cl(py_3tren)$ is estimated to be 97 and 95% for **3** and **5**, respectively. Using the same analysis, complex **2** has an overall purity of 88% with a significant presence of dicobalt **1** (8%). This suggests that either dicobalt **1** is carried over from the first metalation step and/or that iron and cobalt ions exchange during the second metalation. Because of the high purity of the related cobalt-containing complex **3**, we conclude it is the mixing of the similar iron and cobalt centers during the second metalation of **2** that generates the dicobalt impurities. While these results are promising for single crystals, it does not assess the purity of the bulk material. Hence, we sought to independently verify the metal composition of the bulk

using inductively coupled plasma optical emission spectrometry (ICP-OES). The metal compositions are in excellent agreement with those determined by the anomalous measurements (Table 2.3, last column).

Table 2.3. Compositions of the metals (Co, Fe, Mn) at the unique binding sites (M_1, M_2) in the heterobimetallic complexes (**2**, **3**, **5**) as determined by X-ray anomalous scattering studies.[a]

Cpd.	M_1	M_2	purity (%)	$M_1 : M_2$ [a]
2	Co 0.957(11) Fe 0.043(11)	Fe 0.916(11) Co 0.084(11)	88	Co : Fe 1.04 : 0.96 (1.01 : 0.99)
3	Co 0.983(12) Mn 0.017(12)	Mn 0.985(11) Co 0.015(11)	97	Co : Mn 1.00 : 1.00 (0.99 : 1.01)
5	Fe 0.952(16) Mn 0.048(16)	Mn 0.995(15) Fe 0.005(15)	95	Fe : Mn 0.96 : 1.04 (0.92 : 1.08)

[a] Metal ratios of the *bulk* sample as determined by ICP-OES are given in parentheses.

2.3.5 Electrochemistry

All the bimetallic coordination complexes have been characterized by cyclic voltammetry in 0.1− 0.4 M [nBu$_4$N]PF$_6$/THF. To aid the interpretations of the cyclic voltammogram (CVs), we have also examined the neutral ligand and the monometallic complexes. The ligand, H$_3$(py$_3$tren), shows an irreversible oxidation at E_{pa} = 0.5 V (Figure A1.6), which shifts cathodically to 0.2 and −0.2 V in mono-iron and mono-cobalt, respectively. The mononuclear species also have an additional, quasi-reversible oxidation at −0.5 V for cobalt and −1.4 V for iron, where the mono-iron complex is significantly easier to oxidize than the mono-cobalt derivative by nearly 1 V (Figure

A1.6). No reductive processes were observed for $H_3(py_3tren)$ or the monometallic species.

The CVs of the bimetallic complexes are shown in Figure 2.5, with the corresponding redox potentials given in Table 2.4. Complexes **1** − **5** all show an irreversible oxidation at E_{pa} = 0.41 to 0.50 V, which is attributed to a ligand-based oxidation (not shown in figure). In the cobalt series, complexes **1**, **2**, and **3**, all have one quasi-reversible/irreversible oxidative process at $E^{\circ\prime}$ (or E_{pa}) = 0.0 V. Because of the similarity in the redox potentials of the mono-cobalt complex and the cobalt series, the redox reaction occurring at 0 V is likely to be Co(II)/Co(III) in nature. The iron series, consisting of **4** and **5**, differ from the cobalt series in that two additional oxidative processes are observed at $E^{\circ\prime}$ (or E_{pa}) = −0.40 and 0.19 V, and thus, are significantly different from mono-iron. Presumably, the former redox potential corresponds to an Fe(II)/Fe(III) couple. In related work, Berry et al. showed that even a weak Cr_2•••Fe interaction can significantly perturb the Fe(II)/Fe(III) redox potential.[100] The second redox couple can be attributed to either M_2(II)/M_2(III) , or perhaps, even further oxidation to Fe(IV). Strangely, M_2(II)/M_2(III) redox couples are not observed in the cobalt series, and Fe(III)/Fe(IV) redox couples can be as low as 0.25 V (Vs. Fc/Fc^+) with tris(amido)amine ligands.[101] On the other hand, the mono-iron showed no indication of a second iron-based oxidation.

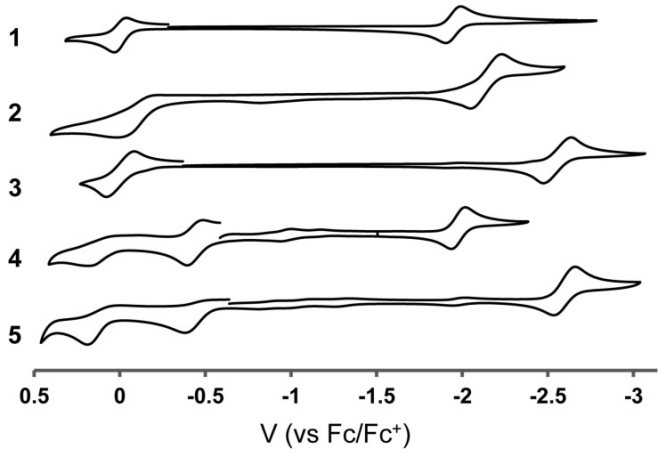

Figure 2.5 Cyclic voltammograms of **1**−**5** in 0.4 M [nBu$_4$N]PF$_6$/THF at 300 mV/s (except for **2**, 0.1 M [nBu$_4$N]PF$_6$/THF at 10 mV/s).

Table 2.4. Reduction and oxidation potentials (V)[a] of **1**−**5**.

Cpd.	oxidations ($E°'$ or E_{pa})[b]	reduction ($E°'$)
1	−0.01, *0.48*	−1.95
2	*−0.04*, *0.41*	−2.06
3	0.00, *0.49*	−2.55
4	−0.45, *0.19*, *0.44*	−1.98
5	*−0.39*, *0.19*, *0.50*	−2.61

[a] vs. Fc/Fc$^+$ [b] E_{pa} denoted in italics

Complexes **1** − **5** each exhibit a single quasi-reversible/reversible reductive process. Due to the lack of any similar processes in the monometallic species, we believe that these reductions are localized at the top metal, i.e. M_2. In support of this hypothesis, when M_2 = Mn as in cobalt-manganese **3** and iron-manganese **5**, the reduction potentials are nearly identical at −2.6 V. Also, in the cobalt series, the reduction potentials shift as a function of M_2, from −1.95 V for **1** (M_2 = Co) to −2.06 V for **2** (M_2 = Fe) to −2.55 V for **3** (M_2 = Mn). While these potentials correspond to the one-electron M(II)/M(I) redox couples, they follow the same trend as the two-electron redox potentials for the M(II) ions, where M(II)(aq) + 2e → M(s). However, when M_2 = Fe, the reduction potentials are

slightly different for **2** (−2.06 V) and **4** (−1.98 V). Perhaps this difference arises from the dissimilarity of the metal-metal interactions in **2** versus **4**, where the latter has a more delocalized metal-metal bond compared to the former.

To summarize the CV studies, bimetallic complexes **1** − **5** can undergo multiple electron transfers, and these reactions appear to be primarily localized at the individual metal centers. Specifically, the first oxidative processes are associated with M_1; and, their potentials correspond to M_1(II)/M_1(III) redox couples. The potentials of the reductive processes, on the other hand, change with M_2 and are consistent with the M_2(II)/M_2(I) redox couple.

2.3.6 Mössbauer Spectroscopy

The iron-containing bimetallic complexes were further characterized by ^{57}Fe Mössbauer spectroscopy (0 T, 77 K). As expected, one major doublet was observed for the heterobimetallic compounds **2** and **5**, while two main signals were observed for diiron **4**, which is consistent with its two unique iron sites (Figure 2.6, Table 2.5). In cobalt-iron **2**, the iron center has an isomer shift (δ) of 0.88 mm/s with a quadrupole splitting (ΔE_Q) of 2.62 mm/s. These parameters are typical of mononuclear, high-spin Fe(II). However, in iron-manganese **5**, both δ and ΔE_Q have significantly decreased to 0.46 mm/s and 1.69 mm/s, respectively. A similar drop in isomer shift is observed for both iron centers in diiron **4** (δ = 0.58 and 0.48 mm/s). Although these isomer shifts are atypically low for S = 2 Fe(II) centers, they are also unusually high for either S = 1 or S = 0 Fe(II). In the literature, decreased isomer shifts have been reported for systems where the iron center is engaged in metal-metal bonding. For example, trigonal diiron(II,II) complexes with iron-

iron distances ranging from 2.58 to 2.87 Å have isomer shift values ~0.60 mm/s.[42] A tri-iron(II,II,II) system with short metal-metal bond distances of 2.30 Å (comparable to **4**) has an even lower isomer shift of 0.38 mm/s, although this could also be attributed to the overall lower spin, $S = 1$.[44]

For diiron **4**, the two Mössbauer signals can be tentatively assigned by comparing to **5**. Specifically, the doublet centered at 0.48 mm/s in complex **4** is remarkably similar to that of **5**. Since **4** and **5** have a common iron site at M_1, we believe that this doublet for **4** corresponds to M_1, and that the other signal at 0.58 mm/s belongs to M_2. Although complexes **2** and **4** share a common iron site at the M_2 position, their isomer shift values are dramatically different, and this variation may be attributed to the significant metal-metal bonding in **4** that is not present in **2**.

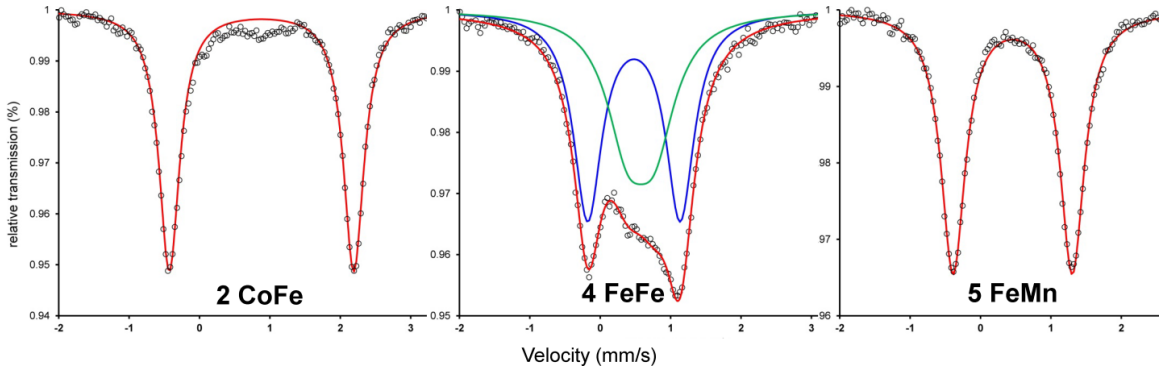

Figure 2.6. Zero-field Mössbauer spectra of **2** (left), **4** (center), and **5** (right) at 77 K. The experimental data is plotted as dots. Total fits are shown as red lines. Mössbauer parameters, δ (ΔE_Q) in mm/s, are for **2**, 0.88 (2.62); for **4**, 0.58 (0.38) (in green) and 0.48 (1.31) (in blue); and for **5**, 0.46 (1.69) mm/s.

Table 2.5. Zero-field ^{57}Fe-Mössbauer parameters (mm/s) for **2**, **4**, and **5**.

Cpd.	δ	ΔE_Q	line width [a]
2	0.88	2.62	0.35
4	0.58	0.38	0.72
	0.48	1.31	0.48
5	0.46	1.69	0.42

[a] Modeled as two Lorentzian lines with equal intensities and widths.

2.3.7 Magnetic Susceptibility

We have conducted variable temperature magnetic susceptibility measurements of the bimetallic complexes **1** – **5** under an applied dc field of 1 Tesla. The magnetic susceptibility (χ) data are plotted as χT versus T, where T is temperature, in Figure 7. All the χT plots show temperature dependence and appear to reach ground state configurations in the low temperature range of 15 to 50 K. Below 15 K, changes in χT may arise from several factors, including field saturation, magnetic anisotropy, and/or intermolecular effects. As we were primarily interested in understanding metal-metal exchange interactions, which are evident at higher T, no additional measurements were made to elucidate the factors that manifest themselves in the temperature regime below 15 K.

At low T (from 15 to 50 K) χT approaches 0 for dicobalt **1**, indicating a singlet ground state. For cobalt-iron **2** and iron-manganese **5**, χT plateaus to 0.36 and 0.45 cm^3 K/mol at low T, respectively. These values are near 0.375 cm^3 K/mol, the expected value for $S = ½$. For cobalt-manganese **3**, χT decreases slowly to 0.95 cm^3 K/mol at low T, which is consistent with $S = 1$ (for $g = 2$, $\chi T = 1.0$ cm^3 K/mol). One general explanation is that the ground spin states are the net outcome of two high-spin M(II) spins that are antiferromagnetically coupled, where the overall spin state, S_{tot}, is equivalent to $S_1 - S_2$. Thus, when the two M(II) ions are both cobalt like in **1**, a singlet state is generated. When the two M(II) ions belong to neighboring groups of the periodic table, as in **2** and **5**, a

doublet spin state results. Finally, a triplet state is derived for **3**, where the group numbers of the two M(II) ions differ by two.

For **1**, **2**, **3**, and **5**, χT rises slightly with increasing temperature. The increase in χT suggests thermal population of higher spin states, which likely arise from the decoupling of the two high-spin M(II) centers. By using a two-spin Hamiltonian to simulate the magnetic data, we determined the average *g* values and antiferromagnetic exchange coupling constants (*J*) for these various metal-metal interactions. These parameters are provided in Table 2.6. We find that the magnitude of the coupling constants decreases significantly (> 50 cm^{-1}) from dicobalt **1** to cobalt-iron **2** to iron-manganese **5** with a smaller decrease of 25 cm^{-1} to cobalt-manganese **3**.

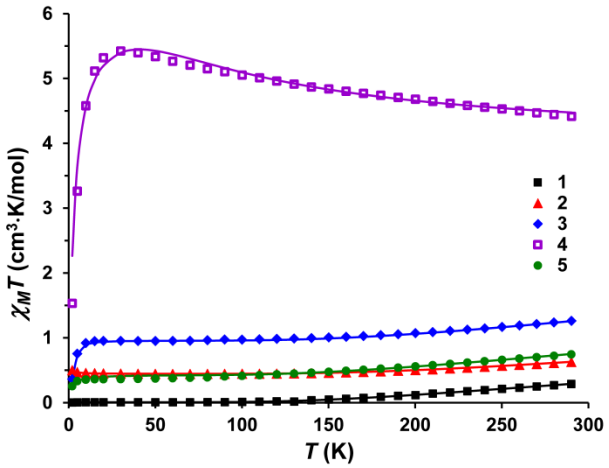

Figure 2.7. Temperature dependence of the magnetic susceptibility, plotted as χ_MT, of **1** (black solid squares), **2** (red triangles), **3** (blue diamonds), **4** (purple, open squares), and **5** (green circles) at 1 Tesla, from 2 to 290 K. Solid lines represent the best fit. See Table 2.6 for simulation parameters.

Table 2.6. Magnetic couplings, anisotropy constants, and *g*-values of **1**−**5**[a].

Cpd.	S_{tot}	S_1	S_2	J (cm^{-1})	g_1	g_2	$D_{1,2}$ [b] (cm^{-1})	θ_w [b] (K)
1	0	1.5	1.5	−231	2.16	2.16	0	0
2	0.5	1.5	2.0	−184	2.00	2.09	0	0.3
3	1.0	1.5	2.5	−120	2.06	2.00	2.5[c]	0
4[d]	*3.0*	*2.0*	*1.0*	*+14*	*2.00*	*2.00*	*0*	*−3.0*
5	0.5	2.0	2.5	−145	2.00	2.06	0	−1.5

[a] Some spectra have been corrected for temperature-independent paramagnetism (TIP). See experimental section. [b] As discussed in the text, we cannot differentiate between magnetic anisotropy arising from zero-field splitting (D) or intermolecular interactions (θ_w) below 15 K, so these values are not well parameterized. [c] D_1 and D_2 were arbitrarily set to be equal. [d] Parameters are from imposing a *localized* treatment, though we propose that a *delocalized* treatment is more appropriate for **4**.

Notably, diiron **4** stands apart from the other members in that it exhibits higher χT values, peaking to 5.42 cm^3 K/mol at 30 K. This value is near the spin-only value for S = 3 (χT = 6.0 cm^3 K/mol). Coincidentally, a χT value of 6.0 cm^3 K/mol is also expected for two non-interacting S = 2 spins, e.g. high-spin Fe(II). However, the latter interpretation is inconsistent with the temperature dependence of χT, which decreases with increasing temperature. It is further improbable that **4** should have non-interacting spins when it is the only complex in this series with a bonafide metal-metal bond. Therefore, the magnetic data suggests a very different type of magnetic interaction in **4**.

Magnetic behavior of complexes featuring multiple metal centers can be complex, as several exchange mechanisms are possible, including direct exchange (via metal-metal), superexchange (via a bridging ligand), and double exchange. Double exchange pathways, which may occur in mixed-valent systems, are easily ruled out in these systems since the metal ions are in the same oxidation states of +2. While some of the heterobimetallic systems, e.g. cobalt-iron **2**, may superficially resemble mixed-valent systems (with a d^7-d^6 electron count), it is unreasonable for an electron to move between

the metal ions as the alternate d^6-d^7 configuration would formally correspond to Co(III)-Fe(I).

In systems featuring weak metal-metal interactions, direct and super- exchange pathways can compete. With the exception of **4**, the metal ions in these bimetallic systems couple antiferromagnetically. We conclude at this stage that the primary pathway is superexchange. Our reasoning is based on the fact that metal-metal interactions in complexes **1**, **2**, **3**, and **5** are weak at best. If direct exchange was dominating, then complex **4**, which should have the best *d*-*d* orbital overlap, should strongly couple antiferromagnetically, which is not observed. Moreover, Goodenough-Kanamori rules predict that single electrons occupying *d*-orbitals of δ-symmetry (with respect to the M-M axis), would couple antiferromagnetically through the π-system of the pyridyl-amide bridge. On the other hand, it is not obvious how single electrons occupying *d*-orbitals of π-symmetry would interact (as there are no matching orbitals on the ligand), so it is possible that direct exchange via a weak metal-metal interaction may also play a significant role in the overall antiferromagnetism.

In the case of **4**, we have scrutinized similar exchange interactions but no satisfactory model has yet emerged. For instance, we have considered **4** as two localized spins that couple ferromagnetically. To obtain a good fit of the experimental data and in order to produce $S_{tot} = 3$, one of the spins was set to high-spin Fe(II) while the other had to be modeled as intermediate-spin Fe(II). A weak ferromagnetic coupling of +14 cm^{-1} was thus determined (Table 2.6). The fit, however, is problematic because we cannot explain the origin of the different spins at the two Fe(II) centers. We also considered an

alternative fit with two equal $S = 1.5$ centers; but to maintain the +4 charge of the diiron core, the oxidation states would have to be different, namely Fe(III)Fe(I). The failure of the localized models is not surprising in the light of the work by Betley *et al.* The authors have described the shortcomings in the localized description for explaining the magnetic behavior of systems with strong metal-metal interactions.[42] Instead, the authors advocated the use of a delocalized molecular orbital (MO) scheme to account for the temperature variation of χT. Basically, metal *d* orbitals that engage in metal-metal bonding give rise to a delocalized *d*-orbital manifold, which by population according to Hund's rules yields higher-spin ground states. In the delocalized model, the decrease in χT would result from spin crossover to a lower spin state.

2.3.8 Theoretical Studies

To validate our hypothesis of delocalized metal-metal bonding in **4**, we performed multi-configurational calculations on the full experimental structures of compounds **1** – **5** using the CASSCF method, followed by CASPT2 calculations to recover additional dynamical correlation. For each compound, the active space comprised twelve orbitals, including all ten, valence *3d* orbitals and two additional *4d* orbitals that correlated with the *3d* orbitals. The energies of various spin states were computed; and with the exception of **4**, the calculated ground states matched the experimentally determined states (Table A2.5). To correctly predict the ground state of **4**, we investigated a much larger active space of 20 orbitals (all *3d* and *4d* orbitals) with restricted active space (RAS) SCF and PT2 calculations. While these ultimately preferred higher spin states, the energy difference between the nonet and septet states was nominal (< 0.02 kcal/mol).

For metal-metal bonds in trigonal symmetry, the maximum overlap of the two metals' *3d* orbitals would ideally yield a highly delocalized MO manifold with σ, π, and δ bonds, e.g. (σ)(π)(δ)(δ*)(π*)(σ*). Poor overlap of the metal orbitals, however, would cause electron density to localize at the individual metal centers. The heterobimetallic species are expected to have greater localization than the homobimetallics because different metal centers should have worse overlap versus same metal centers. Thus, it is interesting that dicobalt **1** is low-spin and shares similar characteristics with the heterobimetallic species, whereas diiron **4** is higher spin and the lone stand out. To elucidate the physical bases of their different properties, the bonding nature of **1** and **4** were further investigated.

The main electronic configurations of **1** and **4** are compared in Figure 2.8. Of note, the MO diagram of **4** shows the idealized metal-metal bond that is fully delocalized. The main electronic configuration of **4**, which accounts for 28% of the total wavefunction, is $(\sigma)^2(\pi)^4(\delta)^2(\delta^*)^2(\pi^*)^2(\sigma^*)^0$. The septet state thus arises from the population of energetically close δ, δ*, and π* MOs. This configuration also corresponds to a formal double bond between the iron centers. However, the sum of all the contributing configurations yields MOs with the following natural populations, $(\sigma)^{1.27}(\pi)^{3.42}(\delta)^{2.01}(\delta^*)^{1.99}(\pi^*)^{2.52}(\sigma^*)^{0.72}$, where the increased population in anti-bonding orbitals such as π* and σ* lowers the effective bond order (EBO) to 0.73, which is reasonably close to a single bond.

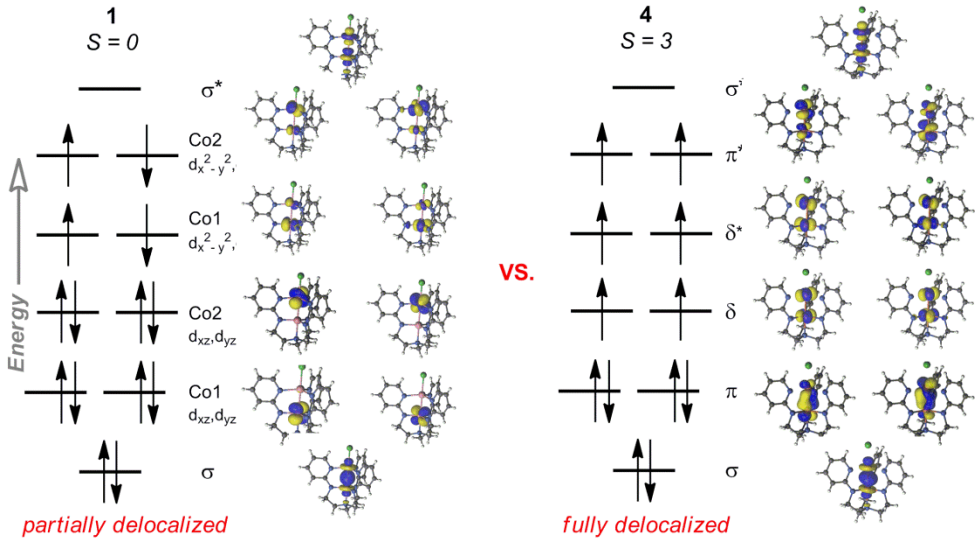

Figure 2.8. Qualitative MO diagrams showing the natural orbitals for dicobalt **1** (left) and diiron **4** (right). Only the dominating electronic configurations are shown.

In contrast, complex **1** is characterized by a significantly more localized MO diagram, where the only, truly delocalized natural orbitals are σ and σ*. (The δ-symmetry MO's are predominantly localized at one metal center, as the ratio of the electron density of the two cobalt centers ranges from 5:1 to 9.5:1). The main electronic configuration of **1**, which accounts for 19% of the total wavefunction, is $(\sigma)^2(Co_1\ d_{yz},d_{xz})^4(Co_2\ d_{yz},d_{xz})^4(Co_1\ d_{xy},d_{x2-y2})^2(Co_2\ d_{xy},d_{x2-y2})^2(\sigma^*)^0$. Formally, this configuration predicts a single bond between the cobalt centers. Again, however, the sum of all configurations, $(\sigma)^{1.22}(Co_1\ d_{yz},d_{xz})^{3.98}(Co_2\ d_{yz},d_{xz})^{3.96}(Co_1\ d_{xy},d_{x2-y2})^{2.08}(Co_2\ d_{xy},d_{x2-y2})^2(\sigma^*)^{0.78}$, provides an EBO of only 0.22, which is consistent with a metal-metal interaction that is weaker than a single bond.

For all the heterobimetallic complexes, **2**, **3**, and **5**, the ground states were predicted to be highly multiconfigurational, where the main electronic configuration accounts for only 7% or less of the total wavefunction (Table A1.6). Thus, the "main"

configurations for the heterobimetallics are not representative of the whole bonding picture, and we do not delve further into their bonding descriptions. One important finding, however, is that the EBOs are all low, between 0.22 and 0.31 (Table A1.6), which is consistent with the long metal-metal bond lengths observed experimentally.

Finally, density functional theory (DFT) calculations were performed to shed light on the magnetic interactions between the metal centers within the bimetallic complexes. Magnetic coupling constants can be extracted from DFT solutions of the high-spin and broken-symmetry states, which were calculated with three different exchange-correlation functionals: PBE0, HSE, and LC-ωPBE (Table 2.7). For "purely" magnetic systems, where the magnetic electrons are localized at the individual metal centers, the HSE and LC-ωPBE functionals typically give more accurate coupling values compared to PBE0.[102,103] For bimetallic **1**, **2**, **3**, and **5**, the calculated magnetic coupling values are fairly consistent across the functionals. In contrast, the computed magnetic couplings for diiron **4** were quite inconsistent for the various functionals, and thus, compound **4** was excluded from the present study. Although the predicted magnetic coupling constants are generally overestimated, the *trend* in $|J|$ values (Figure 2.9) shows good correspondence between theory and experiment, especially for LC-ωPBE. All the functionals correctly reproduce an important periodic trend for the cobalt series, namely, that the antiferromagnetic coupling decreases in the CoM complexes from M = Co to M = Fe to M = Mn. One discrepancy between theory and experiment is that a weaker coupling is predicted for **5** compared to **3**, rather than vice versa. We hypothesize that this discrepancy arises from a problem with electron correlation, which can become even

more complicated when magnetic orbitals overlap. Thus, there is still room for the development of new and more generally applicable exchange-correlation functionals for computing isotropic magnetic couplings.

Table 2.7. Calculated magnetic coupling constants J (in cm^{-1}) for various functionals.

Cpd.	PBE0	HSE	LC-ωPBE	J_{exp}
1	−333	−350	−370	−231
2	−207	−244	−304	−184
3	−210	−217	−231	−120
5	−181	−187	−198	−145

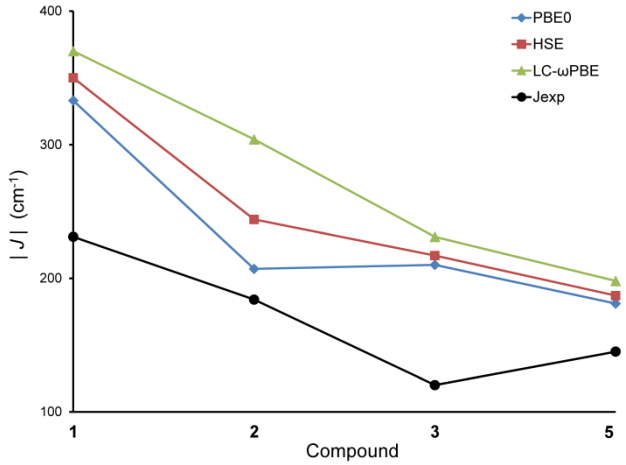

Figure 2.9. Plot of |J| values for compounds **1**, **2**, **3**, and **5**.

2.4 Conclusions

A simple ligand design allows the preparation of bimetallic complexes containing Mn(II), Fe(II), and/or Co(II) ions with high compositional purity. Gratifyingly, minute disorder resulting from metal-mixing was observed, despite the fact that these metal ions are typically substitutionally labile and share similar covalent radii. Three heterobimetallic complexes (CoMn, CoFe, and FeMn) were isolated and are highly substitutionally pure in the two metal-binding sites. With these different metal-metal pairings in hand, we were able to characterize their spectroscopic, electronic, and magnetic properties. We do not yet understand why the diiron complex is an outlier of this series, but we correlate its short metal-metal bond and higher spin state with a more delocalized electron density between the two metal centers. Future efforts will focus on exchanging the chloride ligand with more reactive groups in order to study the effects of the metal-metal bonding on reactivity.

2.5 Experimental Section

General Considerations

Unless otherwise stated, all manipulations were performed under an N_2 atmosphere inside a glovebox. Standard solvents were deoxygenated by sparging with dinitrogen and dried by passing through activated alumina columns of a SG Water solvent purification system. Benzylpotassium (KBn) was prepared according to literature methods.[104] Deuterated solvents were purchased from Cambridge Isotope Laboratories, Inc., degassed via freeze-pump-thaw cycles, dried over activated alumina, and stored over activated 4 Å molecular sieves. Tris(2-aminoethyl)amine (tren) was purchased from Pressure Chemical Co. All other reagents were purchased from Aldrich or Strem and used without further purification. Elemental analyses were performed by Complete Analysis Laboratories, Inc. (Parsippany, NJ). Inductively coupled plasma optical emission spectrometry (ICP-OES) data were collected at the University of Minnesota Earth Sciences Analytical Geochemistry Lab using a Thermo Scientific iCAP 6500 dual view instrument, with the addition of cesium as a matrix modifier and yttrium as an internal standard. The weight percent is an average of three or four measurements is reported with standard deviations.

Synthesis of tris(2-(2-pyridylamino)ethyl)amine (H_3[py_3tren]). Tren (9.77 g, 66.8 mol), 2-bromopyridine (20.0 mL, 210 mmol), and K_2CO_3 (47.0 g, 268 mmol) were heated at 180°C in 200 mL DMSO for 3 days. After cooling to rt, the crude reaction mixture was diluted into $CHCl_3$, and washed with NaOH (1X) and brine (4X). After removing the volatiles from the organic layer, the crude product was warmed to 50°C in

toluene and loaded onto a silica gel column. The crude product was purified by silica gel chromatography (3:1:0.12 hexanes:EtOAc:7 N NH_3 in CH_3OH). The product fractions were combined, and the solvents removed *in vacuo.* The product was dried overnight *in vacuo* at 60°C. The product was brought into the glovebox, extracted with THF, and dried *in vacuo* at 50°C overnight. This workup provided the product as a tan solid (14.2 g, 56%). ^{1}H NMR (500 MHz, $CDCl_3$): δ 8.05 (dd, $^3J_{HH}$ = 6 Hz, $^4J_{HH}$ = 1 Hz, 1H), 7.31 (ddd, $^3J_{HH}$ = 8 Hz, $^3J_{HH}$ = 6 Hz , $^4J_{HH}$ = 1 Hz, 1H), 6.52 (t, $^3J_{HH}$ = 6 Hz, 1H), 6.32 (d, $^3J_{HH}$ = 8 Hz, 1H), 5.61 (br, 1H, N*H*), 3.30 (dt, $^3J_{HH}$ = 6 Hz), 2.78 (t, $^3J_{HH}$ = 6 Hz). ^{13}C NMR (126 MHz, $CDCl_3$): δ 159.0, 148.2, 137.4, 113.0, 108.0, 53.5, 40.0. ESI-MS-TOF *m/z*: $[M + H]^+$ calc'd for $C_{21}H_{28}N_7$, 378.2406; found 378.2426.

Synthesis of K[Co(py$_3$tren)]. To a cold solution of H_3[py$_3$tren] (0.995 g, 2.64 mmol) in 30 mL THF, a cold solution of KBn (1.06 g, 8.14 mmol) in 60 mL THF was added dropwise (CO_2/acetone coldwell bath). After stirring for 30 min, $CoCl_2$ (0.361 g, 2.78 mmol) was added, and then the green solution was immediately removed from the cold bath and stirred overnight. The reaction solution was filtered through Celite and dried *in vacuo* to give a green resin. The resin was stirred in 3x10 mL Et_2O, 10 mL pentane, and dried *in vacuo* for several hours, yielding K[Co(py$_3$tren)] as a fine green powder (1.10 g, 88% yield). ^{1}H NMR (300 MHz, d_8-THF): δ 140, 88, 34, 0.3, -36. UV-Vis-NIR (CH_2Cl_2) λ_{max} (ε, L mol^{-1} cm^{-1}): 314 (24,500), 347 sh (10,100), 386 sh (6,700), 595 (110), 820 (10), 1620 (80). Anal. Calcd for $C_{21}H_{24}N_7CoK$: C, 53.38; H, 5.12; N, 20.75. Found: C, 53.31; H, 5.19; N, 20.69.

Synthesis of K[Fe(py$_3$tren)]. A solution of H_3[py$_3$tren] (0.392 g, 1.04 mmol) in 10 mL THF was deprotonated with a solution of KBn (0.407 g, 3.13 mmol) in 10 mL THF at rt and stirred for several hours. $FeCl_2$ (0.132 g, 1.04 mmol) was then added, and the reaction mixture was stirred overnight. The mixture was then filtered through Celite and dried *in vacuo* to yield a red-orange resin. The resin was stirred in 2x10 mL Et_2O, 10 mL pentane, and dried *in vacuo*. The resultant powder was then rinsed with 2x5 mL toluene, 1x5 mL Et_2O, and 2x5 mL hexanes, and dried *in vacuo* for several hours, yielding K[Fe(py$_3$tren)] as an orange powder (0.215 g, 44% yield). ^{1}H NMR (300 MHz, d_8-THF): δ 183, 82.4, 30.9, 14.3, −23.6, −33.7. UV-Vis-NIR (THF) λ_{max} (ε, L mol^{-1} cm^{-1}): 311 (14,100), 489 (2,000), 1650(40). Anal. Calcd for $C_{21}H_{24}N_7FeK$: C, 53.73; H, 5.15; N, 20.89. Found: C, 53.68; H, 5.08; N, 20.81.

Synthesis of CoCoCl(py$_3$tren) (1). To K[Co(py$_3$tren)] (639 mg, 1.36 mmol) in 100 mL THF was added $CoCl_2$ (176 mg, 1.36 mmol) at rt. The green solution rapidly turned into a dark green suspension. After stirring for 11 h, the volatiles were removed *in vacuo*. The crude was then extracted repeatedly with CH_2Cl_2 and filtered through Celite. The filtrate was dried *in vacuo*, and the resultant residue was dissolved in CH_2Cl_2 and layered with hexanes, yielding 312 mg of a dark green-brown solid (0.591 mmol, 43% yield). X-ray quality crystals were grown from layering Et_2O onto a THF solution. ^{1}H NMR (300 MHz, CD_2Cl_2): δ 21.7, 20.9, 11.5, 7.7, 6.7, −1.6. UV-Vis-NIR (CH_2Cl_2) λ_{max} (ε, L mol^{-1} cm^{-1}): 317 (28,700), 340 sh (17,900), 450 (8,500), 572 (620), 650 (680), 1027 (130),

1650 (40). Anal. Calcd for $C_{21}H_{24}N_7Co_2Cl$: C, 47.79; H, 4.58; N, 18.58. Found: C, 47.77; H, 4.52; N, 18.61.

Synthesis of CoFeCl(py$_3$tren) (2). To a cold THF slurry of $FeCl_2(THF)_{1.5}$ (121 mg, 0.515 mmol), a cold solution of K[Co(py$_3$tren)] (243 mg, 0.514 mmol) was added dropwise (CO_2/acetone coldwell bath). After stirring overnight, the volatiles were removed *in vacuo*. The resultant residue was dissolved in CH_2Cl_2 and filtered through Celite. The filtrate was concentrated *in vacuo* to 10 mL, filtered again, and layered with Et_2O to obtain 137 mg (0.261 mmol, 51% yield) of dark red-orange crystals. UV-Vis-NIR (CH_2Cl_2) λ_{max} (ε, L mol^{-1} cm^{-1}): 317 (25,000), 356 sh (11,500), 448 (7,500), 574 sh (420), 1258 (90). ^{1}H NMR (300 MHz, CD_2Cl_2): δ 32.5, 26.6, 16.8, 1.7, −3.6, −20.3. Anal. Calcd for $C_{21}H_{24}N_7CoFeCl$: C, 48.07; H, 4.61; N, 18.69. Found: C, 48.13; H, 4.56; N, 18.78. ICP-OES (wt %): Fe, 10.96(3); Co, 11.83(2), which is consistent with $Co_{1.01}Fe_{0.99}$.

Synthesis of CoMnCl(py$_3$tren) (3). To a cold THF slurry of $MnCl_2(THF)_2$ (116 mg, 0.431 mmol), a cold solution of K[Co(py$_3$tren)] (203 mg, 0.430 mmol) was added dropwise (CO_2/acetone coldwell bath). The reaction immediately turned green-yellow. After stirring overnight, the reaction mixture was dried *in vacuo*, redissolved in 60 mL CH_2Cl_2, and filtered through Celite. X-ray quality crystals were grown from Et_2O layered on a concentrated CH_2Cl_2 solution (141 mg, 0.269 mmol, 63% crystalline yield). ^{1}H NMR (500 MHz, CD_2Cl_2): δ 40, 31.1, 28.6, −9.2, −24.4, −39.4. UV-Vis-NIR (CH_2Cl_2) λ_{max} (ε, L mol^{-1} cm^{-1}): 317 (22,600), 349 sh (9,800), 397 sh (6,800), 435 (9,000), 608

(140), 1240 (90). Anal. Calcd for $C_{21}H_{24}N_7CoMnCl$: C, 48.15; H, 4.62; N, 18.72. Found: C, 48.09; H, 4.69; N, 18.71. ICP-OES (wt %): Mn, 12.21(7); Co, 12.80(2), which is consistent with $Co_{0.99}Mn_{1.01}$.

Synthesis of FeFeCl(py$_3$tren) (4). A THF solution of K[Fe(py$_3$tren)] (300 mg, 0.639 mmol) was added to a THF slurry of $FeCl_2(THF)_{1.5}$ (163 mg, 0.690 mmol) at rt. The reaction rapidly turned dark red. After stirring overnight, the filtrate was dried *in vacuo*, redissolved in 80 mL CH_2Cl_2, and filtered through Celite. Dark red crystals were grown from Et_2O layered on a CH_2Cl_2 solution (94 mg, 0.18 mmol, 28% crystalline yield). ^{1}H NMR (500 MHz, CD_2Cl_2): δ 168, 77.5, 42.1, 9.5, 0.8, −15.7. UV-Vis-NIR (CH_2Cl_2) λ_{max} (ε, L mol^{-1} cm^{-1}): 315 (18,000), 530 (5,600), 997 (190). Anal. Calcd for $C_{21}H_{24}N_7Fe_2Cl$: C, 48.36; H, 4.64; N, 18.80. Found: C, 48.32; H, 4.69; N, 18.73.

Synthesis of FeMnCl(py$_3$tren) (5). To a cold THF slurry of $MnCl_2(THF)_2$ (58 mg, 0.22 mmol), a cold solution of K[Fe(py$_3$tren)] (101 mg, 0.215 mmol) was added dropwise (CO_2/acetone coldwell bath). The reaction immediately turned orange. After stirring overnight, the reaction mixture was dried *in vacuo*, redissolved in 80 mL CH_2Cl_2, and filtered through Celite. The filtrate was dried *in vacuo* to a bright orange solid. Orange crystals (49 mg, 0.094 mmol, 44% crystalline yield) were obtained from Et_2O layered on a CH_2Cl_2 solution. ^{1}H NMR (500 MHz, CD_2Cl_2): δ 43.7, 16.8, 12.6, 6.5, 2.0, −0.3. UV-Vis-NIR (CH_2Cl_2) λ_{max} (ε, L mol^{-1} cm^{-1}): 310 (14,400), 498 (2,600), 1019 (40), 1555 (60). Anal. Calcd for $C_{21}H_{24}N_7FeMnCl$: C, 48.44; H, 4.65; N, 18.83. Found: C, 48.33; H,

4.63; N, 18.88. ICP-OES (wt %): Mn, 12.13(2); Fe, 10.6(1), which is consistent with $Fe_{0.92}Mn_{1.08}$.

X-Ray Crystallographic Data Collection and Refinement of the Structures

Single crystals of K[Co(py_3tren)] were grown from a mixture of pentane, Et_2O, and THF (see Table 2.9 for crystallographic data). Single crystals of CoCoCl(py_3tren) (**1**) were grown from Et_2O layered on a THF solution. Single crystals of CoFeCl(py_3tren) (**2**), CoMnCl(py_3tren) (**3**), FeFeCl(py_3tren) (**4**), and FeMnCl(py_3tren) (**5**) were grown from Et_2O layered on a CH_2Cl_2 solution. A green plate of K[Co(py_3tren)], red blocks of **2** (0.40 x 0.20 x 0.20 mm^3) and **4** (0.50 x 0.20 x 0.20 mm^3), a green block of **3** (0.60 x 0.40 x 0.20 mm^3), and an orange block of **5** (0.40 x 0.40 x 0.20 mm^3) were placed on the tip of a glass capillary and mounted on a Bruker APEX II Platform CCD diffractometer for data collection at 173(2) K, and a green block of **1** (0.40 x 0.40 x 0.20 mm^3) was collected at 123(2) K. The data collection was carried out using Mo-Kα radiation (graphite monochromator). The data intensity was corrected for absorption and decay (SADABS). Final cell constants were obtained from least squares fits of all measured reflections. The structure was solved using SHELXS-97 and refined using SHELXL-97. A direct-methods solution was calculated which provided most non-hydrogen atoms from the E-map. Full-matrix least squares / difference Fourier cycles were performed to locate the remaining non-hydrogen atoms. All non-hydrogen atoms were refined with anisotropic displacement parameters. Hydrogen atoms were placed in ideally and refined as riding atoms with relative isotropic displacement parameters. Crystallographic data for **1** − **5** are summarized in Table 2.8.

Table 2.8. Crystallographic details for the MM'Cl(py$_3$tren) series, where MM' = CoCo **1**, CoFe **2**, CoMn **3**, FeFe **4**, FeMn **5**.

	1	**2**	**3**	**4**	**5**
chemical formula	$C_{21}H_{24}N_7Co_2Cl$	$C_{21}H_{24}N_7CoFeCl$	$C_{21}H_{24}N_7CoMnCl$	$C_{21}H_{24}N_7Fe_2Cl$	$C_{21}H_{24}N_7FeMnCl$
formula weight	527.78	524.70	523.79	521.62	520.71
crystal system	orthorhombic	monoclinic	monoclinic	monoclinic	monoclinic
space group	$P2_12_12_1$	$P2_1/n$	$P2_1/n$	$P2_1/n$	$P2_1/n$
a (Å)	9.5717(14)	9.2450(6)	9.3125(7)	9.206(3)	9.3535(4)
b (Å)	14.824(2)	12.5597(8)	12.5159(9)	12.673(3)	12.5109(5)
c (Å)	14.934(2)	18.475(1)	18.574(1)	18.423(5)	18.5566(8)
α (deg)	90	90	90	90	90
β (deg)	90	98.724(1)	98.631(1)	100.544(3)	98.5002(4)
γ (deg)	90	90	90	90	90
V (Å^3)	2119.0(5)	2120.4(2)	2140.4(3)	2113(1)	2147.7(2)
Z	4	4	4	4	4
D_{calcd} (g cm^{-3})	1.654	1.644	1.625	1.640	1.610
l (Å), μ (mm^{-1})	0.71073, 1.716	0.71073, 1.617	0.71073, 1.514	0.71073, 1.524	0.71073, 1.412
T (K)	123(2)	173(2)	173(2)	173(2)	173(2)
θ range (deg)	1.94 to 27.42	1.97 to 27.42	1.97 to 27.48	1.96 to 27.48	1.97 to 27.48
reflns collected	4812	23646	24156	23676	24203
unique reflns	2945	4801	4900	4831	4918
data/restraints /parameters	2945 / 0 / 280	4801 / 0 / 281	4900 / 0 / 280	4831 / 0 / 281	4918 / 0 / 280
R_1, wR_2 ($I > 2\sigma(I)$)	0.0187, 0.0491	0.0226, 0.0607	0.0297, 0.0695	0.0234, 0.0689	0.0265, 0.0659

Anomalous Diffraction Data Collection and Refinement of Metal Occupancies

Single crystals of the heterobimetallic compounds, **2**, **3**, and **5**, were mounted on a glass fiber and cooled to 100 K using an Oxford Instruments Cryojet cryostat. The Bruker D8 diffractometer, integrated with an APEX-II CCD detector, was modified for synchrotron use at the ChemMatCARS 15-ID-B beam line at the Advanced Photon Source (Argonne National Laboratory). For each crystal, diffraction data were collected at seven different energies with 0.3 second frames while manually attenuating the beam to minimize overages of individual pixels. The scan at 30.0 keV (λ=0.41328 Å), which is

energetically far from any atomic absorption energies, gave a least-squares refinement of all model positional- and displacement parameters to 0.5 Å resolution. In addition, six anomalous diffraction data sets were collected to span the absorption K-edges of both M_1 and M_2 (at the two metals' K-edges (λ_{edge}) and ± 50 eV) per complex. The specific energies (keV) [wavelengths (Å)] that were used are: for iron, 7.062 [1.7557], 7.112 [1.7433], and 7.162 [1.7312]; for cobalt, 7.659 [1.6188], 7.709 [1.6083], 7.759 [1.5980]; and for manganese, 6.489 [1.9107], 6.539 [1.8961], and 6.589 [1.8817]. The anomalous diffraction can distinguish Mn/Fe/Co compositions at the two metal sites because of the expected differences in the anomalous scattering factors ($\Delta f'$ and $\Delta f''$) for these elements, as shown in Figure 1. Basically, $\Delta f'$ and $\Delta f''$ values of an element change dramatically near the element's absorption edge, but, for other element(s), they remain relatively constant. Each anomalous diffraction data sets thus provides a different view of the electrons present at both sites. Of the 6 anomalous data sets collected per compound, only two sets ($\lambda > \lambda_{edge}$) were used to solve for metal occupancies. The others were excluded for the following reasons. For $\lambda = \lambda_{edge}$, the data is less reliable because of inaccuracies in the metal K-edge energies, which shift for coordination compounds. For $\lambda < \lambda_{edge}$, the data is also less reliable due to potential problems with adsorption and/or fluorescence.[98] For each complex, the two anomalous datasets were simultaneously used in a least-squares refinement to determine the Mn/Fe/Co occupancies at the two metal sites (M_1, M_2). GSAS-II was employed because it allows multiple diffraction data sets as an input with subsequent refinement using a common crystallographic model.[99] The 30 keV data was refined using structural models of **2**, **3**, and **5** that had been previously determined at

173 K. The converged positional- and displacement parameters were then frozen, so that only the metal occupancies were refined. Crystallographic data are summarized in Table 2.12.

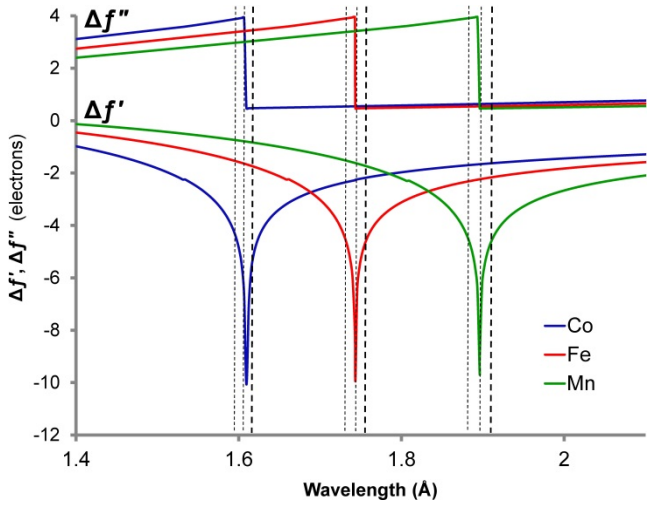

Figure 2.10. Theoretical anomalous dispersion corrections, including the real ($\Delta f'$) and imaginary ($\Delta f''$) scattering factors, for Co(blue), Fe(red) and Mn (green), as a function of wavelength (Å). The dotted lines represent the experimental wavelengths (λ) for the anomalous data collections, which were selected to span the Co, Fe, and Mn absorption edge energies. The datasets collected at $\lambda > \lambda_{edge}$ were used to determine the metal occupancies (bold, dotted lines).

Physical Measurements

NMR spectra were collected on Varian Inova 300 and 500 MHz spectrophotometers. UV-Vis-NIR absorption data were collected on a Cary-14 spectrophotometer. Cyclic voltammetry was conducted using a CH Instruments 600 electrochemical analyzer. The one-cell setup utilized a platinum working electrode, Pt wire counter electrode, and $Ag/AgNO_3$ reference electrode in CH_3CN. Analyte solutions were prepared in a THF solution of NBu_4PF_6 (0.4 M) and referenced internally to the Fc/Fc^+ redox couple. Mössbauer data were recorded on an alternating constant acceleration spectrometer. The

minimum experimental line width was 0.24 mm s^{-1} (full width at half-height). The ^{57}Co/Rh source (1.8 GBq) was positioned at rt inside the gap of the magnet system at a zero-field position. Isomer shifts are quoted relative to iron metal at 300 K.

Magnetic susceptibility data were measured from powder samples of solid material in the temperature range 2 - 300 K by using a SQUID susceptometer with a field of 1.0 T (MPMS-7, Quantum Design, calibrated with standard palladium reference sample, error <2%). The experimental data were corrected for underlying diamagnetism by use of tabulated Pascal's constants ($\chi_{dia} < 0$),[105,106] as well as for temperature-independent paramagnetism ($\chi_{TIP} > 0$).[107] Specifically, χ_{TIP} (units of 10^{-6} emu) = 630 for **1**, 860 for **2**, 550 for **4**, and 350 for **5**. Also, in the simulation of **1**, a very small (0.4 %) $S = 3/2$ impurity, e.g. monocobalt(II), was accounted for. The susceptibility and magnetization data were simulated with the program julX for exchange coupled systems.[108] The simulations are based on the usual spin-Hamiltonian operator for mononuclear complexes with spin S:

$$\hat{H}_e = g\beta\,\hat{\vec{S}}\cdot\vec{B} + D[\hat{S}_z^{\,2} - 1/3S(S+1) + E/D(\hat{S}_x^{\,2} - \hat{S}_y^{\,2})]$$

where g is the average electronic g value, and D and E/D are the axial zero-field splitting and rhombicity parameters. Magnetic moments are calculated after diagonalization of the Hamiltonian from the eigenfunctions using the Hellman-Feyman theorem $\vec{\mu}_i(\vec{B}) = \langle\psi_i|dH/d\vec{B}|\psi_i\rangle$. Intermolecular interactions were considered by using a Weiss temperature, Θ_W, as perturbation of the temperature scale, $kT' = k(T-\Theta_W)$ for the calculation. Powder summations were done by using a 16-point Lebedev grid. For the

bimetallic complexes, we adopted two sub-spins S_1 and S_2 (one per metal) with an exchange coupling constant, J, as defined by:

$$\hat{H} = -2J[\hat{\vec{S}}_1 \cdot \hat{\vec{S}}_2] + \hat{H}_{e,1} + \hat{H}_{e,2}$$

Computational Methods

CASSCF/CASPT2 Calculations. All complete active space self-consistent field (CASSCF) calculations, which were followed by perturbation theory to second order (CASPT2), were performed with the MOLCAS 7.8 package[109] on experimental structures without symmetry constraints. Relativistic all-electron ANO-RCC basis sets were used for all elements.[110,111] Double-ζ quality (ANO-RCC-VDZP) basis sets were used for Co, Fe, Mn, N, and Cl atoms and minimal basis sets (ANO-RCC-MB) were used for C and H atoms. The following contractions were used: [5s4p2d1f] for the metals, [3s2p1d] for N and Cl, [2s1p] for C, and [1s] for H. To include relativistic effects in the calculation, the Douglas-Kroll-Hess-Hamiltonian[112,113] was used. Resolution of identity combined with the Cholesky decomposition (RICD) was used to reduce the computational cost associated with the treatment of 2-electron integrals.[114] Lowest energy solutions were calculated for all spin states at the CASSCF level of theory and subsequent CASPT2 calculations were performed to recover more dynamical correlation, in which an imaginary level shift of 0.2 a.u. was used to prevent the occurrence of intruder states.[115]

The active spaces for the five complexes were chosen to include the ten valence 3*d* electrons plus two correlating 4*d* orbitals. The active spaces for **1**, **2**, **3** and **5** respectively, are 14 electrons in 12 orbitals or (14,12), (13,12), (12,12), and (11,12), respectively. Only twelve active orbitals were considered to obtain a reasonable level of

accuracy while limiting the computational cost. Diiron **4** was a more challenging system and required the use of a larger active space. Thus, restricted active space (RAS) SCF calculations including a large configuration interaction space were performed, denoted by (12,20)/(12,10)/2, where the first set of parenthesis corresponds to the total number of electrons in RAS1 and RAS2 and total number of orbitals in all RAS spaces. The second set of parentheses corresponds to the number of active electrons and orbitals in RAS2 and the final value of 2 indicates the number of allowed particles into RAS3.

The natural orbital occupation numbers were used for the evaluations of the effective bond order (EBO), which is calculated as the difference between the total occupancies of the bonding and anti-bonding molecular orbitals of the metal-metal bond divided by two.[116,117]

DFT Calculations. Density functional theory (DFT) calculations were performed to evaluate the magnitude of the isotropic magnetic couplings between the two metal centers in **1**, **2**, **3** and **5**. As proposed by Noodleman for weakly coupled systems, magnetic coupling constants in two-spin systems can be obtained from a high-spin and a spin-symmetry-broken solution within spin unrestricted formalisms.[118] The isotropic magnetic couplings are introduced via the phenomenological Heisenberg-Dirac-van-Vleck (HDVV) Hamiltonian:

$\hat{H}^{HDVV} = -2 \sum_{ij} J_{ij} \hat{S}_i \hat{S}_j$

where J_{ij} is the coupling constant, and $\hat{S}_i$ and $\hat{S}_j$ are the spin operators on the magnetic centers i and j. The difference in energy between the spin-broken symmetry (BS) solution and high spin (HS) solution are used to extract the coupling values. In Noodleman's approach, or the weak-coupling limit scheme, the BS solution is considered to be an ideal mixture of spin states corresponding to the appropriate Clebsch-Gordan coefficients. This situation corresponds to the case in which there is no orbital overlap between the magnetic centers i and j. In the studied complexes, a partly covalent interaction between the (local) magnetic orbitals is possible, and thus we chose to use the intermediate coupling scheme proposed by Yamaguchi:[119]

$$(\langle S^2\rangle^{HS}-\langle S^2\rangle^{BS})J_{ij}=E_{BS}-E_{HS}$$

where $\langle S^2\rangle^{HS}$ and $\langle S^2\rangle^{BS}$ are the expectation values of the total spin squared operator coming from the spin unrestricted calculations. All DFT calculations were performed with the *Gaussian 09* program package.[120] The BS solutions have been obtained from the HS solutions by flipping the spins on one of the magnetic centers and breaking all symmetry and spin constraints up to a stable solution using the *stable=opt* keyword of *Gaussian*. Three functionals, one global hybrid (PBE0),[121,122] one range separated functional with long-range screened Hartree-Fock exchange (HSE),[123,124] and one range separated functional with a 100% of Hartree-Fock exchange at long range (LC-ωPBE)[125] were used together with the TZVP basis set on the Co, Mn, Fe Cl, and N atoms and the SVP basis set on the C and H atoms.[126,127]

Chapter 3

Synthesis, Characterization, and Reactivity of Bimetallic Cobalt Organometallics: How the Supporting Metal Affects C-C Bond Forming Reactions

3.1. Overview

Metal-metal bonded complexes with mid-to-late first row transition metals constitute a group of compounds that have recently been the subject of increased scrutiny in the literature. The reactivity of metal-metal bonded complexes is of great interest due to the attractiveness of modulating the reactivity by changing the identity of the metals. However, few examples of reactivity using metal-metal bonded complexes with mid-to-late first row transition metals have been identified. In particular, systems in which the reactivity is examined with a common "active" metal but variable "supporting" metals are lacking. In this chapter, organometallic cobalt-metal bonded complexes are prepared and characterized, including a dicobalt benzyl complex and a family of cobalt-aluminum molecules. The electronic structure and reactivity of isostructural dicobalt and cobalt-aluminum benzyl molecules are compared. It is found that the dicobalt complex is prone to one-electron transformations, including C-C and C-O bond forming reactions, whereas the cobalt-aluminum complex can undergo both one- and two-electron C-C bond forming reactions. The one-electron reactivity of the dicobalt complex is tied to its electronic structure, in which two cobalt(II) centers are coupled antiferromagnetically, whereas the aluminum-cobalt complex contains a cobalt(I) center datively bonding to an aluminum(III) center.

3.2 Introduction

The development of catalysts for C-C and C-N bond formation is an important challenge. In this area, dirhodium catalysts are prized for their ability to mediate C-H bond insertions, cyclopropanations and aziridinations, and ylide formation, in many cases with asymmetry provided by chiral ligands.[45-47,128-137] One of the reasons dirhodium compounds are successful with these transformations is that rhodium-rhodium bonding plays a key role in the electronic structure of dirhodium nitrene and carbene intermediates.[132] One of the drawbacks of dirhodium catalysts is the expense of rhodium. Preparing catalysts containing earth-abundant and environmentally benign first-row transition metals, such as the Group IX congener of rhodium, cobalt, would overcome this limitation. Cobalt-mediated C-C bond forming catalysis is a burgeoning field.[138-144] In this context, the investigation of C-C bond forming reactions with cobalt bimetallics is of fundamental interest. In particular, the synthesis and reactivity of cobalt-containing bimetallics with organometallic ligands would be desirable, as their reactivity with, e.g., R-X electrophiles could represent key bond-forming steps in a catalytic cycle. With the design of an appropriate ligand, different pairs of cobalt-supporting metal bimetallic organometallics could be prepared, allowing for the study of reactivity depending on the supporting metal choice. For example, one target could be to increase the propensity for the bimetallic to undergo oxidative addition of an electrophile.

The electronic structure of late first-row transition metal polymetallic compounds – in particular, their metal-metal interactions – have been the subject of a number of recent investigations.[16,20,21,28,33,35-38,40,41,43,44,49,50,145,146] However, how the electronic structure

and metal-metal interactions influence reactivity in these complexes has been little studied.[16,38,49] Previously, we synthesized and characterized a series of late first-row transition metal homo- and heterobimetallics with the metals manganese, iron, and cobalt in the binucleating ligand *N*,*N*,*N*-tris(2-(2-pyridylamino)ethyl)amine, abbreviated as py_3tren.[145] In the present study, we have prepared a dicobalt organometallic compound and have explored its reactivity. To provide electronic structure and reactivity comparisons to a bimetallic with only *one* transition metal, we also have prepared a series of aluminum-cobalt organometallics in the same ligand scaffold. We find that the dicobalt organometallic compound is susceptible to one-electron chemistry, whereas the isostructural aluminum-cobalt organometallic molecule can carry out either one-electron or two-electron reactions. The origin of the differing abilities of these substrates to undergo two-electron reactions is intimately tied to their electronic structures and metal-metal interactions: the aluminum-cobalt compound can be described as having a dative bond from cobalt(I) to aluminum(III), whereas the dicobalt compound contains two cobalt(II) centers that are coupled antiferromagnetically.

3.3 Results and Discussion

3.3.1 Synthesis

The dicobalt organometallic precursor CoCoBr(py_3tren) **1** (py_3tren = L) was prepared in the same manner as CoCoCl(L).[145] Addition of benzylpotassium to **1** in THF in a dry ice/acetone bath gave red-orange CoCo(Bn)(L) **2** upon warming overnight (Scheme 3.1). While additional organometallics such as CoCo(Me)(L) were targeted, addition of LiMe to CoCoX(L) did not afford the metathesis product and instead resulted in a mixture of CoCo(L) and the monocobalt species K[Co(L)]. Addition of Grignards to CoCoX(L) gave unidentified paramagnetic products.

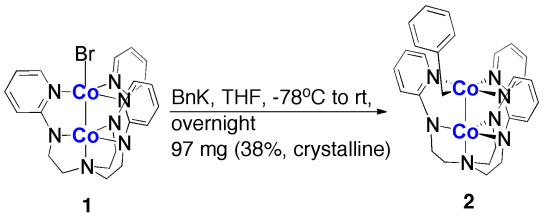

Scheme 3.1. Synthesis of CoCo(Bn)(L) **2** from CoCoBr(L) **1**.

Incorporation of aluminum(III) into the tren pocket of the ligand was accomplished by heating H_3py_3tren to 65°C overnight in the presence of 1.0 eq $AlMe_3$ in THF (Scheme 3.2). This procedure afforded the monoaluminum species Al(py_3tren) as an off-white solid in good yield (1.03 g, 68% yield). Installation of cobalt was effected by adding the commercially available $CoCl(PPh_3)_3$ to Al(py_3tren) in THF in a dry ice/acetone bath and warming slowly overnight with stirring. This procedure gave 370 mg AlCoCl(L) **3** (82% yield) as a yellow powder (Scheme 3.2). The syntheses of the Al-Co organometallics

were accomplished in the same manner as **2**: by addition of organoalkali reagents to **3** to give AlCo(R)(L) (R = Bn for **4**, Me for **5**, and Ph for **6**) at dry ice/acetone temperatures (Scheme 3.2). Complex **5** could also be synthesized by the addition of an Et_2O slurry of a 1:1 mixture of MeMgBr and TMEDA to a THF slurry of **3**.

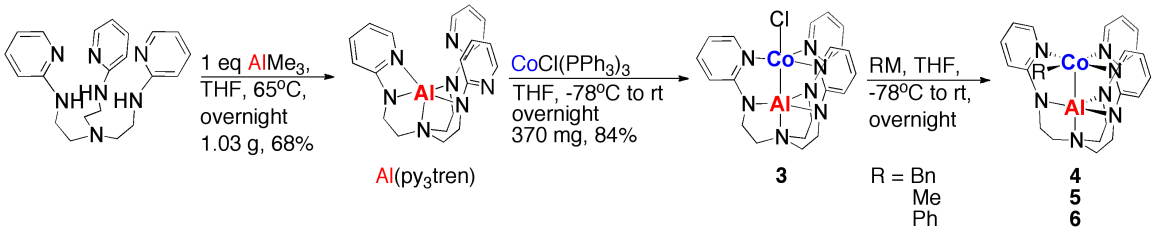

Scheme 3.2. Synthesis of Al(L), AlCoCl(L) **3**, and AlCo(R)(L) (R = Bn **4**, Me **5**, Ph **6**).

3.3.2 NMR Spectroscopy

The ^{1}H NMR spectra of compounds Al(py$_3$tren) and **1** – **5** all show solution C_{3v} symmetry at room temperature. For the chloride species CoCoCl(L) **1** and AlCoCl(L) **3**, this is expected since X-ray crystallography shows only slight deviations from threefold symmetry. In the cases of Al(L), **2**, **4**, and **5**, the solution symmetries are not in accordance with those in the solid state structures (*vide infra*). For example, the solid state structure of Al(L) has one unique pyridyl ring coordinated to Al. The discrepancy between the ^{1}H NMR spectrum and the crystal structure can be rationalized by invoking a rapid pyridyl exchange at the aluminum center. Instead of having four sharp pyridyl resonances, one of the four pyridyl resonances in Al(L) is a broad singlet at 6.59 ppm in CD_2Cl_2 at room temperature (Figure A2.1). Based on comparisons to the chemical shifts of H_3py$_3$tren and the multiplicity of the sharp peaks, it is likely that this is the β' proton of the pyridyl ring. It is likely that the broadness can be attributed to the β' proton's

experiencing significantly different chemical environments (i.e., pointing towards or away from the center of the molecule depending on the orientation of the pyridyl ring) averaged on the NMR timescale.

Like CoCoCl,[145] the dicobalt organometallics CoCoBr(L) **1** and CoCo(Bn)(L) **2** are paramagnetic at room temperature, though the NMR spectrum of **2** exhibits different behavior than CoCoCl(L) upon cooling (*vide infra*). AlCoCl(L) **3** is also paramagnetic at room temperature, which is what is expected for $S = 1$, d^8 cobalt(I) in a trigonal bipyramidal geometry (*vide infra*). In contrast, the aluminum-cobalt organometallics **4** – **6** are all diamagnetic at room temperature. For **4** – **6**, this consistent with an $S = 0$, d^8 cobalt(I) in a square planar geometry (*vide infra*). The change in spin state from $S = 1$ to $S = 0$ comparing **3** with **4** – **6** can be understood in terms of the increased ligand field strength of an organometallic ligand compared to chloride. This type of spin state change upon axial ligand substitution has been observed in other cobalt systems. [147,148]

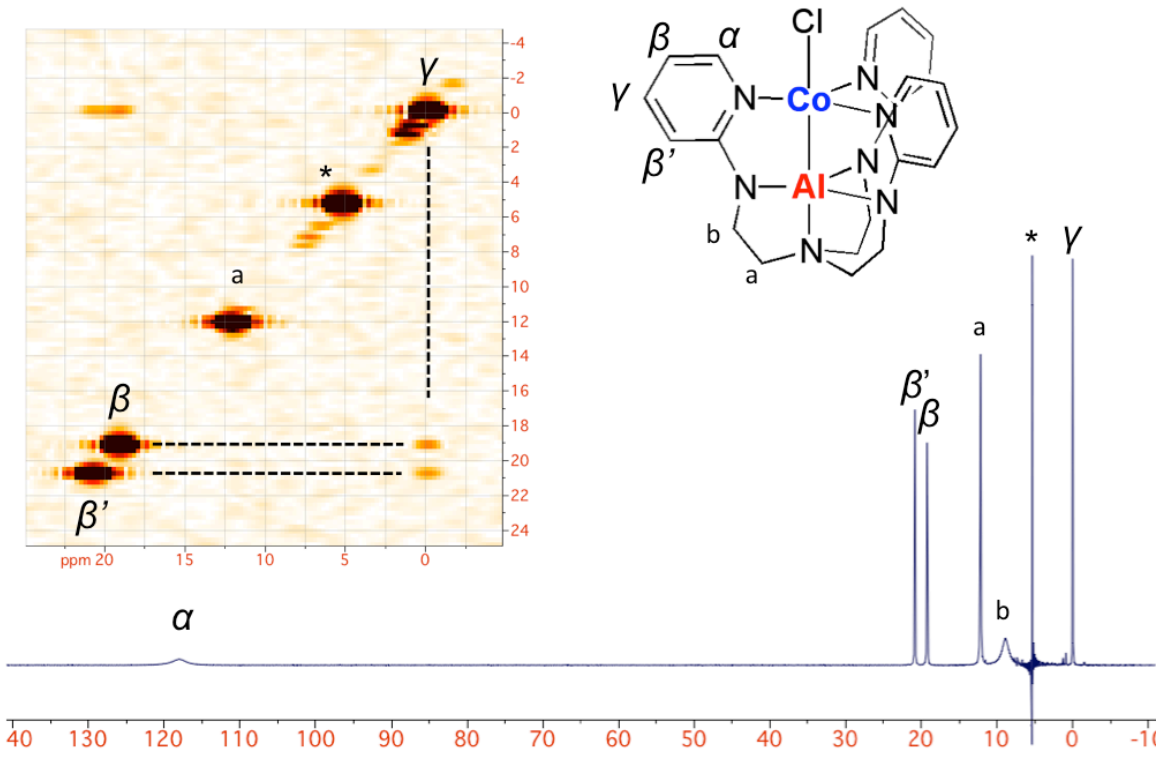

Figure 3.1. ^{1}H NMR spectrum of paramagnetic AlCoCl(L) **3** in CD_2Cl_2 with assignments. Solvent marked with an asterisk. (Inset) COSY spectrum of AlCoCl(L) **3** in CD_2Cl_2.

Table 3.1. T_1 values for AlCoCl(L) **3** with assignments.

Chemical Shift (ppm)	T_1 (ms)	Assignment
118	0.4	α
20.8	20.6	β'
19.2	14.3	β
12.1	15.0	a
8.9	10.5	b
0.0	45.2	γ

The ^{1}H NMR spectrum of paramagnetic AlCoCl(L) **3** was assigned through a combination of T_1 measurements and ^{1}H-^{1}H correlation spectroscopy (COSY). The COSY spectrum of **3** is shown in the inset of Figure 3.1, and the T_1 values are included in Table 3.1. The pyridyl peaks could be distinguished from the tren peaks by integration, as each pyridyl peak integrates to 3 H whereas each tren peak integrates to 6 H. As is typical

for most of the $M_1M_2Cl(py_3tren)$ compounds, the pattern of pyridyl peaks is consistent with a dominant spin delocalization mechanism.[149,218] The β vs. β' protons were assigned on the basis of the shorter T_1 value corresponding to the β proton, as it is closer to the cobalt center. The COSY spectrum shows the β-γ and γ-β' cross peaks. The two different tren peaks were assigned on the basis that the shorter T_1 value should correspond to the tren methylene protons adjacent to the amide, as these are closer to the cobalt center.

While CoCo(Bn)(L) **2** and AlCo(Bn)(L) **4** are isostructural by X-ray crystallography, **2** is paramagnetic at room temperature while **4** is diamagnetic. The Lewis acidic aluminum(III) center unambiguously supports $S = 0$ cobalt(I) in **4**, but the assignment of spin and oxidation states for the individual cobalt centers in **2** is not obvious. The ^{1}H NMR spectra of both **2** and **4** show 10 peaks at room temperature, as expected for solution C_{3v} symmetry, which in comparison to their solid-state structures indicates that both **2** and **4** undergo a fluxional process (*vide infra*). Variable low temperature ^{1}H NMR spectra for **2** reveal that certain peaks decoalesce as the sample is cooled, and the peaks spread further apart as the temperature is lowered further. The latter observation is not what is expected for a diamagnetic ground state, and indeed, solid-state measurements show a paramagnetic ground state for **2** (*vide infra*).

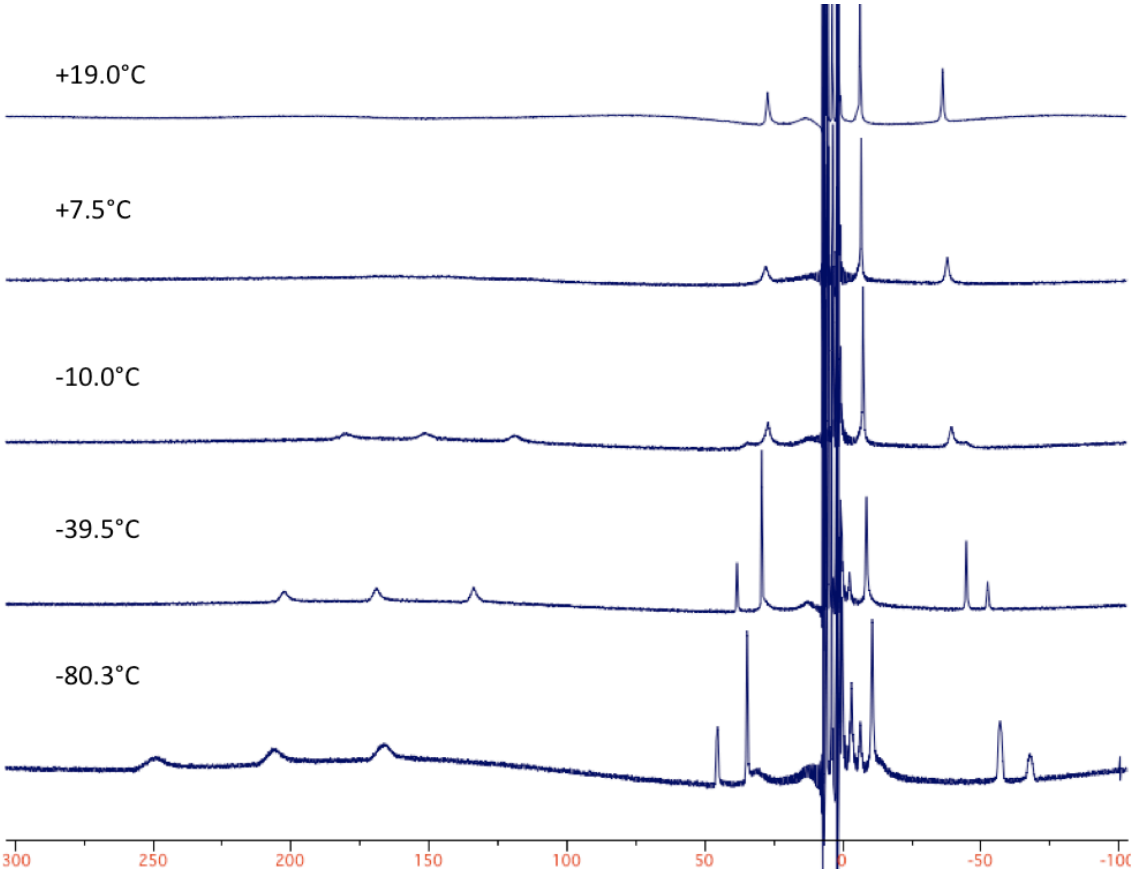

Figure 3.2. Variable-temperature ^{1}H NMR spectra of paramagnetic CoCo(Bn)(L) **2** in d_8-toluene.

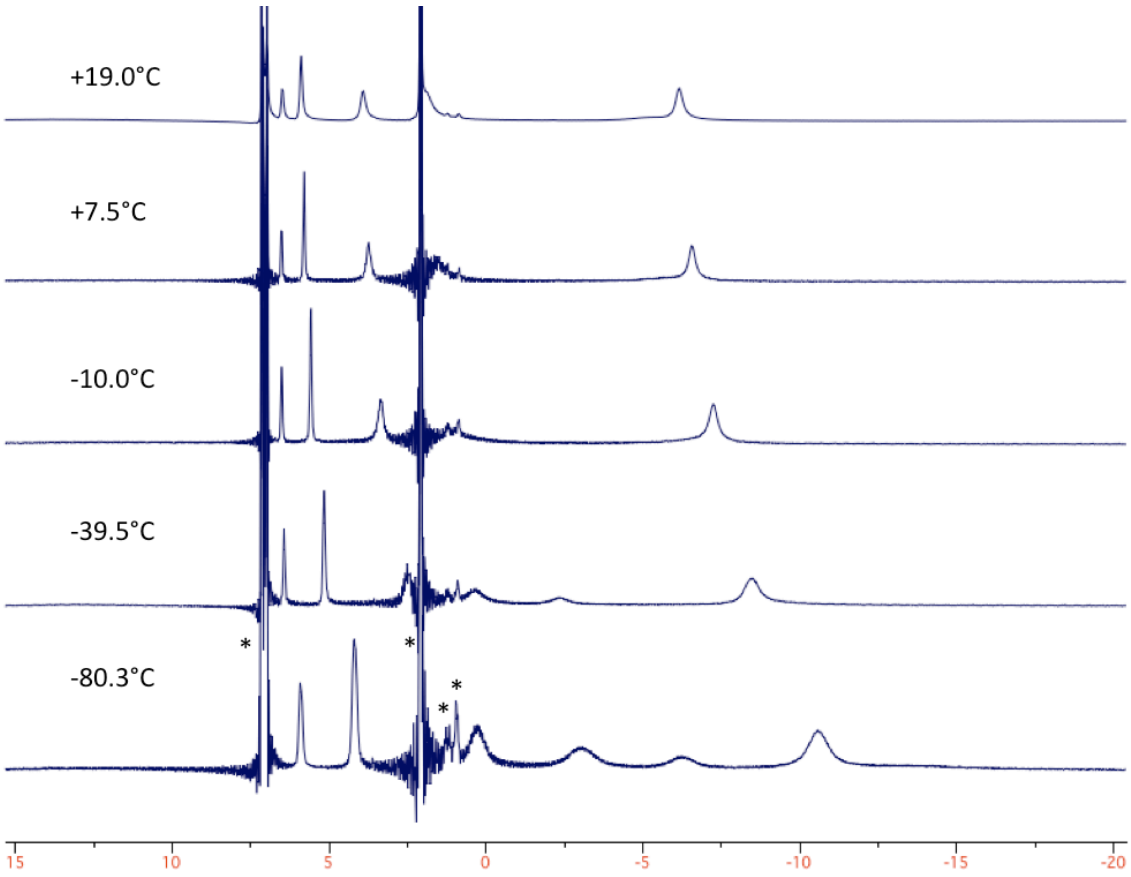

Figure 3.3. Variable-temperature ^{1}H NMR spectra of paramagnetic CoCo(Bn)(L) **2** in d_8-toluene – a close-up of the +15 to -20 ppm region. Asterisks in the -80°C spectrum denote solvent peaks.

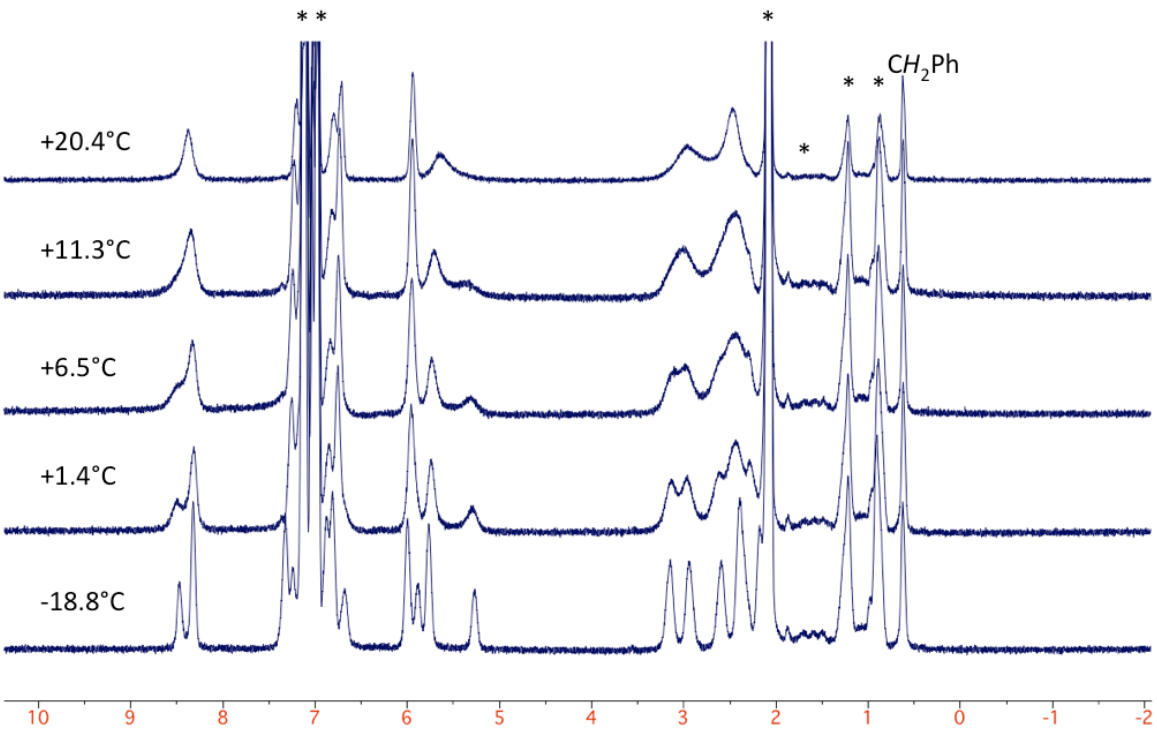

Figure 3.4. VT ^{1}H NMR profile of AlCo(Bn)(L) **4** in d_8-toluene. Solvents are denoted with asterisks.

Two different decoalescence events are clearly observed for **2**: a broad peak at 140 ppm becomes three peaks (165 ppm, 143 ppm, and 114 ppm) when the temperature is lowered from 19°C to 7.5°C; and three peaks (27.4 ppm, 1.9 ppm, and -36.1 ppm at 19°C) each decoalesce to two peaks in a 2:1 ratio when the temperature is lowered to -10°C (Figures 3.2 and 3.3). The spectrum of paramagnetic **2** makes peak assignments difficult, and so further analysis of diamagnetic **4** was undertaken. Several pyridyl peaks in **4** decoalesce into a 2:1 ratio when the temperature is lowered to -19°C (Figure 3.4). The tren peaks of **4**, which are two broad singlets at room temperature, decoalesce into five peaks at -19°C. If two different tren peaks have accidental chemical equivalence, then these observations are consistent with solution C_s symmetry (since six different tren

resonances would be expected), which is what is observed in the solid state structures of **2** and **4** (*vide infra*).

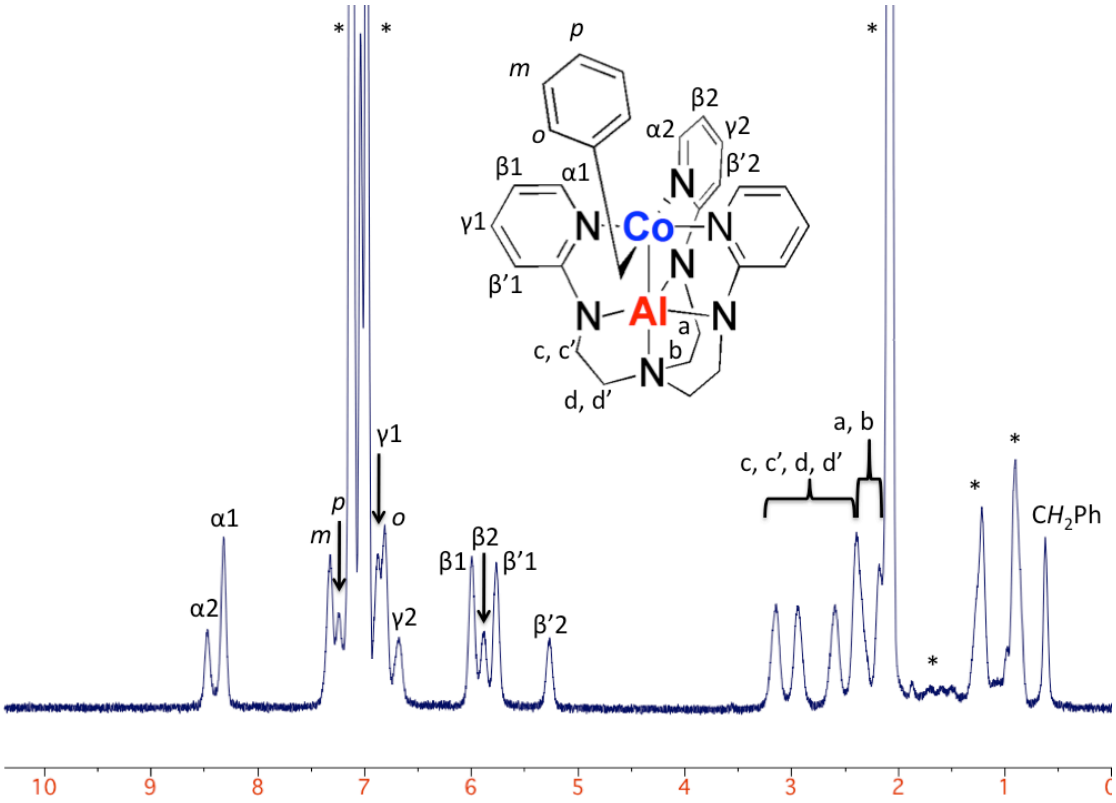

Figure 3.5. ^{1}H NMR spectrum of **4** in d_8-toluene at -19°C. Solvents marked with asterisks.

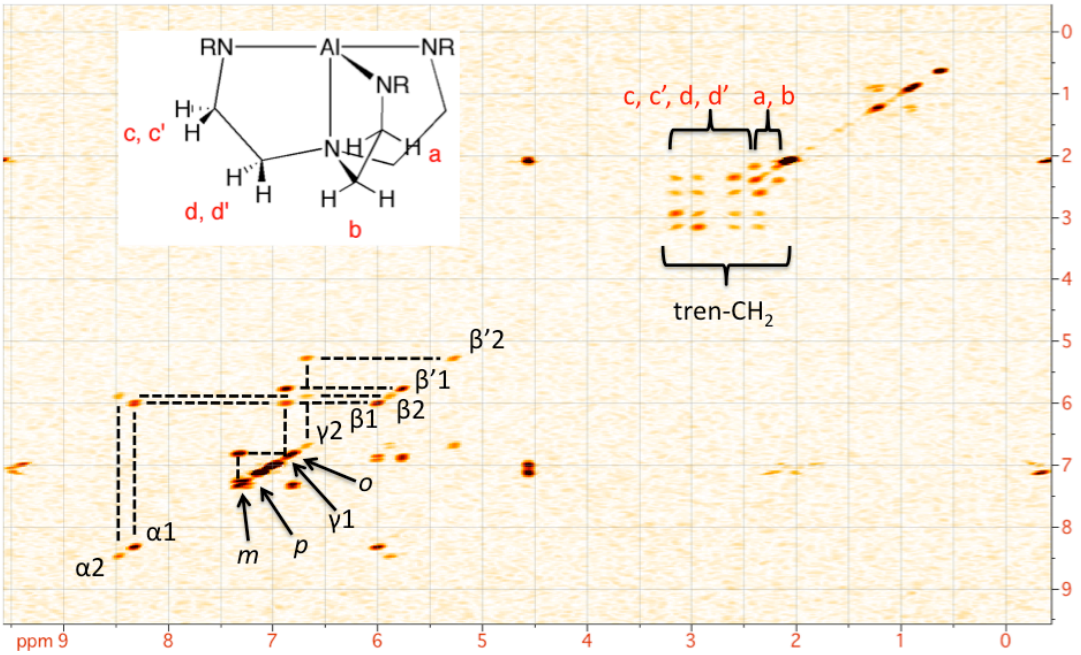

Figure 3.6. ^{1}H-^{1}H COSY spectrum of **4** at -19°C. Inset: Scheme showing the notation of tren protons in **4**.

A COSY spectrum of **4** collected at -19°C clearly shows the connectivity in the two unique pyridyl rings consistent with C_s symmetry (Figure 3.6). The pyridyl peaks have been assigned based on the COSY spectrum and the fact that α protons are typically shifted the most downfield (Figure 3.5). In addition, the phenyl resonances have been assigned on the basis of the splittings and integrations seen in the room temperature spectrum of **4** in C_6D_6 (Figure A2.7) along with a cross peak for the *ortho*/*meta* protons.

In both sp^3-ligated cobalt-aluminum organometallics, the protons on the organometallic carbon are shifted upfield: 0.80 ppm for **4** in C_6D_6 vs. 2.11 ppm for toluene, and -0.57 ppm for **5** in C_6D_6 vs. 0.16 ppm for methane (Figure A2.8). The upfield chemical shifts of **4** and **5** are consistent with coordination of the organometallic ligand to the electron-rich cobalt(I) center.

Unlike **4** and **5**, the benzyl and methyl derivatives, **6** exhibits solution C_s symmetry at room temperature (Figure A2.9). This is consistent with the greater steric bulk of a phenyl ligand compared to a benzyl or methyl ligand. One would expect that the decoalescence temperature for converting to C_s symmetry from C_{3v} symmetry should be higher the greater the steric bulk of the ligand. The phenyl ligand resonances are observed at 7.96 ppm (*ortho*), 7.05 ppm (*meta*), and 6.82 ppm (*para*). While the solid state structure of **6** shows that the phenyl ring is oriented in such a way that all five protons could be chemically distinct (*vide infra*), the barrier to rotation of the phenyl ring evidently is low enough that, at 19°C, the two *ortho* protons and the two *meta* protons are chemically equivalent. The *ortho* resonance is shifted far downfield of the other peaks. This could be because the *ortho* protons pass through the induced magnetic field of the pyridyl rings as the phenyl ring rotates, introducing an additional deshielding effect aside from that of the phenyl ring itself.

3.3.3 X-Ray Crystallography

The X-ray crystal structures of Al(py$_3$tren) and **2** – **6** have been collected; those of CoCoCl(L) and **2** – **6** are tabulated in Table 3.2. The organometallics **2** and **4** – **6** will be discussed together later. The Al center of Al(py$_3$tren) coordinates the three amide donors and the apical amine, as well as also one of the three pyridyls (Figure A3.7). As discussed in the NMR section, the pyridyls must exchange in solution to account for the observed solution C_{3v} symmetry. More significantly, since aluminum sits in the amide plane and the pyridyl coordination is reversible at room temperature, Al(py$_3$tren) is poised to bind a second metal.

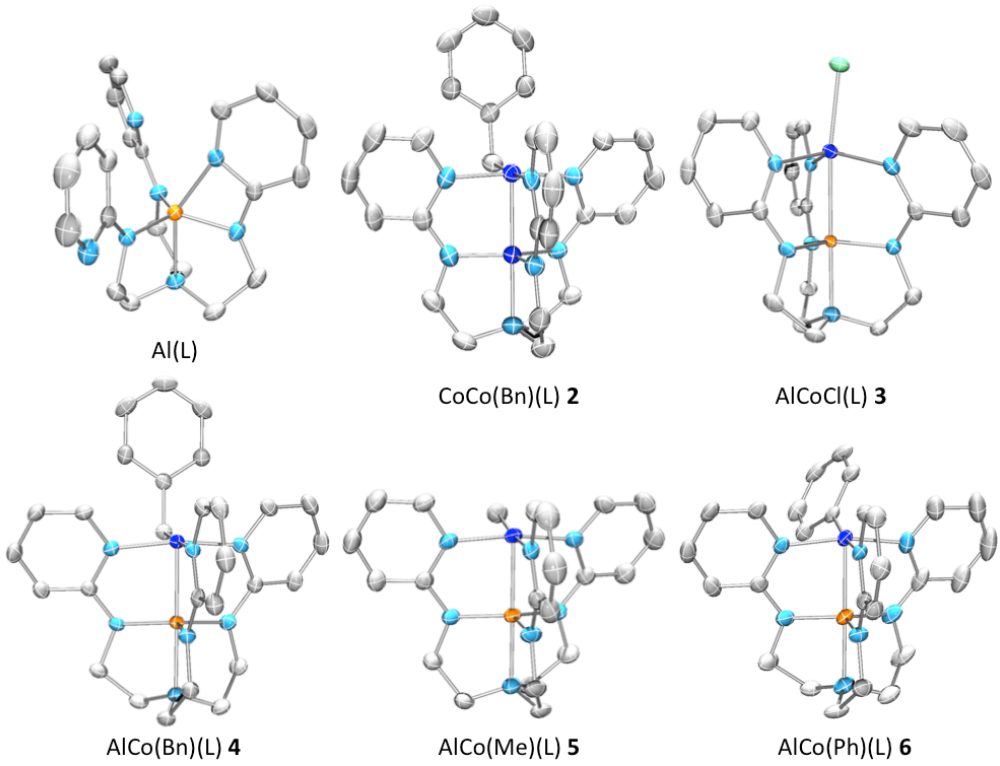

Figure 3.7. X-ray crystal structures of Al(L) and **2**-**6**.

Table 3.2. Geometrical parameters, including bond lengths and angles, for CoCoCl(L) and compounds **2** – **6**.[a]

	CoCoCl (L)	AlCoCl (L) **3**	CoCo(Bn) (L) **2**[d]	AlCo(Bn) (L) **4**[d]	AlCo(Me) (L) **5**	AlCo(Ph) (L) **6**
M_1-Co (Å)	2.4986(4)	2.4671(8)	2.2594 ± 0.0054	2.2324 ± 0.0009	2.2360(8)	2.2582(9)
r[b]	1.08	1.03	0.98	0.93	0.93	0.94
M_1-N_{ap} (Å)	2.012(1)	2.021(2)	1.996 ± 0.002	2.020 ± 0.007	2.032(2)	2.020(2)
M_1-N_{eq} (Å)[c]	1.885 ± 0.004	1.859 ± 0.006	1.880 ± 0.011	1.861 ± 0.004	1.862 ± 0.003	1.860 ± 0.007
Co-X (Å)	2.3487(5)	2.3963(8)	1.998 ± 0.001	2.013(2)	1.957(2)	1.931(3)
Co-N_{py} (Å)[c]	2.074 ± 0.007	2.067 ± 0.013	1.975 ± 0.030	1.957 ± 0.021	1.953 ± 0.032	1.961 ± 0.026
M1-Co-X (°)	177.69(2)	172.77(3)	96.61 ± 1.24	96.18 ± 2.28	102.20(8)	104.88(9)

[a] Estimated standard deviations (esd) are provided in parentheses. [b] *r* = ratio of M_1–Co bond distance to the sum of M_1 and Co single-bond radii. [c] M_1–N_{eq} and Co–N_{py} bond lengths are reported as averages ± standard deviations. [d] CoCo(Bn)(L) **2** and AlCo(Bn)(L) **4** each have two independent molecules in the asymmetric unit; hence, all values are given as averages ± standard deviations.

The crystal structure metrics of **3** are quite similar to those found for CoCoCl(L) (Table 3.2). The *r* value is smaller for **3** (1.03) than for CoCoCl(L) (1.08) by 0.05 but is consistent with a dative bond. CoCoCl(L) has a weak covalent interaction between two Co(II) centers with an effective bond order (EBO) of 0.22;[145] in the same vein, for **3**, the Al-Co interaction can be considered a weak dative bond with Co(I) as the donor and Al(III) as the acceptor. The metal-ligand bond lengths are all very close for the two molecules with the exception of the Co-Cl distances: that for **3**, at 2.3963(8) Å, is greater by nearly 0.05 Å than for CoCoCl(L) (Table 3.2). A possible reason for this difference is that the Co centers are in different oxidation states in the two complexes, providing another reason for the Co-Cl bond lengthening in **3** relative to CoCoCl(L).

Compared to the halide species CoCoCl(L) and **3**, the metal-metal bonds in the organometallics **2** and **4**-**6** are much shorter (Table 3.2). The MCoX(L) *r* values for a given M decrease by 0.10 when swapping Cl for Bn) The MCo(R)(L) *r* values are all slightly smaller than that for a single bond. Some of this decrease can be attributed to the loss of an apical ligand in the organometallic compounds **2** and **4** – **6** compared to CoCoCl(L) and **3**, which alleviates antibonding interactions with the d_{z2} orbital. This leads to a stronger dative interaction between cobalt and aluminum in **4** – **6** compared to **3**, as the d_{z2} orbital should drop significantly in energy. The spin state difference between **3** and **4** – **6** could also play a role, as the radius of the $S = 1$ cobalt(I) center in **3** should be larger than the radius of the $S = 0$ cobalt(I) centers in **4** – **6** (Figure 3.8).

It is also instructive to compare the Co-N_{py} bond lengths of these molecules. CoCoCl(L) and **3** have Co-N_{py} bond lengths of approximately 2.07 Å, whereas the Co-

N_{py} bond lengths of **2** and **4** – **6** are all much shorter (Table 3.2). The Co-N_{py} distances *trans* to the organometallic ligand range from 1.98 Å to 2.00 Å, while the other two Co-N_{py} distances in each molecule are shorter at 1.93 Å to 1.95 Å. The noticeable difference in Co-N_{py} bond lengths *trans* to another N_{py} compared to those *trans* to an organometallic ligand can be attributed to the greater *trans* influence of an organometallic σ donor compared to a pyridyl donor. The shortening in the Co-N_{py} distances of the MCo(R)(L) compounds **2** and **4** – **6** compared to the MCoCl(L) compounds is due to the geometry change at cobalt. In the MCoCl(L) derivatives, which are distorted trigonal bipyramidal, the d_{x2-y2} and d_{xy} orbitals are half filled (Figure 3.8). Because the MCo(R)(L) compounds are square pyramidal, as discussed earlier, the high-lying d_{x2-y2} orbital is empty. This alleviates Co-N_{py} σ antibonding interactions that are found in the MCoCl compounds.

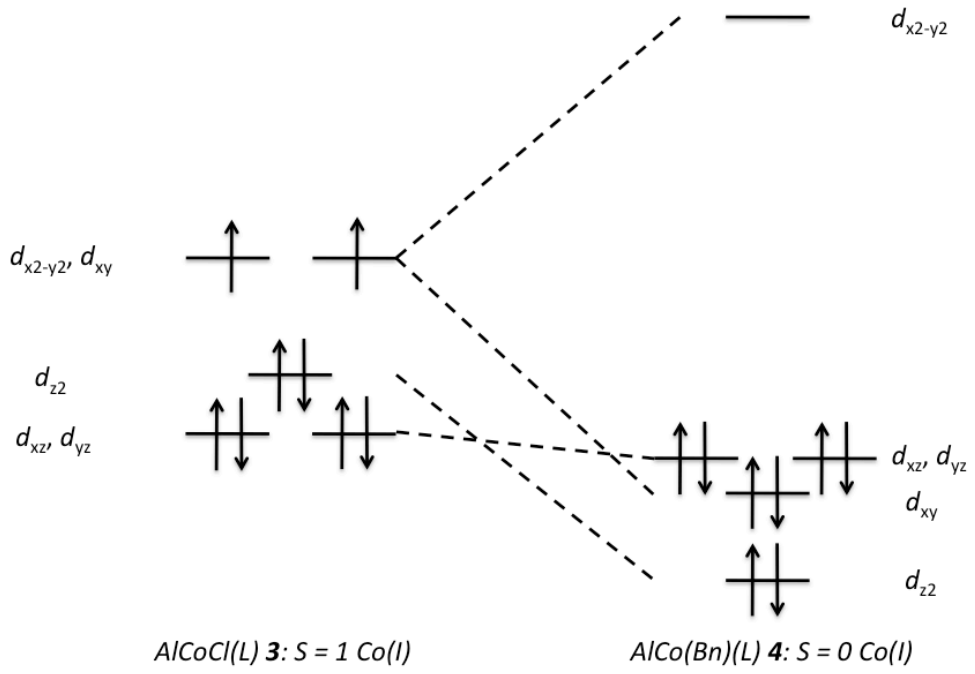

Figure 3.8. Qualitative *d*-orbital splitting diagrams for AlCoCl(L) **3** and AlCo(Bn)(L) **4.**

An interesting trend to evaluate is the changing Co-C distance in the AlCo(R)(L) bimetallics **4**-**6**. The distance shortens from 2.013(2) Å in **4** to 1.957(2) Å in **5** to 1.931(3) Å in **6**. This trend follows the bond dissociation enthalpies, DH_{298}(R-H), as seen in Table 3.3.[150] The shortest Co-C bond corresponds to the highest bond dissociation enthalpy, or equivalently, the strongest C-H bond of the corresponding R-H molecule. Hence, **4** should be more susceptible to Co-C bond homolysis than **5** or **6**. Additionally, the organometallic ligand in **4** – **6** experiences a distortion from planarity with the three pyridyl nitrogen donors. This has been measured in terms of the Al-Co-C angle (90° would mean that the organometallic ligand is orthogonal to the Al-Co bond). The trend in this angle correlates with the Co-C bond length: 96.18° (± 2.28°) for **4** to 102.20(8)° for **5** to 104.88(9)° for **6** (Table 3.2). The strong σ donors presumably distort out of the plane to relieve their *trans* influence with the pyridyl donors. The phenyl ring of **6** is tilted with respect to the Al-Co bond; the Al-Co-C_{ipso}-C_{ortho} torsion angle is 38.3°. This metric has little consequence in solution at room temperature, because the chemical equivalence of the two *ortho* and the two *meta* protons by ^{1}H NMR spectroscopy at 19°C implies that the phenyl ring freely rotates.

Table 3.3. Comparison of Co-C bond lengths of **4** - **6** and bond dissociation enthalpies of RH molecules.

Molecule	Co-C Bond Length (Å)	DH_{298}(R-H) (kcal/mol)[a]
AlCo(Bn)(L) **4**	2.013(2)	89.8 ± 0.6
AlCo(Me)(L) **5**	1.957(2)	104.99 ± 0.03
AlCo(Ph)(L) **6**	1.931(3)	112.9 ± 0.5

[a] Obtained from reference 150.[150]

The differences in the bond metrics of the two benzyl complexes, **2** and **4**, are subtle. While one might think this is because the pyridyl-ligated cobalt centers in both

molecules are $S = 0$ cobalt(I), this is not necessarily the case. The Co-N_{py} bond lengths are statistically indistinguishable in CoCoCl(L) and **3** (Table 3.2), in which the former has the Co(II)Co(II) oxidation state assignment[145] while the latter must be Al(III)Co(I). The molecule CoCo(Bn)(L) has an overall $S = 1$ spin state (*vide infra*), and so this can be attained *via* a dative interaction between $S = 0$ cobalt(I) and $S = 1$ cobalt(III) (Figure 3.9). However, another model which can equally explain the data is antiferromagnetic coupling between an $S = 1/2$ tetragonal cobalt(II) and $S = 3/2$ trigonal cobalt(II). In both models, the d_{x2-y2} orbital is empty, leading to the short Co-L distances of **2**. Looking at the amide-ligated cobalt, in both models the d_{x2-y2} and d_{xy} orbitals are half filled, and so comparison of the bottom cobalt metrics is no more helpful. The only differences in the orbital filling diagrams lie in the d_{z2} orbitals of the two cobalts. The reactivity differences between **2** and **4** suggest they have different electronic structures (*vide infra*).

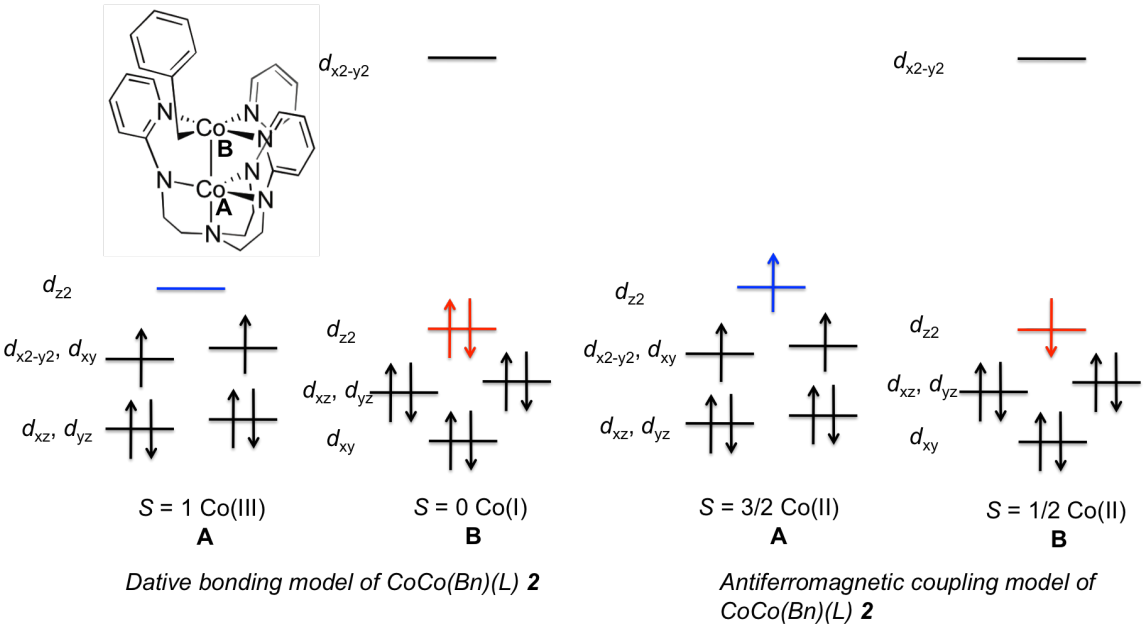

Figure 3.9. Limiting models of the bonding in CoCo(Bn)(L) **2**. On the left is the dative bonding model, and on the right is the antiferromagnetic coupling model.

3.3.4 UV-Vis-NIR Spectroscopy

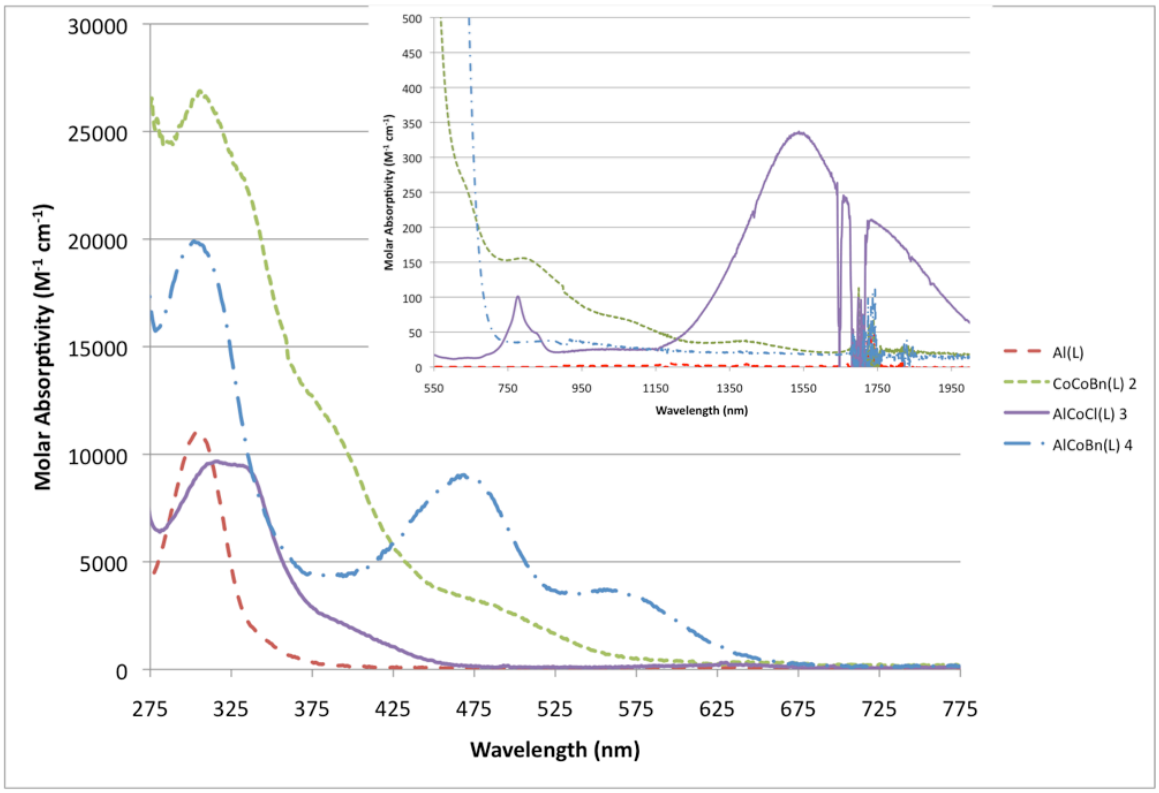

Figure 3.10. UV-Vis spectra of monoaluminum, CoCo(Bn)(L) **2**, AlCoCl(L) **3**, and AlCo(Bn)(L) **4** in THF. (Inset) Vis-NIR spectra. The red long dashed line represents monoaluminum, the green line with small dashes represents **2**, the purple solid line represents **3**, and the blue line with alternating dots and dashes represents **4**.

Complex **1** is olive green, **3** is yellow, **2** is red-orange, and **4** – **6** are all shades of red. The UV-Vis-NIR spectrum of **1** (Figures A2.4 and A2.5) is very similar to the previously reported CoCoCl(L) and will not be discussed further. The UV-Vis-NIR spectra of Al(L) and **2** – **4** can be found in Figure 3.10. Complex **3** has an absorption at 333 nm with an extinction coefficient of 9,500 M^{-1} cm^{-1}, just a little lower in energy than the 316 nm pyridyl $\pi \rightarrow \pi^*$, as well as a shoulder at 380 nm with an extinction coefficient of 2,200 M^{-1} cm^{-1}. These absorptivities are consistent with charge transfer bands.

Additional features of **3** at 777 nm (100 M^{-1} cm^{-1}), a shoulder at 823 nm (50 M^{-1} cm^{-1}), and 1537 nm (340 M^{-1} cm^{-1}) have absorptivities in line with *d-d* transitions.

Though **2** and **4** have similar colors, their UV-Vis-NIR spectra are quite different (Figure 3.10). **2** exhibits a series of shoulders in the UV-Vis region and weak absorptions in the NIR region that are likely *d-d* transitions, as was proposed for CoCoCl(L).[145] Unlike **2**, **4** has two strong features in the UV-Vis spectrum and is featureless in the NIR region. Its strong UV-Vis features at 468 nm and 555 nm are likely charge transfer transitions. Given that cobalt is unambiguously in the cobalt(I) oxidation state for **4**, the most likely assignment for these transitions are metal-to-ligand charge transfer transitions (MLCTs). The lack of weak features in the NIR region of **4** is not surprising since the geometry at cobalt(I) is square pyramidal; the d_{x2-y2} orbital is quite high in energy compared to the four filled *d* orbitals.

It is also instructive to compare the UV-Vis spectra of **3** and **4**. Both of these molecules have two charge transfer bands in the UV-Vis region. Given the cobalt(I) oxidation state, it is likely that both are MLCT bands. That **3** has *d-d* transitions while **4** does not is not surprising, since **3** has a relatively smaller ligand field with unpaired electrons in the d_{xy} and d_{x2-y2} orbitals whereas **4** has a high-lying, empty d_{x2-y2} orbital and four other filled orbitals. Upon metathesis of the chloride ligand for the benzyl ligand, the ligand field becomes stronger, and the resulting diamagnetism can be rationalized by the loss of degeneracy of the d_{xy} and d_{x2-y2} orbitals (Figure 3.8). The two unpaired electrons in **3** are now paired in the d_{xy} orbital of **4**. An additional effect is that the d_{z2} orbital also drops in energy because of the shorter Al-Co interaction in **4** relative to **3**, as well as the

loss of an apical ligand in **4**.

3.3.5 Cyclic Voltammetry

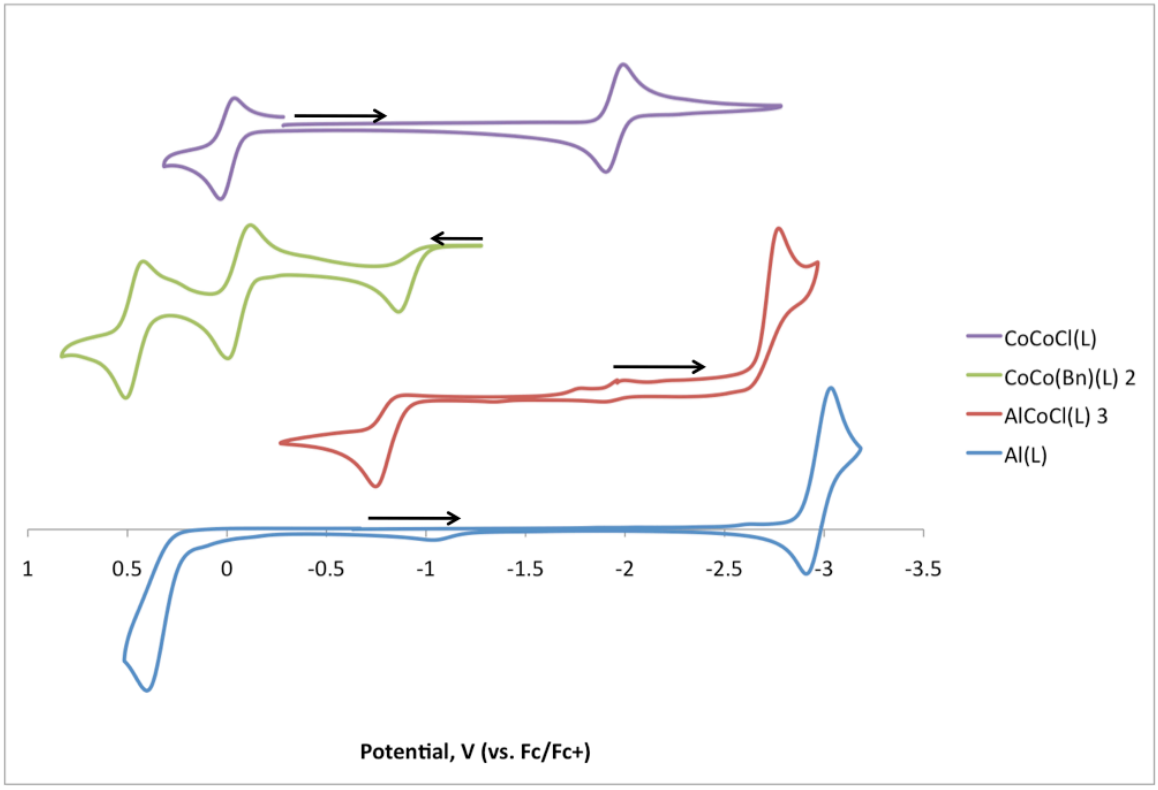

Figure 3.11. Cyclic voltammograms of (top) CoCoCl(L) (0.3 V/s), (middle left) CoCo(Bn)(L) **2** (0.05 V/s), (middle right) AlCoCl(L) **3** (0.02 V/s), and (bottom) Al(L) (0.3 V/s) (all in 0.4 M nBu_4PF_6 at room temperature).

The cyclic voltammograms of Al(L), AlCoCl(L) **3**, and CoCo(Bn)(L) **4** have been collected (Figure 3.11). The cyclic voltammogram of **3** has an irreversible reduction at -2.77 V and a quasireversible oxidation at -0.75 V vs. Fc/Fc^+ at 0.020 V/s. For help in assigning these redox events, the CV of Al(L) was also collected. Al(L) displays a quasireversible reduction at -2.98 V and an irreversible oxidation at 0.40 V vs Fc/Fc^+ at 0.300 V/s. The reversibility of the reduction, however, worsens with multiple scans; the waves of the experiment gradually decay, and a black layer was deposited on the working

electrode. On the basis of these observations, it seems that the monoaluminum anion is not stable. The irreversible oxidation of **3** is assigned as a cobalt(I/II) couple due to the lack of a comparable wave in the CV of Al(L). The irreversible reduction of **3** is assigned as either an aluminum- or ligand-based reduction, given the presence of a cathodic wave with a similar potential in Al(L). The one-electron reduced form of **3** is not stable, as evidenced by the irreversibility of the reduction. This is in contrast to CoCoCl(L), which exhibits a reversible one-electron reduction at -1.98 V vs. Fc/Fc^{+}.[145] Indeed, $CoCo(py_3tren)$ could be observed by ^1H NMR spectroscopy upon one-electron reduction of $[CoCo(py_3tren)][PF_6]$ **7** with KC_8.

The cyclic voltammogram of CoCo(Bn)(L) **2** has a mild, irreversible one-electron oxidation E_{pa} of -0.86 V vs. Fc/Fc^{+}. Oxidations are also seen at $E°'$ = -0.06 (quasireversible) and E_{pa} = 0.51 V (irreversible). These values are close to oxidation potentials observed in the CV of CoCoCl(L),[145] and chemical oxidation with $FcPF_6$ gives **7**, bibenzyl, and a little toluene as products, suggesting that one-electron oxidation of **2** results in an unstable $[CoCo(Bn)(L)]^{+}$ core that ejects benzyl radical, accounting for the similarity of the second and third oxidation potentials of **2** to the oxidation wave potentials of CoCoCl(L).

3.3.6 SQUID Magnetometry of CoCo(Bn)(L) 2

As mentioned above, **2** is paramagnetic at room temperature, and the ^1H NMR peaks spread out more as the temperature is lowered, suggesting that the ground state of the molecule is paramagnetic. To gain more information about the magnetism of **2**, we conducted variable-temperature magnetic susceptibility measurements on a solid sample

of **2** under an applied dc field of 1 T. The magnetic susceptibility (χ) data are plotted as χT vs. T, where T is temperature, in Figure 3.12. Compared to CoCoCl(L), the χT vs. T plot of **2** is different in several aspects. A large decrease in the χT of **2** below 90 K is evident – from 1.02 to 0.05 at 2 K. In this regime, the magnetism of CoCoCl(L) is practically 0, consistent with its diamagnetic ground state.[145] Only a very small decrease in χT from 290 K to 90 K is observed for **2**, while χT for CoCoCl(L) decreases in this regime by a noticeable amount.

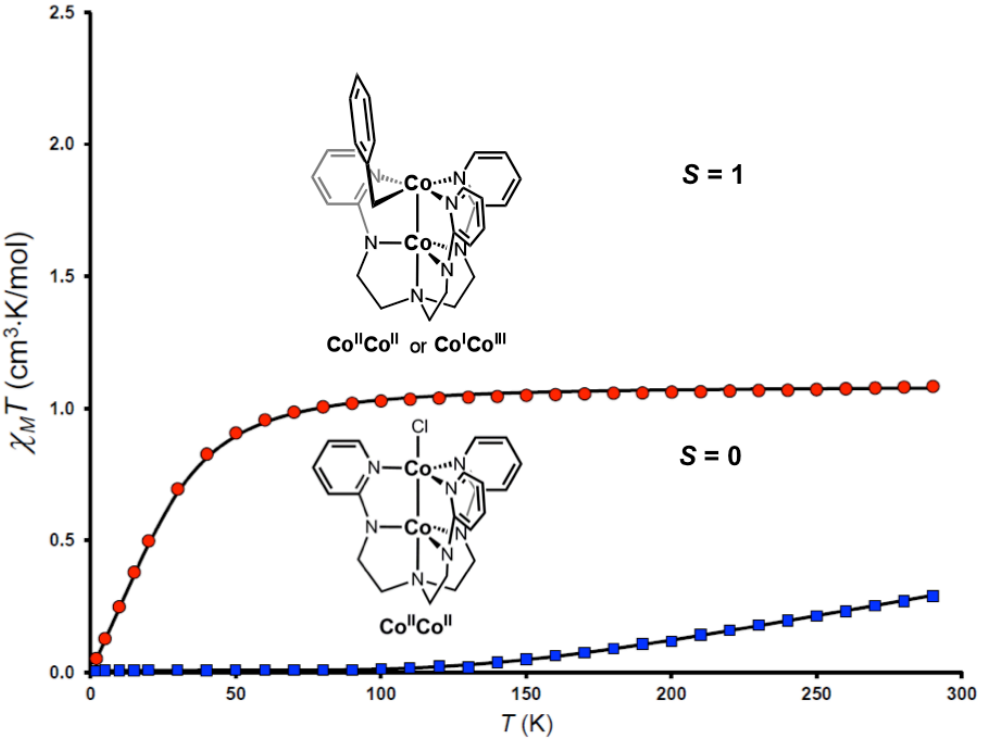

Figure 3.12. SQUID plot of the temperature dependence of the magnetic susceptibility, plotted as χT vs. T, of CoCo(Bn)(L) **2** and CoCoCl(L) from 2 K to 290 K at 1 T. The red circles represent the experimental data of **2**, with a black line representing the fit to the data of **2** (see text). The blue squares represent the experimental data of CoCoCl(L), with a black line representing the fit to the data of CoCoCl(L) (parameters of the fit for CoCoCl(L) can be found in reference 145).

The large differences between the χT vs. T plots of CoCoCl(L) and **2** are due to different ground states in the two molecules. Based on the χT vs. T data, CoCoCl(L) was assigned as a ground state $S = 0$ molecule arising from the antiferromagnetic coupling of two $S = 3/2$ Co(II) centers ($J = -231$ cm^{-1}).[145] The χT vs. T plot of **2** could be fit to a one-spin model with parameters $S = 1$, $g = 2.08$, $D = 61.5$ cm^{-1}, and a small TIP of 50 x 10^{-6} emu. The large decrease in χT below 90 K is due to the large D value. This fit could apply equally well to the dative bonding model or the antiferromagnetic coupling model described above (Figure 3.9). While the χT value decreases to 0.05 at 2 K, which could be argued as supporting an $S = 0$ ground state that originates by antiferromagnetic coupling of two $S = ½$ cobalt(II) centers (theoretical χT for a ground state $S = 0$ molecule is 0), fitting the data under these conditions requires unreasonably large g values of 2.43 for each cobalt, and is an overall worse fit in the low-temperature regime. In addition, plots of the molar magnetization M_{mol} against μ_BB with applied fields of 1, 4, and 7 T reveal that the magnetization saturates at each different applied field (Figure 2.14). The molar magnetization plot and the χT vs. T plot were iteratively fit against each other for the one spin $S = 1$ model. In particular, the molar magnetization plot in the saturation regime is quite sensitive to the D values in the Hamiltonian. Fitting the molar magnetization plot with an antiferromagnetically coupled $S = 0$ ground state from two $S = ½$ cobalt(II) centers gives theoretical traces that do not match the experimental data. Hence, we conclude that the ground state of CoCo(Bn)(L) **2** is $S = 1$. However, this still does not answer the question of whether the dative model or the antiferromagnetic coupling model describes the interaction between the two cobalts.

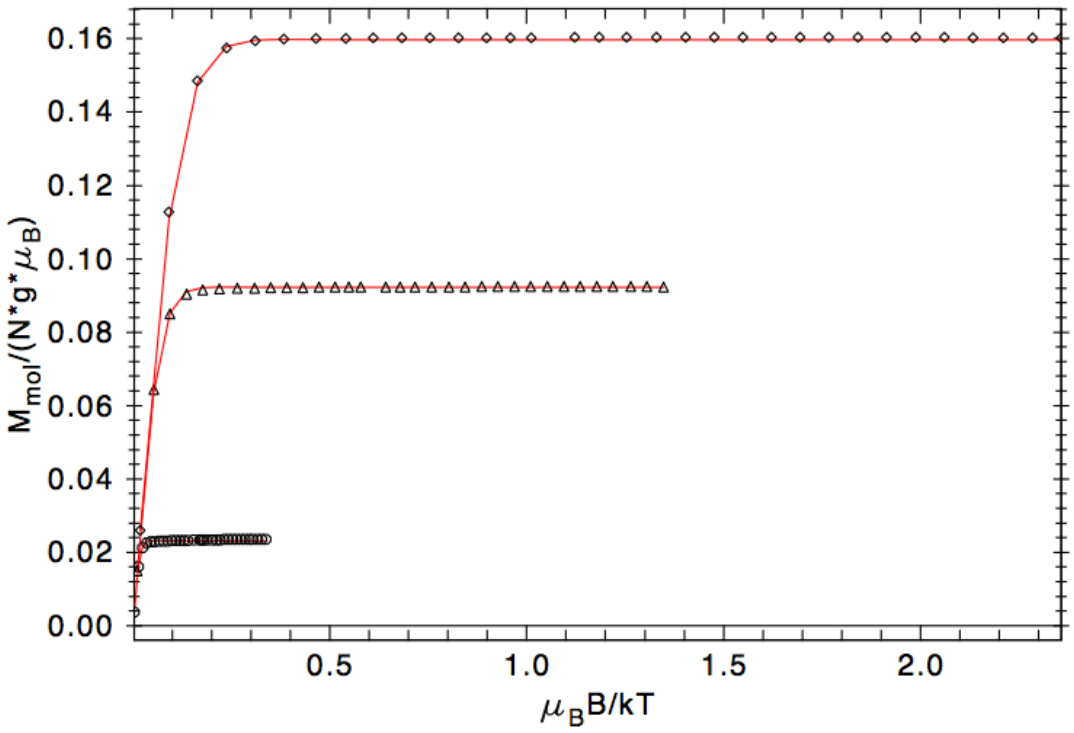

Figure 3.13. Plot of the molar magnetization M_{mol} of CoCo(Bn)(L) **2** vs. the product of magnetic field and magnetic moment. Magnetic fields used were 1 T, 4 T, and 7 T. The solid lines represent the fit to the data with $g = 2.08$, $S_{TOT} = 1$, $D = 61.5$ cm^{-1}, and TIP = 50 x 10^{-6} emu.

3.4 Reactivity Studies

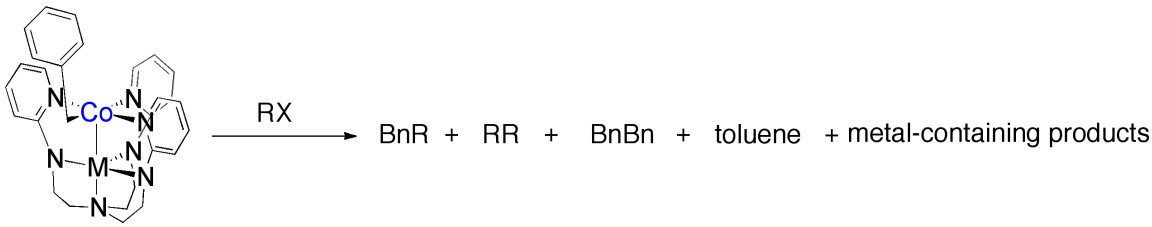

Scheme 3.3. General scheme of the reactivity studies of CoCo(Bn)(L) **2** and AlCo(Bn)(L) **4** with RX reagents.

We commenced reactivity studies with CoCo(Bn)(L) **2** and AlCo(Bn)(L) **4** with the aim of studying stoichiometric transformations relevant to C-C bond forming reactions,

seeking differences depending on the supporting metal. The first reaction studied was the addition of CPh_3Br. This reagent is prone to one-electron chemistry; the trityl radical is well known as a stable radical in its dimerized form (Gomberg's dimer).[151,152] Addition of CPh_3Br to either **2** or **4** at room temperature produced a rapid color change to olive green in the case of **2** and yellow in the case of **4**. ^{1}H NMR spectra showed in both reactions a distinctive singlet at 3.81 ppm, characteristic of the methylene protons of CPh_3Bn. GC-MS analysis of the reaction with **2** showed that CPh_3Bn was produced cleanly with only trace amounts of CPh_3H and CPh_3OH present, potentially generated by radical H-atom chemistry from the THF solvent and from a hydrolysis reaction upon aqueous workup of CPh_3Br, respectively. Analysis of the paramagnetic ^{1}H NMR spectra showed that CoCoBr(L) **1** was the major product from the dicobalt benzyl complex **2**. The complex AlCoBr(L) was identified as the sole metal-based product by the similarity of its ^{1}H NMR chemical shifts to those of AlCoCl(L) **3** (Scheme 3.4).

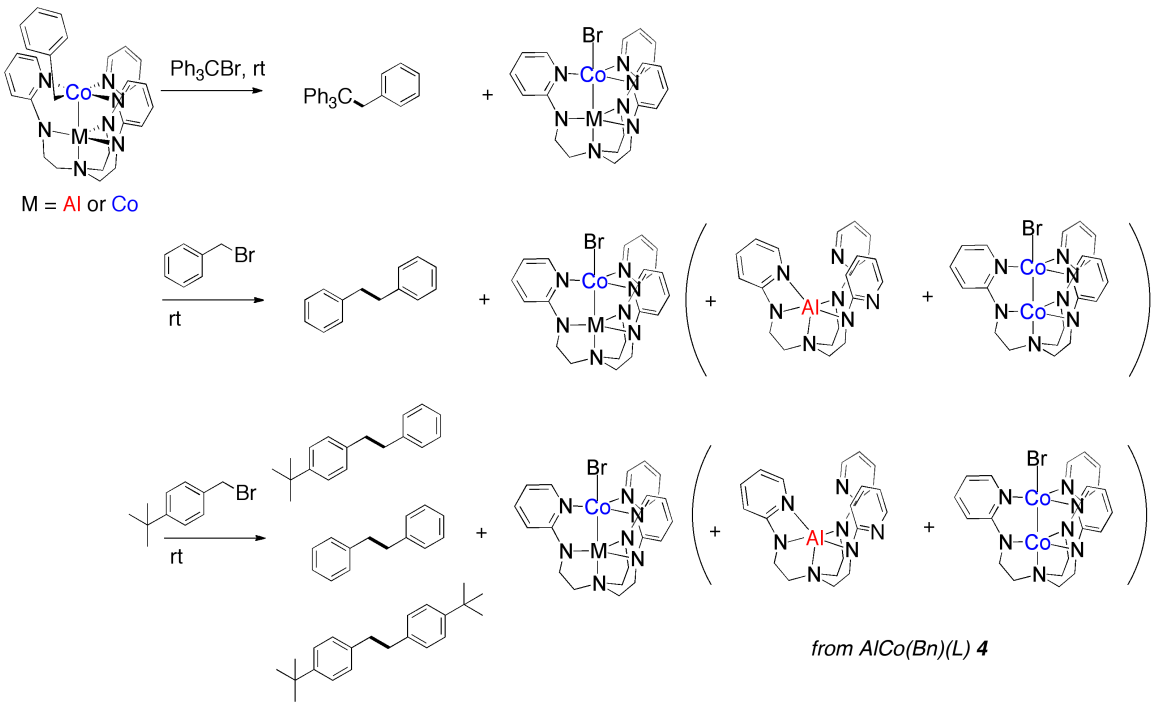

Scheme 3.4. Reactivity of CoCo(Bn)(L) **2** and AlCo(Bn)(L) **4** with trityl bromide, benzyl bromide, and (4-*tert*-butyl)benzyl bromide.

Next, we moved to RX reagents less prone to reduction. Addition of benzyl bromide to both **2** and **4** at room temperature gave bibenzyl as the major organic product (Scheme 3.4). However, when 4-(*tert*-butyl)benzyl bromide was used instead, a mixture of the cross-coupled product 1-(4-(*tert*-butyl)phenyl)-2-phenylethane as well as the homocoupled products bibenzyl and bi(4-(*tert*-butyl))benzyl was identified. As with CPh_3Br, CoCoBr(L) **1** was identified in the paramagnetic ^1H NMR spectrum from the reaction of either benzyl bromide reagent with **2**. However, the reaction of **4** with either benzyl bromide reagent gave a mixture of metal-based products unlike with CPh_3Br. In addition to AlCoBr(L), **1** and Al(L) were observed in the ^1H NMR spectra. Presumably, a demetallation/redistribution process occurred.

Looking for more challenging substrates, we targeted RX reagents that are less

prone to one-electron chemistry. MeI was chosen as a substrate that is known to react in an S_N2 fashion with cobalt(I), especially in the context of vitamin B_{12} reactivity and models thereof.[153-156] Adding MeI to CoCo(Bn)(L) **2** in a J Young NMR tube in C_6D_6 produced no color change after standing for 15 minutes, and ^{1}H NMR spectroscopy confirmed that no reaction occurred. The reaction was then heated to 60°C; a mixture of CoCoI(L) and CoCo(L) had been generated along with unreacted **2** after 90 minutes. Continued heating of the reaction overnight resulted in the total consumption of **2** as well as CoCo(L). The only metal-based product that could be identified by NMR spectroscopy was CoCoI(L). The diamagnetic region showed that bibenzyl was the major product, along with some toluene and ethane, in a ratio of 1:0.20:0.16, respectively (Scheme 3.5). The amount of ethane is underestimated since it is a gas; undetected quantities are in the headspace of the J Young tube. The complex CoCo(Bn)(L) **2** slowly decomposes when heated to 80°C for several days in C_6D_6 without a substrate; the paramagnetic ^{1}H NMR spectrum of this reaction has a clean-looking set of new peaks along with **2** (Figure A2.59), and the diamagnetic ^{1}H NMR spectrum has a 0.74:1.00 ratio of bibenzyl to toluene. The paramagnetic product in this latter decomposition reaction has not been observed in any of the reactions of **2** with substrates, and the bibenzyl to toluene ratio is significantly lower than what is seen when **2** is exposed to MeI, the latter suggesting that H-atom abstraction may be enhanced in the substrate-free decomposition of **2**.

In contrast, the reaction of MeI with **4** in C_6D_6 proceeded rapidly at room temperature. A mixture of AlCoI(L), Al(L), and CoCo(L) was identified by ^{1}H NMR spectroscopy. This metal scrambling is similar to that observed in the benzyl bromide

reactivity, with the difference that CoCo(L) instead of CoCoX(L) was identified (Scheme 3.5). Bibenzyl and ethylbenzene were observed in the *in situ* reaction mixture. Vacuum transfer of the volatiles showed the ethylbenzene quartet at 2.45 ppm and triplet at 1.08 ppm,[157] as well as ethane and toluene (the methyl resonance of the latter had been obscured in the *in situ* reaction mixture by a peak due to Al(L)).

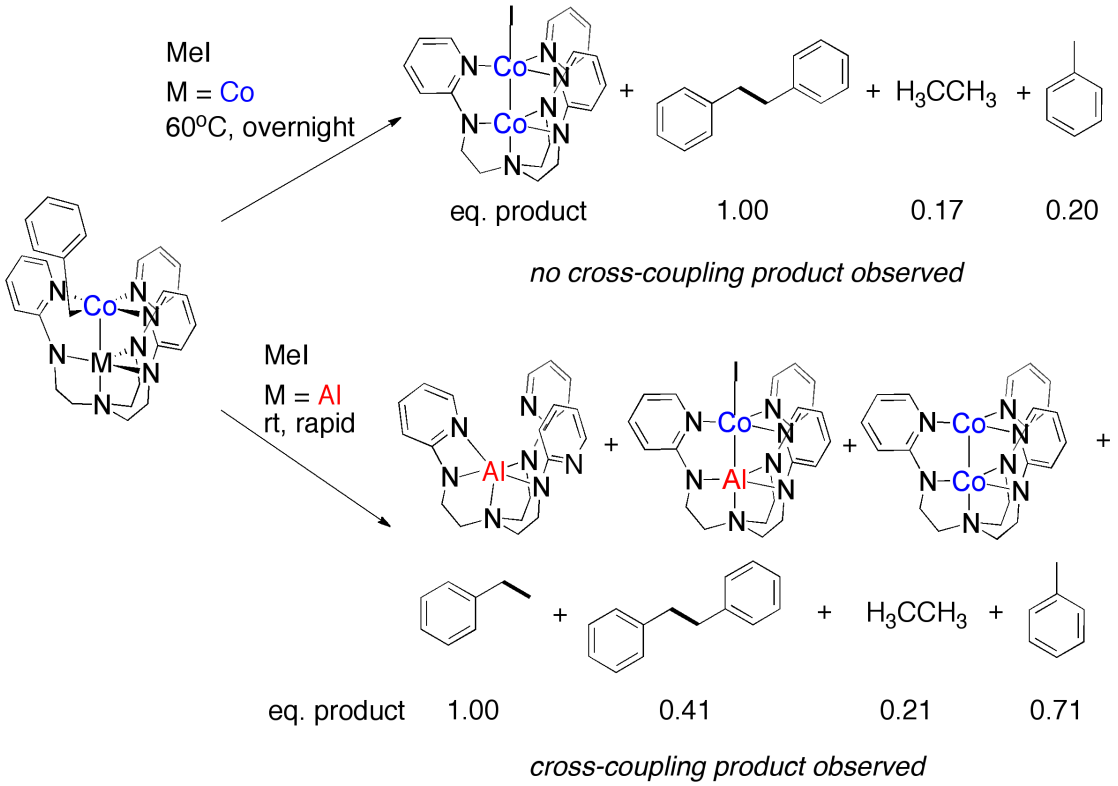

Scheme 3.5. Reactivity of **2** and **4** towards MeI. The most concentrated organic product by ^{1}H NMR spectroscopy was normalized to be 1 equivalent.

We wanted to investigate the possibility of cross coupling with aryl halides, as these are substrates that undergo concerted oxidative addition in metal-mediated cross coupling reactions.[158] Addition of PhI to **2** in C_6D_6, as was seen in the case of MeI, did not give a discernable reaction at room temperature after 15 minutes. Heating the reaction at 60°C for 90 minutes showed that some CoCoI(L) had been generated, but much of the

starting material **2** remained. The aliphatic region of the diamagnetic NMR showed that a very small amount of bibenzyl and toluene had been generated. After overnight heating, practically all of the starting material had been consumed, leaving CoCoI(L) as the major metal-based product. GC-MS analysis revealed the presence of toluene, biphenyl, diphenylmethane, and bibenzyl, along with a small amount of stilbene (Scheme 3.6).

Similar observations of the reaction of PhI with **4** were made as in the case of MeI. An NMR spectrum taken an hour after the addition of PhI to **4** showed that all the starting material had been consumed. However, the metal-based products were somewhat different than in the case of MeI: only AlCoI(L) and Al(L) were seen, with very little to no dicobalt products observed (Scheme 3.6). The GC-MS analysis, like for the reaction with **2**, showed that a mixture of the cross-coupled diphenylmethane was present, along with toluene, biphenyl, and bibenzyl. Conducting the reaction of PhBr with **4**, it was found that the reaction was slower than with PhI, as unreacted **4** was present nearly 4 hours after addition, along with AlCoBr(L) and Al(L). A difference from the PhI reaction was that a noticeable amount of **2** was also observed in the paramagnetic ^{1}H NMR spectrum.

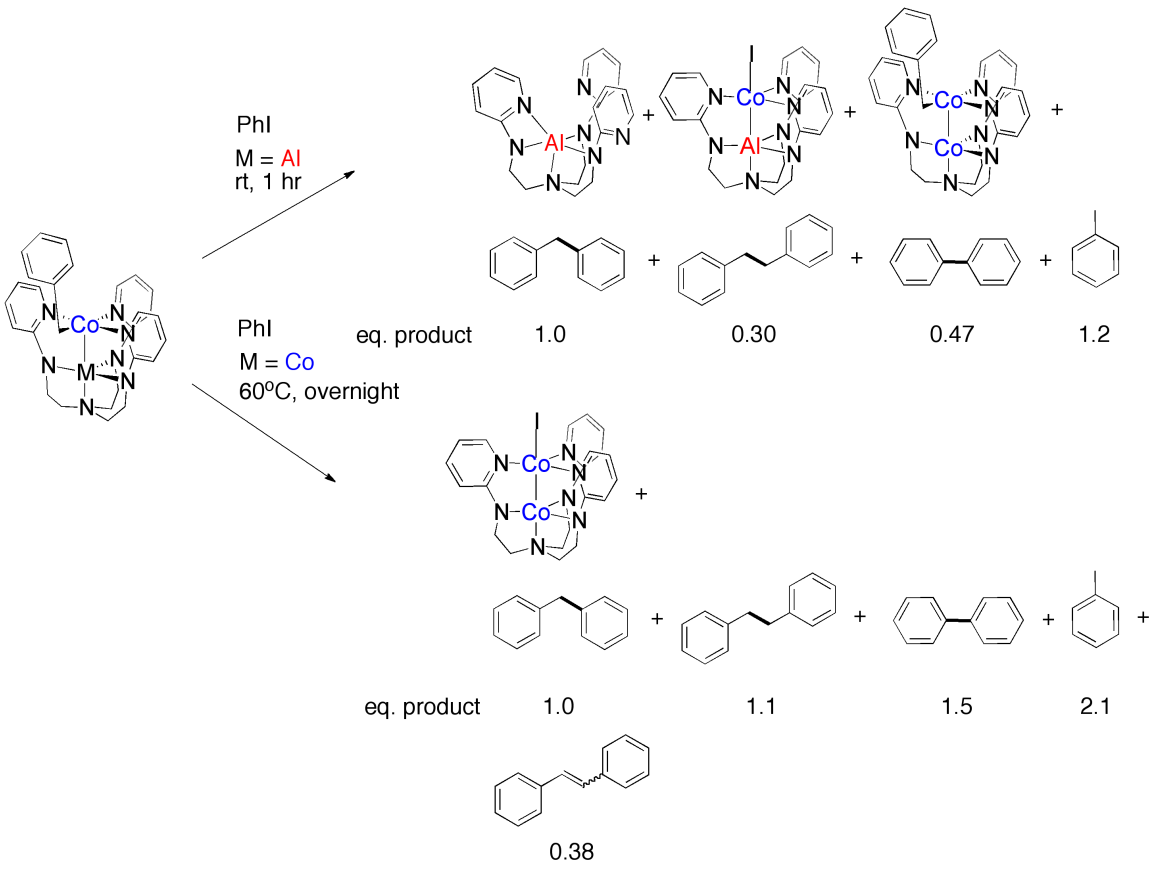

Scheme 3.6. Reactivity of **2** and **4** with PhI.

To further investigate radical reactivity of CoCo(Bn)(L) **2**, we chose the stable free radical TEMPO (TEMPO = (2,2,6,6-tetramethylpiperidin-1-yl)oxy) as a probe thereof. Addition of one equivalent of TEMPO to **2** in toluene at dry ice/acetone temperatures with slow warming overnight resulted in the generation of a diamagnetic product, identified as TEMPO-Bn by comparison of its ^{1}H NMR shifts to those in the literature,[159] as well as a new paramagnetic product. A significant amount of **2** was also observed in the NMR spectrum. In a separate reaction, addition of two equivalents of TEMPO rather than one resulted in full consumption of **2**. The paramagnetic product was crystallized

and identified as CoCo(TEMPO)(L) **9** (Table 3.4, Scheme 3.7). In principle, a minimum of one equivalent of TEMPO could have scavenged benzyl to provide CoCo(L), but CoCo(L) was not observed as a product by NMR. One can infer that the rate of the formation of TEMPO-Bn in this reaction is slow relative to the trapping of CoCo(L) with TEMPO. The N-O bond length of 1.438(4) Å and the Co-O bond length of 1.936(3) Å are both consistent with a one-electron reduced, closed-shell TEMPO anionic ligand (the N-O bond length in **9** is elongated compared to the value found in the crystal structure of TEMPO, 1.2849(14) Å, consistent with addition of an electron to the N-O π* orbital).[160] Hence, the charge balance requires that the dicobalt core is in the +4 oxidation state.

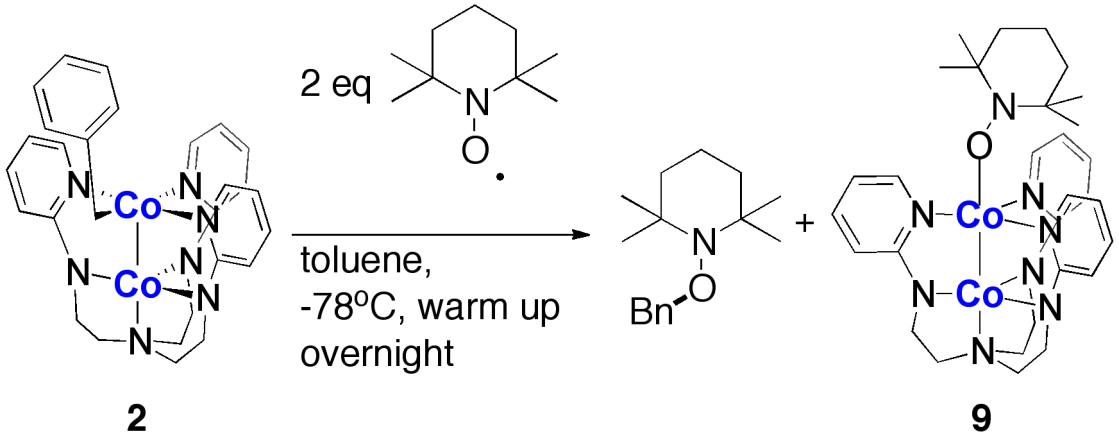

2 **9**

Scheme 3.7. The formation of CoCo(TEMPO)(L) **9** from addition of TEMPO to **2**.

Insertion of unsaturated bonds into the Co-C bond was investigated with **2**. Addition of one equivalent of benzophenone to **2** in THF with heating to 60ºC overnight resulted in a major paramagnetic product identified in the ^{1}H NMR spectrum along with some decomposition. The major product was produced cleanly *via* the addition of one equivalent of BnK to benzophenone in THF, which was then added to **1**. An X-ray crystal structure of this product established it as an alkoxide product CoCo(OCPh$_2$Bn)(L) **10**

(Scheme 3.8 and Table 3.4). The Co-O bond length is 1.920(2) Å, similar to that of **9**, which is expected given that both compounds have axial, anionic O-donating ligands. The Co-Co bond length in **10** is 2.5482(6) Å, which represents an intermediate value between CoCoCl and **9**.

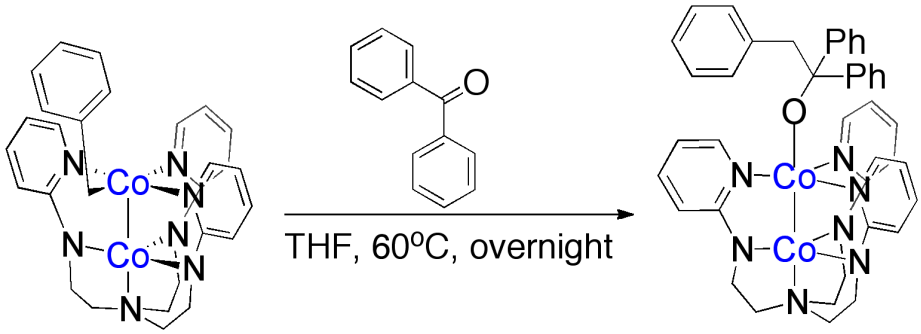

2 **10**

Scheme 3.8. Insertion of benzophenone into the Co-Bn bond of **2**.

We wished to attempt this reactivity on a ketone with two alkyl groups, as the insertion chemistry should also be possible with a dialkyl ketone. Heating **2** in C_6D_6 in the presence of acetone at 70°C over three days lead to the formation of a major paramagnetic product in the ^{1}H NMR spectrum, toluene, and unidentified paramagnetic decomposition with numerous peaks. An X-ray crystal structure of the major product was obtained. Instead of the desired C-C bond formation as observed in **10**, an enolate $^-$OC(Me)=CH_2 ligand was obtained in CoCo(OC(Me)=CH_2)(L) **12** (Table 3.4, Scheme 3.9). Formally, this corresponds to a deprotonation of acetone, which explains the formation of toluene as a major species in the diamagnetic ^{1}H NMR spectrum. The bond metrics are consistent with the enolate formulation: Two different C-C bond lengths are observed in the enolate ligand (1.336(7) and 1.490(7) Å) along with a C-O bond length of 1.293(6) Å, and the sum of the bond angles around the central C is 360°. Several lines of

evidence favor the O-bound rather than the C-bound isomer: the ligand is bound in the apical position of the pyridyl-ligated cobalt, like **9** and **10**, both of which have O-bound ligands, and unlike the C-bound compound **2**. The two vinylic hydrogen atoms were observed in the difference map. Also, a crystal structure solution was attempted by switching the methylene group and O atom. The resulting solution had an unreasonably small thermal ellipsoid for the Co-bound methylene C and an unreasonably large thermal ellipsoid for the distal O. Hence, the O-bound enolate isomer appears to be the correct one. Based on a Cambridge Structural Database (CSD) search, **12** represents the first crystal structure of the O-bound enolate ligand derived from acetone bound to a transition metal. Several C-bound Co-acetonyl compounds have been reported in the literature, all formally cobalt(III) compounds supported by ligands with planar tetradentate donor sets at each cobalt such as salen^{2-} derivatives or porphyrinates.[161-165]

There are several examples in the literature of formation of a metal-alkoxide adduct M-OCPh$_2$Bn from a M-Bn species and benzophenone. Examples of benzophenone insertion into a Group IV or yttrium-benzyl bond are known.[166,167] In uranium chemistry, benzophenone is known to coordinate as ketyl radical as in the species ((^{tBu}ArO)$_3$tacn)U(OC(4-*t*BuC$_6$H$_4$)$_2$) (^{tBu}ArO)$_3$tacn = 1,4,7-tris(3,5-di-*tert*-butyl-2-hydroxybenzyl))-1,4,7-triazacyclononane dianion),[168] and generation of Tp*U(OCPh$_2$Bn)(Bn)$_2$ from the addition of benzophenone to Tp*U(Bn)$_2$(THF) was proposed to occur by attack of benzyl radical on an intermediate Tp*U(Bn)$_2$(OCPh$_2$) with a ketyl radical ligand.[169] The uranium example is facilitated by the uranium(III/IV) redox couple to reduce benzophenone to ketyl radical in the coordination sphere. The oxidation

potential of **2**, -0.86 V vs. Fc/Fc^+, is not reducing enough to generate ketyl radical from benzophenone (-2.30 V vs. Fc/Fc^+).[170] However, a process in which the Co-Bn bond is homolyzed to generate CoCo(L) and benzyl radical, followed by attack of benzyl radical on benzophenone and recombination with CoCo(L), is more likely.

We think a similar process occurs when the substrate is acetone rather than benzophenone; however, in this case, the C-H bond succumbs to the radical chemistry. While the C-H bond dissociation energy of toluene (89.8 ± 0.06 kcal/mol[150]) is somewhat less than that of acetone (94[171] or 92 ± 2 [172] kcal/mol, depending on the reference), which one might think would mean H-atom abstraction from acetone by benzyl radical would be unfavorable, the generation of the Co-O bond is also important and likely contributes to the formation of the enolate product.

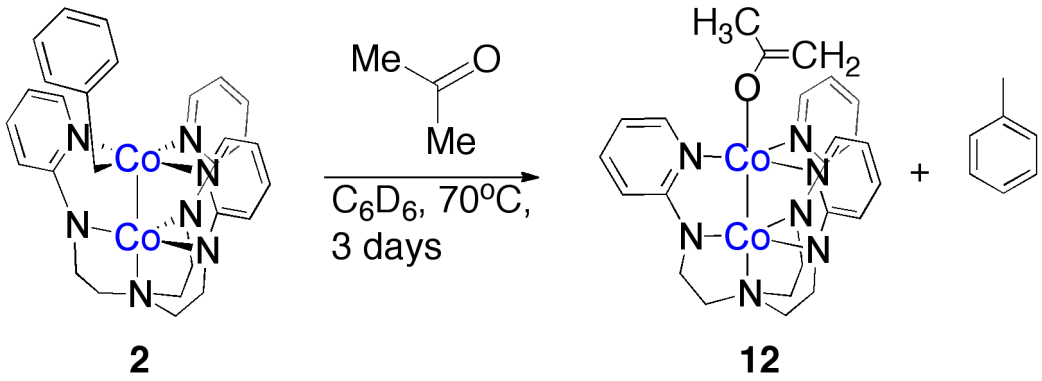

2 **12**

Scheme 3.9. Formation of the cobalt-bound enolate **12** from acetone and **2**.

Formation of a N-C bond with **2** was attempted *via* the addition of one equivalent of *N*-bromosuccinimide (NBS). However, it was established that the proper stoichiometry of the reaction was 0.5 equivalents of NBS per **2**, and that the major products by ^1H NMR spectroscopy were bibenzyl, **1**, and a diamagnetic product established as CoCo(Su)(L) **11** (Su = succinimide anion) (Scheme 3.10, Table 3.4). A small amount of toluene was also

identified in the NMR spectrum. An X-ray crystal structure of **11** showed that both cobalt centers are tetragonal, with a bridging succinimide anion. The N donor of succinimide bonds to the pyridine-ligated cobalt, whereas one of the two O atom bonds to the amide-ligated cobalt. The short Co_{py}-N_{su} bond of 1.905(3) Å and the long Co_{am}-O_{su} bond of 2.038(2) Å are most consistent with the anionic charge localized on the N atom. This is also reasonable given that the N donor binds to the pyridine-ligated cobalt, which has three neutral pyridine donors, and that the O donor binds to the amide-ligated cobalt, which has three anionic amide donors. The Co-Co bond of **11** is short at 2.2764(7) Å, which is an *r* value of 0.98, which is consistent with a cobalt-cobalt single bond, and is similar to other tetragonal lantern $(CoCo)^{4+}$ literature examples with formal single bonds.[25,26,173,174]

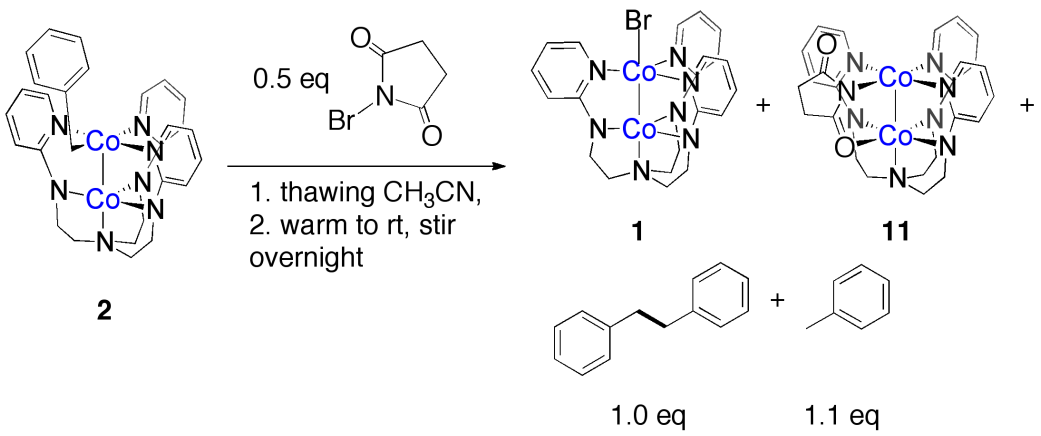

Scheme 3.10. The reaction of *N*-bromosuccinimide with CoCo(Bn)(L) **2**.

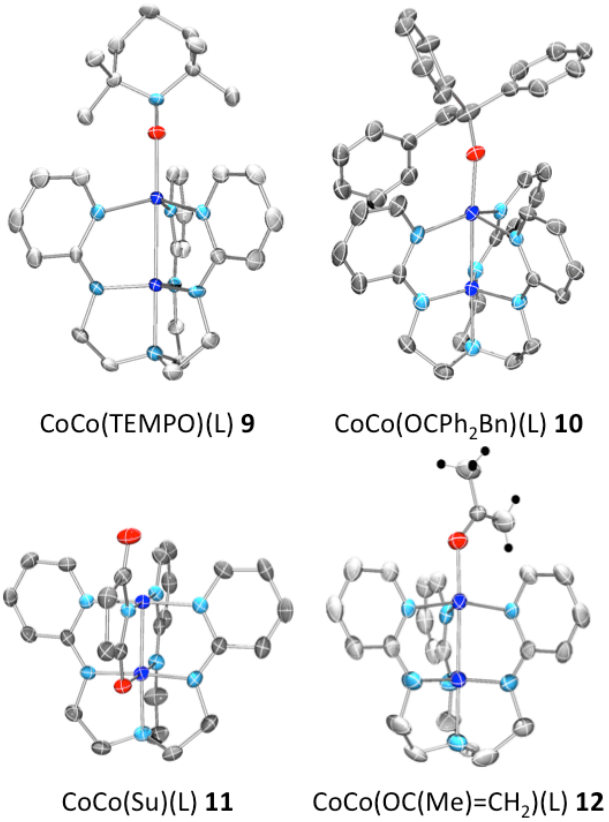

Figure 3.14. Crystal structures of reactivity products CoCo(TEMPO)(L) **9**, CoCo($OCPh_2Bn$)(L) **10**, CoCo(Su)(L) **11**, and CoCo($OC(Me)=CH_2$)(L) **12**.

Table 3.4. Geometrical parameters, including bond lengths and angles, for compounds **9** – **12**.[a]

	CoCo(TEMPO)(L) **9**	CoCo($OCPh_2Bn$)(L) **10**	CoCo(Su)(L) **11**	CoCo($OC(Me)=CH_2$)(L) **12**
Co-Co (Å)	2.5685(8)	2.5482(6)	2.2764(7)	2.5046(8)
r[b]	1.11	1.10	0.98	1.08
Co-N_{ap} (Å)	2.022(3)	2.032(2)	1.978(3)	2.016(4)
Co-N_{eq} (Å)[c]	1.888 ± 0.008	1.899 ± 0.010	1.883 ± 0.015	1.884 ± 0.010
Co-X (Å)	1.936(3)	1.920(2)	1.905(3)	1.946(3)
Co-N_{py} (Å)[c]	2.088 ± 0.007	2.086 ± 0.006	1.936 ± 0.024	2.065 ± 0.010
Co-Co-X (°)	173.98(9)	176.09(7)	87.90(9)	176.76(10)
Co_{am}-O	-	-	2.038(2)	-

[a] Estimated standard deviations (esd) are provided in parentheses. [b] r = ratio of M_1–Co bond distance to the sum of M_1 and Co single-bond radii. [c] M_1–N_{eq} and Co–N_{py} bond lengths are reported as averages ± standard deviations. [d] CoCo(Bn)(L) **2** and AlCo(Bn)(L) **4** each have two independent molecules in the asymmetric unit; hence, all values are given as averages ± standard deviations.

3.5 Reactivity Discussion

The scrambling of the *tert*-butyl group upon the addition of 4-(tert-butyl)benzyl bromide to either CoCo(Bn)(L) **2** or AlCo(Bn)(L) **4** to give both the cross-coupled product as well as the homocoupled products bibenzyl and bi(4-*tert*-butyl)benzyl suggests that this chemistry occurs by one-electron steps. In this vein, addition of one equivalent of $FcPF_6$ to **2** affords ferrocene, [CoCo(L)](PF_6) **7** and bibenzyl as the major organic product, along with a small amount of toluene. Hence, the one-electron oxidized $[CoCo(Bn)(L)]^+$ **2+** core is unstable and decomposes *via* ejection of benzyl radical. This has also been demonstrated by cyclic voltammetry, in which an irreversible one-electron oxidation of **2** was observed at -0.86 V (vs. Fc/Fc^+) at all scan speeds sampled (from 0.01

V/s to 2.0 V/s, *vide infra*). The reactivity exhibited by CoCo(Bn)(L) **2** and AlCo(Bn)(L) **4** towards CPh_3Br, benzyl bromide, and 4-(*tert*-butyl)benzyl bromide is not surprising in light of comparisons to the literature. Fryzuk observed that addition of benzyl chloride to the cobalt(II) organometallic $(P^{Ph}_2NP^{Ph}_2)Co(Me)$ ($P^{Ph}_2NP^{Ph}_2 = N(SiMe_2CH_2PPh_2)_2)^-$) afforded bibenzyl and $(P^{Ph}_2NP^{Ph}_2)CoCl$.[175] In this system, the proposed mechanism was a one-electron oxidation of the metal center to give benzyl radical and the cobalt(III) intermediate $(P^{Ph}_2NP^{Ph}_2)CoCl(Me)$, which was unstable and decomposed by ejecting methyl radical to ultimately provide $(P^{Ph}_2NP^{Ph}_2)CoCl$. Caulton found that the naked cobalt(I) compound $(P^{tBu}_2NP^{tBu}_2)Co$ ($P^{tBu}_2NP^{tBu}_2 = N(SiMe_2CH_2P^tBu_2)_2)^-$) rapidly reacted with benzyl chloride to give $(P^{tBu}_2NP^{tBu}_2)CoCl$ as well as bibenzyl, also a one-electron oxidation (this time to a stable cobalt product).[176]

Unlike the benzyl halide substrates, which reacted at room temperature with both CoCo(Bn)(L) **2** and AlCo(Bn)(L) **4**, PhI and MeI reacted at room temperature with **4** but not with **2**. To observe reactivity with **2**, heating was required. The one-electron reduction potentials of PhI and MeI, $E_{p,c}$, are -2.69 V and -2.72 V vs. Fc/Fc^+ in DMF, respectively.[177,178] For **2**, with a one-electron oxidation potential of -0.86 V vs. Fc/Fc^+ in THF, this difference of ~1.8 V is far too large to consider an outer-sphere one-electron oxidation from **2** to RI relevant. An inner-sphere oxidation, perhaps through a transition state with halogen coordination, could be relevant: for the reaction of PhBr with $(DIMPY)Co(N_2)$ (DIMPY = $2,6\text{-}((2,6\text{-}Me_2C_6H_3)N{=}C(Me))_2C_5H_3N$) to give (DIMPY)CoBr and (DIMPY)Co(Ph), a transition state with the bromine atom of PhBr coordinating to cobalt was identified using DFT calculations.[179] Exposure of Caulton's

($P^{tBu}_2NP^{tBu}_2$)Co to PhI gave a rapid reaction to afford ($P^{tBu}_2NP^{tBu}_2$)CoI; the organic products were not disclosed.[176,180] Hence, the ultimate product in this case is a one-electron oxidation at cobalt.

While a mixture of cross-coupled and homocoupled products was seen for the reaction of PhI with either **2** or **4**, this was not the case for MeI. Only the homocoupled products bibenzyl and ethane were observed by ^{1}H NMR, along with toluene, as products of the reaction of MeI with **2**. None of the cross-coupled product, ethylbenzene, was present. This is in contrast to the reaction of MeI with **4**, in which bibenzyl, ethane, toluene, and ethylbenzene were present. We propose that the difference in the reaction outcomes is due to a difference in mechanism. The reaction with **2** likely proceeds by one-electron chemistry, generating a benzyl radical and CoCo(L). MeI then slowly reacts with CoCo(L) with heat to give the one-electron oxidized product CoCoI and methyl radical, which dimerizes to make ethane.

One-electron chemistry of MeI has been proposed for PNP pincer-supported cobalt(I) compounds.[147,175] For example, Chirik found that addition of 2 equivalents of MeI to 3 equivalents of (^{iPr}PNP)Co(Me) (^{iPr}PNP = 2,6-($CH_2P^iPr_2$)$_2C_5H_3N$) gave two equivalents of (^{iPr}PNP)Co(Me)(I) as well as one equivalent of (^{iPr}PNP)Co(Me)$_3$.[147] They proposed that the reaction happens initially by iodine atom abstraction from MeI, followed by addition of two methyl radicals to a second molecule of (^{iPr}PNP)Co(Me). Fryzuk also observed radical chemistry with MeI.[175] When MeI was added to ($P^{Ph}_2NP^{Ph}_2$)Co(Me), ($P^{Ph}_2NP^{Ph}_2$)CoI was produced as well as two equivalents of methane and one equivalent of bibenzyl. It is thought that, analogously to the Chirik chemistry,

iodine atom abstraction of MeI by cobalt was the first step, yielding a cobalt(III) intermediate ($P^{Ph}_2NP^{Ph}_2$)Co(Me)(I) as well as a methyl radical, which then abstracted a hydrogen atom from toluene solvent. The ($P^{Ph}_2NP^{Ph}_2$)Co(Me)(I) intermediate, as mentioned earlier, can decompose by loss of methyl radical, which also abstracts a hydrogen atom from toluene. The bibenzyl is formed by recombination of two benzyl radicals. Milstein and coworkers, using an excess of MeI with (^{tBu}PNP)Co(Me) (^{tBu}PNP = 2,6-($CH_2P^tBu_2$)C_5H_3N), observed oxidation to [(^{tBu}PNP)Co(Me)]I.[181] Other examples of net one-electron oxidation of cobalt by MeI include that of the zirconium-cobalt bimetallic [{ClZr(^{i}PrNPPh$_2$)$_3$Co(N_2)}$_2$(μ-Na(THF)$_4$)][Na(THF)$_6$] to yield ClZr(^{i}PrNPPh$_2$)$_3$CoI[55] and that of (P_2N_2)Co (P_2N_2 = ^{t}BuNSiMe$_2$N($C_2H_4P^iPr_2$)$_2$ to give (P_2N_2)CoI.[182] Interestingly, the diiminopyridine-supported compound (DIMPY)Co(CH_2SiMe_3) reacted with MeI to give $EtSiMe_3$ as the only observed product, despite the radical nature of most of the other RX chemistry with the (DIMPY)CoR' family of compounds.[179,183]

In the case of the reaction of MeI with AlCo(Bn)(L) **4**, we believe that oxidative addition is the first step in the reaction (Scheme 3.11). As mentioned before, two-electron chemistry of MeI with cobalt(I) compounds is known for Vitamin B_{12} and related compounds.[153-156] Oxidative addition of MeI has been observed with the zirconium-cobalt bimetallic complex (THF)Zr(MesNP^{i}Pr$_2$)$_3$Co(N_2) to afford (η^2-MesNP^{i}Pr$_2$)Zr(MesNP^{i}Pr$_2$)$_2$(μ-CH_3)CoI. Because only one coordination site is available in **4**, the cobalt(III) intermediate could either deligate a pyridyl substituent from the ligand to accommodate both methyl and iodide ligands, or the iodide may remain outside

of the coordination sphere. The next step could either be reductive elimination from cobalt(III) to produce the observed ethylbenzene, or ejection of benzyl or methyl radical as Fryzuk had observed in ($P^{Ph}_2NP^{Ph}_2$)CoCl(Me),[175] which would give the observed homocoupled products. The observation of CoCoI(L) and Al(L) as products could be due to downstream cobalt(II) intermediates following Co-C bond homolysis: the addition of $CoCl_2$ to Al(L) produces a significant amount of CoCoCl(L), as observed by ^{1}H NMR spectroscopy. These processes evidently occur competitively given the distribution of products observed.

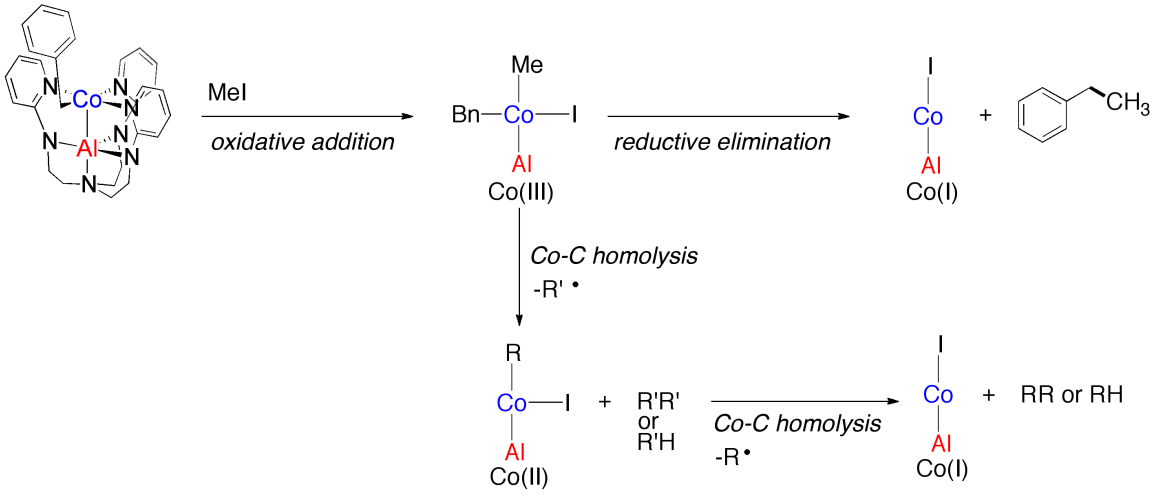

Scheme 3.11. Proposal of the mechanism of the reaction of MeI with **4**.

That raises the question of why **2** does not oxidatively add MeI. We believe that the electronic structure of **2** plays a fundamental role. From magnetic susceptibility data, it is clear that **2** has an $S = 1$ ground state. This can arise from either dative bonding of $S = 0$ cobalt(I) to $S = 1$ cobalt(III) or antiferromagnetic coupling between $S = ½$ cobalt(II) and $S = 3/2$ cobalt(II) (Figure 3.9). We believe the latter model better represents the true bonding picture due to the reactivity of MeI with **2**. In the antiferromagnetic coupling

model, only one electron populates the d_{z2} orbital, and so oxidative addition of MeI is not possible. Instead, the first step is homolysis of the Co-Bn bond to give bibenzyl and the naked species **8**, which then slowly reacts with MeI by an iodine abstraction mechanism to generate CoCoI(L) and methyl radical, which finally dimerizes to produce the observed ethane.

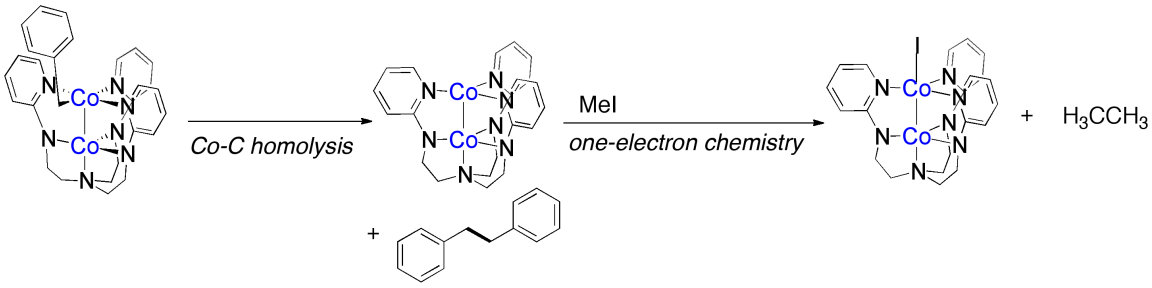

Scheme 3.12. Proposed reactivity of CoCo(Bn)(L) **2** with MeI under heating.

The reactivity of PhX with MCo(Bn)(L) (X = I for **2** and **4**, X = Br for **4**), while showing a similar dependence on temperature as that of MeI depending on the identity of the supporting metal, gives a mixture of cross-coupled and homocoupled products for both Co(Bn) bimetallics, unlike MeI. While oxidative addition of Ar-X to cobalt(I) has been proposed in a number of cobalt-mediated Ar-C bond forming catalyses[140,184-193] and a Ar-N bond forming catalysis,[194] Caulton's naked cobalt(I) compound ($P^{tBu}_2NP^{tBu}_2$)Co abstracts halogen radical from PhX (X = Cl or I) to generate ($P^{tBu}_2NP^{tBu}_2$)CoX.[176] Additionally, Budzelaar has observed binuclear oxidative addition of aryl halides to (DIMPY)Co(N_2) to give (DIMPY)CoX and (DIMPY)Co(Ar), a one-electron oxidation of two cobalt molecules; (DIMPY)Co(N_2) has been characterized as an $S = 0$ cobalt(I) center with a DIMPY radical anion.[148,179,183,195] The presence of homocoupled products in our chemistry could be due to downstream radical processes (such as ejection of benzyl

radical) that make a definitive proposal of a mechanism difficult.

The TEMPO reactivity to generate **9** contrasts with recent chemistry from Milstein and Chirik in which TEMPO was added to (^{R}PNP)Co(X) (R = ^{i}Pr, X = Me; R = ^{t}Bu, ^{R}PNP = 2,6-($CH_2P^tBu_2$)C_5H_3N; X = Cl, H, CCPh, or Me).[181,196] While TEMPO reacted rapidly at room temperature with these PNP-supported cobalt compounds, TEMPO-H was generated in all cases. The metal-based products were identified as (^{R}mPNP)Co(X), and X-ray crystallography (R = ^{t}Bu, X = Cl, H) showed that the ^{tBu}PNP ligand lost an H-atom from one of the two methylene groups along with dearomatization of the pyridyl donor to generate ^{tBu}mPNP.[196] The ligand, in these cases, is the source of the radical chemistry. The reaction of TEMPO with **2** to generate TEMPO-Bn and **9** does not appear to have involvement from py_3tren based on the clean formation of TEMPO-Bn.

3.6 Theoretical Studies

To gain a more detailed understanding of the bonding situation in CoCo(Bn)(L) **2**, we performed multi-configurational calculations on a density functional theory (DFT)-optimized structure of **2** and experimental structures of **2**, AlCoCl(L) **3**, AlCo(Bn)(L) **4**, and CoCoCl(L)[145] using the CASSCF method, followed by CASPT2 calculations to recover additional dynamical correlation. For each compound, the active space comprised twelve orbitals, including all ten, valence *3d* orbitals and two additional *4d* orbitals that correlated with the *3d* orbitals. The singlet and triplet state energies of **2** were compared both by DFT (PBE functional) and CASSCF/PT2. Whether the crystal structure geometry was used in the DFT calculations, or the geometry optimized to a singlet or triplet state, the triplet state of **2** was lower in energy, consistent with experiment (SQUID

magnetometry) (Table 3.5). With the CASSCF/PT2 computations, if the crystal structure geometry was used, the singlet state was lower in energy by ~2 kcal/mol, but if the DFT optimized structure was used, the triplet state was lower in energy by ~1 kcal/mol.

Table 3.5. Relative energies of $S = 0$ and $S = 1$ states of CoCo(Bn)(L) **2**[a]

	DFT single point[c]	**DFT Optimized**[b]	**X-Ray CAS/PT2**[d,e]	**DFT-Optimized CAS/PT2**[d]
$S = 0$	17.61	5.76	0.0/0.0	6.28/0.97
$S = 1$	0.0	0.0	1.54/2.91	0.0/0.0

[a] All energies given in kcal/mol. [b] PBE functional used (with TZVP Co, Al, & N and SVP for C & H basis sets). [c] PBE0 functional used on the crystal structure geometry. [d] Active space comprised 14 electrons in 12 orbitals (ANO-RCC-VDZP Co, Al & N and ANO-RCC-MC for C & H basis sets). [e] Geometry used was the DFT-optimized structure.

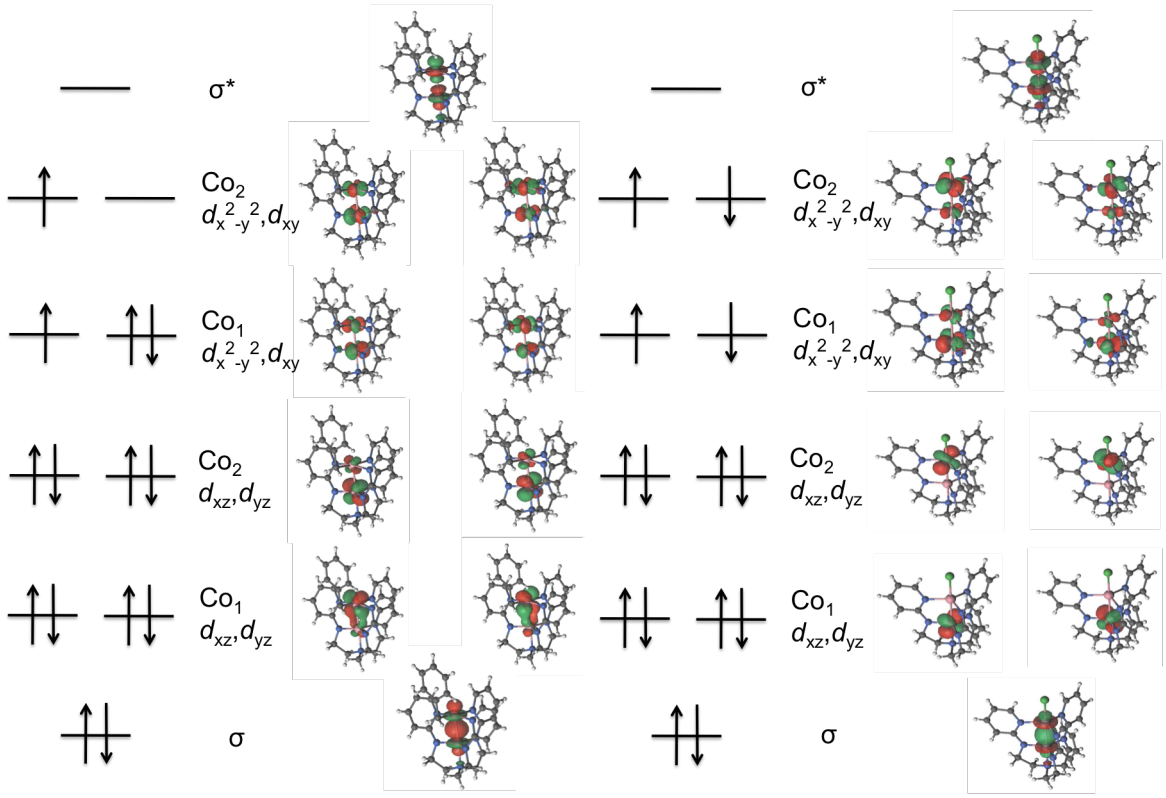

Figure 3.15. Comparison of qualitative MO diagrams of CoCo(Bn)(L) **2** (left) and CoCoCl(L) (right). For **2**, one of four dominant configurations (each ~10%) is shown, while the dominant configuration for CoCoCl(L) (19%) is shown. Co_1 is on the bottom (amide ligated), and Co_2 is on the top (pyridyl ligated).

To determine whether CoCo(Bn)(L) **2** could better be described as Co(II)Co(II) or Co(III)Co(I), comparisons with CoCoCl(L) have been drawn. Figure 3.15 shows the qualitative MO diagrams of **2** and CoCoCl(L). Similarities between the two molecules are apparent; both have σ and σ* overlap, along with some delocalization of the d_{x2-y2}/d_{xy} orbitals between the two cobalts. While both molecules have some delocalization of these δ-symmetry orbitals, the ratio across the two cobalts is 58%/34% polarized for **2**, whereas for CoCoCl(L)L, this ratio is more polarized at 71%/20% for the bonding combination and 85%/15% for the antibonding combination. In addition, CoCoCl(L) has no π/π* overlap, whereas **2** shows minimal overlap with a 90%/10% polarization across the two cobalts, suggesting there is no π bonding in either. The main configuration of CoCoCl(L) is $(\sigma)^2(Co_1\ d_{yz},d_{xz})^4(Co_2\ d_{yz},d_{xz})^4(Co_1\ d_{xy},d_{x2-y2})^2(Co_2\ d_{xy},d_{x2-y2})^2(\sigma^*)^0$, comprising 19% of the total wavefunction, whereas four approximately equal configurations of **2** are present, with two having the configuration $(\sigma)^2(Co_1\ d_{yz},d_{xz})^4(Co_2\ d_{yz},d_{xz})^4(Co_1\ d_{xy},d_{x2-y2})^3(Co_2\ d_{xy},d_{x2-y2})^1(\sigma^*)^0$ and two having the configuration $(\sigma)^2(Co_1\ d_{yz},d_{xz})^4(Co_2\ d_{yz},d_{xz})^4(Co_1\ d_{xy},d_{x2-y2})^1(Co_2\ d_{xy},d_{x2-y2})^3(\sigma^*)^0$, adding up to a total of 38% of the wavefunction. The difference, then, between CoCoCl(L) and **2** lies in the occupation of the d_{xy} and d_{x2-y2} orbitals, as all four of these are singly occupied in the main configuration of CoCoCl(L), while the main configurations of **2** contain two singly-occupied orbitals, one filled orbital, and one empty orbital. This explains the $S = 1$ state of **2**, since the two singly occupied orbitals both have spin-up electrons, whereas the four singly occupied orbitals of CoCoCl(L) have two spin-up electrons and two spin-down electrons to give an $S = 0$ state. This difference is reasonable since the unoccupied orbitals in each of the four main

configurations of **2** are likely of d_{x2-y2} parentage, which has strong Co_2-L antibonding character, whereas the d_{x2-y2} orbitals of CoCoCl(L) lack this strong Co-L antibonding character. The main configurations of both molecules predict a weak interaction, less than a single bond. The sum of all configurations for CoCoCl(L) is $(\sigma)^{1.22}(Co_1\ d_{yz},d_{xz})^{3.98}(Co_2\ d_{yz},d_{xz})^{3.96}(Co_1\ d_{xy},d_{x2-y2})^{2.08}(Co_2\ d_{xy},d_{x2-y2})^{2.00}(\sigma^*)^{0.78}$, leading to an effective bond order (EBO) of 0.22, while for **2**, the sum of all configurations is $(\sigma)^{1.28}(Co_1\ d_{yz},d_{xz})^{3.94}(Co_2\ d_{yz},d_{xz})^{3.92}(Co_1\ d_{xy},d_{x2-y2})^{2.10}(Co_2\ d_{xy},d_{x2-y2})^{2.00}(\sigma^*)^{0.72}$, leading to an EBO of 0.34. The slightly greater EBO of **2** compared to CoCoCl(L) mainly arises from the somewhat greater σ occupation relative to the σ* occupation in **2** compared to CoCoCl(L).

A comparison of Loprop and Mulliken charges of **2** and CoCoCl(L) further supports the Co(II)Co(II) formulation of **2** (Table 3.6). The LoProp charges on CoCoCl(L) and **2** are quite similar, with about 1.3 charges on both cobalts in both molecules. The Mulliken charges show that the benzyl-ligated cobalt of **2** has about 0.25 more charge than CoCoCl(L), while the amide-ligated cobalts of both molecules have about 1.4 charges. The two Co centers in **2** have similar charges using both methods. Overall, the similarity of CoCoCl(L) and **2** by these CAS-computed charges, as well as the even distribution of charge across the two Co centers of **2**, supports the Co(II)Co(II) formulation of **2**.

Table 3.6. CAS-computed charges on CoCoCl(L) and CoCo(Bn)(L) **2**.

Type of charge	CoCoCl(L) (Co_{am}, Co_{py})	CoCo(Bn)(L) **2** (Co_{am}, Co_{py})
LoProp	1.26, 1.32	1.27, 1.29
Mulliken	1.43, 1.17	1.38, 1.42

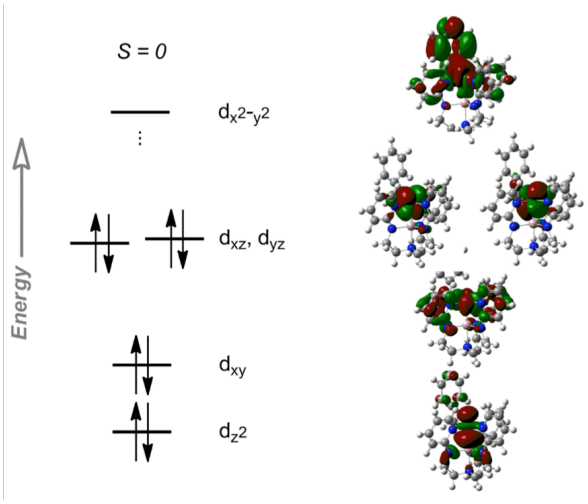

Figure 3.16. DFT orbitals of AlCo(Bn)(L) **4** with an orbital filling diagram.

DFT calculations of AlCo(Bn)(L) **4** using the PBE functional show that the d_{z2} orbital is the lowest in energy (Figure 3.16, Figure 3.8). This is little surprise due to the d_{z2} orbital's stabilizing interaction with the aluminum(III) Lewis acid. CAS calculations for **4** using an active space of 8 electrons in 10 orbitals for the $S = 0$ state paint a similar picture as the DFT calculations, as the occupations are $(d_{xy})^{1.98}(d_{xz},d_{yz})^{3.94}(d_{z2})^{1.91}(d_{x2-y2})^{0.04}$(Al 3*d*/Co 4*d*)$^{0.09}$ (Figure A2.62). The d_{z2} orbital has a slightly lower occupation than the other *d* orbitals, but the Al 3*d*/Co 4*d* orbital, which also has a dative interaction from Co(I) to Al(III) like the d_{z2} orbital, makes up for this difference.

On the other hand, for AlCoCl(L) **3**, DFT calculations show that the d_{xz}/d_{yz} orbitals are lower than the d_{z2} orbital (Figure A2.64). This difference compared to **4** is likely due to the presence of the Cl^- ligand, which is σ-antibonding with respect to the d_{z2} orbital. For the $S = 1$ state of AlCoCl(L) **3** computed with an active space of 8 electrons in 10 orbitals, the CAS occupations are $(d_{xz},d_{yz})^{3.96}(d_{z2})^{1.83}(d_{x2-y2})^{1.00}(d_{xy})^{1.00}$(Al 3*d*/Co 4*d*)$^{0.17}$, which is approximately what is expected based on a qualitative MO diagram (Figure

A2.63, Figure 3.8).

3.7 Conclusions

This study has revealed that the reactivity of MCo(Bn)(py_3tren) (M = Co **2**, Al **4**; R = Bn) organometallic compounds can be modulated by the identity of the supporting metal. The range of reactivity with **2** includes C-C cross-couplings with benzyl halides, insertion of benzophenone into the Co-C bond, scavenging of Bn with TEMPO, and bimolecular addition of *N*-bromosuccinimide. In contrast, PhI and MeI only react with **2** upon heating, but their reactions with **4** are complete within an hour at room temperature. Moreover, the cross-coupling product, ethylbenzene, was not observed in the reaction between MeI and **2**, but was observed in the reaction between MeI and **4**. The differences in reactivity between **2** and **4** are due to different intrametallic interactions in the two compounds. Reactions with **2** likely occur by one-electron processes, which are facilitated by antiferromagnetic coupling between a high-spin cobalt(II) center and a low-spin cobalt(II) center to provide an $S = 1$ ground state. For **4**, $S = 0$ cobalt(I) datively bonds to aluminum(III). This means that **4** can react *via* oxidative addition using its filled *d* orbitals as well as undergo one-electron transformations with substrates like benzyl halides. For **4**, all reactivity occurs at room temperature with various C-X bonds, though the system is prone to metal scrambling, presumably *via* ligand dechelation. Moving forward, raising the energy of the cobalt-based d_{z2} orbital to enhance the nucleophilic reactivity of the bimetallics is a worthy goal. This would be accomplished by the incorporation of a Lewis base rather than a Lewis acid (i.e., aluminum(III)) as the supporting metal.

3.8 Experimental Section

General Considerations

Unless otherwise stated, all manipulations were performed under an N_2 atmosphere inside a glovebox. Standard solvents were deoxygenated by sparging with dinitrogen and dried by passing through activated alumina columns of a SG Water solvent purification system. Benzylpotassium (KBn)[104] and H_3py_3tren[145] were prepared according to literature methods. Deuterated solvents were purchased from Cambridge Isotope Laboratories, Inc., degassed via freeze-pump-thaw cycles, dried over activated alumina, and stored over activated 4 Å molecular sieves. All other reagents were purchased from Aldrich or Strem and used without further purification. Elemental analyses were performed by either Complete Analysis Laboratories, Inc. (Parsippany, NJ) or Robertson Microlit Laboratories (Ledgewood, NJ).

Synthesis of Al(py_3tren). In the glovebox, a 250 mL three-necked round bottom flask was fitted with a glass stopper, a reflux condenser, and, on top of the condenser, a 24/40 gas adapter with a sealable Teflon valve inlet as well as an outlet to a bubbler. Py_3tren (1.44 g, 0.00381 mol) dissolved in 100 mL THF was added to the RBF along with a stir bar. A septum was added to the third neck, and the apparatus was taken out of the glovebox and placed under a flow of N_2. Then, 1.9 mL $AlMe_3$ (2.0 M in hexanes, 0.0038 mol) was added *via* syringe through the septum. The septum was quickly replaced with a closed 24/40 vacuum gas adapter. The reaction was then heated to 65˚C overnight. Upon

cooling, the volatiles were removed *in vacuo* via the vacuum gas adapter to leave a yellow foamy solid. The apparatus was brought back into the glovebox, where the foam was redissolved in THF, transferred to a scintillation vial, and pumped down to a solid. The solid was washed on a frit twice with 3 mL benzene, once with 3 mL hexanes, and pumped down several hours *in vacuo*. This procedure gave Al(py_3tren) as a white solid (1.04 g, 68%). ^{1}H NMR (300 MHz, CD_2Cl_2): δ 8.08 (d, $^3J_{HH}$ = 4.2 Hz, 1H), 7.34 (ddd, $^3J_{HH}$ = 8 Hz, $^3J_{HH}$ = 7 Hz, $^4J_{HH}$ = 2 Hz, 3H), 6.59 (bs, 3H), 6.32 (t, $^3J_{HH}$ = 7 Hz, 3H), 3.37 (t, $^3J_{HH}$ = 6 Hz, 6H), 2.97 (t, $^3J_{HH}$ = 6 Hz, 6H). ^{13}C{^{1}H} NMR (75 MHz, CD_2Cl_2): δ 164.4, 147.0, 138.4, 109.9, 107.5, 50.2, 40.4. UV-Vis-NIR (CH_2Cl_2) λ_{max} (ε, L mol^{-1} cm^{-1}): 305 (11,100). Anal. Calcd for $C_{21}H_{24}N_7Al$: C, 62.83; H, 6.03; N, 24.42. Found: C, 63.00; H, 6.32; N, 24.44.

Synthesis of CoCoBr(py_3tren) 1. K[Co(py_3tren)] (700 mg, 1.48 mmol) was dissolved in 30 mL THF in a 60 mL container. $CoBr_2$ (324 mg, 1.48 mmol) was added as a solid, and the residual material was dissolved in THF and added to the reaction vessel. The vessel was capped, and the reaction was stirred overnight. Then, the volatiles were removed *in vacuo*. The solids were extracted with a total of 80 mL CH_2Cl_2, filtered through Celite, and layered with Et_2O. After a week, crystalline CoCoBr(py_3tren) was collected (613 mg, 72% crystalline yield). ^{1}H NMR (300 MHz, CD_2Cl_2): δ 22.4 (1H), 20.6 (2H, tren-CH_2), 11.4 (1H), 7.9 (1H), 6.8 (1H), -1.8 (2H, tren-CH_2). UV-Vis-NIR (CH_2Cl_2) λ_{max} (ε, L mol^{-1} cm^{-1}): 315 (17,000), 346 sh (10,400), 454 (5,200), 570 (720), 690 (730), 1033 (160), 1666 (90). Anal. Calcd for $C_{21}H_{24}N_7Co_2Br$: C, 44.08; H, 4.23; N, 17.13. Found: C,

44.11; H, 4.18; N, 16.81.

Synthesis of CoCo(Bn)(py$_3$tren) 2. A slurry of CoCoBr(py$_3$tren) **1** (247 mg, 0.432 mmol) in 40 mL THF was cooled in a 60 mL vessel with a dry ice/acetone bath in the glovebox cold well. A 10 mL THF solution of KBn (62.3 mg, 0.478 mmol) was also cooled. The benzylpotassium solution was added to **1** in 6 portions over the course of 70 minutes. The vessel was capped, and the reaction was allowed to warm slowly with stirring overnight. The volatiles were removed *in vacuo*, and then the solids were redissolved in 12 mL benzene, filtered, and layered with pentane. This gave 97.0 mg crystalline **2** (38% yield). ^{1}H NMR (300 MHz, d$_8$-toluene): δ 140, 27.4, 13.9, 6.5, 5.9, 3.9, 1.9, -5.5, -6.2, -36.1. UV-Vis-NIR (THF) λ_{max} (ε, L mol^{-1} cm^{-1}): 306 (26,900), 330 sh (23,100), 384 sh (11,700), 475 sh (3,300), 636 sh (260), 794 (160), 1017 sh (70), 1371 (40). Anal. Calcd for $C_{28}H_{31}N_7Co_2$•0.5C_6H_6: C, 59.81; H, 5.51; N, 15.75. Found: C, 59.28; H, 5.48; N, 15.53.

Synthesis of AlCoCl(py$_3$tren) 3. A slurry of Al(py$_3$tren) (357 mg, 0.902 mmol) in 15 mL THF was added to a 60 mL jar and cooled with a dry ice/acetone bath in the glovebox cold well. A 15 mL THF slurry of CoCl(PPh$_3$)$_3$ (750 mg, 0.851 mmol) was also cooled. Then, the CoCl(PPh$_3$)$_3$ slurry was added to Al(py$_3$tren) with stirring, and the reaction vessel was capped and allowed to warm slowly to room temperature overnight. The reaction turned from a bright green slurry to a yellow slurry once all the CoCl(PPh$_3$)$_3$ was consumed. The yellow precipitate was collected on a frit, washed once with 1 mL THF,

and pumped down *in vacuo*. This afforded AlCoCl(py$_3$tren) as a yellow powder (370 mg, 84% yield). ^{1}H NMR (300 MHz, CD_2Cl_2): δ 118 (1H), 20.8 (1H), 19.2 (1H), 12.1 (2H, tren-CH_2), 8.9 (2H, tren-CH_2), 0.0 (1H). UV-Vis-NIR (CH_2Cl_2) λ_{max} (ε, L mol^{-1} cm^{-1}): 316 (9,700), 327 (9,500), 392 sh (2,200), 777 (100), 823 sh (50), 1537 (340). Anal. Calcd for $C_{21}H_{24}N_7AlCoCl$: C, 50.87; H, 4.88; N, 19.77. Found: C, 51.04; H, 4.99; N, 19.75.

Synthesis of AlCo(Bn)(py$_3$tren) 4. A slurry of AlCoCl(py$_3$tren) **3** (57.4 mg, 0.116 mmol) and a THF solution of KBn (15.9 mg, 0.122 mmol) were cooled with a dry ice/acetone bath in the glovebox cold well. The benzylpotassium solution was added to **3** in two portions over 10 minutes, and then the reaction vial was capped and allowed to warm to room temperature overnight. Then, the volatiles were removed *in vacuo*. The resulting solids were extracted with 8 mL benzene, filtered, and layered with hexanes. This gave 17.8 mg AlCo(Bn)(py$_3$tren) **4** as a crystalline solid (28% crystalline yield). ^{1}H NMR (300 MHz, C_6D_6): δ 8.47 (br, 3H), 7.32 (t, $^3J_{HH}$ = 7 Hz, *m*-$C_6H_5CH_2$, 2H), 7.23 (t, $^3J_{HH}$ = 7 Hz, *p*-$C_6H_5CH_2$, 1H), 6.89 (d, $^3J_{HH}$ = 7 Hz, *o*-$C_6H_5CH_2$, 2H), 6.85 (br, 1H), 5.99 (t, $^3J_{HH}$ = 5 Hz, 3H), 5.71 (br, 3H), 2.95 (br, tren-CH_2, 6H), 2.42 (br, tren-CH_2, 6H), 0.80 (s, $C_6H_5CH_2$, 2H). UV-Vis-NIR (THF) λ_{max} (ε, L mol^{-1} cm^{-1}): 302 (19,900), 468 (9,000), 555 (3,700). Anal. Calcd for $C_{28}H_{31}N_7AlCo \bullet 0.5C_6H_6$: C, 63.05; H, 5.80; N, 16.60. Found: C, 61.82; H, 5.86; N, 16.23.

Synthesis of AlCo(Me)(py$_3$tren) 5. A slurry of AlCoCl(py$_3$tren) **3** (10.1 mg, 0.020 mmol) in THF, as well as a 0.21 M Et_2O solution of MeLi (96 μL, 0.020 mmol) diluted

in THF, were cooled with a dry ice/acetone bath in the glovebox cold well. Then, the MeLi solution was added to **3**. A rapid color change to orange was observed, and the reaction turned deep maroon-red within 25 minutes. After 2.5 hours, no more color change was observed. The reaction was pumped down *in vacuo* after 5.25 hours. The reaction was taken up in benzene, filtered, and layered with pentane. This gave single crystals of AlCo(Me)(py_3tren)•C_6D_6. ^{1}H NMR (300 MHz, d_8-toluene): δ 8.82 (br, 3H), 6.83 (t, J_{HH} = 7.5 Hz, 3H), 6.01 (m, 3H), 5.66 (br, 1H), 2.91 (br, tren-CH_2, 6H), 2.49 (br, tren-CH_2, 6H), -0.81 (bs, 3H, H_3C-Co).

Synthesis of AlCo(Ph)(py_3tren) 6. A slurry of AlCoCl(py_3tren) **3** (108 mg, 0.218 mmol) in THF, as well as a 1.6 M ^{n}Bu_2O solution of PhLi (135 μL, 0.218 mmol) diluted in THF, were cooled with a dry ice/acetone bath in the glovebox cold well. Then, the PhLi solution was added to **3**. A rapid color change to orange was observed, and the reaction turned deep red-orange within 90 minutes. The reaction slowly warmed to room temperature with stirring overnight. The volatiles were pumped down *in vacuo*. The crude was taken up in benzene, filtered, and layered with pentane. This gave 10.0 mg (8.5% yield) of crystalline AlCo(Ph)(py_3tren). ^{1}H NMR (300 MHz, C_6D_6): δ 8.97 (br, 1H), 8.63 (br, 2H), 7.96 (d, $^3J_{HH}$ = 7.5 Hz, *o*-C_6H_5, 2H), 7.05 (t, $^3J_{HH}$ = 7.2 Hz, *m*-C_6H_5, 2H), 6.82 (t, $^3J_{HH}$ = 7.5 Hz, *p*-C_6H_5, 1H), 6.76 (m, 3H), 6.09 (br, 1H), 5.91 (br, 2H), 5.66 (br, 2H), 5.52 (br, 1H), 3.09 (br, tren-CH_2), 2.95 (br, tren-CH_2), 2.61 (br, tren-CH_2), 2.39 (br, tren-CH_2), 2.32 (br, tren-CH_2). Anal. Calcd for $C_{27}H_{29}N_7AlCo$: C, 60.34; H, 5.44; N, 18.24. Found: C, 57.82; H, 5.66; N, 15.27.

Synthesis of [CoCo(py$_3$tren)](PF$_6$) 7. To **1** (99.8 mg, 0.174 mmol) in 16 mL CH_3CN was added solid $TlPF_6$ (60.9 mg, 0.174 mmol). The reaction rapidly turned red. After stirring overnight, a white precipitate was filtered off, and the filtrate was pumped down. The resulting solid was redissolved in 2 mL CH_3CN, filtered, and placed in a -20°C freezer. A powder of [CoCo(py$_3$tren)](PF$_6$) **7** (58.4 mg, 53% yield) was obtained. ^{1}H NMR (300 MHz, CD_3CN): δ 17.0, 14.3, 9.8, 8.0, 6.8, -0.8.

Synthesis of CoCo(py$_3$tren). To [CoCo(py$_3$tren)](PF$_6$) **7** (123 mg, 0.193 mmol) in THF was added KC_8 (27.4 mg, 0.203 mmol) at dry ice/acetone temperatures. After 50 minutes, the reaction was removed from the cold bath. At this time, it looked deep green. After 30 minutes at room temperature, the reaction looked paler green-yellow and was pumped down. The solids were extracted with 7 mL benzene and filtered to give a dark yellow-orange filtrate, and the filtrate was pumped down. This gave 38 mg of CoCo(py$_3$tren) (40% crude yield). ^{1}H NMR (300 MHz, C_6D_6): δ 82, 34, 23, 16, 7.8, 1.8, 0.

Synthesis of CoCo(TEMPO)(py$_3$tren) 9. To CoCo(Bn)(py$_3$tren) **2** (9.3 mg, 0.016 mmol) in toluene at dry ice/acetone temperatures was added a solution of TEMPO (5.0 mg, 0.032 mmol) in toluene. The reaction was stirred overnight with slow warming to room temperature. The reaction was pumped down, redissolved in benzene, and layered with pentane. This afforded single crystals of **9**. ^{1}H NMR (300 MHz, C_6D_6): δ 72.0, 33.1, 28.3, 19.2, 8.8, 7.9, 6.0, 3.5, 2.5, 0.9, -7.9.

Synthesis of CoCo(OCPh$_2$Bn)(py$_3$tren) 10. BnK (19.2 mg, 0.147 mmol) was added to benzophenone (24.4 mg, 0.134 mmol). The reaction turned blue. Then, this solution was added to a slurry of **1** (76.8 mg, 0.134 mmol) in 8 mL THF. The reaction turned dark brown and was stirred overnight. The reaction was filtered through Celite and layered with pentane. This gave 62.7 mg of **10** (61% crystalline yield). Crystals suitable for X-ray crystallography were grown from a benzene solution layered with pentane. ^{1}H NMR (300 MHz, C_6D_6): δ 30.8, 24.3, 15.0, 14.2, 7.9, 7.6, 6.8, 6.2, 6.0, 5.9, 5.6, 2.9, -1.3.

Synthesis of CoCo(Su)(py$_3$tren) 11. CoCo(Bn) **2** (105 mg, 0.180 mmol) was dissolved in 3 mL CH_3CN. Then, succinimide was added (18.0 mg, 0.182 mmol). The reaction was stirred overnight. A green precipitate was filtered off, washed with 2 mL CH_3CN, then dissolved in 5 mL CH_2Cl_2 and pumped down to give 77.0 mg **11** (72% yield). X-ray quality crystals were grown from layering Et_2O on a CH_2Cl_2 solution. ^{1}H NMR (300 MHz, CD_2Cl_2): δ 12.43 (br), 7.62 (br), 7.46 (m), 7.35 (m), 6.00 (m), 2.78 (s, tren-CH_2), 2.50 (s, tren-CH_2).

Synthesis of CoCo(OC(Me)=CH$_2$) 12. Acetone (9.3 μL, 0.134 mmol) was cooled to -20°C. Then, it was added to THF at -20°C, and BnK (19.3 mg, 0.148 mmol) was added. Immediately afterwards, the enolate solution was added to **1** (76.2 mg, 0.133 mmol) and stirred overnight. The reaction was filtered and layered with pentane. This gave 13.7 mg

(19% crystalline yield) of **12** with a minor unidentified impurity. ^{1}H NMR (500 MHz, C_6D_6): δ 25.5, 25.4, 12.7, 7.2, 5.8, 4.3, -1.8, -4.6, -12.0.

Reactivity Studies

General Considerations

Unless otherwise stated, organic products were identified by GC-MS. The compound CoCoI(py_3tren) was identified in the ^{1}H NMR spectra of the RI reactions with MCo(Bn)(py_3tren) by the similarity of the relevant peaks to those of CoCoCl(py_3tren) and CoCoBr(py_3tren) **1**. AlCoX(py_3tren) (X = Br, I) was identified in the ^{1}H NMR spectra of the RX reactions with AlCo(Bn)(py_3tren) by the similarity of the relevant peaks to those of AlCoCl(py_3tren) **3**. CoCo(py_3tren) **8** was identified in the *in situ* reaction mixtures, where applicable, by comparison of the appropriate reaction mixture ^{1}H NMR spectrum to the ^{1}H NMR spectrum resulting from KC_8 addition to CoCo(PF_6)(py_3tren) **7**.

Stoichiometric Additions of RX Reagents to MCo(Bn)(py_3tren)

In a typical reaction, 3.7 μL 4-*t*-butylbenzyl bromide (4.6 mg, 0.020 mmol) was added to an NMR tube with CoCo(Bn)(py_3tren) **2** dissolved in C_6D_6 in the glovebox. A color change was observed within a few minutes. ^{1}H NMR spectra showed that the starting material CoCo(Bn)(py_3tren) was consumed, and CoCoBr(py_3tren) **1** was visible. The reaction was then diluted with diethyl ether and extracted with water. The organic fraction was then dried with $MgSO_4$, filtered through a GC filter, and submitted for GC-

MS analysis. The GC-MS showed the presence of (4-t-butylbenzyl)benzyl, bibenzyl, and bi(4-*t*-butyl)benzyl along with a little unreacted 4-*t*-butylbenzyl bromide.

Stoichiometric Addition of Ph_3CBr to CoCo(Bn)(py_3tren) ***2***

CPh_3Br (6.6 mg, 0.020 mmol) was added to CoCo(Bn)(py_3tren) (11.9 mg, 0.020 mmol) in THF. The reaction rapidly turned green. After overnight stirring, the volatiles were removed *in vacuo*, and a ^1H NMR spectrum of the solids extracted with C_6D_6 revealed the presence of CPh_3Bn as a distinctive singlet at 3.81 ppm. The NMR sample was then diluted with diethyl ether and extracted with water. The organic fraction was then dried with $MgSO_4$, filtered through a GC filter, and submitted for GC-MS analysis. The GC-MS showed the presence of CPh_3Bn along with a very small amount of CPh_3H.

Stoichiometric Addition of Ph_3CBr to AlCo(Bn)(py_3tren) ***4***

CPh_3Br (5.9 mg, 0.018 mmol) was added to CoCo(Bn)(py_3tren) (9.9 mg, 0.018 mmol) in benzene. The reaction rapidly turned light yellow. After stirring for five hours, the volatiles were removed *in vacuo*, and a ^1H NMR spectrum of the solids extracted with C_6D_6 revealed the presence of CPh_3Bn as a distinctive singlet at 3.81 ppm. A second extraction of the solids with CD_2Cl_2 revealed AlCoI(py_3tren) as the dominant paramagnetic product.

Stoichiometric Addition of MeI to CoCo(Bn)(py_3tren) ***2***

1.3 μL MeI (3.0 mg, 0.021 mmol) was added to CoCo(Bn)(py_3tren) **2** dissolved in C_6D_6 in a J Young NMR tube in the glovebox. The J Young was sealed. After 15 minutes at room temperature, ^{1}H NMR spectroscopy revealed that no reaction had occurred. The reaction was heated to 60°C for 90 minutes. The reaction had turned darker from the initial red color. ^{1}H NMR showed the generation of CoCoI(py_3tren), CoCo(py_3tren), toluene, bibenzyl, and ethane. After heating at 60°C overnight, all of the starting material **2** had been consumed, and CoCo(py_3tren) was no longer observed. The other products were still observed.

*Addition of $FcPF_6$ to CoCo(Bn)(py_3tren) **2***

$FcPF_6$ was added to CoCo(Bn)(L) **2** in a scintillation vial in the glovebox. After 50 minutes, the reaction was pumped down. ^{1}H NMR spectra in CD_3CN showed the presence of CoCo(PF_6)(L) **7**, ferrocene, bibenzyl, and a small amount of toluene.

*Addition of benzophenone to CoCo(Bn)(py_3tren) **2***

Benzophenone (4.5 mg, 0.025 mmol) was added to CoCo(Bn)(L) **2** in THF in a scintillation vial at room temperature. The reaction was heated to 50ºC for three hours, and then to 60ºC overnight. After cooling, the reaction was pumped down. The major product was identified as **10** by ^{1}H NMR spectroscopy.

*Addition of N-bromosuccinimide to CoCo(Bn)(py_3tren) **2***

Acetonitrile solutions of NBS (2.4 mg, 0.013 mmol) and **2** (15.7 mg, 0.027 mmol) were cooled in a dry ice/acetone bath in the glovebox cold well. Upon freezing, the solutions were taken out, and NBS was added to **2** with stirring immediately upon thawing. After stirring overnight, the reaction was pumped down, and the crude was taken up in CD_2Cl_2. The major products were identified by ^{1}H NMR spectroscopy as bibenzyl, **1** and **11**.

*Addition of acetone to CoCo(Bn)(py$_3$tren) **2***

Acetone (1.6 μL, 0.022 mmol) was added to **2** (14.5 mg, 0.025 mmol) dissolved in C6D6 in a J Young NMR tube. There was no immediate color change. Heating up to 60°C produced little change in the ^{1}H NMR spectrum. Upon heating to 70°C for one hour, a new set of NMR signals appeared. The reaction was heated overnight at 70°C, checked again by NMR, and then heated until a total of three days reaction time had passed. The NMR tube was brought into the glovebox, the sample was transferred into three 1 mL vials placed in a 20 mL scintillation vial, and hexanes was added in the scintillation vial outside the 1 mL vials. This gave crystals suitable for X-ray diffraction.

X-Ray Crystallographic Data Collection and Refinement of the Structures

Single crystals of Al(py$_3$tren) were grown from layering a THF solution with hexanes. Single crystals of CoCo(Bn)(py$_3$tren) **2** and AlCo(Bn)(py$_3$tren) **4** were grown by layering a toluene solution with pentane. Single crystals of AlCoCl(py$_3$tren) (**3**) and CoCo(Su)(py$_3$tren) **11** were grown from Et_2O layered on a CH_2Cl_2 solution. Single crystals of AlCo(Me)(py$_3$tren) **5**, AlCo(Ph)(py$_3$tren) **6**, CoCo(TEMPO)(py$_3$tren) **9**,

CoCo(OCPh$_2$Bn)(py$_3$tren) **10**, and CoCo(OC(Me)=CH$_2$)(py$_3$tren) **12** were grown from layering a benzene solution with pentane. A yellow block of Al(py$_3$tren) (0.30 x 0.30 x 0.30 mm^3), a red-orange block of **2** (0.20 x 0.10 x 0.10 mm^3), a yellow needle of **3** (0.40 x 0.10 x 0.10 mm^3), a red block of **5** (0.15 x 0.12 x 0.06 mm^3), a brown plate of **9** (0.21 x 0.09 x 0.04 mm^3), an orange block of **10** (0.20 x 0.20 x 0.20 mm^3), a green block of **11** (0.10 x 0.07 x 0.07 mm^3), and a red plate of **12** (0.20 x 0.20 x 0.10 mm^3) were placed on the tip of a glass capillary and mounted on a Bruker APEX II Platform CCD diffractometer for data collection at 173(2) K, and a red block of **4** (0.15 x 0.05 x 0.05 mm^3) and a red block of **6** (0.15 x 0.12 x 0.05 mm^3) were collected at 123(2) K. The data collection was carried out using Mo-Kα radiation (graphite monochromator). The data intensity was corrected for absorption and decay (SADABS). Final cell constants were obtained from least squares fits of all measured reflections. The structure was solved using SHELXS-97 and refined using SHELXL-97. A direct-methods solution was calculated which provided most non-hydrogen atoms from the E-map. Full-matrix least squares / difference Fourier cycles were performed to locate the remaining non-hydrogen atoms. All non-hydrogen atoms were refined with anisotropic displacement parameters. Hydrogen atoms were placed in ideally and refined as riding atoms with relative isotropic displacement parameters. Disorder in the tren CH$_2$ groups bonded to the apical amine was modeled in the structures for **5** (74:26 ratio), **6** (77:23 ratio), and **12** (62:38 ratio). Crystallographic data for **2** − **6** are summarized in Table 2.7, and data for Al(py$_3$tren) and **9** – **12** are summarized in Table 2.8.

Table 3.7. Crystallographic details for compounds **2**-**6**.

	2	**3**	**4**	**5**	**6**
chemical formula	$C_{28}H_{31}N_7Co_2$	$C_{21}H_{24}N_7AlCoCl$	$C_{28}H_{31}N_7AlCo$	$C_{22}H_{27}N_7AlCo \bullet C_6H_6$	$C_{27}H_{29}N_7AlCo \bullet C_6H_6$
formula weight	583.46	495.83	551.51	553.52	615.59
crystal system	monoclinic	monoclinic	monoclinic	triclinic	monoclinic
space group	$P2_1/c$	$P2_1/n$	$P2_1/c$	P-1	$P2_1/c$
a (Å)	18.2085(16)	14.511(2)	18.1166(11)	9.3796(15)	9.6283(7)
b (Å)	14.9126(13)	9.9585(14)	14.7536(9)	10.5780(17)	15.6220(11)
c (Å)	19.1696(17)	15.004(2)	19.2420(12)	14.373(2)	19.7691(14)
α (deg)	90	90	90	78.924(2)	90
β (deg)	93.0670(10)	101.548(2)	93.1950(10)	72.613(2)	90.0670(10)
γ (deg)	90	90	90	81.559(2)	90
V (Å^3)	5197.8(8)	2124.2(5)	5135.1(5)	1329.4(4)	2973.5(4)
Z	8	4	8	2	4
D_{calcd} (g cm^{-3})	1.491	1.550	1.427	1.383	1.375
l (Å), μ (mm^{-1})	0.71073, 1.308	0.71073, 1.000	0.71073, 0.735	0.71073, 0.710	0.71073, 0.643
T (K)	173(2)	173(2)	123(2)	173(2)	123(2)
θ range (deg)	1.12 to 27.51	1.78 to 27.49	1.13 to 27.55	1.50 to 26.37	1.50 to 26.37
reflns collected	54256	22407	58569	14052	23810
unique reflns	11923	4854	11790	5394	6103
data/restraints/ parameters	11923 / 0 / 667	4854 / 0 / 280	11790 / 0 / 667	5394 / 0 / 362	6103 / 0 / 407
R_1, wR_2 ($I > 2\sigma(I)$)	0.0554, 0.1254	0.0368, 0.0740	0.0376, 0.0842	0.0408, 0.0920	0.0454, 0.1046

Table 3.8. Crystallographic details for compounds Al(py_3tren) and **9-12**.

	Al(py_3tren)	**9**	**10**	**11**	**12**
chemical formula	$C_{21}H_{24}N_7Al$	$C_{30}H_{42}N_8Co_2O$	$C_{41}H_{41}N_7Co_2O$	$C_{25}H_{28}N_8Co_2O_2$	$C_{24}H_{29}N_7Co_2O$
formula weight	401.45	648.58	765.67	590.41	549.40
crystal system	monoclinic	monoclinic	triclinic	monoclinic	orthorhombic
space group	$P2_1/n$	$P2_1/c$	P-1	$P2_1/n$	$P2_12_12_1$
a (Å)	8.3699(4)	12.275(2)	8.7935(7)	8.7723(10)	10.1957(7)
b (Å)	10.7774(6)	12.353(2)	13.2721(11)	14.9991(16)	15.1257(10)
c (Å)	22.7215(12)	20.592(4)	15.5042(13)	18.901(2)	15.4593(10)
α (deg)	90	90	93.302(1)	90	90
β (deg)	91.857(1)	101.046(2)	95.717(1)	100.689(1)	90
γ (deg)	90	90	104.383(1)	90	90
V (Å^3)	2048.53(19)	3064.8(9)	1737.7(2)	2443.8(5)	2384.1(3)
Z	4	4	2	4	4
D_{calcd} (g cm^{-3})	1.302	1.406	1.463	1.605	1.531
l (Å), μ (mm^{-1})	0.71073, 0.122	0.71073, 1.120	0.71073, 1.000	0.71073, 1.399	0.71073, 1.423
T (K)	173(2)	173(2)	173(2)	173(2)	173(2)
θ range (deg)	2.09 to 27.55	1.69 to 27.51	1.32 to 27.48	1.75 to 27.49	1.88 to 26.38
reflns collected	23418	28174	20480	28137	11478
unique reflns	4705	6976	7887	5605	4865
data/restraints/ parameters	4705 / 0 / 262	6976 / 0 / 374	7887 / 0 / 460	5605 / 0 / 334	4865 / 0 / 336
R_1, wR_2 ($I > 2\sigma(I)$)	0.0383, 0.0914	0.0567, 0.1296	0.0468, 0.1255	0.0503, 0.0877	0.0457, 0.0813

Physical Measurements

NMR spectra were collected on Varian Inova 300 and 500 MHz spectrometers. UV-Vis-NIR absorption data were collected on a Cary-14 spectrophotometer. Cyclic voltammetry was conducted using a CH Instruments 600 electrochemical analyzer. The one-cell setup utilized a platinum working electrode, Ag wire counter electrode, and Ag/$AgNO_3$ reference electrode in CH_3CN. Analyte solutions were prepared in a THF solution of

NBu_4PF_6 (0.4 M) and referenced externally to the Fc/Fc^+ redox couple. The GC column was a HP-5 ms with dimensions 30 m x 0.25 mm. The standard method used for all runs involved an initial oven temperature of 50°C (held for 2 min) followed by a 20°C min^{-1} ramp to 70°C (held for 6 min) which was followed by a by a 20°C min^{-1} ramp to 230°C (held for 23 min).

Magnetic susceptibility data were measured from powder samples of solid material in the temperature range 2 - 300 K by using a SQUID susceptometer with a field of 1.0 T (MPMS-7, Quantum Design, calibrated with standard palladium reference sample, error <2%). The experimental data were corrected for underlying diamagnetism by use of tabulated Pascal's constants ($\chi_{dia} < 0$),[105,106] as well as for temperature-independent paramagnetism ($\chi_{TIP} > 0$).[107] Specifically, χ_{TIP} (units of 10^{-6} emu) = 50 for 2. The susceptibility and magnetization data were simulated with the program julX for exchange coupled systems.[108] The simulations are based on the usual spin-Hamiltonian operator for mononuclear complexes with spin S:

$$\hat{H}_e = g\beta\,\hat{\vec{S}}\cdot\vec{B} + D[\hat{S}_z^{\,2} - 1/3S(S+1) + E/D(\hat{S}_x^{\,2} - \hat{S}_y^{\,2})]$$

where g is the average electronic g value, and D and E/D are the axial zero-field splitting and rhombicity parameters. Magnetic moments are calculated after diagonalization of the Hamiltonian from the eigenfunctions using the Hellman-Feyman theorem $\vec{\mu}_i(\vec{B}) = \langle\psi_i|dH/d\vec{B}|\psi_i\rangle$. Powder summations were done by using a 16-point Lebedev grid.

Computational Methods

CASSCF/CASPT2 Calculations. All complete active space self-consistent field (CASSCF) calculations, which were followed by perturbation theory to second order (CASPT2), were performed with the MOLCAS 7.8 package[109] on experimental structures without symmetry constraints. Relativistic all-electron ANO-RCC basis sets were used for all elements.[110,111] Double-ζ quality (ANO-RCC-VDZP) basis sets were used for Co, Al, and N atoms and minimal basis sets (ANO-RCC-MB) were used for C and H atoms. The following contractions were used: [5s4p2d1f] for the metals, [3s2p1d] for N, [2s1p] for C, and [1s] for H. To include relativistic effects in the calculation, the Douglas-Kroll-Hess-Hamiltonian[112,113] was used. Resolution of identity combined with the Cholesky decomposition (RICD) was used to reduce the computational cost associated with the treatment of 2-electron integrals.[114] Lowest energy solutions were calculated for all spin states at the CASSCF level of theory and subsequent CASPT2 calculations were performed to recover more dynamical correlation, in which an imaginary level shift of 0.2 a.u. was used to prevent the occurrence of intruder states.[115]

The active space for **2** was chosen to include the ten valence 3*d* orbitals plus two correlating 4*d* orbitals, whereas for **3** and **4** the active space was chosen to include the five valence 3*d* orbitals plus one correlating 4*d* orbital. The active spaces for **2**, **3**, and **4** are 14 electrons in 12 orbitals or (14,12), (8,10), and (8,10), respectively. Only twelve or ten active orbitals were considered to obtain a reasonable level of accuracy while limiting the computational cost.

The natural orbital occupation numbers were used for the evaluations of the effective bond order (EBO), which is calculated as the difference between the total occupancies of the bonding and anti-bonding molecular orbitals of the metal-metal bond divided by two.[116,117]

Chapter 4

Synthesis and Characterization of a Hexairon Cluster Redox Series and Two Tetrairon Cluster Redox Members

4.1 Overview

A series of $Fe_6O_3(L)_3^{n+}$ (n = 0 to 3) and two $Fe_4O(L)_2^{n+}$ (n = 0, 2) clusters have been synthesized and characterized. Two of the hexairon clusters have been characterized by X-ray crystallography, which shows that they have isostructural planar cores with six Fe centers and three μ_3-O atoms. The two tetrairon clusters, also characterized by X-ray crystallography, show unusual distorted square planar (for n = 2) and distorted seesaw (for n = 0) geometries. ^{1}H NMR spectroscopy is consistent with solution C_{3h} symmetry for all four of the hexairon clusters. Mössbauer spectroscopy on two of the mixed-valent hexairon clusters is consistent with 5Fe(III)Fe(II) and 4Fe(III)2Fe(II) oxidation state assignments and confirms that the valences of both these clusters are localized on the Mössbauer timescale. SQUID magnetometry on the all-ferric $Fe_6O_3(L)_3^{3+}$ cluster demonstrates an $S = 0$ ground state, and EPR spectroscopy on the $Fe_6O_3(L)_3$ (formally 3Fe(III)3Fe(II)) cluster is consistent with an $S = 3/2$ ground state. Broad transitions in the NIR spectra of the three mixed-valent hexairon clusters have been assigned as intervalence charge transfer transitions. Taken together, the data on the mixed-valence hexairon clusters is consistent with Class II Robin-Day behavior.

4.2 Introduction

Synthetic polyiron oxide clusters are the subject of many studies because of their potential as single molecule magnets (SMMs) (if they have a nonzero spin ground state *S* and a large, negative zero-field splitting (*D*));[197-200] their analogy to structures in nature that such as iron storage protein ferritin,[201] and minerals such as hematite and ferrihydrite;[202] and their relevance to biomineralization.[203,204] Hence, new Fe/O clusters with interesting electronic and magnetic properties are sought after.

In this chapter, we describe the synthesis and characterization of four hexairon clusters with an unusual planar core geometry that differ only in the total oxidation state of the iron centers, including three mixed-valence clusters. These hexairon clusters are the first that contain a wholly encapsulated $Fe_6(\mu_3\text{-}O)_3$ core without additional Fe centers. The characterization includes ^{1}H NMR spectroscopy, X-ray crystallography, Mössbauer spectroscopy, magnetic characterization (SQUID magnetometry and EPR spectroscopy), cyclic voltammetry, and UV-Vis-NIR spectroscopy. Mössbauer spectroscopy of several mixed-valent clusters establishes localized valences on the Mössbauer time scale. Magnetic characterization on the all-ferric hexairon cluster demonstrates an $S = 0$ ground state, whereas a mixed-valence 3Fe(III)3Fe(II) cluster is shown to have an $S = 3/2$ ground state. In addition, we describe crystal structures of two tetrairon clusters that are formally related by a two-electron redox process; both clusters have unusual core geometries and oxidation states. As will be shown in Chapter 5, some of these clusters have relevance to O_2 reactivity from the diferrous complex FeFe(OTf)(py_3tren): one of the hexairon clusters and one of the tetrairon clusters are reactive intermediates, and the all-ferric

cluster is the thermodynamic sink.

4.3 Results and Discussion

4.3.1 Synthesis and X-Ray Crystallography

Hexairon Clusters 2-5

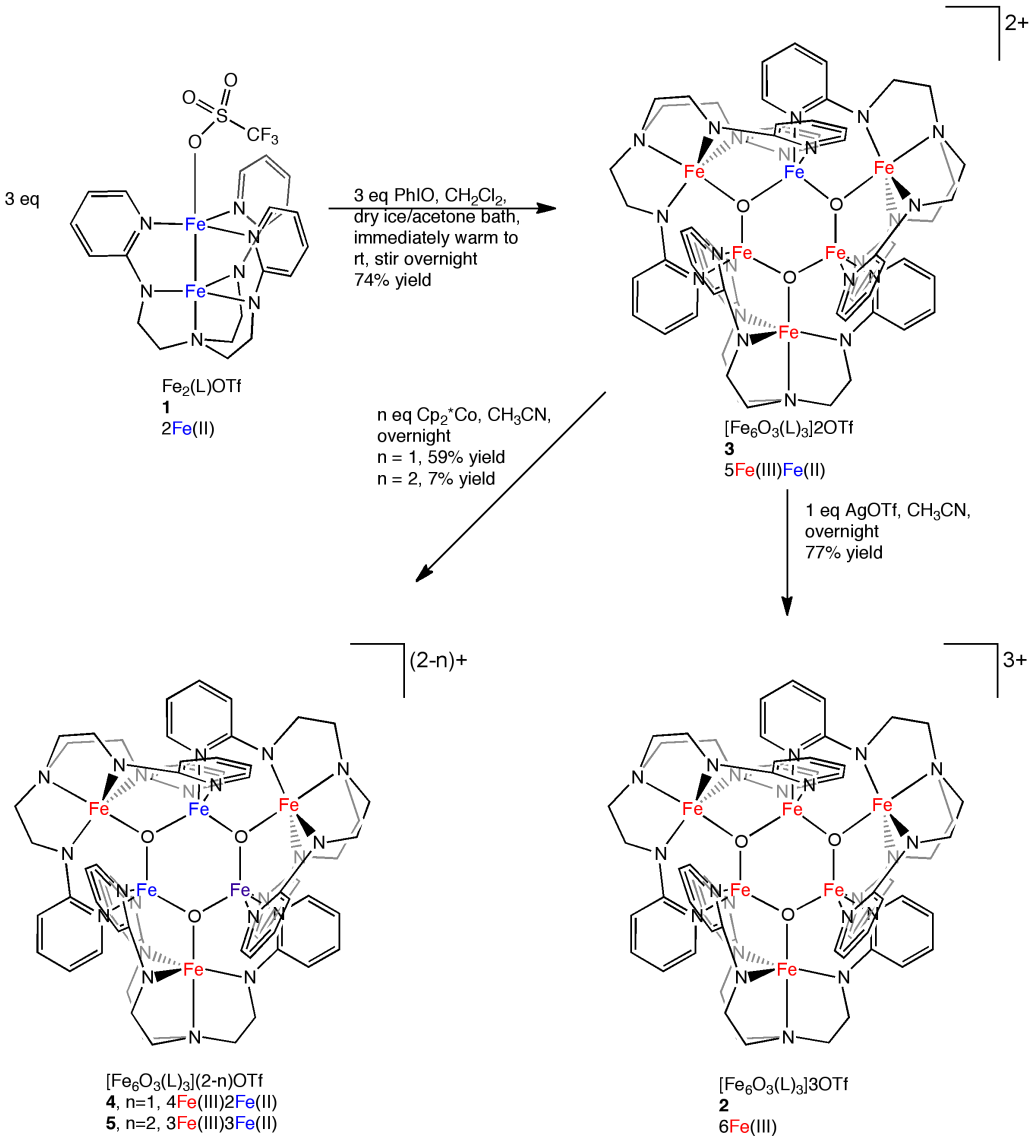

Scheme 4.1. Synthesis of the hexairon clusters **2**-**5**. All yields are isolated yields.

The diferrous complex FeFe(OTf)(py$_3$tren) **1** was prepared by adding

$[Fe(CH_3CN)_6](OTf)_2$ to $K_3(py_3tren)$ in THF. While a crystal structure of this molecule has not been obtained, its paramagnetically shifted ^1H NMR spectrum shows six resonances, indicative of C_{3v} symmetry in solution, like the previously characterized $FeFeCl(py_3tren)$.[145] Entry into the cluster chemistry was provided by adding an O-atom transfer reagent to **1** in CH_2Cl_2 or CH_3CN; one equivalent of iodosobenzene or pyridine *N*-oxide, or a half equivalent of isopropyl 2-iodylbenzoate relative to **1**, all furnished the same product, as judged by ^1H NMR spectroscopy (Scheme 4.1). The reaction was allowed to stir overnight, over which time it turned from the red color of the diferrous precursor to the purple color of the product, the 5Fe(III)Fe(II)3O cluster $[(FeFe(\mu_3\text{-}O)(py_3tren))_3][OTf]_2$ **3**. The dicationic charge and the hexairon core of the complex were confirmed by electrospray ionization-mass spectrometry (ESI-MS) as a distinctive set of peaks spaced 0.5 *m*/*z* apart with the most intense peak at *m/z* 753.1163, which is half the mass of the parent ion (Figure 4.1). The dicationic charge was unexpected, as an O-atom transfer to a diferrous starting material would be expected to yield an all-ferric product since the transfer of an O-atom is typically thought of as a two-electron process. Trimerization of "$FeFeO(L)^+$" should result in a tricationic charge. The reason the product has an additional electron is unclear. The presence of five ferric and one ferrous center in **2** was confirmed by Mössbauer spectroscopy (*vide infra*).

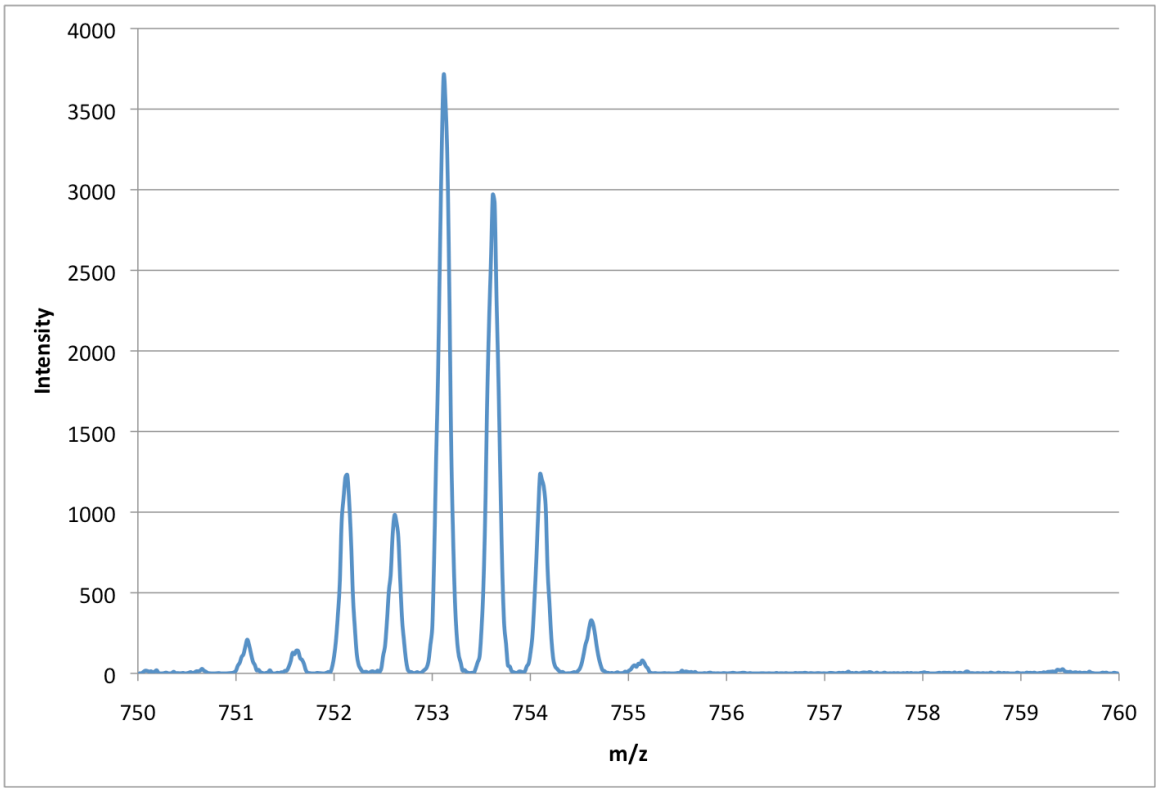

Figure 4.1. ESI-MS data of 5Fe(III)Fe(II)3O **3** in CH_3CN (natural abundance O). The peaks represent the isotopologues of the dication.

Table 4.1. ESI-MS data for natural abundance $[(Fe_6O_3(L))_3]^{2+}$ **3** in CH_3CN .

m/z	Absolute Intensity (max)[a]	Relative Intensity	Simulated Intensity[b]
751.1149	209	5.6	5.4
751.6150	141	3.8	4.6
752.1345	1230	33.2	35.1
752.6157	981	26.5	29.8
753.1163	3708	100	100
753.6171	2968	80.0	82.7
754.0988	1235	33.3	38.2
754.6192	329	8.9	12.4
755.1398	80	2.2	3.1

[a] The intensity listed is the maximum intensity for the peak, which has at the tabulated *m/z* value. [b] Intensities simulated using the Bruker Daltonics IsotopePattern program.

In analogy to other $Fe_3(\mu_3\text{-O})$ "triangles," in which all-Fe(III) clusters can be prepared, as well as their one electron reduced 2Fe(III)1Fe(II) congeners, the all-ferric

cluster [(FeFe(μ_3-O)(py$_3$tren))$_3$][OTf]$_3$ **2** (6Fe(III)3O) is isolable.[205-207] One equivalent of the oxidant AgOTf was added to complex **3** in CH_3CN to obtain complex **2** (Scheme 4.1). The crystal structure of **2** shows an unusual core: a central six-membered $Fe_3(\mu_3\text{-}O)_3$ ring with three additional Fe centers ligated to each O on the outside (Figure 4.2). The motif is essentially planar (the average out-of-plane distance for the nine atoms of the Fe_6O_3 core is 0.040 ± 0.022 Å, which is within error of planarity), unlike many iron oxide clusters, which show boat or chair conformations, or a Fe_4O_4 cubane-type structure. Only two clusters containing a planar $Fe_6(\mu_3\text{-}O)_3$ core, to our knowledge, have been reported: the polyoxotungstenate-supported clusters $[EMIM]_wNa_x[(SiW_9O_{34})_3\{Fe_3(\mu_2\text{-}OH)_2(\mu_3\text{-}O)\}_3(WO_4)(OH_2)_y]\cdot zH_2O$ (EMIM = ethyl-3-methylimidazolium; w = 8 or 9; x = 9 or 8; y = 1 or 0; z = 7 or 0.5), although it should be noted that these have three additional Fe surrounding the $Fe_6(\mu_3\text{-}O)_3$ core.[208,209]

The crystallographic 3-fold axis in the crystal structure of 6Fe(III)3O **2** passes through the center of the ring. The Fe-O bond lengths of the inner ring of **2** alternate: 1.820(1) Å vs. 1.977(3) Å (Table 4.2). As the Fe_{outer}-O bond lengths are 1.912(2) Å, **2** may then be thought of as a trimer of FeFe(μ-O)(L)$^+$ units, which are linked by the long Fe_{inner}-O bond and by bridging pyridyl donors. Per py$_3$tren ligand, one pyridine ligates one Fe center in the plane of the Fe_6O_3 moiety, while the other two pyridines bind a different Fe center above and below the Fe_6O_3 plane. All Fe centers are distorted trigonal bipyramidal in geometry, with the inner Fe centers ligated by two oxides and three pyridyl substituents; two pyridyls bind axially, while the two oxides and one pyridyl bind equatorially. For the outer Fe centers, the axial donors are the apical amine and an O

atom, and the three amide donors are the equatorial ligands.

A cyclic voltammogram of 5Fe(III)Fe(II)3O **3** indicated that clusters more reduced than **3** could potentially be isolated (*vide infra*). Adding a slight excess over one or two equivalents Cp_2*Co in CH_3CN at room temperature afforded the monocationic cluster [(FeFe(μ_3-O)(py_3tren))$_3$][OTf] **4** (4Fe(III)2Fe(II)3O) and the neutral cluster [(FeFe(μ_3-O)(py_3tren))$_3$] **5** (3Fe(III)3Fe(II)3O), respectively (Scheme 4.1). Unlike **2** and **3**, which have good solubility in CH_3CN, **4** is only sparingly soluble in CH_3CN, while **5** is insoluble in CH_3CN. Hence, **4** could be filtered from the crude reaction and washed with small portions of CH_3CN to afford a clean ^{1}H NMR sample in moderate yields. Complex **4** has modest solubility in CH_2Cl_2, from which it was recrystallized. Although a sample of **5** could be cleanly recrystallized from toluene, **5** itself has poor-to-nonexistent solubility in all solvents examined (including toluene, CH_3CN, THF, CH_2Cl_2, C_6H_6, 1,4-dioxane, hexanes, and pentane) and was obtained in poor yield.

While crystals of 3Fe(III)3Fe(II)3O **5** could be grown from toluene, attempts at collecting an X-ray structure with these crystals failed. Dissolving **5** in hot benzene and filtering provided enough solubility to recrystallize **5** upon layering with pentane, and one of these crystals was of sufficient quality for X-ray diffraction. The general structure of the Fe_6O_3 core was verified for **5**, as in **2** (Figure 4.2). However, unlike **2**, **5** did not crystallize in a threefold symmetric space group – three benzene molecules co-crystallized on general positions, and a fourth on the crystallographic inversion center. Nonetheless, the bond metrics of the neutral cluster **5** are consistent with approximate C_{3h} symmetry.

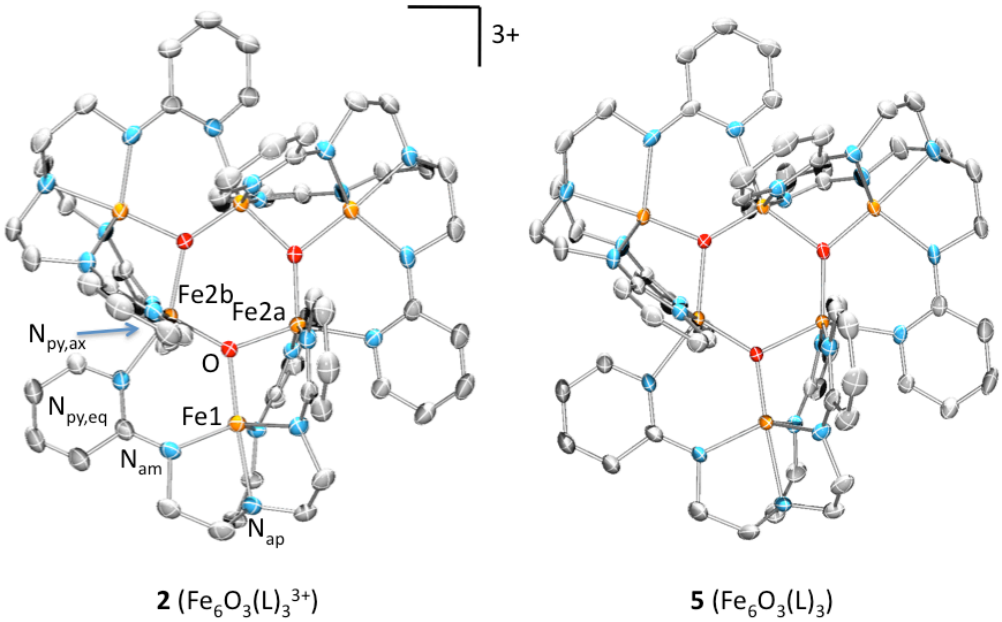

Figure 4.2. X-ray crystallographic comparison of the trication of 6Fe(III)3O **2** (left) and 3Fe(III)3Fe(II)3O **5** (right).

The trication **2** and the neutral species **5** are a natural pair to compare by crystallography because each has only two kinds of Fe centers, and the former has crystallographic threefold symmetry whereas the latter has approximately threefold symmetry. In complex **2**, there are two different kinds of Fe(III) centers: the inner Fe(III) and the outer Fe(III). For complex **5**, there are three Fe(III) centers and three Fe(II) centers, though it is not immediately obvious which oxidation state of Fe is located in the inner ring vs. the outside. Comparisons of the bond metrics of **2** and **5** reveal one main difference that allows one to assign where the Fe(III) and Fe(II) centers are located in **5** (*vide infra*). Almost all bond metrics lengthen in reducing **2** to **5** (Table 4.2). The following evidence leads us to conclude that the reductions are centered on the Fe atoms in the inner ring (Fe2): the Fe1-O distance *shortens* in going from **2** to **5**, unlike all the

other core bond distances. The Fe1-O bond shortening rules out reduction of Fe(1), as Fe1-O bonds would lengthen. The bond shortening is attributed to decreased electrostatic attraction between the O atom and the reduced Fe(II) in the inner ring in **5** compared to between the O atom and the inner Fe(III) in **2**, which leads to comparatively greater electrostatic attraction between the O atom and the outer Fe(III) in **5** compared to **2**.

Table 4.2: Crystallographic bond metric comparison of the trication 6Fe(III)3O **2** and neutral 3Fe(III)3Fe(II)3O **5**.

Metric	**2**	**5**[a]	Difference[b]
Fe1-O (Å)	1.912(2)	1.814 (± 0.005)	-0.098
Fe2a-O (Å)	1.820(2)	1.870 (± 0.002)	0.050
Fe2b-O (Å)	1.977(2)	2.037 (± 0.007)	0.060
Fe1-N_{ap} (Å)	2.128(2)	2.224 (± 0.009)	0.096
Fe1-N_{am} (Å)	2.006 (± 0.025)	2.063 (± 0.008)	0.057
Fe2-$N_{py,eq}$ (Å)	2.107(2)	2.190 (± 0.011)	0.083
Fe2-$N_{py,ax(a)}$ (Å)	2.082(2)	2.156 (± 0.003)	0.074
Fe2-$N_{py,ax(b)}$ (Å)	2.133(2)	2.205 (± 0.008)	0.072
Fe1···Fe2a (Å)	3.013	3.078 (± 0.005)	0.065
Fe1···Fe2b (Å)	3.297	3.329 (± 0.012)	0.032
Fe2a···Fe2b (Å)	3.496	3.458 (± 0.010)	-0.038
O···O (Å)	3.026	3.304 (± 0.017)	0.278
[Fe2a···Fe2b] – [O···O] (Å)	0.470	0.154	-0.316
Fe1-O-Fe2a (º)	101.58(8)	105.98 (± 0.22)	4.40
Fe1-O-Fe2b (º)	124.18(9)	129.33 (± 0.92)	5.15
Fe2a-O-Fe2b (º)	134.05(9)	124.44 (± 1.00)	-9.61
O-Fe2-O (º)	105.61(10)	115.39 (± 0.80)	9.78
[Fe2a-O-Fe2b] – [O-Fe2-O] (º)	28.44	9.05	-19.39

[a] Since **5** crystallized in *P*-1, there is no threefold symmetry in the cluster, so all distances and angles are tabulated as [average (± standard deviation)]. [b] The difference is computed as [**5**] – [**2**].

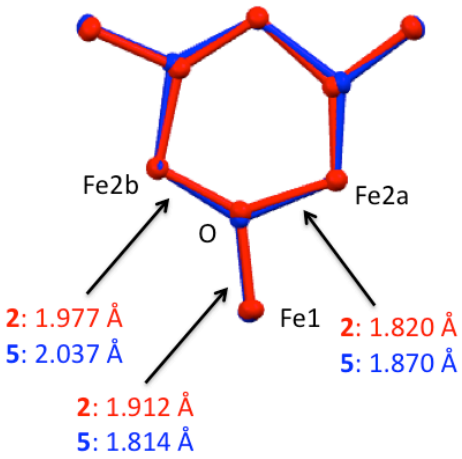

Figure 4.3. Changes in the core Fe-O bond lengths upon reduction of trication **2** (6Fe(III), red) to neutral **5** (3Fe(III)3Fe(II), blue).

A stark observation, when comparing the overlay of the cores of trication **2** and neutral **5**, is that the shape of the inner ring changes (Figure 4.3). On the basis of both bond angles and bond distances, the inner ring is more "symmetric" in **5** than **2** (Table 4.2). Another visual change is that the O are "pinched in" in **2**. The sum of all these effects, when looking at the overlay of **2** and **5**, is that the Fe centers are in similar positions, but the O atoms move further from the center of the inner ring going from **2** to **5**.

Tetrairon Clusters 6-7

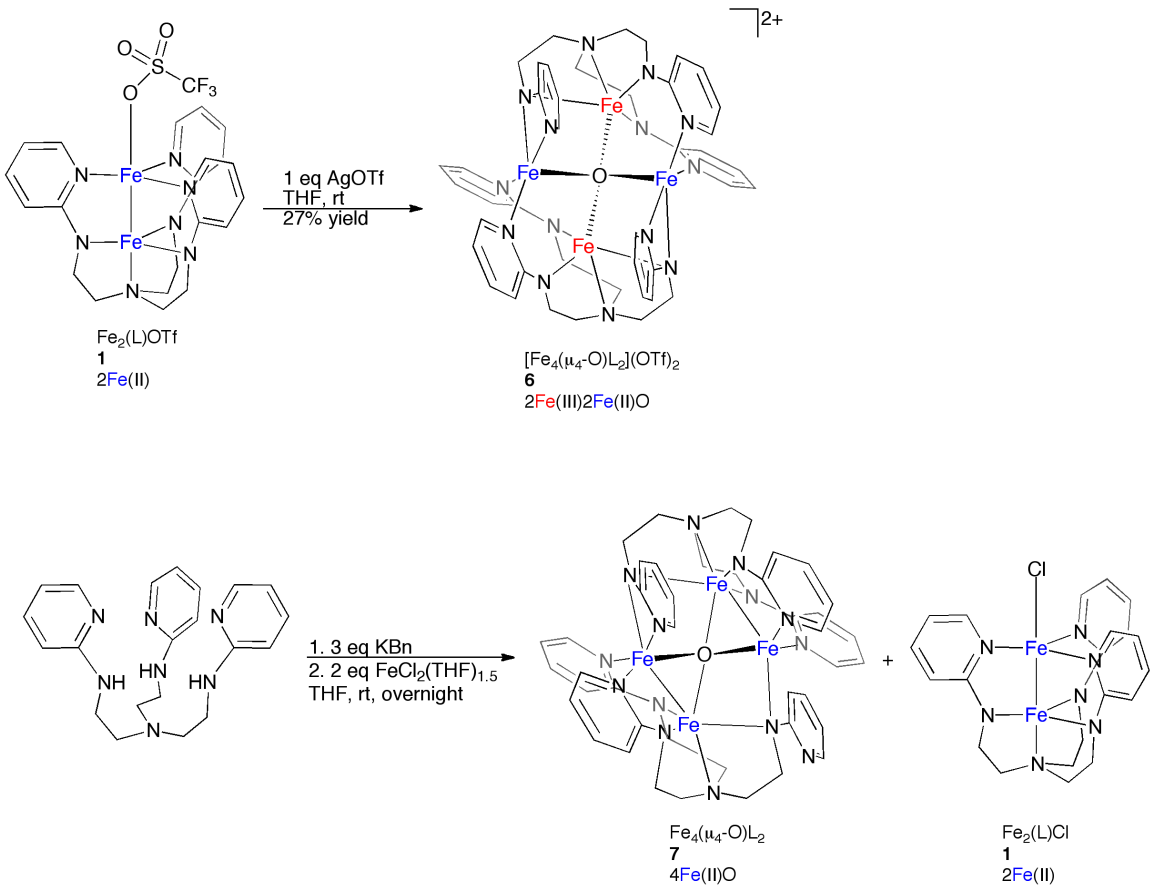

Scheme 4.2. Syntheses of the tetrairon clusters 2Fe(III)2Fe(II)O **6** and 4Fe(II)O **7**.

A *tetrairon* cluster, $[\{Fe_2(L)\}_2(\mu_4\text{-}O)](OTf)_2$ **6** (or 2Fe(III)2Fe(II)O), could be prepared in low yield from the addition of one equivalent of the oxidant AgOTf or FcOTf to **1**. Instead of the desired one-electron oxidation to a mixed-valent Fe(II)/Fe(III) core of the formulation $[FeFe(py_3tren)][OTf]_2$, an O atom is present. This may be due to adventitious water, perhaps from AgOTf (which is generally prepared from $AgNO_3$ and LiOTf in water). In that case, one molecule of "HOTf" per diiron center would have to be lost, probably by a base such as py_3tren. Crude ^1H NMR spectra of this synthesis are messy; in addition to **6**, **2** and other, unidentified impurities are present in the crude.

Based on stoichiometric O_2 addition experiments described in the subsequent chapter, **6** is highly reactive and most likely converts to **2** by reaction with adventitious O_2. Curiously, addition of a half equivalent of an O-atom transfer reagent such as iodosobenzene or pyridine *N*-oxide relative to **1** does *not* provide **6**; in the former case, a different ^{1}H NMR spectrum was obtained with an unidentified product, whereas in the latter case, the only product that could be identified was **2** (though the caveats about decomposition of **6** to **2** apply). The iron centers in **6** have a total +10 charge, which means that it is a mixed-valent, 2Fe(III)2Fe(II)O, cluster.

The crystal structure of 2Fe(III)2Fe(II)O **6** was obtained from a CH_2Cl_2 solution layered with THF (Figure 4.4). Complex **6** contains what is essentially a twofold axis of rotation passing through the O, bisecting both the Fe1-O-Fe3 and the Fe2-O-Fe4 angles. For this reason, bond metrics for **6** are averaged across each half of the core, as **6** can be considered to approximately have C_2 symmetry (Table 4.3). The sum of the bond angles around O, 382.06º, is intermediate between the values for a square planar geometry and a tetrahedral geometry, but is significantly larger than the values for the μ_3-O ligands of **2** and **5**, all of which are essentially 360º. The amide-ligated Fe-O distance is short at 1.928 (± 0.002) Å, while the pyridyl-ligated Fe-O distance is longer at 2.066 (± 0.014) Å. Using similar arguments as for clusters **2** and **5**, the current assignment of oxidation states is that the pyridyl-ligated Fe centers of **6** (Fe2 and Fe4) are Fe(II), whereas the amide-ligated Fe centers (Fe1 and Fe3) are Fe(III), since the Fe-O distances are much shorter for the amide-ligated Fe than the pyridyl-ligated Fe. The Fe-Fe distances, at 2.864 (± 0.002) Å and 3.049 (± 0.021) Å, are too long to consider direct *d* orbital overlap relevant (r = 1.23

and 1.31, respectively, where *r* is equal to the crystallographic distance divided by the sum of the single-bond radii).

Complex **6**, to our knowledge, is the first crystallographically characterized mixed-valent 2Fe(II)2Fe(III) $Fe_4(\mu_4\text{-O})$ compound that is not part of a higher nuclearity arrangement. There is a polymeric 2Fe(II)2Fe(III) $Fe_4(\mu_4\text{-O})$ structure reported in the CSD: $[H_3NC_2H_4NH_3]_2[Fe_4(\mu_4\text{-O})(PO_4)_4]\bullet H_2O$, in which the phosphate ligands link $Fe_4(\mu_4\text{-O})$ units.[210] The $Fe_4(\mu_4\text{-O})$ core is tetrahedral in this phosphate structure. Note that individual Fe(II) and Fe(III) sites cannot be distinguished by bond metrics in $[H_3NC_2H_4NH_3]_2[Fe_4(\mu_4\text{-O})(PO_4)_4]\bullet H_2O$; that is, all the Fe sites are crystallographically equivalent. That is in contrast to **6**, which has a distorted square planar structure, and individual Fe(II) and Fe(III) sites are present. Complex **6** represents, to our knowledge, the second example of a discrete, distorted square planar $Fe_4(\mu_4\text{-O})$ compound. The other is the all-Fe(III) compound $[Fe_4(\mu_4\text{-O})(\mu\text{-OMe})_4(bisi)_4](ClO_4)_2$ (Hbisi = *N*-(benzimidazol-2-yl)-salicylaldimine, which has a large *trans*-(Fe-O-Fe) angle of 159.07(2)°.[211] Thus, $[Fe_4(\mu_4\text{-O})(\mu\text{-OMe})_4(bisi)_4](ClO_4)_2$ is significantly more planar than **6**, whose largest Fe-O-Fe angle is 147.14(12)°.

Like in the hexairon series **2**-**5**, we have isolated another redox member of the tetrairon cluster **6**. A crystal of the formulation $[(FeFe(py_3tren))_2(\mu_4\text{-O})]$ **7** (or 4Fe(II)O) was obtained by the addition of two equivalents of $FeCl_2(THF)_{1.5}$ to py_3tren, followed by recrystallization from layering a CH_2Cl_2 solution with Et_2O (Figure 4.4). While one would expect that the product, in this case, would be $FeFeCl(py_3tren)$, the ^1H NMR spectrum of the recrystallized material showed a mixture of $FeFeCl(py_3tren)$ and a

complex set of other paramagnetic signals. This is in contrast to the published synthesis of FeFeCl(py_3tren), in which the product could be cleanly recrystallized following the addition of one equivalent of $FeCl_2(THF)_{1.5}$ to K[Fe(py_3tren)].[145] All of the Fe centers in **7** can be assigned with the Fe(II) oxidation state on the basis of charge. Formally, **7** is the two-electron reduced congener of **6**. Presumably, the synthesis of **7** involved hydrolysis of the chloride ligand with adventitious water, in the same manner as **6**, giving the byproduct "HCl." Adventitious oxygen is unlikely to be the source of the O atom in **7**, as the oxidation states of the Fe centers in **7** are unchanged from those of **1**.

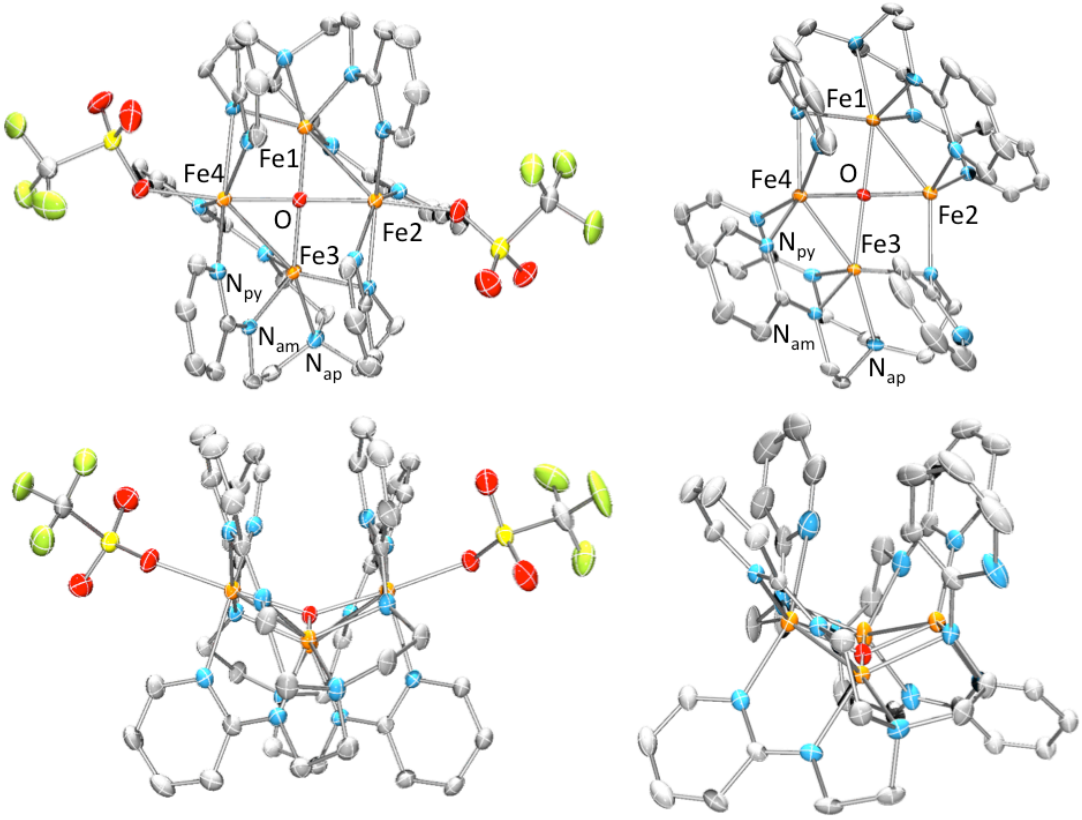

Figure 4.4. Two views of the X-ray crystal structures of 2Fe(III)2Fe(II)O **6** (left) and 4Fe(II) **7** (right). Fe and ligand donors are labeled.

Table 4.3. Comparison of the bond metrics of μ_4-O clusters **6** and **7**.

Metric	**6**[a]	**7**[b]	Difference[c]
Fe(1,3)-O (Å)	1.928 (± 0.002)	1.977 (± 0.003)	0.049
Fe(2,4)-O (Å)	2.066 (± 0.014)	1.947 (± 0.005)	-0.119
Fe-Fe (1-2,3-4) (Å)	2.864 (± 0.002)	2.569 (± 0.012)	-0.295
Fe-Fe (1-4,2-3) (Å)	3.049 (± 0.021)	2.961 (± 0.019)	-0.088
Fe(1,3)-N_{am} (short) (Å)	1.977 (± 0.009)	2.059 (± 0.012)	0.082
Fe(1,3)-N_{am} (long) (Å)	2.123 (± 0.016)	2.246 (± 0.005)	0.123
Fe(2,4)-N_{py}[d] (Å)	2.138 (± 0.004) 2.227 (± 0.014)	2.048(3), 2.077(3) 2.071(2), 2.129(3)	-0.076 -0.127
Fe(2,4)-N_{py}[e] (Å)	2.255 (± 0.021)	2.393(4)	0.138
Fe2-N_{am} (Å)	2.222(3)	2.103(2)	-0.119
Fe4-N_{am} (Å)	2.305(3)	2.159(3)	-0.146
Fe1-O-Fe3 (º)	140.39(13)	179.57(13)	39.18
Fe2-O-Fe4 (º)	147.14(12)	134.29(12)	-12.85
Fe(1,3)-O-Fe(2,4) (º)	91.58 (± 0.40)	81.82 (± 0.49)	-9.76
Fe(1,3)-O-Fe(4,2) (º)	99.45 (± 0.50)	98.02 (± 0.59)	-1.43
Fe(2,4)-plane[f] (Å)	0.090 (± 0.001)	0.605 (± 0.020)	0.515

[a] All distances and angles are tabulated as [average (± standard deviation)] except where otherwise noted. Even though **7** has no symmetry, many of the metrics do not appreciably vary across each half of the cluster, and so distances and angles are tabulated as [average (± standard deviation)] except where otherwise noted. [c] The difference is computed as [**7**] – [**6**]. [d] This metric refers to the N in which two out of three pyridyls bind one Fe. [e] This metric refers to the N in which one out of three pyridyls bind the Fe. [f] This is the minimum distance between Fe2 or Fe4 and the plane created by the three or four nitrogen donors around Fe.

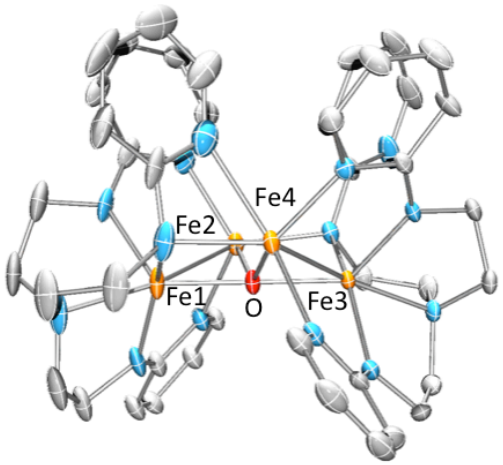

Figure 4.5. X-ray crystal structure perspective of 4Fe(II)O **7** that highlights the linear Fe1-O-Fe3 angle.

A comparison of the bond metrics of 2Fe(III)2Fe(II)O **6** and 4Fe(II)O **7** is not quite

as simple as the comparison between **2** and **5** discussed earlier. While the cores of **6** and **7** are similar, unlike **6**, **7** does not contain an approximate two-fold rotation symmetry passing through the μ_4-O ligand. The reason is that one of the py_3tren ligands in **7** has a pyridyl substituent that is not coordinated. This pyridyl's N donor points away from the center of the cluster. The corresponding pyridyl donor on the other py_3tren ligand binds Fe weakly at best (2.393(4) Å). However, this pyridyl donor undoubtedly exerts an influence on the coordination sphere of the Fe (Fe4), because all the other Fe-ligand bond distances are *ca*. 0.05 Å longer than those of the Fe without this pyridyl interaction (Fe2). The Fe-Fe, Fe-O, and amide-ligated Fe-N interactions are very similar across the two halves of **7**.

The following are the major differences between 2Fe(III)2Fe(II)O **6** and **7** (Table 4.3). The geometry around the μ_4-O changes, as the two large Fe-O-Fe angles in **6** are 140.39(13) and 147.14(12), but the corresponding angles in **7** are 179.57(13) and 134.29(12). The μ_4-O in **6** has a distorted square planar geometry, but the μ_4-O of **7** has a distorted seesaw geometry with two Fe *trans* to each other around O. Intriguingly, the Fe-O-Fe angle that increases a large amount from **6** to **7** involves the two amide-ligated Fe, which are the ones that reduce from Fe(III) in **6** to Fe(II) in **7**.The amide-ligated Fe (Fe1 and Fe3)-O distances increase by 0.049 Å, from 1.928 (± 0.002) Å to 1.977 (± 0.003) Å, whereas the pyridyl-ligated Fe (Fe2 and Fe4)-O distances *decrease* by 0.119 Å, from 2.066 (± 0.014) Å to 1.947 (± 0.005) Å. There are two major factors for these changes: one is that the amide-ligated Fe are reduced from Fe(III) in **6** to Fe(II) in **7**, so the electrostatic attraction between these Fe and O atoms decrease, leading to the increase in

the Fe(1,3)-O bond length. Comparatively, the O atom is more evenly shared among the 4 Fe in **7** compared to those of **6** on the basis of the Fe charges (all Fe in **7** are Fe(II)), so the Fe(2,4)-O distances decrease from **6** to **7**. The other major contributing factor to the decrease of the Fe(2,4)-O distance in **7** compared to **6** is that there are no triflate ligands in the former, so only 4 or 5 ligands bind the pyridyl-ligated Fe in **7**, rather than 6 ligands in **6**. The geometry around the pyridyl-ligated Fe centers also changes dramatically between **6** and **7**. The minimum distance between the pyridyl-ligated Fe and the plane created by the nitrogen donors is only 0.090 (± 0.001) Å in **6**, but in **7**, the corresponding distance is a much larger 0.605 (± 0.020) Å, reflecting the large rearrangements that occur upon the loss of a triflate ligand on reduction from **6** to **7**.

Finally, stark differences in the Fe-Fe distances in 2Fe(III)2Fe(II)O **6** and 4Fe(II)O **7** are also observed (Table 4.3). The short Fe-Fe distance (Fe1-Fe2 and Fe3-Fe4, averaged) undergoes a large decrease from 2.864 (± 0.002) Å in **6** to 2.569 (± 0.012) Å in **7**, or 0.295 Å. The latter distance (r = 1.10) is within the range of MM'Cl(py_3tren) (MM' = CoCo, CoFe, CoMn, FeMn) compounds with high-spin M(II) centers that antiferromagnetically couple.[145] It is tempting to consider direct σ/σ* overlap in **7**, given the short Fe-Fe distance comparable to the aforementioned MM'Cl(py_3tren) compounds, though this is somewhat tempered by the presence of the μ_4-O ligand that provides a different kind of exchange pathway than is available to MM'Cl(py_3tren) compounds.

Tetrairon compounds with the $Fe_4(\mu_4\text{-O})$ motif are few. Complex 4Fe(II)O **7** represents a new type of structure for both all-Fe(II) $Fe_4(\mu_4\text{-O})$ compounds and $Fe_4(\mu_4\text{-O})$ compounds in general, as **7** appears to be the first example of a (distorted) seesaw

geometry for a $Fe_4(\mu_4\text{-}O)$ compound (without considering higher-nuclearity multiiron compounds) with its two largest Fe-O-Fe bond angles of 179.57(13)° and 134.29(12)°. In addition, the short Fe-Fe distance (Fe1-Fe2 and Fe3-Fe4, averaged) of 2.569 (± 0.012) Å in **7** further distinguishes it from other $Fe_4(\mu_4\text{-}O)$ complexes. Three crystallographically characterized examples of all-Fe(III) $Fe_4(\mu_4\text{-}O)$ clusters are known.[211-213] Crystallographically characterized $Fe_4(\mu_4\text{-}O)$ compounds containing all Fe(II) centers reported in the CSD are limited to five examples – $Fe_4(\mu_4\text{-}O)(DPhF)_6$ (DPhF = *N*,*N*'-diphenylformamidinate), $Fe_4(\mu_4\text{-}O)(DBiPhF)_6$ (DBiPhF = *N*,*N*'-bisbiphenylformamidinate), $Fe_4(\mu_4\text{-}O)(dpa)_6$ (dpa = 2,2'-dipyridylamide), $Fe_4(\mu_4\text{-}O)(MBT)_6$ (MBT = 2-mercaptobenzothiazole), and $\{Fe(Ph_2PNCH_2\text{-}2\text{-}Py)\}_4(\mu_4\text{-}O)(\mu\text{-}Cl)_2$.[214-217] All five of these compounds can be considered tetrahedral or distorted tetrahedral. The greatest spread in Fe-O-Fe bond angles among these five compounds is found in $Fe_4(\mu_4\text{-}O)(DPhF)_6$, in which the smallest Fe-O-Fe angle is 93.6(1)° and the largest is 128.6(1)°. (Note that the 3-dimensional coordinates of $Fe_4(\mu_4\text{-}O)(DBiPhF)_6$ were not deposited in the CSD, and its bond metrics were not tabulated in the article in which it appeared, but it was described as having the same kind of structure as $Fe_4(\mu_4\text{-}O)(DPhF)_6$.) It also has the shortest Fe-Fe distance of all these compounds: two of the six Fe-Fe distances are 2.850(1) Å and 2.857(1) Å, which is *ca*. 0.3 Å longer than the short Fe-Fe distance found in **7**.

4.3.2 Cluster ^{1}H NMR Spectroscopy

All four hexairon clusters are paramagnetic at room temperature and show the same characteristic pattern of peaks, though with different chemical shifts. The ^{1}H NMR

spectra are shown in Figure 4.6. The tricationic cluster **2** exhibits thirteen resonances, whereas **3**, **4**, and **5** show fourteen resonances. Comparison of the ^{1}H NMR spectrum of **2** to those of the other three cluster oxidation states suggests that two peaks in **2** are coincidental at 122 ppm; in **3**, these partially overlap at 145 and 143 ppm, whereas in the other two clusters they are fully resolved. Based on the crystal structure of **2** and the discussion to follow in this section, we believe the overlap of the two resonances at 122 ppm is due to accidental chemical equivalence of two tren protons.

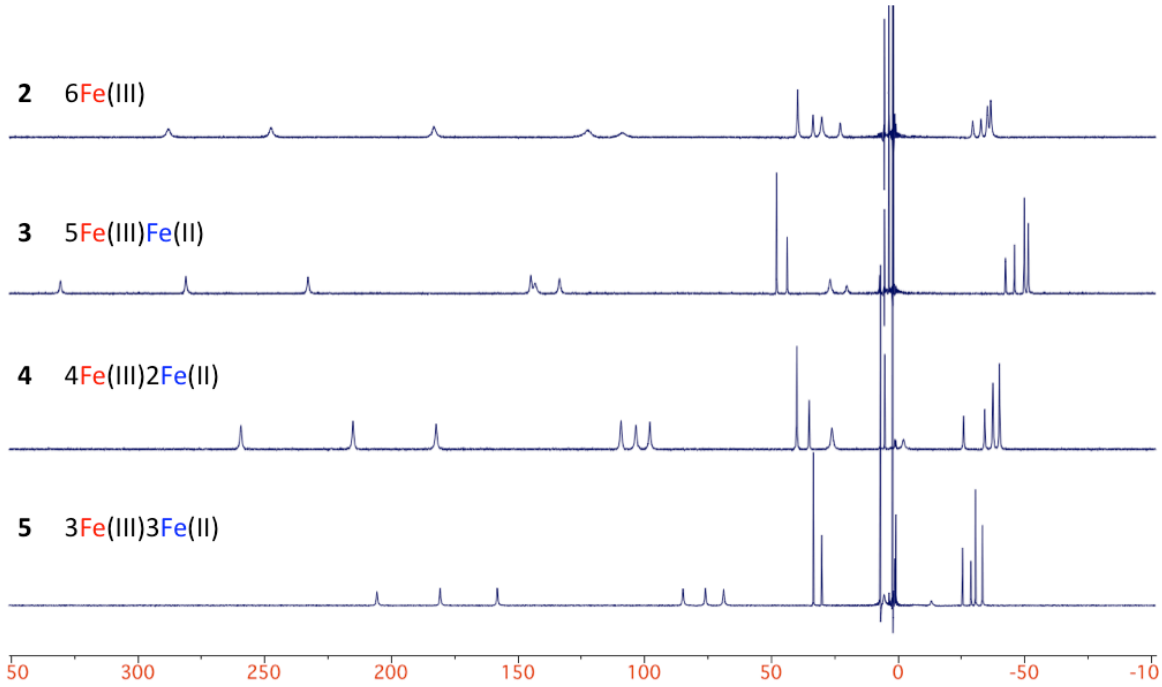

Figure 4.6 ^{1}H NMR spectra of the four $[Fe_6O_3(L)]^{n+}$ clusters (**2**, n = 3; **3**, n = 2; **4**, n = 1; **5**, n = 0). Complexes **2** and **3** are dissolved in CD_3CN, **4** is dissolved in CD_2Cl_2, and **5** is dissolved in d_8-toluene.

The solid-state structures of tricationic **2** and neutral **5** provide some guidance to interpreting the ^{1}H NMR spectra. The solution state structure of each molecule can be described as having C_{3h} symmetry. Hence, the nine total ligand arms can be divided into

two groups: (1) a set of six which are above and below the Fe_6O_3 plane, and (2) the remaining three arms which are in the plane. The two different types of pyridine rings in the molecule give rise to eight peaks in a 2:1 ratio. The tren methylene peaks give rise to six peaks, each with a theoretical integration of 6 H (as shown in Figure 4.8, the actual integrations of the tren protons of **3** are somewhat less than 6 H, and we offer an explanation in the following discussion).

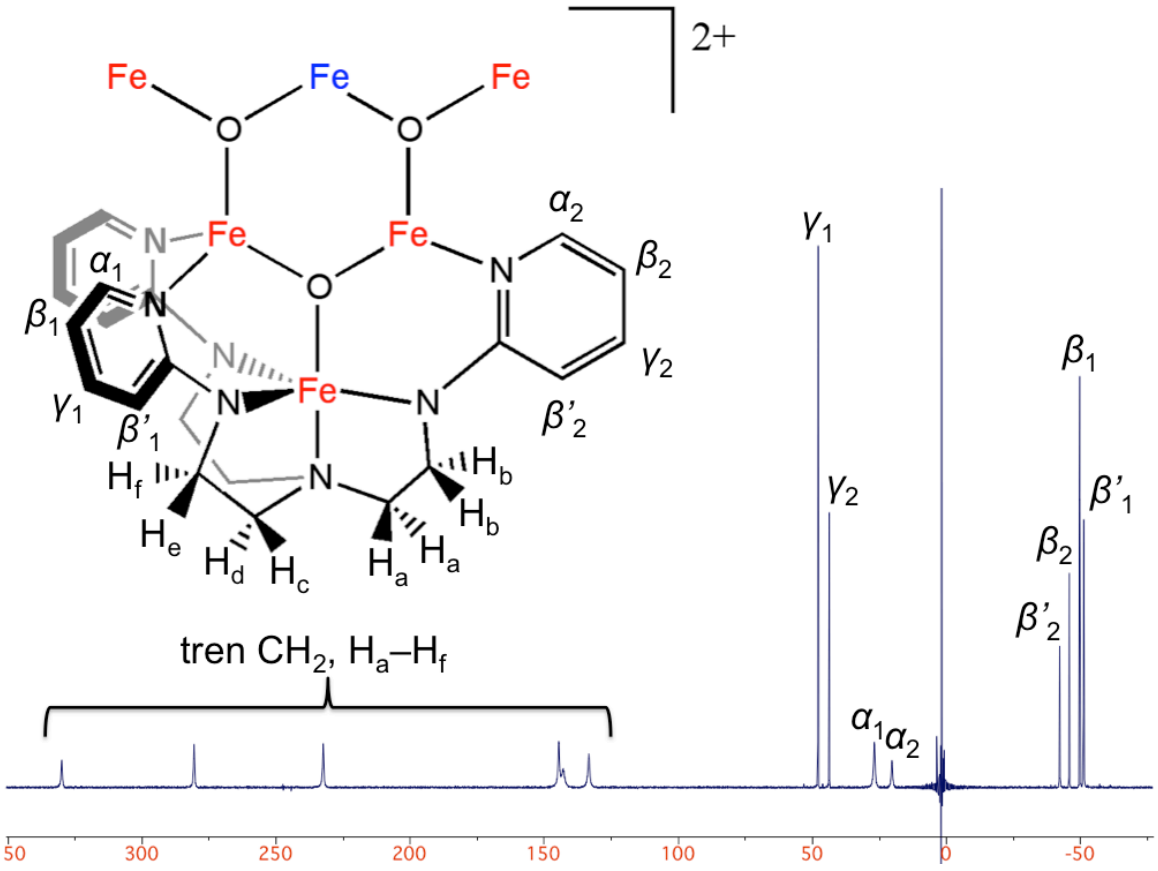

Figure 4.7. Assignment of the protons in the ^{1}H NMR (300 MHz, CD_3CN) spectrum of paramagnetic **3**.

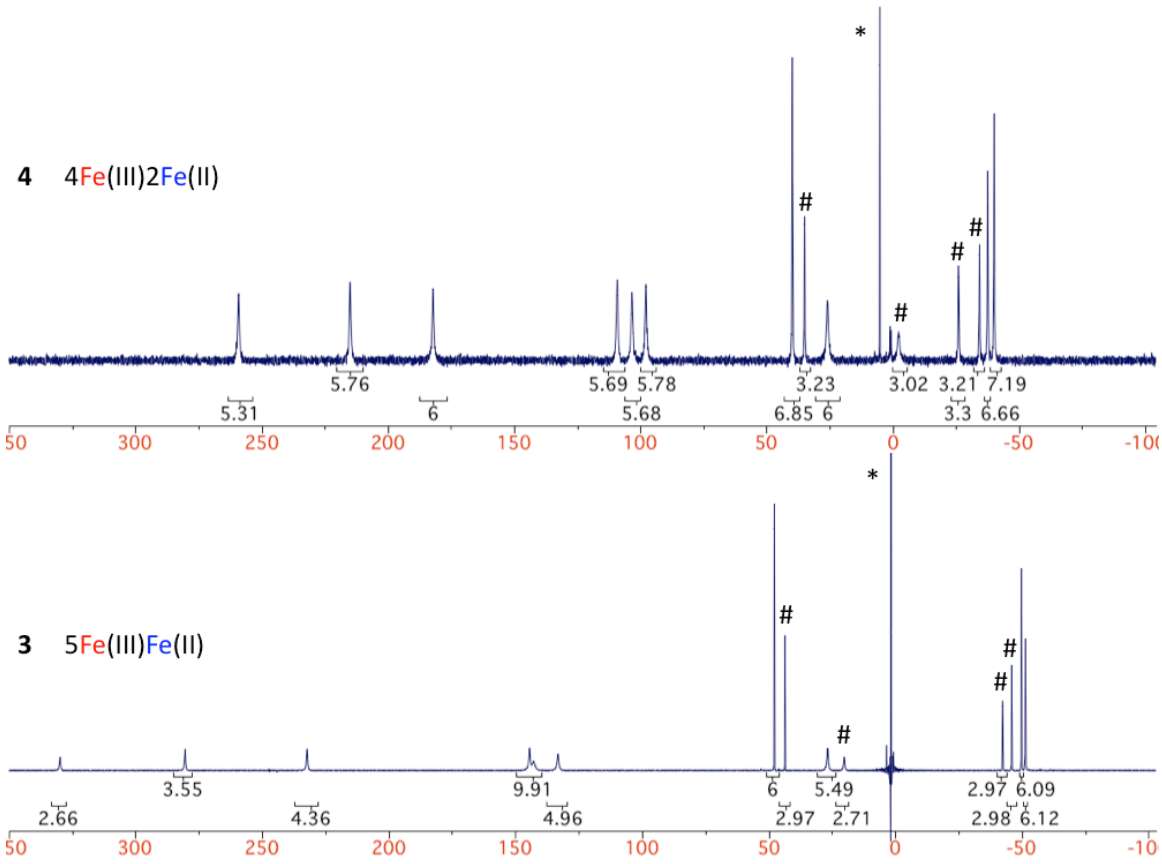

Figure 4.8 The ^{1}H NMR spectra of the clusters 4Fe(III)2Fe(II)3O **4** (top, in CD_2Cl_2) and 5Fe(III)Fe(II)3O **3** (bottom, in CD_3CN). Solvents marked with asterisks. The pound signs represent the four in-plane pyridyl resonances in each molecule.

In Figure 4.8, the integrations of the peaks in the ^{1}H NMR spectra of the monocation **4** and the dication **3** are provided. The four pyridyl protons in the plane of the $Fe_6(\mu_3\text{-}O)_3$ core can be identified since they only integrate to 3 H rather than 6 H like the other ten resonances. For **4**, these four in-plane pyridyl resonances occur at 35, -2, -26, and -34 ppm. Since the equatorial pyridyl rings and the axial pyridyl rings are similar distances from the $Fe_6(\mu_3\text{-}O)_3$ core in both **2** and **5**, one would expect their proton resonances to be shifted similarly to each other (for example, the in-plane β proton and the axial β proton for a given molecule should have similar chemical shifts). Then, the

four axial pyridyl protons of **3** fall at 40, 26, -37, and -40 ppm. The other six resonances, all shifted far downfield of the pyridyl resonances, are then assigned as tren protons. All six of these downfield resonances should integrate to 6, and for the monocation **4**, the values are reasonably close to 6, but for the dication **3**, the integrations are noticeably less than 6 and deviate more from the idealized value the further downfield the peak is (the maximum deviation is 3.44 H less than expected). We think this may have to do generally with the increased paramagnetism of **3** relative to **4**, as the tren peaks of **3** are isotropically shifted further downfield than those of **4**. We also note that, in collecting the T_1 values of dication **3** (*vide infra*), two separate experiments had to be conducted: one with a 90º pulse width of 7.4 μs, and one with a 90º pulse width of 3.6 μs, because the tren protons relaxed much faster than the pyridyl protons.

Table 4.4. Integrations, T_1 values and assignments for the pyridyl protons of dication **3**.

Chemical Shift (ppm)	Integration[a]	T_1 value (ms)	Assignment
330	6	3.0	tren-CH_2
281	6	3.2	tren-CH_2
232	6	2.3	tren-CH_2
145	6	2.5	tren-CH_2
143	6	2.3	tren-CH_2
133	6	2.2	tren-CH_2
48	6	49	γ_1
44	3	50	γ_2
27	6	1.2	α_1
20	3	1.4	α_2
-42	3	12	β'_2
-46	3	25	β_2
-50	6	26	β_1
-51	6	12	β'_1

[a] The integrations given are theoretical values based on the assignments.

To gain further information in assigning the pyridyl protons, the spin-lattice relaxation time (T_1) values of the protons of **3** have been tabulated (Table 4.4). Figure 4.7

provides a guide for where these protons are located in **3**. In the same manner as with the MM'Cl(py_3tren) compounds,[145] we have assigned the protons such that the protons closest to the Fe centers relax the fastest. Pairs of pyridyl peaks have very similar T_1 values, which is expected given that the two different kinds of pyridyl donors are similar distances from the Fe centers. As expected based on the broadness of the peaks, resonances at 27 ppm and 20 ppm are the α_1 and α_2 protons, where the subscript "1" refers to the axial pyridyl resonances, and the subscript "2" refers to the in-plane pyridyl resonances (Figure 4.7). We have assigned the β vs. β' protons based on the greater T_1 values corresponding to the β protons in the same manner as the MM'Cl(py_3tren) compounds, as the β protons are located slightly further away from the Fe centers than the β' protons. The tren protons all have very similar T_1 values, and because we have not collected a COSY spectrum or NOESY data yet, a definitive assignment of the individual tren protons is not possible at this time.

We have not performed T_1 measurements on the other hexairon clusters **2**, **4**, and **5**. However, the pattern of chemical shifts, by examination of Figure X, stays essentially the same, such that we can confidently assume that the four distinct β/β' protons stay upfield of the diamagnetic region, whereas the γ protons stay downfield of the diamagnetic region in all four compounds. The hexairon clusters **2**-**5**, by virtue of their alternating upfield-downfield shifts of the pyridyl protons, exhibit a dominant spin polarization mechanism (Figure 4.9).[218]

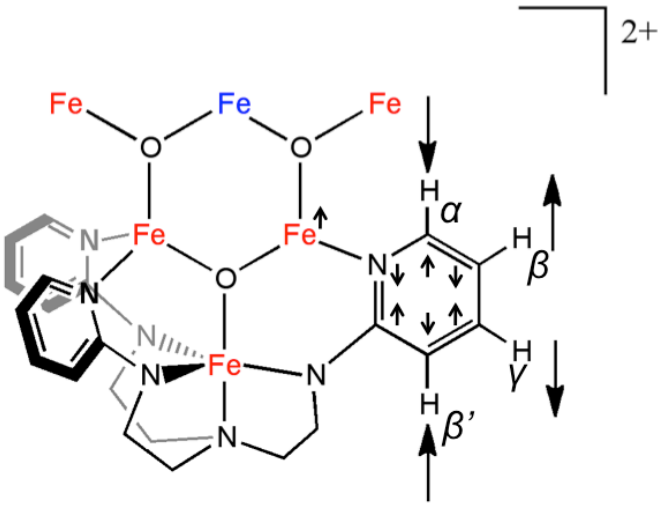

Figure 4.9. Spin polarization mechanism operative in the pyridyl proton chemical shifts of **3** (as well as in the other hexairon compounds **2**, **4**, and **5**). The alternating arrows for the protons indicate alternating chemical shifts (upfield-downfield-upfield-downfield).

Tetrairon Clusters

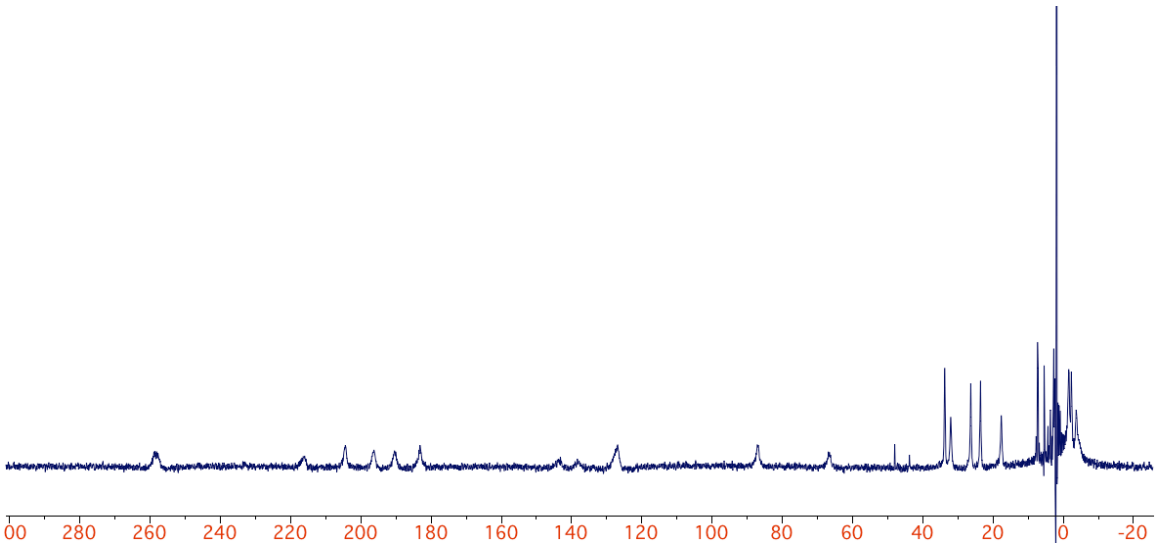

Figure 4.10. ^{1}H NMR spectrum of paramagnetically shifted 2Fe(III)2Fe(II)O **6**.

The ^{1}H NMR spectrum of the 2Fe(III)2Fe(II)O cluster **6** in CD_3CN shows 20 peaks (Figure 4.10). Based on the solid-state structure of **6**, which has approximate C_2 symmetry, all three arms of each py_3tren ligand are distinct, but the two py_3tren ligands

should be equivalent. Hence, all of each py_3tren ligand's protons should be chemically distinct – i.e., 24 peaks should be visible in the NMR spectra. Some of the four "missing" peaks are likely too broad to observe or overlap with other peaks. In the solid state, in contrast to the tricationic hexanuclear cluster **3**, the triflates bind to the pyridyl-ligated Fe centers. It is likely in CD_3CN solution that the triflates are displaced by acetonitrile as ligands. The crystal structure of **6** was obtained from THF layered on a CH_2Cl_2 solution, both solvents that are less donating than acetonitrile.

4.3.3 Mössbauer Spectroscopy

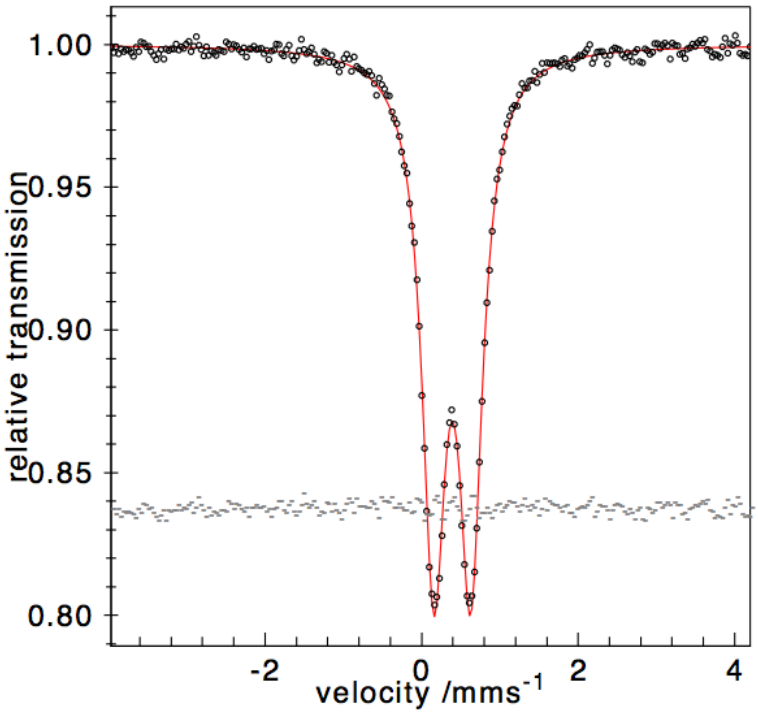

Figure 4.11. Mössbauer spectrum of 6Fe(III)3O **2** recorded at 80 K.

The Mössbauer spectra of compounds 6Fe(III)3O **2**, 5Fe(III)Fe(II)3O **3**, and 4Fe(III)2Fe(II)3O **4** have been collected (Figures 4.11-4.13); their parameters are

recorded in Table X. The spectrum of the 6Fe(III)3O cluster **2** contains only one quadrupole doublet with $\delta = 0.39$ mm s^{-1} and $|\Delta E_Q| = 0.47$ mm s^{-1}. This is at first seemingly counterintuitive given that there are two different Fe sites in the cluster; one might expect that the inner three Fe should give rise to one quadrupole doublet, and the outer three Fe should give rise to a different quadrupole doublet. However, the donor set for the inner Fe (three N, two O) is similar to that of the outer Fe (four N, one O), and evidently they are similar enough to have the same Mössbauer parameters. The isomer shift is consistent with high-spin Fe(III).

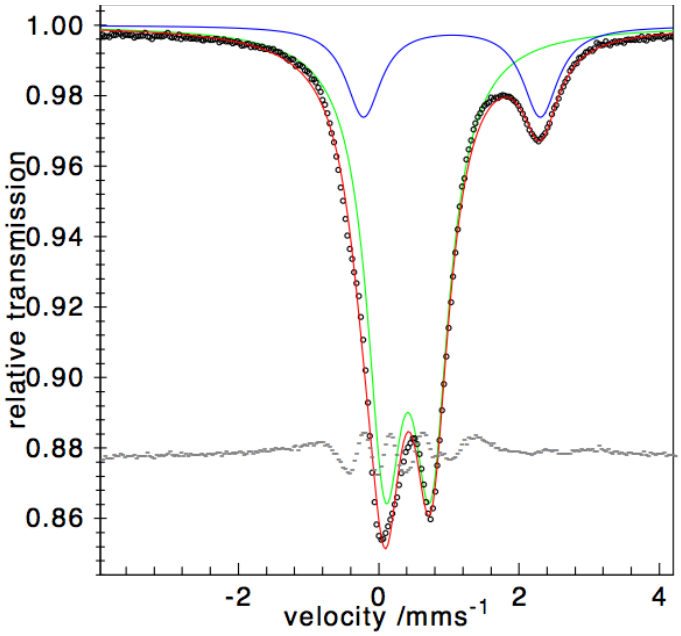

Figure 4.12. Mössbauer spectrum of 5Fe(III)Fe(II)3O **3** recorded at 80 K.

The dicationic 5Fe(III)Fe(II)3O cluster **3** has two different Mössbauer signals. One doublet, with δ and $|\Delta E_Q|$ of 0.42 mm s^{-1} and 0.65 mm s^{-1}, respectively, has a relative intensity of 82%, as expected for five of the six Fe being high-spin Fe(III). The other doublet, with δ and $|\Delta E_Q|$ of 1.04 mm s^{-1} and 2.52 mm s^{-1}, respectively, has a relative

intensity of 18%, as expected for one of the six Fe being high-spin Fe(II). Because two doublets are observed, the valences are localized on the Mössbauer time scale (10^{-7} – 10^{-8} s). Since **3** displays only one quadrupole doublet, it is not possible to tell solely from the Mössbauer spectrum whether the Fe(II) is located in the inner ring or on the outside. However, crystal structure metrics of **5** suggest that Fe(II) is located on the inner ring (*vide supra*). The Mössbauer spectrum is consistent with the expected 5Fe(III)Fe(II) cluster oxidation state based on the molecular charge.

Table 4.5. Mössbauer fitting parameters of compounds **2**, **3**, and **4**.

Compound, overall charge	Isomer shift (δ, mm s^{-1})	Quadrupole splitting ($\lvert\Delta E_Q\rvert$, mm s^{-1})	%
6Fe(III)3O **3,** 3+	0.39	0.47	100
5Fe(III)Fe(II)3O **2**, 2+	0.42 1.04	0.65 2.52	82 18
4Fe(III)2Fe(II)3O **4**, 1+	0.43 0.67 1.01	0.88 1.75 3.10	67 17 17

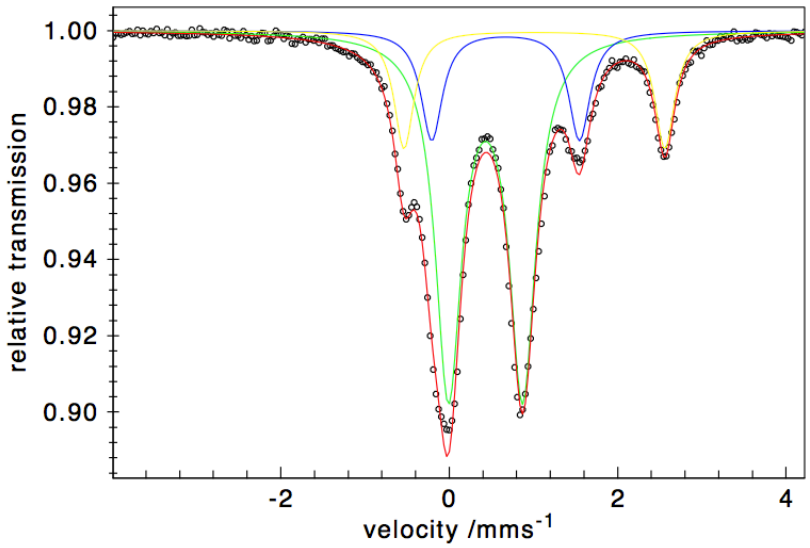

Figure 4.13. Mössbauer spectrum of 4Fe(III)2Fe(II)3O **4** recorded at 80 K.

The monocationic 4Fe(III)2Fe(II)3O cluster **4** shows three quadrupole doublets. One of the three doublets, with δ = 0.43 mm s^{-1} and $|\Delta E_Q|$ = 0.88 mm s^{-1} along with a relative intensity of 67%, corresponds to the expected four high-spin Fe(III) centers. A subspectrum with δ = 1.01 mm s^{-1} and $|\Delta E_Q|$ = 3.10 mm s^{-1}, which has a similar δ to that found in **3**, integrates to only 17% of the total intensity, or one high-spin Fe(II) center in the molecule. The third doublet, with an integration of 17% of the total intensity, δ = 0.67 mm s^{-1}, and $|\Delta E_Q|$ = 1.75 mm s^{-1}, must correspond to a Fe(II) center by virtue of the molecule's monocationic charge, but its parameters are not in line with high-spin Fe(II). The isomer shift is too large to be consistent with low-spin Fe(II).[219] Mononuclear S = 1 Fe(II) compounds have only been definitively identified for four-coordinate geometries, most of these planar.[220] That being said, the isomer shift of the putative S = 1 signal in **4** is only slightly larger than those in select S = 1 Fe(II) compounds (e.g., δ = 0.61 mm s^{-1} in α-Fe(OEP) (OEP = octaethylporphyrin) at 115 K).[221] Intriguingly, it appears that this 4Fe(III)2Fe(II)3O cluster has one high-spin Fe(II) center and one intermediate-spin Fe(II) center coexisting, which is unexpected given that the 5Fe(III)Fe(II)3O cluster **3** and 3Fe(III)3Fe(II)3O cluster **5** contain only high-spin Fe(II) (*vide infra* and *vide supra*). Unfortunately, we do not have magnetic data at this time to identify the spin ground state of **4**.

The observation of localized valences in the dicationic 5Fe(III)Fe(II)3O cluster **3** and the monocationic 4Fe(III)2Fe(II)3O cluster **4** at 80 K would be consistent with the assignment of these compounds as exhibiting either Class I or Class II behavior in the Robin-Day classification system at 80 K.[222] A variable temperature Mössbauer study of **4**

showed that valence localization persisted up to 230 K, the highest temperature studied, ruling out Class III behavior up to 230 K (Figures A3.6 and A3.7, Table A3.1). The observation of intervalence charge transfer (IVCT) bands in the NIR spectra of Fe(II)-containing compounds **3**-**5** suggests that these mixed-valent compounds likely belong to Class II (*vide infra*).

4.3.4 Magnetic Measurements

SQUID magnetometry was collected for 6Fe(III)3O **2**. Magnetic susceptibility data are plotted in Figure 4.14 as χT vs. T. At 290 K, χT for **2** is 4.20 cm^3 K/mol, which is much less than the value for six noninteracting $S = 5/2$ Fe(III) centers (χT = 26.25 cm^3 K/mol). χT decreases to a value of 0.08 at 2 K, which is in line with the value for $S = 0$ (χT = 0). The data are consistent with net strong antiferromagnetic coupling among high-spin Fe(III) centers to give an $S = 0$ ground state (Figure 4.15, top left). As is evident from the aligned spins in the middle of the ring in the top left of Figure 4.15, the system is spin frustrated, because the data are consistent with net antiferromagnetic coupling, but any pictorial depiction of the spins will inevitably include ferromagnetic interactions. Modeling the SQUID without simplifying assumptions is beyond the capabilities of the julx program, which can handle up to four spins, because **2** has six spins and nine exchange interactions (Figure 4.15, top right). The molecule has crystallographic three-fold symmetry, with alternating Fe-O bond lengths in the central $Fe_3(\mu_3\text{-}O)_3$ ring, so the problem could be simplified by treating the smallest number of unique exchange interactions, which is the same as the number of crystallographically unique Fe-O bonds, which is three (an outer Fe-O bond and two unique inner Fe-O bonds) (Figure 4.15,

bottom left). This would correspond to three exchange interactions among six Fe(III) centers (two different sets of three Fe(III) centers). However, this simplified model is still too complex for the julx program.

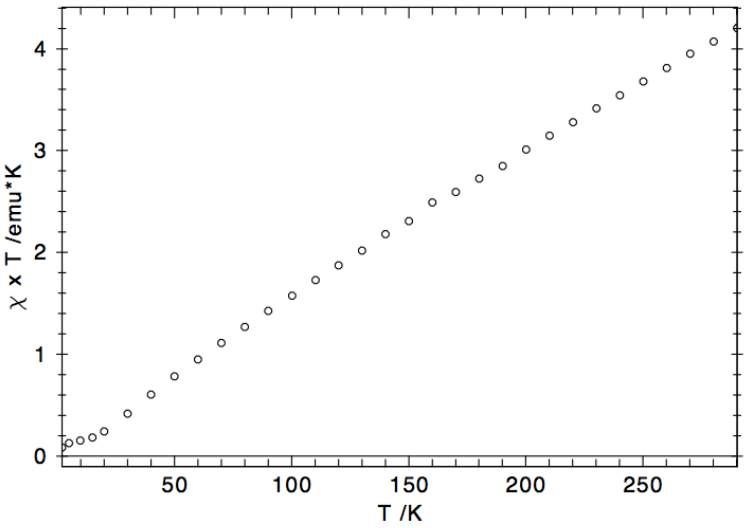

Figure 4.14. Experimental (open circles) χT vs. T plot for **3**.

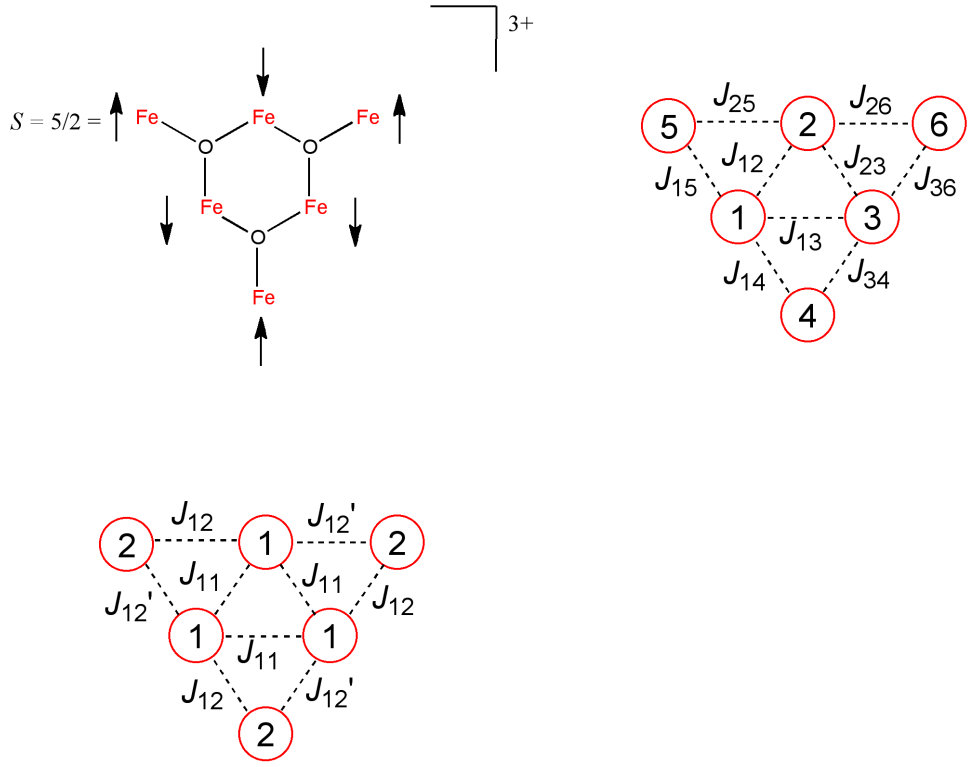

Figure 4.15. Top left: One depiction of net antiferromagnetic coupling in **2** to give an overall $S = 0$ ground state; the system has spin frustration, as evidenced by the ferromagnetic interactions between the Fe in the middle. Top right: the exact exchange coupling model, with six $S = 5/2$ centers and nine exchange coupling interactions. Bottom left: A simplified exchanged coupling model with three unique exchange coupling interactions.

Problems of the sort discussed above are well known in the literature, as high-nuclearity Fe(III) clusters are studied for their interesting magnetic properties, including spin frustration.[223] As a result, magnetostructural correlations have been derived for O-bridged Fe(III) clusters. One of these, developed by Gorun and Lippard specifically using a set of multiply bridged Fe(III)Fe(III) compounds including at least one bridging O atom, assumes that the antiferromagnetic exchange coupling value between two Fe(III) centers depends only on one-half the distance of the shortest superexchange pathway.[224] Longer superexchange pathways and Fe-O-Fe angles are ignored. The Gorun-Lippard

expression is found in Equation 1,

$$J = -Ae^{-BP} \quad (1)$$

where P is one-half the distance of the shortest superexchange pathway, and A and B are parameterization constants equal to 8.763 x 10^{11} cm^{-1} and 12.663 $Å^{-1}$, respectively. Weihe and Güdel later developed an expression that also considers the Fe-O-Fe angle as well as the mean Fe-O length.[225] Christou and coworkers used the Weihe and Güdel expression with a set of O-bridged hexairon clusters but ran a least-squares fitting program to optimize the constants for their compounds.[223] The expression they used is found in Equation 2,

$$J = A(B + C\cos\phi + \cos^2\phi)e^{Dr} \quad (2)$$

where r is the mean Fe-O length, ϕ is the Fe-O-Fe angle, A is 2 x 10^7 cm^{-1}, B is 0.2, C is -1, and D is -7 $Å^{-1}$. J values for each of the unique exchange interactions in **3** are calculated using Equations 1 and 2 and tabulated in Table 4.6.

Table 4.6. Calculated antiferromagnetic exchange coupling constants for each Fe-Fe interaction in **2**.

Fe-Fe Interaction	J_a $(cm^{-1})^a$	J_b $(cm^{-1})^b$
Fe1-Fe2a	-47.9	-18.7
Fe1-Fe2b	-16.7	-26.4
Fe2a-Fe2b	-31.7	-36.7

[a] Calculated using Equation 1. [b] Calculated using Equation 2.

The J values calculated using Equations 1 and 2 only agree well for the Fe2a-Fe2b interaction in **3**. The Fe1-Fe2a interaction nicely illustrates the differences in Equations 1 and 2. The Fe1-Fe2a interaction has the largest J_a value in magnitude out of the three interactions since it has the shortest mean Fe-O bond length. On the other hand, the Fe1-Fe2a interaction has the smallest J_b value in magnitude because it has a much smaller Fe-

O-Fe angle (102º vs. 124º for the other two interactions). These calculated values are similar to those calculated for other polynuclear Fe(III) compounds and only slightly smaller than values derived from fitting experimental data for Fe_3O triangles to a Hamiltonian expression.[223,226]

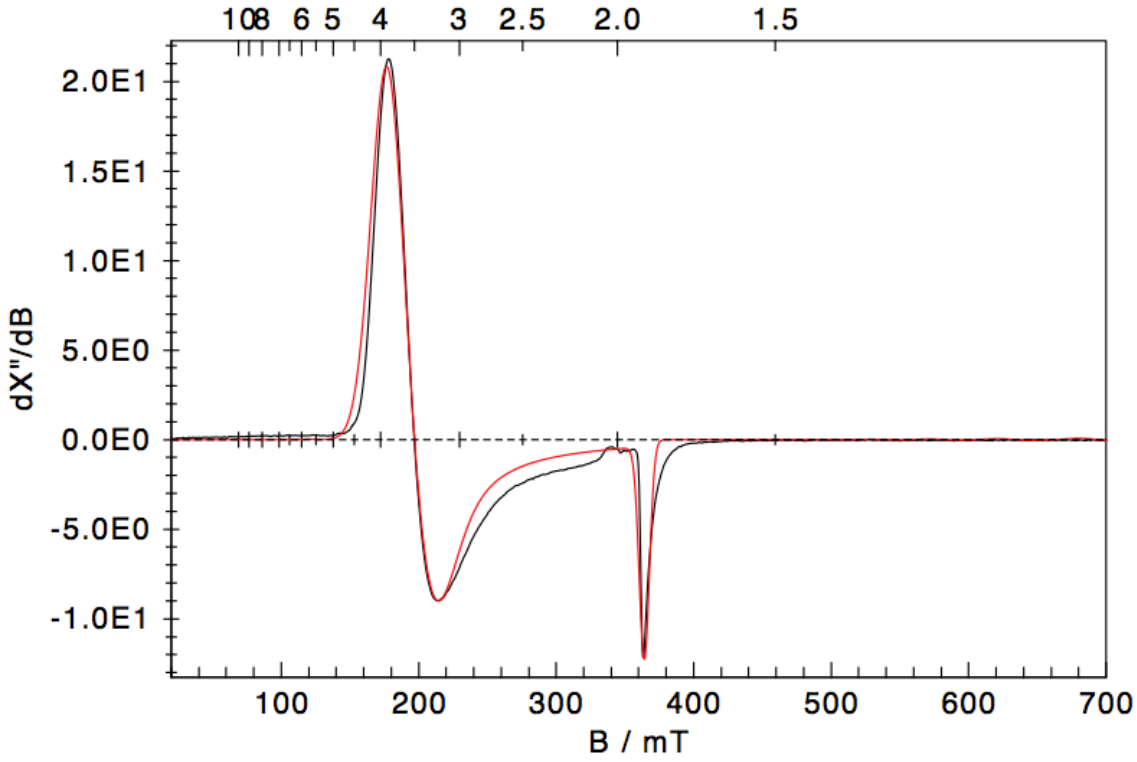

Figure 4.16. EPR spectrum of 3Fe(III)3Fe(II)3O **5** in toluene glass (2.4 K, frequency = 9.646 GHz, modulation to 30 dB). The black trace represents the experimental data, while the red trace represents the model. The spectrum was modeled according to the parameters in the text.

The electron paramagnetic resonance spectrum of 3Fe(III)3Fe(II)3O **5** was collected at 2.4 K in toluene glass (Figure 4.16). It exhibits an axial signal containing effective g values of 3.50 and 1.89 and was modeled with $S = 3/2$, $g_{\perp} = 1.85$, $g_{\parallel} = 1.90$, $D = 4$ cm^{-1}, $E/D = 0.035$, and $W = [410, 300, 100]$ G. Since the cluster contains essentially

C_{3h} symmetry by X-ray crystallography, there are two kinds of Fe: the inner Fe(II) and the outer Fe(III) (*vide supra*). Then, the options to produce a net $S = 3/2$ spin are limited. Our proposal is the following: each pair of outer Fe and inner Fe antiferromagnetically couple to give an S = ½ spin with the spin located on the outer Fe(III) (Figure 4.17, top). The spins of the inner Fe(II) align, or *ferromagnetically* couple, in the middle of the ring. This means that the unpaired electrons of each Fe(III) center are aligned parallel to each other. In other words, three $S = ½$ coupled Fe(II)Fe(III) units ferromagnetically couple to produce the overall $S = 3/2$ spin (Figure 4.17, bottom).

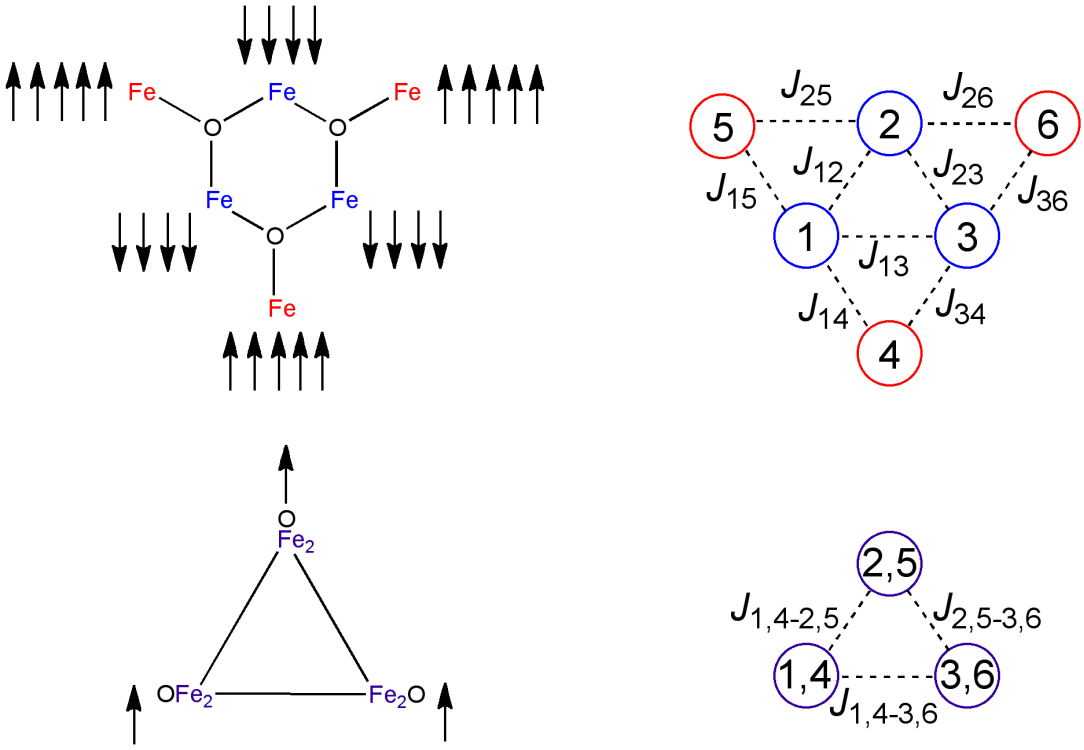

Figure 4.17. Top left: Proposed arrangement of individual spins in 3Fe(III)3Fe(II)3O **5**. Top right: the exact exchange coupling model, with three $S = 5/2$ centers, three S = 2 centers, and nine exchange coupling interactions. Bottom left: Simplified model with one spin for each $S = ½$ Fe_2O^{3+} unit. Bottom right: the simplified exchange coupling model with three interacting Fe_2O^{3+} units.

Support for this proposal comes from comparison of the EPR metrics to those of

mixed-valent Fe(II)Fe(III) metalloenzyme active sites and model compounds. The low g values of $g_{\perp} = 1.85$ and $g_{\|} = 1.90$ are similar to those found in a number of mixed-valent Fe(II)Fe(III) metalloenzymes such as purple acid phosphatase, myo-inositol oxygenase (MIOX), and the hydroxylase and reductase components of methane monooxygenase[227-231] as well as model compounds thereof.[232-234] The D value of 4 cm^{-1} is comparable to that found in biological Fe(II)Fe(III) moieties and model compounds.[232,235]

4.3.5 Cyclic Voltammetry

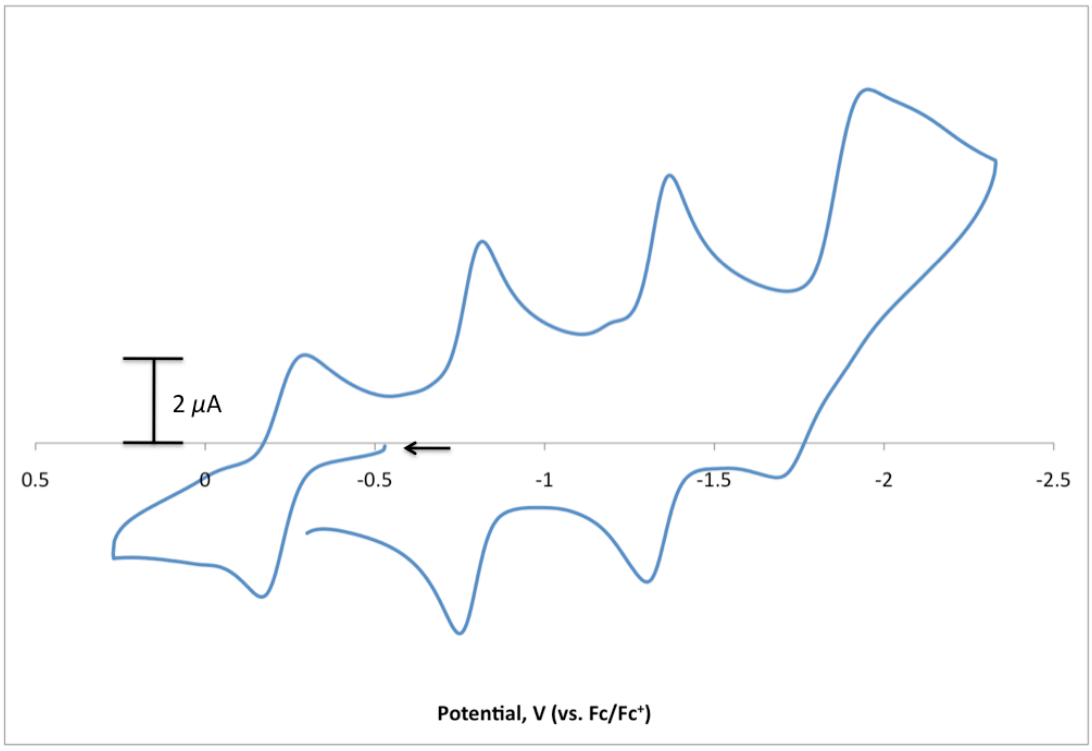

Figure 4.18. Cyclic voltammogram of 5Fe(III)Fe(II)3O **3** (0.05 V/s, 0.1 M $TBAPF_6$ in CH_3CN).

The dication **3** was analyzed by cyclic voltammetry. Three reversible events were observed: one oxidation and two reductions, as well as a quasireversible reduction at -

1.95 V (Figure 4.18, Table 4.7). The reversibility of the oxidation and the first two reductions, as well as their evenly spaced separations of *ca.* 0.55 V, indicates that there are no major structural reorganizations of the core in converting from **2** to **3** to **4** to **5**. It is intriguing to consider the nature of the quasireversible reduction at -1.95 V. At this time, we think it is most likely that this is another Fe-based Fe(III/II) reduction to give what would formally be an anion with four Fe(II) centers and two Fe(III) centers, $Fe_6O_3(L)_3^-$; however, this anion is unstable on the CV timescale. Figure 4.19 includes the three reversible electrochemical relationships of the hexairon clusters, as well as the formal two-electron redox relationship of the $Fe_4O(L)_2$ tetrairon clusters **6** and **7**, which is based on the crystal structures, though we do not have electrochemical data for this pair.

Table 4.7. Table of oxidation and reduction potentials of 5Fe(III)Fe(II)3O **3**.

Event	Potential, $E°'/E_{pc}$, V[a]	ΔE, V[b]	$i_{p,a}/i_{p,c}$[e]	Assignment
Oxidation	-0.22	0.093	0.99	6Fe(III)/5Fe(III)Fe(II)
First reduction	-0.79	0.066	0.97	5Fe(III)Fe(II)/4Fe(III)2Fe(II)
Second reduction	-1.34	0.066	1.01	4Fe(III)2Fe(II)/3Fe(III)3Fe(II)
Third reduction	*-1.95*[cd]	0.27[d]	0.38[d]	3Fe(III)3Fe(II)/2Fe(III)4Fe(II)

[a] All values are against Fc/Fc^+. [b] The peak-to-peak separation is defined as $\Delta E = E_{pc} - E_{pa}$. Values are calculated at 0.01 V/s unless otherwise noted. [c] The third reduction is quasireversible, and so the E_{pc} is tabulated. [d] Calculated at 0.05 V/s. [e] All values are calculated at 0.01 V/s unless otherwise noted.

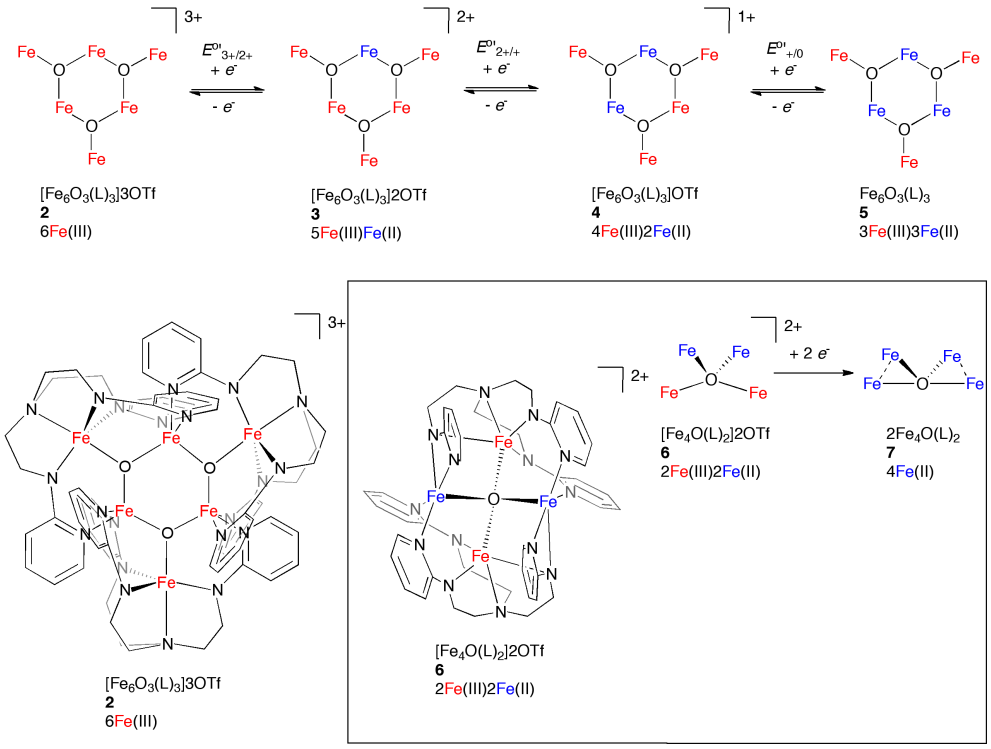

Figure 4.19. Electrochemical relationships of the four hexairon clusters **2**-**5** and the two tetrairon clusters **6** and **7**.

4.3.6 UV-Vis-NIR Spectroscopy

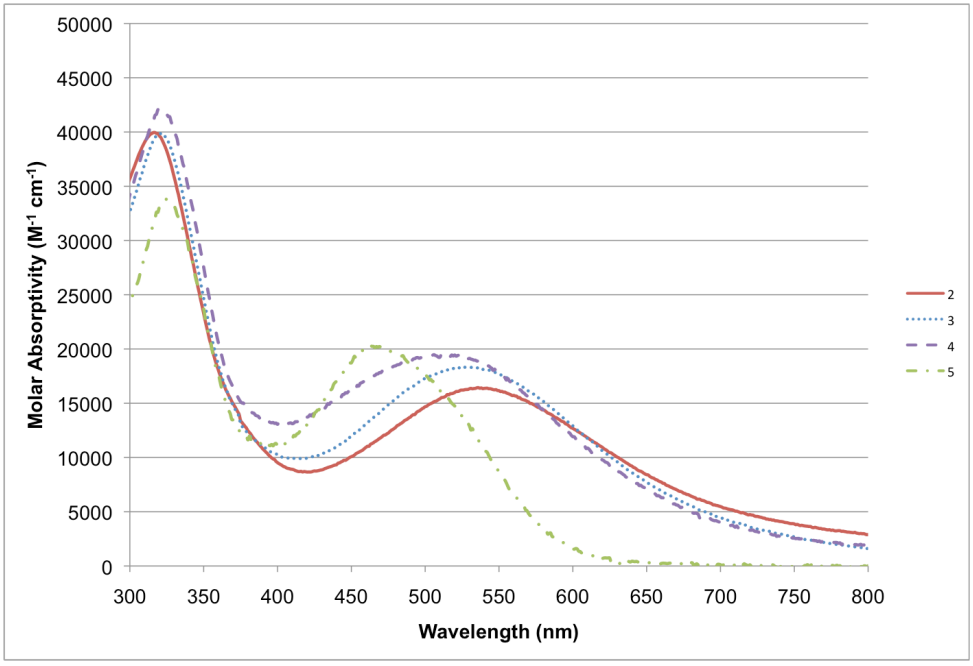

Figure 4.20. UV-Vis spectra of the clusters **2**-**5**. The red solid line is the spectrum of 6Fe(III)3O **2** in CH_3CN, the blue squares represent the spectrum of 5Fe(III)Fe(II)3O **3** in CH_3CN, the purple dashes are the spectrum of 4Fe(III)2Fe(II)3O **4** in CH_2Cl_2, and the green alternating squares and dashes are the spectrum of 3Fe(III)3Fe(II)3O **5** in toluene.

The clusters **2**-**4** are all different shades of purple, whereas the neutral cluster 3Fe(III)3Fe(II)3O **5** is red. The UV-Vis spectra of the clusters display a visible feature that increases in energy as the clusters become more reduced (Figure 4.20). Due to the intensity of the transition (~16,000-~20,000 M^{-1} cm^{-1}), it can be confidently assigned as a charge transfer band. Given that **3**, which has only Fe(III) centers, has this feature, it is likely an LMCT transition: either an amide-to-Fe(III) charge transfer or an oxide-to-Fe(III) charge transfer. A mononuclear Fe(III) compound would be a good control for the amide LMCT scenario, but no mononuclear Fe(III) compound in the py_3tren ligand has been structurally characterized to date. Since we think that the inner Fe centers are the

ones that are reduced to Fe(II), then the outer Fe centers (which remain Fe(III) in the whole series) have the metal acceptor orbitals in the LMCT band. This LMCT band shifts higher in energy progressing from the 6Fe(III)3O cluster **2** (λ_{max} = 512 nm) to the 3Fe(III)3Fe(II)3O cluster **5** (λ_{max} = 463 nm).

The following constitutes a rationalization for the observed increase in the energy of the LMCT transition going from 6Fe(III)3O **2** to 3Fe(III)3Fe(II)3O **5** (Figure 4.21). Going by the crystal structures, the Fe_{outer}-N_{am} and Fe_{outer}-N_{ap} bond distances are longer in **5** than in **2**. The Fe_{outer}-O bond distance is *shorter* in **5** than in **2**. The d_{x2-y2} and d_{xy} orbitals, which are σ- and π-antibonding with respect to the amide sp^2 and p orbitals, respectively, must drop in energy progressing from **2** to **5** due to the Fe_{outer}-N_{am} bond lengthening. The d_{z2} and d_{xz} orbitals, which are σ- and π-antibonding with respect to the oxide sp^2 and p orbitals, respectively, must *increase* in energy in going from **2** to **5** (while the Fe_{outer}-N_{ap} bond lengthens, this likely has a weaker effect than the Fe_{outer}-O bond shortening as a tertiary amine is a poorer ligand than an oxide, and the Fe_{outer}-O bonds are longer than the Fe_{outer}-N_{ap} bonds). The d_{yz} orbital, which is nonbonding with respect to the ligand orbitals, should not change in energy in going from **2** to **5**. Therefore, the increase in the energy of the LMCT band in going from **2** to **5** can be explained if the Fe(III) acceptor orbital is either the d_{xz} or the d_{z2}.

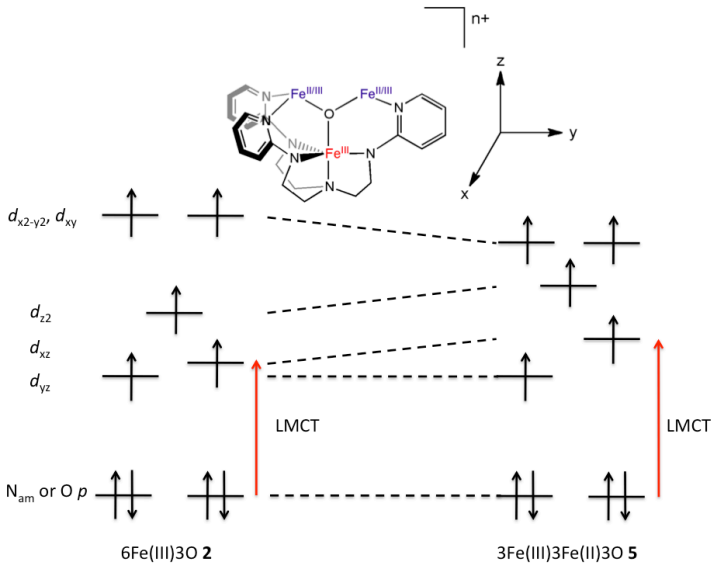

Figure 4.21. Molecular orbital rationalization for the increase in energy of the LMCT by UV-Vis spectroscopy in progressing from 6Fe(III)3O **2** to 3Fe(III)3Fe(II)3O **5**. The coordinate system is provided on the top right.

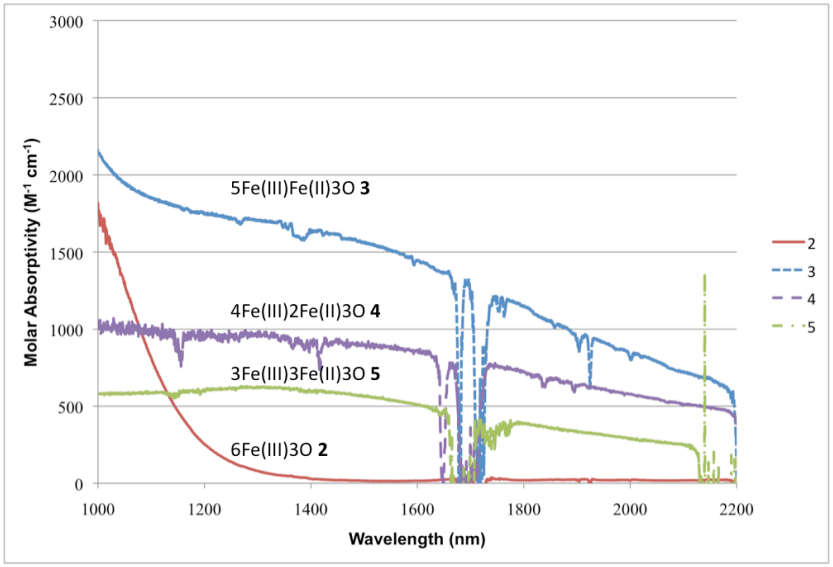

Figure 4.22. NIR spectra of the clusters **2**-**5**. The spectra are identified directly on the figure as well as in the legend. The red solid line is the spectrum of **3** in CH_3CN, the blue squares represent the spectrum of **2** in CH_3CN, the purple dashes are the spectrum of **4** in CH_2Cl_2, and the green alternating squares and dashes are the spectrum of **5** in toluene.

A broad near-IR feature is seen in the spectra of the Fe(II)-containing clusters **3**, **4**, and **5** (Figure 4.22). Because **2** lacks this feature, the transition likely involves Fe(II). In the cases of **3** and **4**, it appears as a shoulder, whereas a maximum is visible in the neutral cluster **5** at 1277 nm with an extinction coefficient of 630 M^{-1} cm^{-1}. The monoiron(II) compound K[Fe(py_3tren)] has a NIR feature, but its maximum appears at 1650 nm with an extinction coefficient of only 40 M^{-1} cm^{-1}. Due to the intensity of the transition (ε_{max} = ~600-~1600 M^{-1} cm^{-1}), the significant difference in the energy of the maximum compared to that of K[Fe(py_3tren)], and the breadth of the transition, it is most likely that this is a Class II IVCT band. While the transitions of **3** and **4** appear as shoulders of the visible features, the transition of **5** is separated enough from the visible feature so that the maximum is visible at 1277 nm (7831 cm^{-1}). For this reason, the full width half maximum (FWHM) can be calculated as the energy at half the absorptivity of the maximum (315 M^{-1} cm^{-1}) can be identified at 1954 nm (5117 cm^{-1}). Then, the FWHM is twice the difference of the energy at maximum absorptivity and the energy at half maximum, or 5428 cm^{-1}. The FWHM and ε_{max} values are in line with typical Class II (dinuclear) systems,[222] though extension of the equations derived for dinuclear systems to multinuclear systems may represent an oversimplification. While the solvent dependence of the energy of the maximum is frequently used as a probe for distinguishing between Class II and Class II-III,[222] the poor solubility of **5** has precluded these efforts.

The observation of localized valences in the dicationic 5Fe(III)Fe(II)3O cluster **3** and the monocationic 4Fe(III)2Fe(II)3O cluster **4** at 80 K by Mössbauer spectroscopy would be consistent with the assignment of these compounds as exhibiting either Class I

or Class II behavior in the Robin-Day classification system at 80 K.[222] A variable temperature Mössbauer study of **4** showed that valence localization persisted up to 230 K, the highest temperature studied, ruling out Class III behavior up to 230 K (Figures A3.6 and A3.7, Table A3.1). Since the room temperature UV-Vis spectra of 5Fe(III)Fe(II)3O **3**, 4Fe(III)2Fe(II)3O **4**, and 3Fe(III)3Fe(II)3O **5** show IVCT bands in the NIR region (Figure 4.22), these mixed-valent compounds must be Class II or Class III at room temperature. Given the different inner and outer Fe binding environments, it seems unlikely that these compounds would exhibit Class III behavior. Since the μ_3-O bridges are effective at mediating communication between metal centers (consider the $S = 0$ ground state of 6Fe(III)3O **2** and the $S = 3/2$ ground state of 3Fe(III)3Fe(II)3O **5**, *vide infra*), it also seems unlikely that the compounds would exhibit Class I behavior at lower temperatures.[222] Given all the evidence, we believe that mixed-valent compounds **3**-**5** are best described as Class II complexes in the Robin-Day classification scheme from 2 K to room temperature.

4.4 Conclusions

Four planar $Fe_6O_3(L)_3$ clusters, differing only in the oxidation state of the core (6Fe(III)3O, 5Fe(III)1Fe(II)3O, 4Fe(III)2Fe(II)3O, and 3Fe(III)3Fe(II)3O), have been synthesized and characterized, and the crystal structures of two $Fe_4O(L)_2$ clusters (2Fe(III)2Fe(II)O and 4Fe(II)O) have been obtained. The ^{1}H NMR spectra of the four $Fe_6O_3(L)_3^{n+}$ clusters have the same pattern and differ only in the isotropic shifts of the resonances, establishing that the four clusters have the same solution state C_{3h} structure. A combination of Mössbauer spectroscopy and SQUID magnetometry on the 6Fe(III)3O cluster shows that it can be described as six $S = 3/2$ centers that antiferromagnetically couple to give an $S = 0$ ground state for the cluster. The mixed-valent 5Fe(III)1Fe(II)3O and 4Fe(III)2Fe(II)3O clusters have two and three subspectra, respectively, consistent with localized valences on the Mössbauer time scale. For the 5Fe(III)1Fe(II)3O cluster, the Mössbauer spectrum is consistent with five $S = 3/2$ Fe(III) centers and one $S = 2$ Fe(II) center. Mössbauer spectroscopy shows that the 4Fe(III)2Fe(II)3O cluster has four $S = 3/2$ Fe(III) centers, one $S = 2$ Fe(II) center, and an Fe(II) center that is most likely $S = 1$. The EPR spectrum of the 3Fe(III)3Fe(II)3O cluster demonstrates that the ground state is $S = 3/2$. X-ray crystallography on the 6Fe(III)3O and 3Fe(III)3Fe(II)3O clusters establishes that their cores are isostructural, and that the biggest change in the core upon reduction is that the bridging oxide ligands "stretch out." X-ray crystallography on the 2Fe(III)2Fe(II)O and 4Fe(II)O tetrairon clusters, which have rare oxidation states for iron clusters, shows they have unusual distorted square planar and distorted seesaw geometries, respectively. The facile redox chemistry in the hexairon series, combined

with the isostructural nature of the cores and the coordinatively unsaturated Fe centers, make the 4Fe(III)2Fe(II)3O and 3Fe(III)3Fe(II)3O clusters promising starting points for multielectron reactivity studies.

4.5 Experimental Section

General Considerations

Unless otherwise stated, all manipulations were performed under an N_2 atmosphere inside a glovebox. Standard solvents were deoxygenated by sparging with dinitrogen and dried by passing through activated alumina columns of a SG Water solvent purification system. Benzylpotassium (KBn),[104] $[Fe(CH_3CN)_6][OTf]_2$,[236] H_3py_3tren,[145] iodosobenzene,[237,238] and isopropyl 2-iodylbenzoate[239] were prepared according to literature methods. Deuterated solvents were purchased from Cambridge Isotope Laboratories, Inc., degassed via freeze-pump-thaw cycles, dried over activated alumina, and stored over activated 4 Å molecular sieves. All other reagents were purchased from Aldrich or Strem and used without further purification. Elemental analyses were performed by Complete Analysis Laboratories, Inc. (Parsippany, NJ) or Robertson Microlit Laboratories (Ledgewood, NJ).

Synthesis of FeFe(OTf)(py_3tren) 1. H_3py_3tren (539 mg, 1.43 mmol) was deprotonated with benzylpotassium (571 mg, 4.38 mmol) in THF. After 20 minutes, solid $[Fe(CH_3CN)_6][OTf]_2$ (1.81 x 103 mg, 2.85 mmol) was added. The reaction was stirred overnight. Then, the volatiles were removed *in vacuo*. The crude reaction was filtered through Celite in DCM and pumped down. The DCM filtration and filtrate pumping down procedure was performed a total of four times to remove as much potassium triflate as possible. Then, after layering a DCM solution of the crude with hexanes, 130 mg of large crystals (14% yield) was obtained. For practical purposes, the DCM filtration procedure is repeated until the crude yield is under 100%, and then the resulting powder

can be used without further purification for large scale cluster synthesis. ^{1}H NMR (500 MHz, d_8-THF): δ 196, 91, 49, -2.5, -14, -23. ^{19}F NMR (282 MHz, CD_3CN): δ -77.63. Anal. Calcd for $C_{22}H_{24}N_7Fe_2F_3SO_3$: C, 41.60; H, 3.81; N, 15.43. Found: C, 41.69; H, 3.93; N, 15.38.

Synthesis of [(FeFe(μ_3-O)(py$_3$tren))$_3$][OTf]$_2$ 3. Iodosobenzene (87 mg, 0.395 mmol) was added to **1** (247 mg, 0.389 mmol) in dichloromethane at dry ice/acetone temperatures. The reaction was immediately allowed to warm to room temperature. After stirring overnight, the volatiles were removed in vacuo. Then, the residue was stirred in THF overnight. Afterwards, the slurry was filtered, and the precipitate washed with THF. After drying the precipitate *in vacuo* for several hours, a purple solid (175 mg, 74% relative to iodosobenzene) was obtained. ^{1}H NMR (500 MHz, CD_3CN): δ 330, 281, 232, 145, 143, 133, 48, 44, 27, 20, -42, -46, -50, -51. ^{19}F NMR (470 MHz, CD_3CN): δ -78.65. UV-Vis-NIR (CH_3CN) λ_{max} (ε, L mol^{-1} cm^{-1}): 322 (39,900), 529 (18,300), 1342 (1,700). ESI-MS-TOF *m/z*: $[M + H]^{2+}$ calc'd for $C_{63}H_{72}N_{21}Fe_6O_3$, 753.1107; found 753.1163. Anal. Calcd for $C_{65}H_{72}N_{21}Fe_6F_6S_2O_9$: C, 43.26; H, 4.02; N, 16.30. Found: C, 43.31; H, 3.99; N, 16.24.

Synthesis of [(FeFe(μ_3-O)(py$_3$tren))$_3$][OTf]$_3$ 2. Solid AgOTf (21.6 mg, 0.0841 mmol) was added to **2** in 10 mL CH_3CN. After stirring overnight, the reaction was filtered to remove Ag(0). The filtrate was pumped down, and then the solids were slurried four times with 1 mL THF and filtered off to give a purple solid (126 mg, 77% yield). X-ray

quality crystals were obtained by layering a DCM solution with THF. ^{1}H NMR (300 MHz, CD_3CN): δ 288, 247, 183, 122, 109, 40, 34, 30, 23, -29, -33, -35, -37. UV-Vis-NIR (CH_3CN) λ_{max} (ε, L mol^{-1} cm^{-1}): 316 (40,000), 512 (19,500).

Synthesis of [(FeFe(μ_3-O)(py$_3$tren))$_3$][OTf] 4. Solid Cp_2*Co (46.3 mg, 0.141 mmol) was added to **2** (249 mg, 0.135 mmol) in 15 ml CH_3CN. After stirring overnight, the reaction had turned into a suspension. The suspension was filtered onto a frit, leaving behind a dark-colored precipitate. The precipitate was washed once with 3 mL CH_3CN and dried *in vacuo* overnight. A pink-purple powder of **4** was obtained (133 mg, 59% yield). ^{1}H NMR (300 MHz, CD_2Cl_2): δ 260, 215, 183, 110, 104, 98, 40, 35, 26, -2, -26, -34, -37, -40. ^{19}F NMR (282 MHz, CD_2Cl_2): δ -79.10. UV-Vis-NIR (CH_2Cl_2) λ_{max} (ε, L mol^{-1} cm^{-1}): 321 (42,100), 512 (19,500), 1277 (1,000). Anal. Calcd for $C_{64}H_{72}N_{21}Fe_6F_3SO_6$: C, 46.43; H, 4.38; N, 17.77. Found: C, 45.92; H, 4.59; N, 17.30.

Synthesis of [(FeFe(μ_3-O)(py$_3$tren))$_3$] 5. Solid Cp_2*Co (109 mg, 0.331 mmol) was added **2** (289 mg, 0.157 mmol) in 15 ml CH_3CN. After stirring overnight, the reaction had turned into a suspension. The suspension was filtered onto a frit, leaving behind a reddish-colored precipitate. The precipitate was washed once with 2 mL CH_3CN and dried *in vacuo* overnight. The precipitate was extracted with 30 mL toluene and layered with pentane. Red crystals of **5** were obtained (16.3 mg, 7% yield). X-ray quality crystals were obtained by layering a benzene solution with pentane. ^{1}H NMR (500 MHz, d_8-

toluene): δ 206, 181, 158, 85, 76, 69, 33, 30, 5.6, -13, -25, -29, -31, -33. UV-Vis-NIR (toluene) λ_{max} (ε, L mol^{-1} cm^{-1}): 324 (33,800), 463 (20,300), 1277 (630).

Synthesis of [(FeFe(py$_3$tren))$_2$(μ_4-O)][OTf]$_2$ 6. AgOTf (42.6 mg, 0.166 mmol) was added to **1** (103 mg, 0.162 mmol) in THF. The reaction instantly turned blue, followed by a more purple color. After stirring overnight, the reaction was pumped down, the solids dissolved in 4 mL CH_3CN, filtered, and layered with Et_2O. This gave **6** (29.8 mg, 0.0218 mmol) as a powder with a very small amount of **2** present by ^{1}H NMR spectroscopy (27% yield). X-ray quality crystals were grown from a CH_2Cl_2 solution layered with THF. ^{1}H NMR (300 MHz, CD_3CN): δ 259, 216, 204, 196, 190, 183, 144, 138, 127, 87, 67, 34, 32, 26, 24, 18, 2.7, -1.6, -2.3, -3.7.

Synthesis of [(FeFe(py$_3$tren))$_2$(μ_4-O)] 7. H$_3$py$_3$tren (287 mg, 0.760 mmol) was deprotonated with BnK (319 mg, 2.45 mmol) in 12 mL THF. Then, $FeCl_2(THF)_{1.5}$ (358 mg, 1.52 mmol) was added as a solid. The reaction was stirred overnight, then pumped down *in vacuo*. The solids were taken up in CH_2Cl_2, filtered, and layered with Et_2O. This procedure provided a single crystal of **7** suitable for X-ray diffraction. A ^{1}H NMR spectrum of the recrystallized material showed a mixture of FeFeCl(py$_3$tren) and a complicated set of paramagnetic peaks not belonging to FeFeCl(py$_3$tren).

X-Ray Crystallographic Data Collection and Refinement of the Structures

Single crystals of [(FeFe(μ_3-O)(py$_3$tren))$_3$][OTf]$_3$ **3** and [(FeFe(py$_3$tren))$_2$(μ_4-O)][OTf]$_2$ **6** were grown from a DCM solution layered with THF. Single crystals of [(FeFe(μ_3-

O)(py_3tren))$_3$] **5** were grown from a benzene solution layered with pentane. Single crystals of [(FeFe(py_3tren))$_2$(μ_4-O)] **7** were grown from a DCM solution layered with Et_2O. The data collection for **3** and **6** was carried out using Mo-Kα radiation (graphite monochromator), and the data collection for **5** was carried out using Cu-Kα radiation (monochromator with normal parabolic mirrors). A single crystal of **7** were mounted on a glass fiber and cooled to 100 K using an Oxford Instruments Cryojet cryostat. The Bruker D8 diffractometer, integrated with an APEX-II CCD detector, was modified for synchrotron use at the ChemMatCARS 15-ID-B beam line at the Advanced Photon Source (Argonne National Laboratory). The scan at 30.0 keV (λ=0.41328 Å) gave a least-squares refinement of all model positional- and displacement parameters to 0.5 Å resolution. The data intensity was corrected for absorption and decay (SADABS). Final cell constants were obtained from least squares fits of all measured reflections. The structure was solved using SHELXS-97 and refined using SHELXL-97. A direct-methods solution was calculated which provided most non-hydrogen atoms from the E-map. Full-matrix least squares / difference Fourier cycles were performed to locate the remaining non-hydrogen atoms. All non-hydrogen atoms were refined with anisotropic displacement parameters. Hydrogen atoms were placed in ideally and refined as riding atoms with relative isotropic displacement parameters. A disordered benzene molecule in **5** could not be refined adequately, and so it was removed and the structure treated with SQUEEZE (PLATON). A significant void at (0, 0, 0) was found with a volume of 244 $Å^3$ and 60 electrons. Crystallographic data for **3**, **5**, **6**, and **7** are found in Table X.

Table 4.8. Crystallographic details for [(FeFe(μ_3-O)(py$_3$tren))$_3$][OTf]$_3$ **2**, [(FeFe(μ_3-O)(py$_3$tren))$_3$ **5**, and [(FeFe(py$_3$tren))$_2$(μ_4-O)][OTf]$_2$ **6**, and [(FeFe(py$_3$tren))$_2$(μ_4-O)] **7**.

	2	**5**	**6**	**7**
chemical formula	$C_{64}H_{72}N_{21}Fe_6S_3O_{12}F_9$	$C_{63}H_{72}N_{21}Fe_6O_3 \bullet 2.5C_6H_6$	$C_{44}H_{48}N_{14}Fe_4O_7S_2F_6$	$C_{42}H_{48}N_{14}Fe_4O \bullet 2CH_2Cl_2$
formula weight	1953.73	1701.79	1286.48	1158.20
crystal system	trigonal	triclinic	triclinic	monoclinic
space group	*R*-3	*P*-1	*P*-1	$P2_1/c$
a (Å)	20.1642(8)	12.5908(4)	11.9816(10)	12.7838(8)
b (Å)	20.1642(8)	15.8415(4)	12.6400(10)	20.4024(14)
c (Å)	37.9306(14)	20.3434(6)	19.4658(16)	19.1348(13)
α (deg)	90	85.764(1)	98.661(1)	90
β (deg)	90	87.599(2)	100.422(1)	106.146(1)
γ (deg)	120	74.036(2)	116.472(1)	90
V (Å^3)	13356.2(9)	3889.5(2)	2504.3(4)	4793.9(6)
Z	6	2	2	4
D_{calcd} (g cm^{-3})	1.457	1.453	1.706	1.605
l (Å), μ (mm^{-1})	0.71073, 1.105	1.54178, 9.236	0.71073, 1.307	0.41328, 1.462
T (K)	173(2)	123(2)	173(2)	100(2)
θ range (deg)	1.28 to 27.49	1.87 to 26.37	1.87 to 26.37	1.94 to 36.36
reflns collected	51930	51601	24194	58492
unique reflns	4545	14186	7277	21868
data/restraints/parameters	4545 / 0 / 352	14186 / 0 / 973	7277 / 0 / 694	21868 / 0 / 604
R_1, wR_2 ($I > 2\sigma(I)$)	0.0411, 0.1038	0.0488, 0.1006	0.0405, 0.0919	0.0724, 0.1699

Physical Measurements

NMR spectra were collected on Varian Inova 300 and 500 MHz spectrometers or a Bruker Avance III 500 MHz spectrometer. ESI-MS data were collected on a Bruker BioTOF II instrument and calibrated against an internal PEG standard. The ESI-MS data were simulated with the IsotopePattern program (Bruker Daltonics). UV-Vis-NIR absorption data were collected on a Cary-14 spectrophotometer. Cyclic voltammetry was conducted using a CH Instruments 600 electrochemical analyzer. The one-cell setup

utilized a platinum working electrode, Ag wire counter electrode, and $Ag/AgNO_3$ reference electrode in CH_3CN. Analyte solutions were prepared in a CH_3CN solution of NBu_4PF_6 (0.1 M) and referenced externally to the Fc/Fc^+ redox couple. Mössbauer data were recorded on an alternating constant acceleration spectrometer. The minimum experimental line width was 0.24 mm s^{-1} (full width at half-height). The $^{57}Co/Rh$ source (1.8 GBq) was positioned at rt inside the gap of the magnet system at a zero-field position. Isomer shifts are quoted relative to iron metal at 300 K.

Magnetic susceptibility data were measured from powder samples of solid material in the temperature range 2 - 300 K by using a SQUID susceptometer with a field of 1.0 T (MPMS-7, Quantum Design, calibrated with standard palladium reference sample, error <2%).

Chapter 5

A Reactivity Study of Dioxygen with a Diferrous Compound Containing an Iron-Iron Bond: An All-Ferric Cluster Is the Thermodynamic Sink, and Mixed-Valent Clusters Are Intermediates

5.1 Overview

The reactivity of O_2 with a diferrous compound, $[Fe_2(L)](OTf)$, is reported. One of the hexairon clusters reported in the previous chapter, 6Fe(III)3O, is the thermodynamic sink when $[Fe_2(L)](OTf)$ is exposed to an atmosphere of O_2. Two of the mixed-valent clusters reported in the previous chapter, the tetrairon cluster 2Fe(III)2Fe(II)O and the hexairon cluster 5Fe(III)Fe(II)3O, are identified by ^{1}H NMR spectroscopy as intermediates in the reaction. The addition of a half equivalent of O_2 to $[Fe_2(L)](OTf)$ provides 2Fe(III)2Fe(II)O, while the addition of one equivalent of O_2 to $[Fe_2(L)](OTf)$ provides 5Fe(III)Fe(II)3O. The complex 2Fe(III)2Fe(II)O is identified by ^{1}H NMR spectroscopy as an intermediate in the latter reaction. Exposing 2Fe(III)2Fe(II)O to an atmosphere of O_2 gives 6Fe(III)3O as the only product identified by ^{1}H NMR spectroscopy, with no intermediates observed. The generation of 5Fe(III)Fe(II)3O by the addition of one equivalent of 95% isotopically enriched $^{18}O_2$ to $[Fe_2(L)](OTf)$ was studied by ESI-MS, and the mass spectrum of this reaction was modeled such that 39% of the oxygen content is ^{16}O, and 61% is ^{18}O. These numbers are not quite far off the 36% ^{16}O / 64% ^{18}O ratio that would be expected if one O atom derived from water and two O atoms derived from the 95% isotopically enriched $^{18}O_2$. With this preliminary data, we speculate upon mechanisms for the conversion of $[Fe_2(L)](OTf)$ to 2Fe(III)2Fe(II)O and of 2Fe(III)2Fe(II)O to 5Fe(III)Fe(II)3O. Experiments to learn more about the system are proposed.

5.2 Introduction

The metalloenzyme soluble methane monooxygenase (sMMO) oxidizes methane to methanol, a transformation of great interest since methanol is proposed as an alternative fuel, and the C-H bond of methane is one of the strongest known.[8] Hence, one strategy for developing synthetic oxidation catalysts involves utilizing design principles from sMMO, in particular implementing two iron centers.[8,240-242] The oxidation state of the sMMO enzyme active site, and a number of other diiron enzyme active sites (ribonucleotide reductase, hemerythrin), that reacts with dioxygen is Fe(II)Fe(II). Herculean efforts in this area have been expended in characterizing the Fe(II)Fe(II) model compounds and understanding their reactivity with O_2.[8]

While some of these enzymes are often characterized in a Fe(II)Fe(III) oxidation state, it was thought that the mixed-valent oxidation state was not catalytically relevant in any diiron enzyme.[227-230] This belief changed when it was discovered that the enzyme *myo*-inositol oxygenase (MIOX), which catalyzes the conversion of *myo*-inositol (cyclohexan-1,2,3,5/4,6-hexa-ol or MI) to D-glucuronate (DG) – a C-C bond cleaving, ring-opening, 4-electron oxidation – reacts with dioxygen in the Fe(II)Fe(III) oxidation state to produce a Fe(III)Fe(III) superoxide intermediate.[231,243] The superoxide intermediate then abstracts a hydrogen atom from *myo*-inositol, and ring opening follows (Scheme 5.1). The novelty of the mixed-valent state in MIOX and its unusual reactivity, as well as the general difficulty in preparing diiron active sites in the mixed-valent state,[232] prompts studies of mixed-valent model compounds.[232-234]

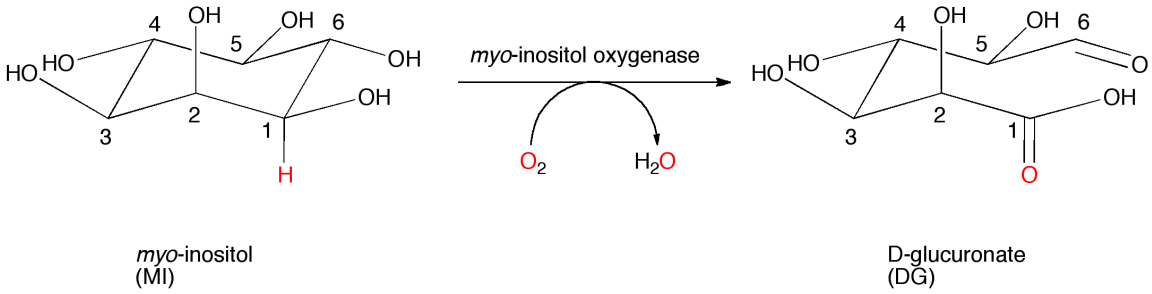

Scheme 5.1. The reaction catalyzed by MIOX.

We are interested in the reactivity of first-row transition metal compounds with metal-metal bonds. Recently, we demonstrated that the 2Fe(II) complex FeFeCl(py_3tren) (py_3tren = *N*,*N*,*N*-tris(2-(2-pyridylamino)ethyl)amine) has an iron-iron single bond. We have undertaken the study of the reaction of O_2 with a very similar compound, FeFe(OTf)(py_3tren), and show that the thermodynamic sink under an atmosphere of O_2 is a 6Fe(III) cluster with oxide bridges. Two clusters with bridging oxide ligands, both in mixed-valent states, have been identified as intermediates in this transformation. One of the intermediate steps involves the conversion of a *tetrairon* mixed-valent cluster into a *hexairon* mixed-valent cluster. In this preliminary study, we present and summarize data of these reactions with O_2. Additionally, we speculate on possible mechanisms of this reactivity and suggest future experiments.

5.3 Results and Discussion

5.3.1 O_2 Reactivity Studies

The O_2 activation studies commenced with the addition of atmospheric O_2 to FeFe(OTf)(py_3tren) **1** (2Fe(II)) in CD_3CN. A rapid color change from red to purple was observed. A ^{1}H NMR spectrum taken five minutes after addition revealed a complex set of paramagnetic resonances (Figure 5.1). Some of the peaks present were identified as belonging to the 5Fe(III)Fe(II)3O cluster [(FeFe(μ_3-O)(py_3tren))$_3$][OTf]$_2$ **3** (py_3tren = L). A second set of peaks was attributed to the 2Fe(III)2Fe(II)O cluster [{Fe_2(L)}$_2$(μ_4-O)](OTf)$_2$ **6**. An NMR spectrum collected 90 minutes after the addition showed that intermediate **3** was almost completely consumed, while intermediate **6** and a new species, identified as the 6Fe(III)3O cluster [(FeFe(μ_3-O)(L))$_3$][OTf]$_3$ **2**, were present. Upon standing overnight, **2** was the only species present. A summary of these observations is given in Scheme 5.2. Addition of an atmosphere of O_2 to 5Fe(III)Fe(II)3O **3** gave conversion to 6Fe(III)3O **2** upon standing overnight (Scheme 5.3). Independently prepared 2Fe(III)2Fe(II)O **6** reacted with an atmosphere of O_2 to give 6Fe(III)3O **2**, with no observable intermediates; a significant amount of **6** was still present one hour after addition, but after overnight standing, all **6** had been consumed (Scheme 5.3).

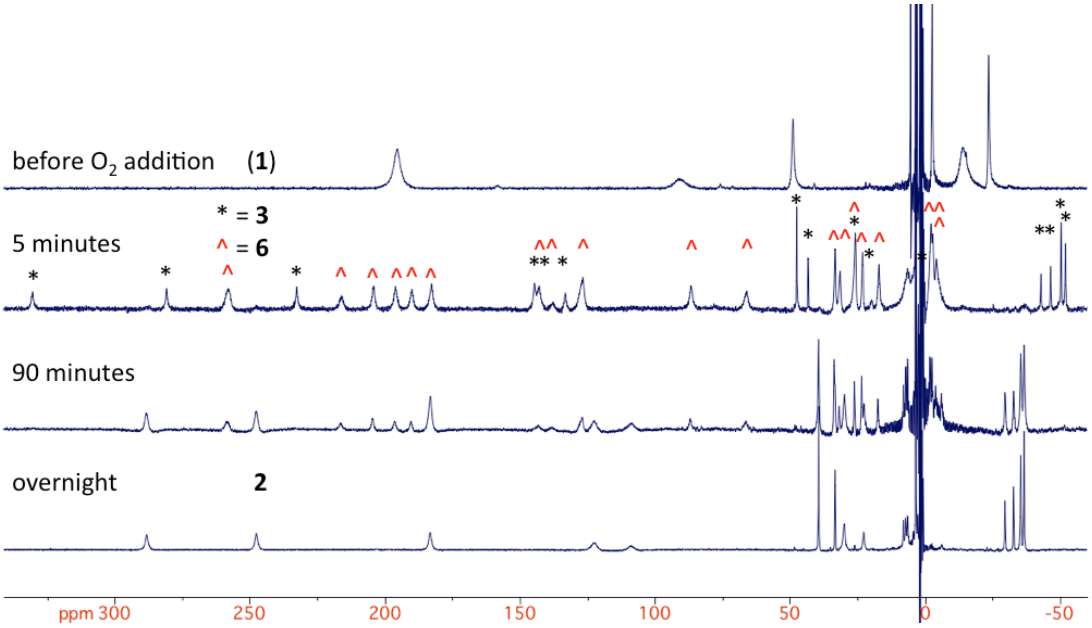

Figure 5.1. Time course of the ^{1}H NMR spectra of the reaction of an atmosphere of O_2 with **1** in CD_3CN.

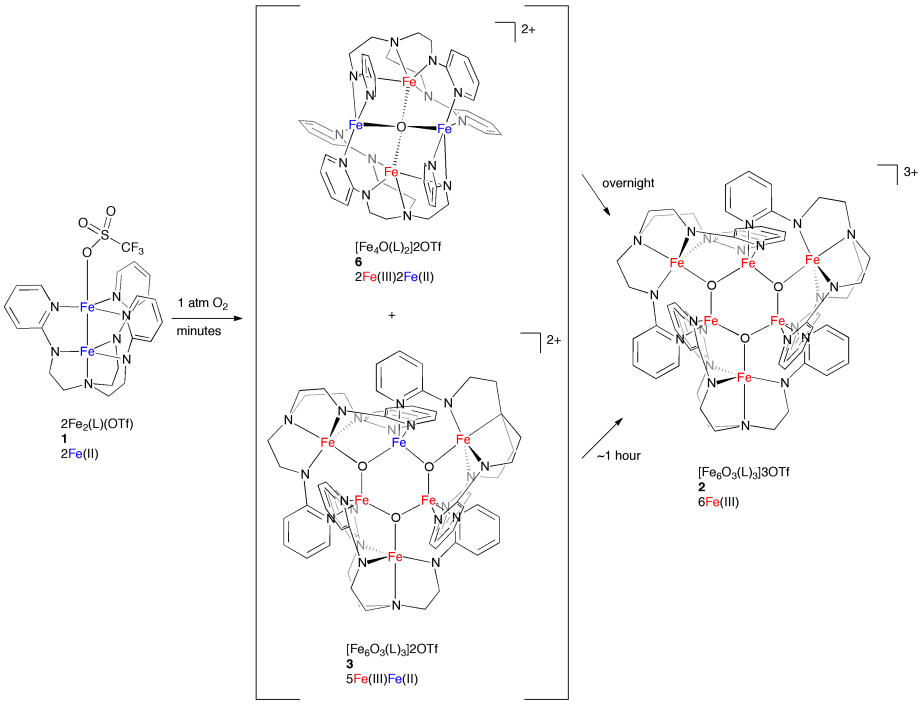

Scheme 5.2. Intermediates and products identified in the reaction of one atmosphere of O_2 to the 2Fe(II) starting material **1**.

To help unravel the changes occurring with an atmosphere of O_2, experiments with limiting O_2 were undertaken. Addition of a half equivalent of O_2 to 2Fe(II) **1** gave 2Fe(III)2Fe(II)O **6** as the major product – out of 22 paramagnetically shifted peaks in the ^{1}H NMR spectrum, 20 could be attributed to **6** (*vide infra*), and the two peaks that did not belong to **6** were of comparable intensity to those of **6**, belonging to a minor, unidentified side product (Scheme 5.3, Figure 5.5). Addition of one equivalent of O_2 to **1** gave a mixture of some **6** and mostly 6Fe(III)3O **3** five minutes after addition (Scheme 5.3). Forty minutes after addition, little **6** was present whereas the spectrum was dominated by **3**, and after standing overnight, **3** was the only product present.

To identify the source of the O atoms in 6Fe(III)3O **3**, one equivalent of $^{18}O_2$ (95% isotopically enriched) was added to 2Fe(II) **1**. Following confirmation of production of **3** by ^{1}H NMR spectroscopy, the ESI-MS spectrum of the reaction mixture was collected. The intensities of peaks observed were compared to those predicted if all the O atoms came from $^{18}O_2$ (see the Experimental Section and Table 5.1 for details). Clearly, the intensities of peaks arising from ^{16}O-containing isotopomers are greater than predicted, and those arising from ^{18}O-containing isotopomers are less than predicted. Hence, not all of the O atoms in the O_2 addition experiment to generate **3** arise from O_2. It is likely that some of the O in **3** arises from adventitious water. H_2O_2 is not a source of O atoms in this stoichiometric experiment, as a test for H_2O_2 was negative (see Experimental Section for details).

Table 5.1. ESI-MS data for **3** prepared from one equivalent of $^{18}O_2$ and **1** in CD_3CN.

m/*z*	Absolute Intensity (max)[a]	Relative Intensity	Relative Intensity, model[b]	Predicted Relative Intensity[c]
751.1282	24	1.0	0.6	0
751.5898	23	1.0	0.5	0
752.1286	136	5.8	5.5	0
752.6483	82	3.5	4.7	0
753.1104	587	25.1	25.5	1.1
753.6304	475	20.3	21.4	0.9
754.1121	1478	63.1	61.3	11.1
754.6324	1213	51.8	49.2	6.9
755.1337	2342	100	100	48.2
755.6159	1751	74.8	77.3	40.5
756.1175	1513	64.6	56.1	100
756.6192	820	35.0	30.2	79.8
757.1212	279	11.9	11.8	36.5
757.6233	100	4.3	3.0	11.7

[a] The intensity listed is the maximum intensity for the peak, which has at the tabulated *m*/*z* value. [b] See text for the calculation of this model. [c] Calculated from the theoretical percentage of each O isotopologue of **2** based on the 95% isotopically enriched $^{18}O_2$ and the simulated ESI-MS data for natural abundance **2**.

The ESI-MS data of the above $^{18}O_2$ experiment was modeled by assuming that each $^{16/18}O_3$ isotopomer of **3** has the same pattern of peaks (shifted by 1 m/z according to the specific O isotopomer) as the simulated spectrum of natural abundance 5Fe(III)Fe(II)3O **3** (Table 4.1, Figure 4.1) and then guessing and checking by adding up the peaks derived from different percentages of the four isotopomers (Figure 5.2, Table 5.1). As a comparison, plots of the simulated mass spectra of natural abundance **3** and of **3** if all of the 95% isotopically enriched $^{18}O_2$ from the experiment described above ended up in the product are provided in Figure 5.3. The model whose peaks are shown in Figure 5.2 and

tabulated in Table 5.1 used 8% $Fe_6{}^{16}O_3$, 19% $Fe_6{}^{16}O_2{}^{18}O$, 56% $Fe_6{}^{16}O{}^{18}O_2$, and 17% $Fe_6{}^{18}O_3$. The overall isotope percentages in this model are 39% ^{16}O and 61% ^{18}O. These numbers are not quite far off the 36% ^{16}O / 64% ^{18}O ratio that would be expected if one O atom derived from water and two O atoms derived from the 95% isotopically enriched $^{18}O_2$. The theoretical 36% ^{16}O / 64% ^{18}O ratio also assumes that in the formation of **3**, the O atoms derived from O_2 do not exchange with water.

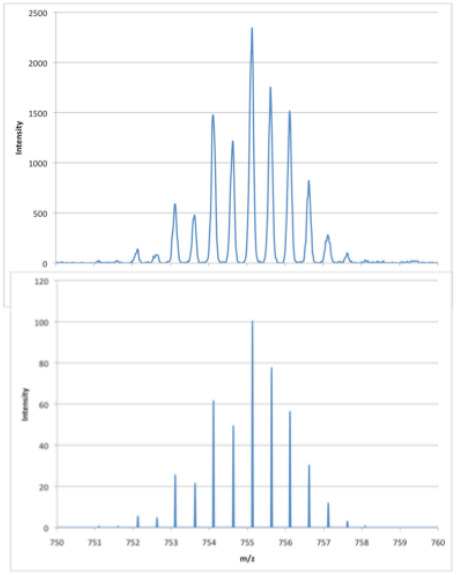

Figure 5.2. Comparison of (top) the experimental ESI-MS data of 5Fe(III)Fe(II)3O **3** made from the addition of 1 equivalent of $^{18}O_2$ (95% $^{18}O_2$) to 2Fe(II) **1** in CD_3CN and (bottom) a model of the mass spectrum of **3** assuming 8% $Fe_6{}^{16}O_3$, 19% $Fe_6{}^{16}O_2{}^{18}O$, 56% $Fe_6{}^{16}O{}^{18}O_2$, and 17% $Fe_6{}^{18}O_3$. See Table 4.1 for intensities.

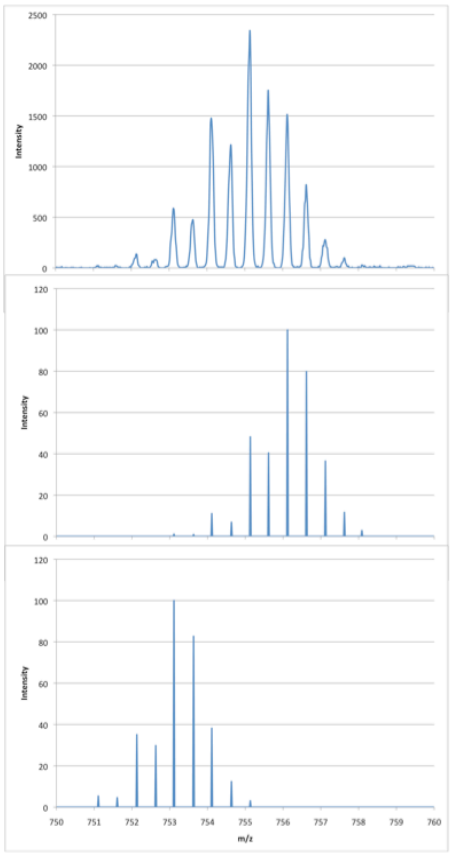

Figure 5.3. (Top) ESI-MS data of 5Fe(III)Fe(II)3O **3** made from the addition of 1 equivalent of $^{18}O_2$ (95% $^{18}O_2$) to 2Fe(II) **1** in CD_3CN. (Middle) Simulated mass spectrum of 5Fe(III)Fe(II)3O **3** if all the O atoms were derived from 95% $^{18}O_2$. (Bottom) Simulated mass spectrum of 5Fe(III)Fe(II)3O **3** if all the O atoms were derived from $^{16}O_2$.

5.3.2 Reactivity Discussion

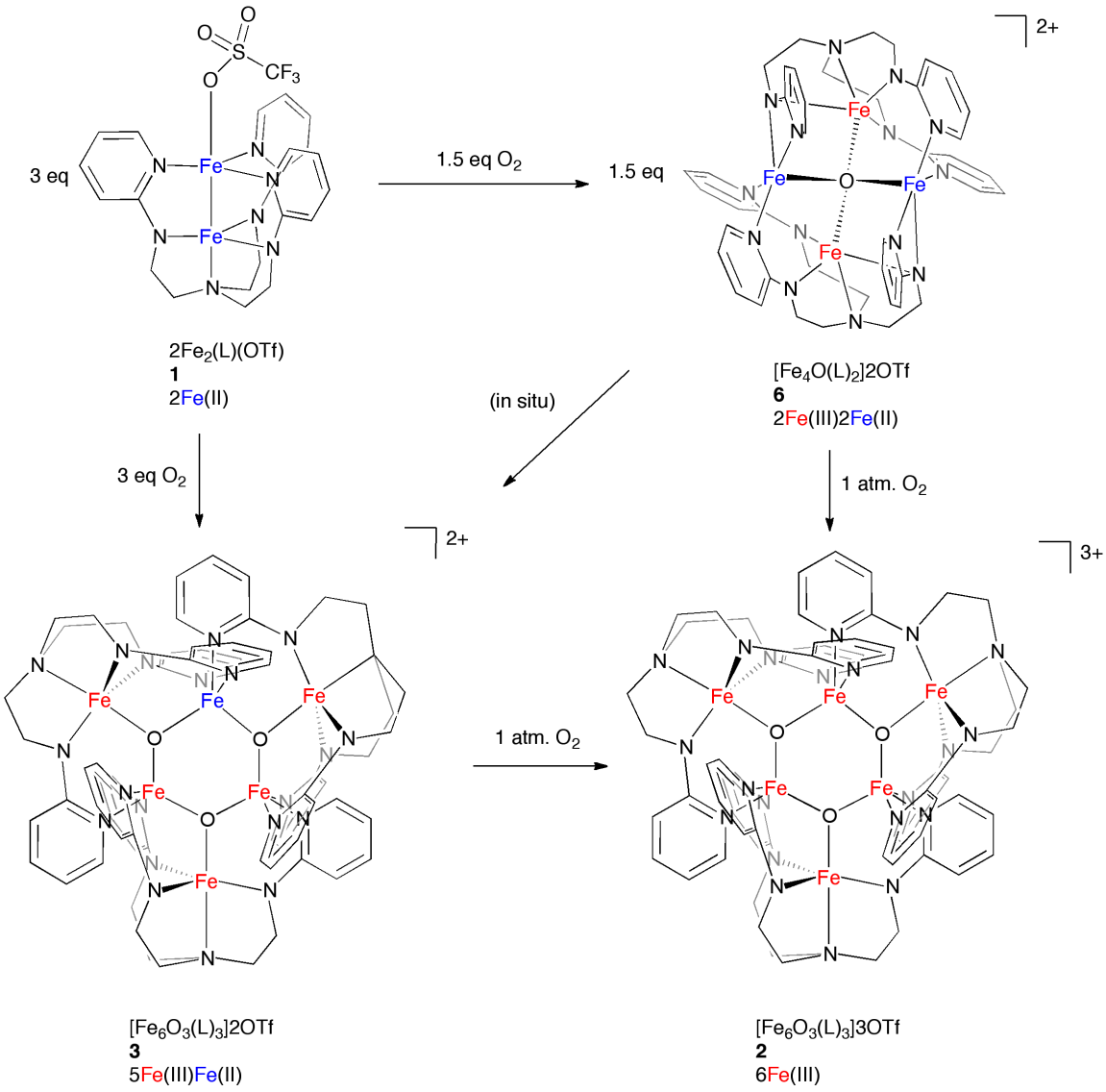

Scheme 5.3. Summary of limiting O_2 reactions and atmospheric O_2 additions to intermediates.

The reaction of O_2 with 2Fe(II) **1** occurs extremely fast, such that adding a half equivalent of O_2 to **1** gives the tetrairon cluster 2Fe(III)2Fe(II)O **6** within five minutes after thawing to room temperature. The following sequence of events may occur if **1** reacts with O_2 and no other substrates to generate **6**. In this time frame, **1** could react with

O_2 to give the intermediate **A**, which could react with a second equivalent of **1** to give an intermediate **B**, which may undergo O-O bond cleavage to give intermediate **C**, which would have to react with another equivalent of **1** to give **6** (Scheme 5.4). Only a quarter equivalent O_2 should be necessary to convert **1** to **6**, but we have not yet performed experiments with this stoichiometry. In principle, on the basis of atom economy and the charge of **1**, one half equivalent O_2 should be able to convert **1** to 6Fe(III)3O **3**, but clearly, this is not what is observed experimentally, as **6** is obtained instead. If there are other oxidized products, we cannot observe them by ^{1}H NMR spectroscopy. The formation of **6** could proceed *via* a tetrairon intermediate with a bridging O_2 ligand such as **B**. A diiron(II)diiron(III) bridging peroxo intermediate has been proposed in other systems for the decay of a diiron(III) peroxo species into a tetrairon(III) dioxide product.[244,245]

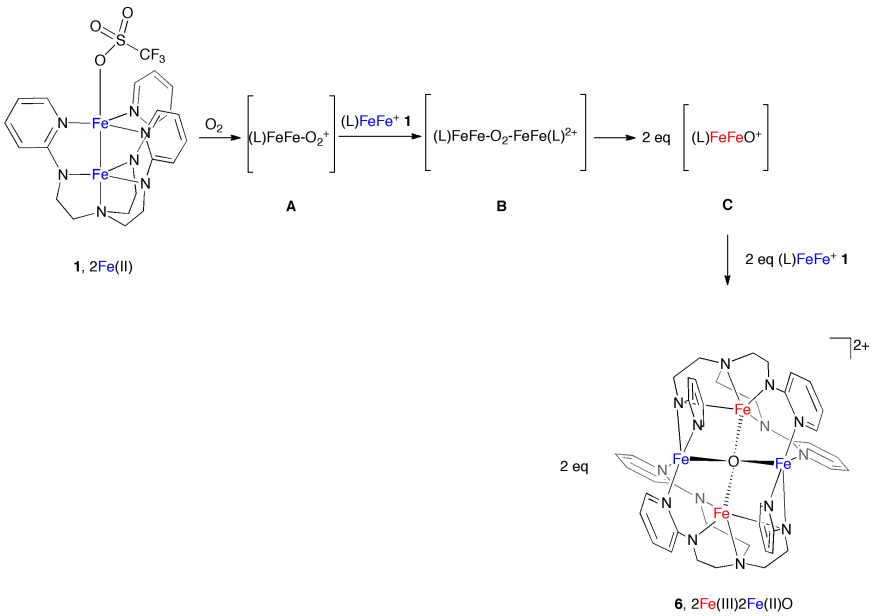

Scheme 5.4. Possible mechanism for the reaction of 2Fe(II) **1** with limiting O_2 to give 2Fe(III)2Fe(II)O **6** assuming only O_2 reacts and that there are no other byproducts.

Adding one equivalent of O_2 to **1** gives 5Fe(III)Fe(II)3O **3** rather than 6Fe(III)3O **2** (Scheme 5.3). The 2Fe(III)2Fe(II)O complex **6** is observed as an intermediate in this transformation. We have not performed a stoichiometric addition of O_2 to **6** to probe whether **6** can covert directly to **3**, but **6** is observed by ^{1}H NMR spectroscopy as an intermediate in the reaction of one equivalent of O_2 with 2Fe(II) **1** to give 5Fe(III)Fe(II)3O **3**, so we believe that **6** converts into **3** under limiting O_2. The conversion of **6** to **3** can be balanced by the following equation:

$$3Fe_4O^{2+} + O_2 + H_2O \longrightarrow 2Fe_6O_3^{2+} + 2H^+ \quad (1)$$

Hence, one-third an equivalent of O_2 per 2Fe(III)2Fe(II)O **6** would be needed to produce 5Fe(III)Fe(II)3O **3**. If one considers that a half equivalent of O_2 was used to generate **6** from 2Fe(II) **1**, and that one equivalent of O_2 was used to generate **3** from **1**, then experimentally, it seems that approximately a half equivalent of O_2 would be needed to generate **3** from **6**. This is close to the one third equivalent of O_2 per equivalent **6** in Equation 1. If Equation 1 is correct, and if the overall reaction for the conversion of **1** into **6** found in Scheme 5.4 is also correct, then five-sixths (or 83%) of the O atoms in **3** would be expected to be derived from O_2, which is much greater than the 61% value found by ESI-MS assuming no water exchange occurs (*vide supra*). Clearly, more studies, such as an ESI-MS study of the addition of $^{18}O_2$ to **1** to generate **6**, are needed.

In the atmospheric addition of O_2 to 2Fe(II) **1** (Scheme 5.3), 5Fe(III)Fe(II)3O **3** is consumed in approximately 1 hour, while 2Fe(III)2Fe(II)O **6** requires a longer period of time to fully react. This seems counterintuitive given that intermediate **6** is the first intermediate observed by stoichiometric ^{1}H NMR spectroscopy experiments. A possible

explanation for these observations includes the following. The conversion of **3** into 6Fe(III)3O **2** only requires a one-electron oxidation of isostructural cores, whereas **6** requires complex molecular reorganizations to be converted into **2** and/or **3** (*vide infra*).

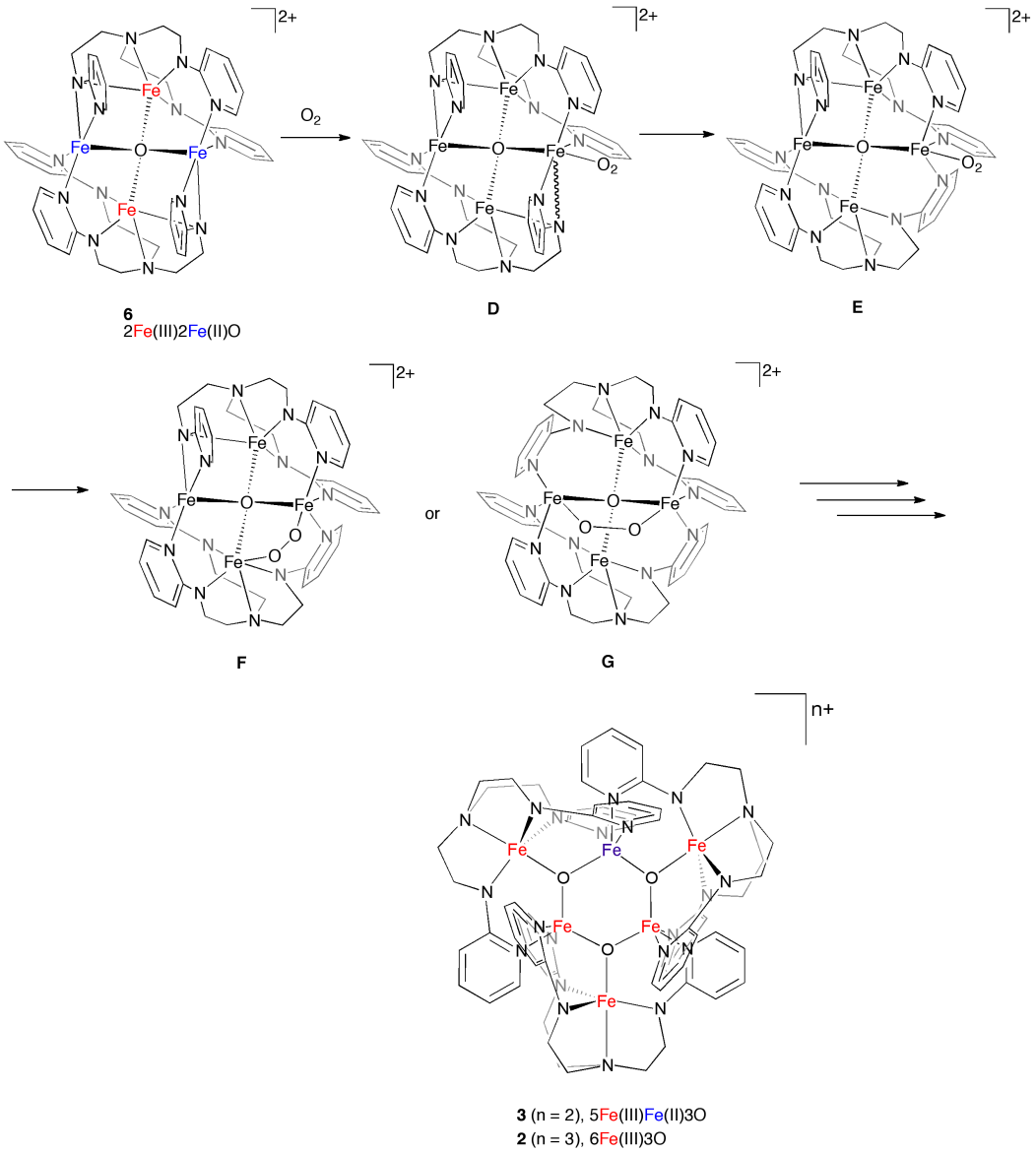

Scheme 5.5. Possible initial intermediates and steps in the reaction of 2Fe(III)2Fe(II)O **6** and O_2 to give hexanuclear clusters **2** or **3**.

What is most intriguing about the O_2 activation studies is that the *tetrairon* cluster

2Fe(III)2Fe(II)O **6** is converted into a *hexairon* cluster with greater O incorporation. While unraveling all the steps is beyond the scope of the information we have at this time, positing some of the early intermediates is worth considering. The pyridyl-ligated Fe(II) centers in **6** must be capable of binding O_2 for the reaction to proceed. As the triflates in the crystal structure are likely labile and able to be displaced by acetonitrile solvent, the apical site of a pyridyl Fe center is a prime candidate for O_2 binding to give an intermediate such as **D** (Scheme 5.5). The next step likely involves breakage of the bond between this O_2-bound Fe center and the bridging amide. Then, the pyridyl associated with this amide could twist to take the place of the amide in the O_2-ligated Fe's coordination sphere (intermediate **E**). This would provide room for bound O_2 to migrate towards the middle of the cluster, perhaps to bridge two Fe to afford either a bridging superoxo ligand (intermediate **F**) or peroxo ligand (intermediate **G**). At some stage in the transformation of **6** into **3**, the μ_4-O also must break a bond with one amide-ligated Fe to form a μ_3-O. According to Equation 1, water would also participate in the reaction.

Recently, the mixed-valent Fe(III)Fe(II) model compound $[Fe_2(N\text{-Et-HPTB})(\mu\text{-PhCOO})(DMF)_2](BF_4)_3$ ($[Fe_2(L)(\mu\text{-PhCOO})(S)_2]^{3+}$, L = *N*-Et-HPTB = the anion of *N*,*N*,*N'*,*N'*-tetrakis[2-(1-ethylbenzimidazolyl)]-2-hydroxy-1,3-diaminopropane) was reported, and its reactivity with dioxygen elucidated by UV-Vis-NIR spectroscopy, Mössbauer spectroscopy, cyclic voltammetry and resonance Raman (rR) spectroscopy.[234] The proposed reaction pathway was that a 2Fe(III) superoxo intermediate was generated, which rapidly reacted with more $[Fe_2(L)(\mu\text{-PhCOO})(S)_2]^{3+}$ to make a metastable 2Fe(III)

peroxo compound and other 2Fe(III) species. While no direct evidence for the superoxo species was found, evidence for the reaction pathway by UV-Vis-NIR spectroscopy included formation of an absorption with a maximum at 595 nm (ε = 2960 ± 210 M^{-1} cm^{-1}) upon bubbling $[Fe_2(L)(\mu\text{-PhCOO})(S)_2]^{3+}$ with O_2, which was attributed to the peroxo species, and could be reversed upon bubbling with N_2 to regenerate some $[Fe_2(L)(\mu\text{-PhCOO})(S)_2]^{3+}$ (albeit with a decreased absorbance compared to at the start of the experiment). Mössbauer spectroscopy of this reaction showed that, upon cooling to 77 K 25 minutes after the reaction started, a mixture of unreacted $[Fe_2(L)(\mu\text{-PhCOO})(S)_2]^{3+}$ (δ = 0.48 mm s^{-1}, 0.71 $|\Delta E_Q|$, mm s^{-1} and δ = 1.17 mm s^{-1}, 3.25 $|\Delta E_Q|$, mm s^{-1}), the 2Fe(III) peroxo species (δ = 0.57 mm s^{-1}, 0.91 $|\Delta E_Q|$, mm s^{-1}) and another Fe(III) species (δ = 0.40 mm s^{-1}, 0.82 $|\Delta E_Q|$, mm s^{-1}) were present. After a day, different Fe(III) species were present, along with none of the mixed-valent starting material or the peroxo species. Studying the reaction of O_2 with $[Fe_2(L)(\mu\text{-PhCOO})(S)_2]^{3+}$ by cyclic voltammetry showed that the quasireversible reduction of the mixed-valent starting material at -0.30 V (vs. Fc/Fc^+) was replaced within 25 minutes by two irreversible reductions at -0.60 and -0.80 V, while over a day, these irreversible reductions are replaced by one irreversible reduction at -0.97 V. Resonance Raman spectroscopy at 110 K of the reaction of O_2 with the mixed-valent starting material indicated that an $^{16}/^{18}O$ sensitive mode was present – 895 cm^{-1} for $^{16}O_2$ and 845 cm^{-1} for $^{18}O_2$, which match a previously characterized peroxo species in the *N*-Et-HPTB ligand platform. The rR spectra did not indicate the presence of a superoxo species. The presence of a 2Fe(III) peroxo and, importantly, additional high-spin Fe(III) species at short reaction times, lead to the conclusion that a 2Fe(III)

superoxo was generated upon the reaction of O_2 with the Fe(III)Fe(II) starting material, and that this rapidly reacted with additional Fe(III)Fe(II) starting material to give the 2Fe(III) peroxo and other 2Fe(III) species.

What the O_2 reactivity studies with the mixed-valent $[Fe_2(N\text{-Et-HPTB})(\mu\text{-PhCOO})(DMF)_2](BF_4)_3$ compound show is that both superoxo and peroxo intermediates such as **G** and **H** (Scheme 5.5) are possible in the reaction of 2Fe(III)2Fe(II)O **6** with atmospheric O_2 to ultimately form **2**. Even species with bridging peroxo ligands between two tetrairon clusters could be possible. More might be learned about the conversion of 2Fe(II) **1** to 2Fe(III)2Fe(II)O **6** to 5Fe(III)Fe(II)3O **3** if additional experiments, such as the following, were performed. Low temperature studies for the addition of O_2 to **1** and **6** could be helpful. Resonance Raman spectroscopy could distinguish between superoxo and peroxo intermediates, particularly by calculating the difference spectrum of samples prepared with $^{16}O_2$ and with $^{18}O_2$. Low temperature UV-Vis-NIR studies could also be worth pursuing, though the intense LMCT transition of 5Fe(III)Fe(II)3O **3** (**3** and **6** are both dark purple) may obscure the transitions of O_2-bound intermediates. Also, given the characteristic paramagnetic ^{1}H NMR spectra of **6** and hexanuclear clusters such as **3**, a low-temperature ^{1}H NMR spectroscopy study would also be worth trying to establish the solution state symmetry of any observed intermediates.

5.4 Conclusions

A diferrous complex with an iron-iron bond, 2Fe(II) **1**, reacts with an atmosphere of O_2 to ultimately give a hexairon product, 6Fe(III)3O **2**, that has a flat $Fe_6(\mu_3\text{-}O)_3$ core. Two intermediates in this reaction were observed by ^{1}H NMR spectroscopy and identified as the μ_4-O-centered tetrairon cluster 2Fe(III)2Fe(II)O **6**, and the hexairon cluster 5Fe(III)Fe(II)3O **3**, the one-electron reduced congener of **2**. Furthermore, it was shown that **6** converts into **2** under an atmosphere of O_2, a remarkable reaction that involves not only the incorporation of more O_2 into the cluster but a complex rearrangement of atoms, including the conversion of a μ_4-O into a μ_3-O and the breaking of multiple Fe-py$_3$tren bonds to transform the *tetrairon* core into a *hexairon* core. These studies have revealed the O_2 reactivity of a metal-metal bonded diiron bimetallic and mixed-valent multiiron clusters.

5.5 Experimental Section

General Considerations

Unless otherwise stated, all manipulations were performed under an N_2 atmosphere inside a glovebox. Standard solvents were deoxygenated by sparging with dinitrogen and dried by passing through activated alumina columns of a SG Water solvent purification system. Deuterated solvents were purchased from Cambridge Isotope Laboratories, Inc., degassed via freeze-pump-thaw cycles, dried over activated alumina, and stored over activated 4 Å molecular sieves. $^{18}O_2$ (95%) was purchased from Cambridge Isotope Laboratories. All other reagents were purchased from Aldrich or Strem and used without further purification. Independent syntheses of 2Fe(II) **1**, 6Fe(III)3O **2**, 5Fe(III)Fe(II)3O **3**, and 2Fe(III)2Fe(II)O **6** were described in Chapter 4.

Reactivity Studies

*Addition of atmospheric O_2 to **1***

An atmosphere of O_2 was added to **1** in CD_3CN in a J Young NMR tube. The reaction instantly turned from red to purple. At the 10 minute time point, the ^1H NMR spectrum showed that **1** had been completely consumed, and the spectrum contained a mixture of **2** and **6**. A second time point at 90 minutes showed that **2** was no longer present; a mixture of **6** and **3** was identified. After standing overnight, the reaction only showed **3** by NMR.

*Addition of atmospheric O_2 to **2***

An atmosphere of O_2 was added to **2** in CD_3CN in a J Young NMR tube. The ^1H NMR spectrum taken 8 minutes after the addition showed that over half of **2** had been consumed and replaced by **3**. Monitoring the reaction showed that **2** was slowly depleted and replaced by **3**; even a little **2** remained after standing overnight.

*Addition of atmospheric O_2 to **6***

An atmosphere of O_2 was added to a crude sample of **6** in CD_3CN in a J Young NMR tube. Monitoring the reaction showed that **3** was present in a significant amount by 1 hour of reaction time, and was the only product identified after standing overnight. Notably, **2** was not observed in the reaction.

*Addition of stoichiometric O_2 to **1***

To **1** (14.6 mg, 0.023 mmol) in CD_3CN in a J Young NMR tube was added 1 equivalent O_2 (106 torr, 0.023 mmol) via a gas addition bulb on the Schlenk line by condensation with liquid nitrogen. Monitoring the reaction showed that, 5 minutes after the addition, a mixture of **2** and **6** was present while no **1** was left. Further time points revealed that **6** was slowly depleted while **2** grew in to be the only product present after standing overnight.

*Addition of substoichiometric O_2 to **1***

To **1** (14.8 mg, 0.023 mmol) in CD_3CN in a J Young NMR tube was added a half equivalent O_2 (53 torr, 0.012 mmol) via a gas addition bulb on the Schlenk line by condensation with liquid nitrogen. Monitoring the reaction showed that, 5 minutes after the addition, the only product observed was **6**, while very little **1** was left. Subsequent time points showed that **1** was completely consumed, and **6** was the major product.

*Addition of stoichiometric $^{18}O_2$ to **1***

To **1** (14.6 mg, 0.023 mmol) in CD_3CN in a J Young NMR tube was added 1 equivalent O_2 (38 torr, 0.023 mmol) via a gas addition bulb on the Schlenk line by condensation with liquid nitrogen. After standing overnight, **2** was the only product observed by ^1H NMR spectroscopy. The J Young NMR tube was brought back into the glovebox, and the sample was transferred to a scintillation vial. A rubber septum was placed on the vial. A hole in the septum was created by a plastic needle, and then the sample was syringed from the vial to the ESI-MS instrument.

Test for H_2O_2

To **1** (17.4 mg, 0.0274 mmol) in CD_3CN was added 0.5 eq O_2 (22 torr, 0.014 mmol). After the addition, the reaction was quenched with water and diluted sulfuric acid. The reaction turned from purple to orange. Then, potassium iodide and ~5 drops of starch was added. The reaction turned brown. The blue color that would have arisen had H_2O_2 been present was not observed.

Physical Measurements

NMR spectra were collected on Varian Inova 300 and 500 MHz spectrometers or a Bruker Avance III 500 MHz spectrometer. ESI-MS data were collected on a Bruker BioTOF II instrument and calibrated against an internal PEG standard.

*ESI-MS [(FeFe(μ_3-O)(py$_3$tren))$_3$][OTf]$_2$ **2** ($^{18}O_2$ Synthesis) Isotopologue Calculation*

A simulated ESI-MS spectrum of natural abundance [(FeFe(μ_3-O)(py$_3$tren))$_3$][OTf]$_2$ **2** was used as a control for calculating the predicted relative intensity of each peak in the ESI-MS spectrum of **2** prepared from the addition of one equivalent of $^{18}O_2$ to FeFe(OTf)(py$_3$tren) **1** (Table 4.1). It is assumed that the abundances of the isotopes of the other elements do not vary among $Fe_6(^{16}O)_3^{2+}$, $Fe_6(^{16}O)_2(^{18}O)^{2+}$, $Fe_6(^{16}O)(^{18}O)_2^{2+}$, and $Fe_6(^{18}O)_3^{2+}$. Natural abundance oxygen is 99.76% ^{16}O, 0.04% ^{17}O, and 0.21% ^{18}O. Given the very small contributions of ^{17}O and ^{18}O to natural abundance O, it is assumed that natural abundance O is 100% ^{16}O to simplify the problem. Given that this is a m/z manifold where $z = 2$, changing one oxygen atom in a given isotopologue from ^{16}O to ^{18}O will increase the peak by $m/z = 1$. The following are the percentages of each isotopologue if all the oxygen came from the 95% isotopically enriched $^{18}O_2$ gas:

$Fe_6(^{16}O)_3^{2+}$: $0.05^3 = 0.01\% \approx 0\%$

$Fe_6(^{16}O)_2(^{18}O)^{2+}$: $3(0.05^2 \times 0.95) = 0.7\%$

$Fe_6(^{16}O)(^{18}O)_2^{2+}$: $3(0.05 \times 0.95^2) = 13.5\%$

$Fe_6(^{18}O)_3^{2+}$: $0.95^3 = 85.8\%$

These percentages, and the simulated relative intensity values from natural abundance $Fe_6O_3^{2+}$, were used to calculate the predicted relative intensity values in Table 5.1.

Bibliography

(1) Smil, V. *Nature* **1999**, *400*, 415.
(2) Lewis, N. S.; Nocera, D. G. *Proc. Acad. Nat. Sci. USA* **2006**, *103*, 15729.
(3) Myhre, G.; Shindell, D.; Bréon, F. M.; Collins, W.; Fuglestvedt, J.; Huang, J.; Koch, D.; Lamarque, J.-F.; Lee, D.; Mendoza, B.; Nakajima, T.; Robock, A.; Stephens, G.; Takemura, T.; Zhang, H. "Anthropogenic and Natural Radiative Forcing." *Climate Change 2013: The Physical Science Basis. Contribution of Working Group I to the Fifth Assessment Report of the Intergovernmental Panel on Climate Change*; Stocker, T. F.; Qin, D.; Plattner, G.-K.; Tignor, M.; Allen, S. K.; Boschung, J.; Nauels, A.; Xia, Y.; Bex, V.; Midgley, P. M., Eds.; Cambridge University Press, New York, NY, 2013; p. 714.
(4) Olah, G. A. *Angew. Chem. Int. Ed.* **2005**, *44*, 2636.
(5) Hoffman, B. M.; Lukoyanov, D.; Dean, D. R.; Seefeldt, L. C. *Acc. Chem. Res.* **2013**, *46*, 587.
(6) Yano, J.; Yachandra, V. *Chem. Rev.* **2014**, *114*, 4175.
(7) Brudvig, G. W. *Phil. Trans. R. Soc. B* **2008**, *363*, 1211.
(8) Tshuva, E. Y.; Lippard, S. J. *Chem. Rev.* **2004**, *104*, 987.
(9) Ogata, H.; Lubitz, W.; Higuchi, Y. *Dalton Trans.* **2009**, 7577.
(10) Basch, H.; Mogi, K.; Musaev, D. G.; Morokuma, K. *J. Am. Chem. Soc.* **1999**, *121*, 7249.
(11) Tsui, E. Y.; Tran, R.; Yano, J.; Agapie, T. *Nature Chem.* **2013**, *5*, 293.
(12) Que, L., Jr.; Tolman, W. B. *Nature* **2008**, *455*, 333.
(13) Lippard, S. J.; Berg, J. M. *Principles of Bioinorganic Chemistry*; University Science Books: Mill Valley, CA, 1994.
(14) Kampa, M.; Pandelia, M.-E.; Lubitz, W.; van Gastel, M.; Neese, F. *J. Am. Chem. Soc.* **2013**, *135*, 3915.
(15) Powers, T. M.; Fout, A. R.; Zheng, S.-L.; Betley, T. A. *J. Am. Chem. Soc.* **2011**, *133*, 3336.
(16) Powers, T. M.; Betley, T. A. *J. Am. Chem. Soc.* **2013**, *135*, 12289.
(17) Lu, D.-Y.; Yu, J.-S. K.; Kuo, T.-S.; Lee, G.-H.; Wang, Y.; Tsai, Y.-C. *Angew. Chem. Int. Ed.* **2011**, *50*, 7611.
(18) Chai, J.; Zhu, H.; Stückl, A. C.; Roesky, H. W.; Magull, J.; Bencini, A.; Caneschi, A.; Gatteschi, D. *J. Am. Chem. Soc.* **2005**, *127*, 9201.
(19) Hicks, J.; Hoyer, C. E.; Moubaraki, B.; Li Manni, G.; Carter, E.; Murphy, D. M.; Murray, K. S.; Gagliardi, L.; Jones, C. *J. Am. Chem. Soc.* **2014**, *136*, 5283.
(20) Fohlmeister, L.; Liu, S.; Schulten, C.; Moubaraki, B.; Stasch, A.; Cashion, J. D.; Murray, K. S.; Gagliardi, L.; Jones, C. *Angew. Chem. Int. Ed.*

2012, *51*, 8294.
(21) Zall, C. M.; Clouston, L. J.; Young, V. G., Jr.; Ding, K.; Kim, H. J.; Zherebetskyy, D.; Chen, Y.-S.; Bill, E.; Gagliardi, L.; Lu, C. C. *Inorg. Chem.* **2013**, *52*, 9216.
(22) Eames, E. V.; Hernández Sánchez, R.; Betley, T. A. *Inorg. Chem.* **2013**, *52*, 5006.
(23) Powers, T. M.; Gu, N. X.; Fout, A. R.; Baldwin, A. M.; Hernández Sánchez, R.; Alfonso, D. M.; Chen, Y.-S.; Zheng, S.-L.; Betley, T. A. *J. Am. Chem. Soc.* **2013**, *135*, 14448.
(24) Cotton, F. A. In *Multiple Bonds Between Metal Atoms*, 3rd ed.; Cotton, F. A.; Murillo, C. A.; Walton, R. A.; Eds.; Springer, New York, 2005.; p. 44.
(25) Cotton, F. A.; Daniels, L. M.; Feng, X.; Maloney, D. J.; Matonic, J. H.; Murilio, C. A. *Inorg. Chim. Acta* **1997**, *256*, 291.
(26) Cotton, F. A.; Poli, R. *Inorg. Chem.* **1987**, *26*, 3652.
(27) Cotton, F. A.; Daniels, L. M.; Murillo, C. A. *Inorg. Chim. Acta* **1994**, *224*, 5.
(28) Timmer, G. H.; Berry, J. F. *Comptes Rendus Chimie* **2012**, *15*, 192.
(29) Cotton, F. A.; Daniels, L. M.; Maloney, D. J.; Murillo, C. A. *Inorg. Chim. Acta* **1996**, *249*, 9.
(30) Cotton, F. A.; Daniels, L. M.; Maloney, D. J.; Matonic, J. H.; Murillo, C. A. *Inorg. Chim. Acta* **1997**, *256*, 283.
(31) Cotton, F. A.; Daniels, L. M.; Falvello, L. R.; Murillo, C. A. *Inorg. Chim. Acta* **1994**, *219*, 7.
(32) Cotton, F. A.; Daniels, L. M.; Falvello, L. R.; Matonic, J. H.; Murillo, C. A. *Inorg. Chim. Acta* **1997**, *256*, 269.
(33) Zall, C. M.; Zherebetskyy, D.; Dzubak, A. L.; Bill, E.; Gagliardi, L.; Lu, C. C. *Inorg. Chem.* **2012**, *51*, 728.
(34) Cotton, F. A.; Feng, X.; Murillo, C. A. *Inorg. Chim. Acta* **1997**, *256*, 303.
(35) Jones, C.; Schulten, C.; Rose, R. P.; Stasch, A.; Aldridge, S.; Woodul, W. D.; Murray, K. S.; Moubaraki, B.; Brynda, M.; La Macchia, G.; Gagliardi, L. *Angew. Chem. Int. Ed.* **2009**, *48*, 7406.
(36) Mathialagan, R.; Kuppuswamy, S.; De Denko, A. T.; Bezpalko, M. W.; Foxman, B. M.; Thomas, C. M. *Inorg. Chem.* **2013**, *52*, 701.
(37) Kuppuswamy, S.; Bezpalko, M. W.; Powers, T. M.; Turnbull, M. M.; Foxman, B. M.; Thomas, C. M. *Inorg. Chem.* **2012**, *51*, 8225.
(38) Kuppuswamy, S.; Powers, T. M.; Johnson, B. M.; Bezpalko, M. W.; Brozek, C. K.; Foxman, B. M.; Berben, L. A.; Thomas, C. M. *Inorg. Chem.* **2013**, *52*, 4802.
(39) Klose, A.; Solari, E.; Floriani, C.; Chiesi-Villa, A.; Rizzoli, C.; Re, N. *J. Am. Chem. Soc.* **1994**, *116*, 9123.
(40) Fout, A. R.; Xiao, D. J.; Zhao, Q.; Harris, T. D.; King, E. R.; Eames, E. V.; Zheng, S.-L.; Betley, T. A. *Inorg. Chem.* **2013**, *51*, 10290.

(41) Fout, A. R.; Zhao, Q.; Xiao, D. J.; Betley, T. A. *J. Am. Chem. Soc.* **2011**, *133*, 16750.
(42) Eames, E. V.; Harris, T. D.; Betley, T. A. *Chem. Sci.* **2012**, *3*, 407.
(43) Zhao, Q.; Harris, T. D.; Betley, T. A. *J. Am. Chem. Soc.* **2011**, *133*, 8293.
(44) Zhao, Q.; Betley, T. A. *Angew. Chem. Int. Ed.* **2011**, *50*, 709.
(45) Doyle, M. P.; Duffy, R.; Ratnikov, M.; Zhou, L. *Chem. Rev.* **2010**, *110*, 704.
(46) Doyle, M. P. *J. Org. Chem.* **2006**, *71*, 9253.
(47) Davies, H. M. L.; Morton, D. *Chem. Soc. Rev.* **2011**, *40*, 1857.
(48) Scepaniak, J. J.; Harris, T. D.; Vogel, C. S.; Sutter, J.; Meyer, K.; Smith, J. M. *J. Am. Chem. Soc.* **2011**, *133*, 3824.
(49) Kuppuswamy, S.; Powers, T. M.; Johnson, B. M.; Brozek, C. K.; Krogman, J. P.; Bezpalko, M. W.; Berben, L. A.; Keith, J. M.; Foxman, B. M.; Thomas, C. M. *Inorg. Chem.* **2014**, *53*, 5429.
(50) Harris, T. D.; Betley, T. A. *J. Am. Chem. Soc.* **2011**, *133*, 13852.
(51) Berry, J. F.; Cotton, F. A.; Murillo, C. A.; Roberts, B. K. *Inorg. Chem.* **2004**, *43*, 2277.
(52) Yeh, C.-Y.; Chou, C.-H.; Pan, K.-C.; Wang, C.-C.; Lee, G.-H.; Su, Y. O.; Peng, S.-M. *J. Chem. Soc., Dalton Trans.* **2002**, 2670.
(53) Clérac, R.; Cotton, F. A.; Jeffery, S. P.; Murillo, C. A.; Wang, X. *Inorg. Chem.* **2001**, *40*, 1265.
(54) Greenwood, B. P.; Rowe, G. T.; Chen, C.-H.; Foxman, B. M.; Thomas, C. M. *J. Am. Chem. Soc.* **2010**, *132*, 44.
(55) Thomas, C. M.; Napoline, J. W.; Rowe, G. T.; Foxman, B. M. *Chem. Commun.* **2010**, *46*, 5790.
(56) Krogman, J. P.; Foxman, B. M.; Thomas, C. M. *J. Am. Chem. Soc.* **2011**, *133*, 14582.
(57) Zhou, W.; Marquard, S. L.; Bezpalko, M. W.; Foxman, B. M.; Thomas, C. M. *Organometallics* **2013**, *32*, 1766.
(58) Marquard, S. L.; Bezpalko, M. W.; Foxman, B. M.; Thomas, C. M. *J. Am. Chem. Soc.* **2013**, *135*, 6018.
(59) Eisch, J. J.; Piotrowski, A. M.; Han, K. I.; Krüger, C.; Tsay, Y. H. *Organometallics* **1985**, *4*, 224.
(60) Ramakrishna, T. V. V.; Sharp, P. R. *Organometallics* **2004**, *23*, 3079.
(61) Velian, A.; Lin, S.; Miller, A. J. M.; Day, M. W.; Agapie, T. *J. Am. Chem. Soc.* **2010**, *132*, 6296.
(62) Keen, A. L.; Johnson, S. A. *J. Am. Chem. Soc.* **2006**, *128*, 1806.
(63) Keen, A. L.; Doster, M.; Johnson, S. A. *J. Am. Chem. Soc.* **2007**, *129*, 810.
(64) Zhou, W.; Napoline, J. W.; Thomas, C. M. *Eur. J. Inorg. Chem.* **2011**, 2029.
(65) Zhou, W.; Saper, N. I.; Krogman, J. P.; Foxman, B. M.; Thomas,

C. M. *Dalton Trans.* **2014**, *43*, 1984.
(66) Beck, R.; Johnson, S. A. *Chem. Commun.* **2011**, *47*, 9233.
(67) *Biological Inorganic Chemistry: Structure and Reactivity*; Bertini, I.; Gray, H. B.; Stiefel, E. I.; Valentine, J. S., Eds.; University Science Books: Sausalito, CA, 2007.
(68) Fontecilla-Camps, J. C.; Volbeda, A.; Cavazza, C.; Nicolet, Y. *Chem. Rev.* **2007**, *107*, 4273.
(69) Ragsdale, S. W. *J. Inorg. Biochem.* **2007**, *101*, 1657.
(70) Dobbek, H.; Svetlitchnyi, V.; Gremer, L.; Huber, R.; Meyer, O. *Science* **2001**, *293*, 1281.
(71) Kung, Y.; Drennan, C. L. *Curr. Opin. Chem. Biol.* **2011**, *15*, 276.
(72) Jiang, W.; Yun, D.; Saleh, L.; Barr, E. W.; Xing, G.; Hoffart, L. M.; Maslak, M.-A.; Krebs, C.; Bollinger, J. M., Jr. *Science* **2007**, *316*, 1188.
(73) Jiang, W.; Bollinger, J. M., Jr.; Krebs, C. *J. Am. Chem. Soc.* **2007**, *129*, 7504.
(74) Stubbe, J.; Nocera, D. G.; Yee, C. S.; Chang, M. C. Y. *Chem. Rev.* **2003**, *103*, 2167.
(75) Dassama, L. M. K.; Boal, A. K.; Krebs, C.; Rosenzweig, A. C.; Bollinger, J. M., Jr. *J. Am. Chem. Soc.* **2012**, *134*, 2520.
(76) Roos, K.; Siegbahn, P. E. M. *Biochemistry* **2009**, *48*, 1878.
(77) Andersson, C. S.; Öhrström, M.; Popović-Bijelić, A.; Gräslund, A.; Stenmark, P.; Högbom, M. *J. Am. Chem. Soc.* **2012**, *134*, 123.
(78) Han, W.-G.; Giammona, D. A.; Bashford, D.; Noodleman, L. *Inorg. Chem.* **2010**, *49*, 7266.
(79) Sano, Y.; Weitz, A. C.; Ziller, J. W.; Hendrich, M. P.; Borovik, A. S. *Inorg. Chem.* **2013**, *52*, 10229.
(80) Carboni, M.; Latour, J.-M. *Coord. Chem. Rev.* **2011**, *255*, 186.
(81) Carboni, M.; Clémancey, M.; Molton, F.; Pécaut, J.; Lebrun, C.; Dubois, L.; Blondin, G.; Latour, J.-M. *Inorg. Chem.* **2012**, *51*, 10447.
(82) Jarenmark, M.; Haukka, M.; Demeshko, S.; Tuczek, F.; Zuppiroli, L.; Meyer, F.; Nordlander, E. *Inorg. Chem.* **2011**, *50*, 3866.
(83) Holman, T. R.; Wang, Z.; Hendrich, M. P.; Que, L., Jr. *Inorg. Chem.* **1995**, *34*, 134.
(84) Hotzelmann, R.; Wieghardt, K.; Flörke, U.; Haupt, H.-J.; Weatherburn, D. C.; Bonvoisin, J.; Blondin, G.; Girerd, J.-J. *J. Am. Chem. Soc.* **1992**, *114*, 1681.
(85) Ross, S.; Weyhermüller, T.; Bill, E.; Bothe, E.; Flörke, U.; Wieghardt, K.; Chaudhuri, P. *Eur. J. Inorg. Chem.* **2004**, 984.
(86) Borovik, A. S.; Que, L., Jr.; Papaefthymiou, V.; Münck, E.; Taylor, L. F.; Anderson, O. P. *J. Am. Chem. Soc.* **1988**, *110*, 1986.
(87) Tsui, E. Y.; Agapie, T. *Proc. Acad. Nat. Sci. USA* **2013**, *110*, 10084.
(88) Rudd, P. A.; Liu, S.; Gagliardi, L.; Young, V. G., Jr.; Lu, C. C. *J. Am. Chem. Soc.* **2011**, *133*, 20724.

(89) Rudd, P. A.; Liu, S.; Planas, N.; Bill, E.; Gagliardi, L.; Lu, C. C. *Angew. Chem. Int. Ed.* **2013**, *52*, 4449.
(90) Clouston, L. J.; Siedschlag, R. B.; Rudd, P. A.; Planas, N.; Hu, S.; Miller, A. D.; Gagliardi, L.; Lu, C. C. *J. Am. Chem. Soc.* **2013**, *135*, 13142.
(91) Nippe, M.; Bill, E.; Berry, J. F. *Inorg. Chem.* **2011**, *50*, 7650.
(92) Nippe, M.; Victor, E.; Berry, J. F. *Eur. J. Inorg. Chem.* **2008**, 5569.
(93) Kim, M.; Kim, Y.-U.; Han, J. *Polyhedron* **2007**, *26*, 4003.
(94) Shin, B. K.; Kim, M.; Han, J. *Polyhedron* **2010**, *29*, 2560.
(95) Massoud, S. S.; Broussard, K. T.; Mautner, F. A.; Vicente, R.; Saha, M. K.; Bernal, I. *Inorg. Chim. Acta* **2008**, 361, 123.
(96) *Multiple Bonds Between Metal Atoms*; Cotton, F. A.; Murillo, C. A.; Walton, R. A., Eds.; 3rd ed.; Springer, New York, 2005.
(97) Freedman, D. E.; Han, T. H.; Prodi, A.; Müller, P.; Huang, Q.-Z.; Chen, Y.-S.; Webb, S. M.; Lee, Y. S.; McQueen, T. M.; Nocera, D. G. *J. Am. Chem. Soc.* **2010**, *132*, 16185.
(98) Wulf, R. *Acta Crystrallogr.* **1990**, *A46*, 681.
(99) Toby, B. H.; Von Dreele, R. B. *J. Appl. Crystallogr.* **2013**, *46*, 544.
(100) Nippe, M.; Berry, J. F. *J. Am. Chem. Soc.* **2007**, *129*, 12684.
(101) Lacy, D. C.; Gupta, R.; Stone, K. L.; Greaves, J.; Ziller, J. W.; Hendrich, M. P.; Borovik, A. S. *J. Am. Chem. Soc.* **2010**, *132*, 12188.
(102) Rivero, P.; Moreira, I. de P. R. ; Illas, F.; Scuseria, G. E. *J. Chem. Phys.* **2008**, *129*, 184110.
(103) Valero, R.; Costa, R.; Moreira, I. de P. R.; Truhlar, D. G.; Illas, F. *J. Chem. Phys.* **2008**, *128*, 114103.
(104) Bailey, P. J.; Coxall, R. A.; Dick, C. M.; Fabre, S.; Henderson, L. C.; Herber, C.; Liddle, S. T.; Loroño-González, D.; Parkin, A.; Parsons, S. *Chem.-Eur. J.* **2003**, *9*, 4820.
(105) O'Connor, C. J. *Prog. Inorg. Chem.* **1982**, *29*, 203.
(106) *CRC Handbook of Chemistry and Physics*, 59th ed.; Weast, R. C.; Astle, M. J., Eds.; CRC Press: Boca Raton, FL, 1979.
(107) Kahn, O. *Molecular Magnetism*; VCH: Weinheim, Germany, 1993.
(108) Bill, E. *julX*, version 1.4.1; Germany, 2008.
(109) Aquilante, F.; De Vico, L.; Ferré, N.; Ghigo, G.; Malmqvist, P.-Å.; Neogrády, P.; Pedersen, T. B.; Pitoňák, M.; Reiher, M.; Roos, B. O.; Serrano-Andrés, L.; Urban, M.; Veryazov, V.; Lindh, R. *J. Comput. Chem.* **2010**, *31*, 224.
(110) Roos, B. O.; Lindh, R.; Malmqvist, P.-Å.; Veryazov, V.; Widmark, P.-O. *J. Phys. Chem. A* **2004**, *108*, 2851.
(111) Roos, B. O.; Lindh, R.; Malmqvist, P.-Å.; Veryazov, V.; Widmark, P.-O. *J. Phys. Chem. A* **2005**, *109*, 6575.
(112) Douglas, M.; Kroll, N. M. *Ann. Phys.* **1974**, *82*, 89.
(113) Hess, B. A. *Phys. Rev. A* **1986**, *33*, 3742.

(114) Aquilante, F.; Pedersen, T. B.; Lindh, R. *J. Chem. Phys.* **2007**, *126*, 114107.
(115) Forsberg, N.; Malmqvist, P.-Å. *Chem. Phys. Lett.* **1997**, *274*, 196.
(116) Brynda, M.; Gagliardi, L.; Roos, B. O. *Chem. Phys. Lett.* **2009**, *471*, 1.
(117) Roos, B. O.; Borin, A. C.; Gagliardi, L. *Angew. Chem. Int. Ed.* **2007**, *46*, 1469.
(118) Noodleman, L. *J. Chem. Phys.* **1981**, *74*, 5737.
(119) Yamaguchi, K; Takahara, Y.; Fueno, T. In *Applied Quantum Chemistry*; Smith, V. H., Jr., Schaefer, H. F., III, Morokuma, K., eds.; Reidel: Boston, 1986; p. 155.

(120) Frisch, M. J.; Trucks, G. W.; Schlegel, H. B.; Scuseria, G. E.; Robb, M. A.; Cheeseman, J. R.; Scalmani, G.; Barone, V.; Mennucci, B.; Petersson, G. A.; Nakatsuji, H.; Caricato, M.; Li, X.; Hratchian, H. P.; Izmaylov, A. F.; Bloino, J.; Zheng, G.; Sonnenberg, J. L.; Hada, M.; Ehara, M.; Toyota, K.; Fukuda, R.; Hasegawa, J.; Ishida, M.; Nakajima, T.; Honda, Y.; Kitao, O.; Nakai, H.; Vreven, T.; Montgomery, J. A., Jr.; Peralta, J. E.; Ogliaro, F.; Bearpark, M.; Heyd, J. J.; Brothers, E.; Kudin, K. N.; Staroverov, V. N.; Kobayashi, R.; Normand, J.; Raghavachari, K.; Rendell, A.; Burant, J. C.; Iyengar, S. S.; Tomasi, J.; Cossi, M.; Rega, N.; Millam, J. M.; Klene, M.; Knox, J. E.; Cross, J. B.; Bakken, V.; Adamo, C.; Jaramillo, J.; Gomperts, R.; Stratmann, R. E.; Yazyev, O.; Austin, A. J.; Cammi, R.; Pomelli, C.; Ochterski, J. W.; Martin, R. L.; Morokuma, K.; Zakrzewski, V. G.; Voth, G. A.; Salvador, P.; Dannenberg, J. J.; Dapprich, S.; Daniels, A. D.; Farkas, Ö.; Foresman, J. B.; Ortiz, J. V.; Cioslowski, J.; Fox, D. J. Gaussian 09, revision D.01; Gaussian, Inc.: Wallingford, CT, 2009.

(121) Ernzerhof, M.; Perdew, J. P. *J. Chem. Phys.* **1998**, *109*, 3313.
(122) Perdew, J. P.; Ernzerhof, M.; Burke, K. *J. Chem. Phys.* **1996**, *105*, 9982.
(123) Heyd, J.; Scuseria, G. E.; Ernzerhof, M. *J. Chem. Phys.* **2003**, *118*, 8207.
(124) Heyd, J.; Scuseria, G. E.; Ernzerhof, M. *J. Chem. Phys.* **2006**, *124*, 219906.
(125) Vydrov, O. A.; Scuseria, G. E. *J. Chem. Phys.* **2006**, *125*, 234109.
(126) Schäfer, A.; Horn, H.; Ahlrichs, R. *J. Chem. Phys.* **1992**, *97*, 2571.
(127) Schäfer, A.; Huber, C.; Ahlrichs, R. *J. Chem. Phys.* **1994**, *100*, 5829.
(128) Doyle, M. P. In *Modern Rhodium-Catalyzed Organic Reactions*; Evans, P. A., Ed.; Wiley-VCH, Weinheim, 2005; p. 341.
(129) Timmons, D. J.; Doyle, M. P. In *Multiple Bonds Between Metal Atoms*; Cotton, F. A.; Murillo, C. A.; Walton, R. A., Eds.; Springer, New York, 2005.

(130) Doyle, M. P.; McKervey, M. A.; Ye, T. *Modern Catalytic Methods for Organic Synthesis with Diazo Compounds*; Wiley-Interscience, New York, 1998.
(131) Hansen, J.; Davies, H. M. L. *Coord. Chem. Rev.* **2008**, *252*, 545.
(132) Berry, J. F. *Dalton Trans.* **2011**, *41*, 700.
(133) Davies, H. M. L.; Dick, A. R. *Top. Curr. Chem.* **2010**, *292*, 303.
(134) Doyle, M. P.; Forbes, D. C. *Chem. Rev.* **1998**, *98*, 911.
(135) Davies, H. M. L.; Denton, J. R. *Chem. Soc. Rev.* **2009**, *38*, 3061.
(136) Davies, H. M. L.; Beckwith, R. E. J. *Chem. Rev.* **2003**, *103*, 2861.
(137) Espino, C. G.; Du Bois, J. In *Modern Rhodium-Catalyzed Organic Reactions*; Evans, P. A., Ed.; Wiley-VCH, Weinheim, 2005; p. 379.
(138) Cahiez, G.; Moyeux, A. *Chem. Rev.* **2010**, *110*, 1435.
(139) Gosmini, C.; Moncomble, A. *Isr. J. Chem.* **2010**, *50*, 568.
(140) Gosmini, C.; Bégouin, J.-M.; Moncomble, A. *Chem. Commun.* **2008**, 3221.
(141) Gibson, V. C.; Redshaw, C.; Solan, G. A. *Chem. Rev.* **2007**, *107*, 1745.
(142) Bianchini, C.; Giambastiani, G.; Rios, I. G.; Mantovani, G.; Meli, A.; Segarra, A. M. *Coord. Chem. Rev.* **2006**, *250*, 1391.
(143) Pellissier, H.; Clavier, H. *Chem. Rev.* **2014**, *114*, 2775.
(144) Hess, W.; Treutwein, J.; Hilt, G. *Synthesis* **2008**, *22*, 3537.
(145) Tereniak, S. J.; Carlson, R. K.; Clouston, L. J.; Young, V. G., Jr.; Bill, E.; Maurice, R.; Chen, Y.-S.; Kim, H. J.; Gagliardi, L.; Lu, C. C. *J. Am. Chem. Soc.* **2014**, *136*, 1842.
(146) Harris, T. D.; Zhao, Q.; Hernández Sánchez, R.; Betley, T. A. *Chem. Commun.* **2011**, *47*, 6344.
(147) Semproni, S. P.; Hojilla Atienza, C. C.; Chirik, P. J. *Chem. Sci.* **2014**, *5*, 1956.
(148) Bowman, A. C.; Milsmann, C.; Bill, E.; Lobkovsky, E.; Weyhermüller, T.; Wieghardt, K.; Chirik, P. J. *Inorg. Chem.* **2010**, *49*, 6110.
(149) Ming, L.-J.; Jang, H. G.; Que, L., Jr. *Inorg. Chem.* **1992**, *31,* 359.
(150) Blanksby, S. J.; Ellison, G. B. *Acc. Chem. Res.* **2003**, *36*, 255.
(151) Gomberg, M. *J. Am. Chem. Soc.* **1900**, *22*, 757.
(152) Lankamp, H.; Nauta, W. T.; MacLean, C. *Tetrahedron Lett.* **1968**, *9*, 249.
(153) Schrauzer, G. N. *Acc. Chem. Res.* **1968**, *1*, 97.
(154) Schrauzer, G. N.; Deutsch, E.; Windgassen, R. J. *J. Am. Chem. Soc.* **1968**, *90*, 2441.
(155) Schrauzer, G. N.; Deutsch, E. *J. Am. Chem. Soc.* **1969**, *91*, 3341.
(156) Marlier, E. E.; Ulrich, B. A.; McNeill, K. *Inorg. Chem.* **2012**, *51*, 2079.
(157) Spielmann, J.; Buch, F.; Harder, S. *Angew. Chem. Int. Ed.* **2008**, *47*, 9434.
(158) Spessard, G. O.; Miessler, G. L. *Organometallic Chemistry*; 2nd

ed.; Oxford University Press: Oxford, 2009.
(159) Merkley, N.; El-Saidi, M.; Warkentin, J. *Can. J. Chem.* **2000**, *78*, 356.
(160) Ciunik, Z. *J. Mol. Struct.* **1997**, *412*, 27.
(161) Kastner, M. E.; Scheidt, W. R. *J. Organomet. Chem.* **1978**, *157*, 109.
(162) Haak, R. M.; Martínez Belmonte, M.; Escudero-Adán, E. C.; Benet-Buchholz, J.; Kleij, A. W. *Dalton Trans.* **2009**, *39*, 593.
(163) Cesari, M.; Neri, C.; Perego, G.; Perrotti, E.; Zazzetta, A. *J. Chem. Soc. D* **1970**, 276.
(164) Schaefer, W. P.; Waltzman, R.; Huie, B. T. *J. Am. Chem. Soc.* **1978**, *100*, 5063.
(165) Mallah, T.; Parsons, S.; Messenger, D. Private communication to the Cambridge Structural Database, deposition number CCDC 279614, 2005.
(166) Mills, D. P.; Cooper, O. J.; McMaster, J.; Lewis, W.; Liddle, S. T. *Dalton Trans.* **2009**, 4547.
(167) Scott, M. J.; Lippard, S. J. *Organometallics* **1998**, *17*, 1769.
(168) Lam, O. P.; Anthon, C.; Heinemann, F. W.; O'Connor, J. M.; Meyer, K. *J. Am. Chem. Soc.* **2008**, *130*, 6567.
(169) Matson, E. M.; Forrest, W. P.; Fanwick, P. E.; Bart, S. C. *Organometallics* **2013**, *32*, 1484.
(170) Connelly, N. G.; Geiger, W. E. *Chem. Rev.* **1996**, *96*, 877.
(171) Alnajjar, M. S.; Zhang, X.-M.; Gleicher, G. J.; Truksa, S. V.; Franz, J. A. *J. Org. Chem.* **2002**, *67*, 9016.
(172) Holmes, J. L.; Lossing, F. P.; Terlouw, J. K. *J. Am. Chem. Soc.* **1986**, *108*, 1086.
(173) He, L. P.; Yao, C. L.; Naris, M.; Lee, J. C.; Korp, J. D.; Bear, J. L. *Inorg. Chem.* **1992**, *31*, 620.
(174) Murillo, C. A. In *Multiple Bonds Between Metal Atoms*; Cotton, F. A.; Murillo, C. A.; Walton, R. A., Eds.; New York, 2005; p. 447.
(175) Fryzuk, M. D.; Leznoff, D. B.; Thompson, R. C.; Rettig, S. J. *J. Am. Chem. Soc.* **1998**, *120*, 10126.
(176) Ingleson, M. J.; Pink, M.; Fan, H.; Caulton, K. G. *J. Am. Chem. Soc.* **2008**, *130*, 4262.
(177) Pause, L.; Robert, M.; Saveant, J. M. *J. Am. Chem. Soc.* **1999**, *121*, 7158.
(178) Fedurco, M.; Sartoretti, C. J.; Augustynski, J. *J. Phys. Chem. B* **2001**, *105*, 2003.
(179) Zhu, D.; Korobkov, I.; Budzelaar, P. H. M. *Organometallics* **2012**, *31*, 3958.
(180) Ingleson, M. J.; Pink, M.; Caulton, K. G. *J. Am. Chem. Soc.* **2006**, *128*, 4248.
(181) Khaskin, E.; Diskin-Posner, Y.; Weiner, L.; Leitus, G.; Milstein, D. *Chem. Commun.* **2013**, *49*, 2771.

(182) Chomitz, W. A.; Arnold, J. *Inorg. Chem.* **2009**, *48*, 3274.
(183) Zhu, D.; Thapa, I.; Korobkov, I.; Gambarotta, S.; Budzelaar, P. H. M. *Inorg. Chem.* **2011**, *50*, 9879.
(184) Amatore, M.; Gosmini, C. *Angew. Chem. Int. Ed.* **2008**, *47*, 2089.
(185) Moncomble, A.; Le Floch, P.; Gosmini, C. *Chem. Eur. J.* **2009**, *15*, 4770.
(186) Gülak, S.; Stepanek, O.; Malberg, J.; Rad, B. R.; Kotora, M.; Wolf, R.; Jacobi von Wangelin, A. *Chem. Sci.* **2013**, *4*, 776.
(187) Gomes, P.; Gosmini, C.; Périchon, J. *Tetrahedron* **2003**, *59*, 2999.
(188) Amatore, M.; Gosmini, C.; Périchon, J. *Eur. J. Org. Chem.* **2005**, 989.
(189) Gomes, P.; Buriez, O.; Labbé, E.; Gosmini, C.; Périchon, J. *J. Electroanal. Chem.* **2004**, *562*, 255.
(190) Gomes, P.; Fillon, H.; Gosmini, C.; Labbé, E.; Périchon, J. *Tetrahedron* **2002**, *58*, 8417.
(191) Amatore, M.; Gosmini, C.; Périchon, J. *J. Org. Chem.* **2006**, *71*, 6130.
(192) Amatore, M.; Gosmini, C. *Chem.-Eur. J.* **2010**, *16*, 5848.
(193) Moncomble, A.; Floch, P. L.; Lledos, A.; Gosmini, C. *J. Org. Chem.* **2012**, *77*, 5056.
(194) Brennan, M. R.; Kim, D.; Fout, A. R. *Chem. Sci.* **2014**, In press.
(195) Bowman, A. C.; Milsmann, C.; Atienza, C. C. H.; Lobkovsky, E.; Wieghardt, K.; Chirik, P. J. *J. Am. Chem. Soc.* **2010**, *132*, 1676.
(196) Semproni, S. P.; Milsmann, C.; Chirik, P. J. *J. Am. Chem. Soc.* **2014**, *136*, 9211.
(197) McCusker, J. K.; Vincent, J. B.; Schmitt, E. A.; Mino, M. L.; Shin, K.; Coggin, D. K.; Hagen, P. M.; Huffman, J. C.; Christou, G.; Hendrickson, D. N. *J. Am. Chem. Soc.* **1991**, *113*, 3012.
(198) Christou, G.; Gatteschi, D.; Hendrickson, D. N.; Sessoli, R. *MRS Bull.* **2011**, *25*, 66.
(199) Christou, G. *Polyhedron* **2005**, *24*, 2065.
(200) Gatteschi, D.; Sessoli, R. *Angew. Chem. Int. Ed.* **2003**, *42*, 268.
(201) Xu, B.; Chasteen, N. D. *J. Biol. Chem.* **1991**, *266*, 19965.
(202) Ammala, P. S.; Batten, S. R.; Cashion, J. D.; Kepert, C. M.; Moubaraki, B.; Murray, K. S.; Spiccia, L.; West, B. O. *Inorg. Chim. Acta* **2002**, *331*, 90.
(203) Gorun, S. M.; Papaefthymiou, G. C.; Frankel, R. B.; Lippard, S. J. *J. Am. Chem. Soc.* **1987**, *109*, 4244.
(204) Taft, K.; Papaefthymiou, G.; Lippard, S. *Science* **1993**, *259*, 1302.
(205) Dziobkowski, C. T.; Wrobleski, J. T.; Brown, D. B. *Inorg. Chem.* **1981**, *20*, 671.
(206) Sorai, M.; Kaji, K.; Hendrickson, D. N.; Oh, S. M. *J. Am. Chem. Soc.* **1986**, *108*, 702.
(207) Oh, S. M.; Hendrickson, D. N.; Hassett, K. L.; Davis, R. E. *J. Am.*

Chem. Soc. **1985**, *107*, 8009.
(208) Chen, W.-L.; Chen, B.-W.; Tan, H.-Q.; Li, Y.-G.; Wang, Y.-H.; Wang, E.-B. *J. Solid State Chem.* **2010**, *183*, 310.
(209) Lin, S.; Liu, W.; Li, Y.; Wu, Q.; Wang, E.; Zhang, Z. *Dalton Trans.* **2010**, *39*, 1740.
(210) DeBord, J. R. D.; Reiff, W. M.; Warren, C. J.; Haushalter, R. C.; Zubieta, J. *Chem. Mater.* **1997**, *9*, 1994.
(211) Murali, M.; Nayak, S.; Costa, J. S.; Ribas, J.; Mutikainen, I.; Turpeinen, U.; Clémancey, M.; Garcia-Serres, R.; Latour, J.-M.; Gamez, P.; Blondin, G.; Reedijk, J. *Inorg. Chem.* **2010**, *49*, 2427.
(212) Sutradhar, M.; Carrella, L. M.; Rentschler, E. *Eur. J. Inorg. Chem.* **2012**, 4273.
(213) Sutradhar, M.; Roy Barman, T.; Drew, M. G. B.; Rentschler, E. *J. Molec. Struct.* **2013**, *1041*, 44.
(214) Cotton, F. A.; Daniels, L. M.; Falvello, L. R.; Matonic, J. H.; Murillo, C. A.; Wang, X.; Zhou, H. *Inorg. Chim. Acta* **1997**, *266*, 91.
(215) Cotton, F. A.; Daniels, L. M.; Jordan, G. T., IV; Murillo, C. A.; Pascual, I. *Inorg. Chim. Acta* **2000**, *297*, 6.
(216) Malassa, A.; Schulze, B.; Stein-Schaller, B.; Görls, H.; Weber, B.; Westerhausen, M. *Eur. J. Inorg. Chem.* **2011**, 1584.
(217) Jian, F.; Xiao, H.; Bai, Z.; Zhao, P. *J. Mater. Chem.* **2006**, *16*, 3746.
(218) Ming, L.-J. In *Physical Methods in Bioinorganic Chemistry: Spectroscopy and Magnetism*; Que, L., Jr., Ed.; University Science Books: Sausalito, CA, 2000; p. 375.
(219) Münck, E. In *Physical Methods in Bioinorganic Chemistry: Spectroscopy and Magnetism*; Que, L., Jr., Ed.; University Science Books: Sausalito, CA, 2000; p. 287.
(220) Gütlich, P.; Bill, E.; Trautwein, A. X. In *Mossbauer Spectroscopy and Transition Metal Chemistry: Fundamentals and Applications*; New York, 2011; p. 391.
(221) Dolphin, D.; Sams, J. R.; Tsin, T. B.; Wong, K. L. *J. Am. Chem. Soc.* **1976**, *98*, 6970.
(222) D'Alessandro, D. M.; Keene, F. R. *Chem. Rev.* **2006**, *106*, 2270.
(223) Cañada-Vilalta, C.; O'Brien, T. A.; Brechin, E. K.; Pink, M.; Davidson, E. R.; Christou, G. *Inorg. Chem.* **2004**, *43*, 5505.
(224) Gorun, S. M.; Lippard, S. J. *Inorg. Chem.* **1991**, *30*, 1625.
(225) Weihe, H.; Güdel, H. U. *J. Am. Chem. Soc.* **1997**, *119*, 6539.
(226) Sameera, W. M. C.; Piñero, D. M.; Herchel, R.; Sanakis, Y.; McGrady, J. E.; Raptis, R. G.; Zueva, E. M. *Eur. J. Inorg. Chem.* **2012**, 3500.
(227) Cheesman, M. R.; Greenwood, C.; Thomson, A. J. In *Advances in Inorganic Chemistry*; Sykes, A. G., Ed.; Academic Press, 1991; Vol. 36, p. 201.
(228) Fox, B. G.; Hendrich, M. P.; Surerus, K. K.; Andersson, K. K.; Froland, W. A.; Lipscomb, J. D.; Münck, E. *J. Am. Chem. Soc.* **1993**, *115*,

3688.
(229) Palmer, G. In *Physical Methods in Bioinorganic Chemistry: Spectroscopy and Magnetism*; Que, L., Jr., Ed.; Sausalito, CA, 2000; p. 121.
(230) Davis, J. C.; Averill, B. A. *Proc. Acad. Nat. Sci. USA* **1982**, *79*, 4623.
(231) Xing, G.; Hoffart, L. M.; Diao, Y.; Prabhu, K. S.; Arner, R. J.; Reddy, C. C.; Krebs, C.; Bollinger, J. M., Jr. *Biochemistry* **2006**, *45*, 5393.
(232) Li, F.; Chakrabarti, M.; Dong, Y.; Kauffmann, K.; Bominaar, E. L.; Münck, E.; Que, L., Jr. *Inorg. Chem.* **2012**, *51*, 2917.
(233) Payne, S. C.; Hagen, K. S. *J. Am. Chem. Soc.* **2000**, *122*, 6399.
(234) Majumdar, A.; Apfel, U.-P.; Jiang, Y.; Moënne-Loccoz, P.; Lippard, S. J. *Inorg. Chem.* **2014**, *53*, 167.
(235) Guigliarelli, B.; Bertrand, P.; Gayda, J. P. *J. Chem. Phys.* **1986**, *85*, 1689.
(236) Heintz, R. A.; Smith, J. A.; Szalay, P. S.; Weisgerber, A.; Dunbar, K. R. In *Inorganic Syntheses*; Coucouvanis, D., Ed.; New York, 2002; Vol. 33.
(237) Sharefkin, J. G.; Saltzman, H. *Org. Synth.* **1962**, *43*, 60.
(238) Sharefkin, J. G.; Saltzman, H. *Org. Synth.* **1962**, *43*, 62.
(239) Zhdankin, V. V.; Litvinov, D. N.; Koposov, A. Y.; Luu, T.; Ferguson, M. J.; McDonald, R.; Tykwinski, R. R. *Chem. Commun.* **2004**, 106.
(240) Costas, M.; Chen, K.; Que, L., Jr. *Coord. Chem. Rev.* **2000**, *200-202*, 517.
(241) Que, L., Jr.; Tolman, W. B. *Angew. Chem. Int. Ed.* **2002**, *41*, 1114.
(242) McDonald, A. R.; Que, L., Jr. *Coord. Chem. Rev.* **2013**, *257*, 414.
(243) Bollinger, J. M., Jr.; Diao, Y.; Matthews, M. L.; Xing, G.; Krebs, C. *Dalton Trans.* **2009**, 905.
(244) Feig, A. L.; Masschelein, A.; Bakac, A.; Lippard, S. J. *J. Am. Chem. Soc.* **1997**, *119*, 334.
(245) Feig, A. L.; Becker, M.; Schindler, S.; van Eldik, R.; Lippard, S. J. *Inorg. Chem.* **1996**, *35*, 2590.
(246) Bill, E. Personal communication, 2014.

Appendix 1: Supporting Information Figures for Chapter 2

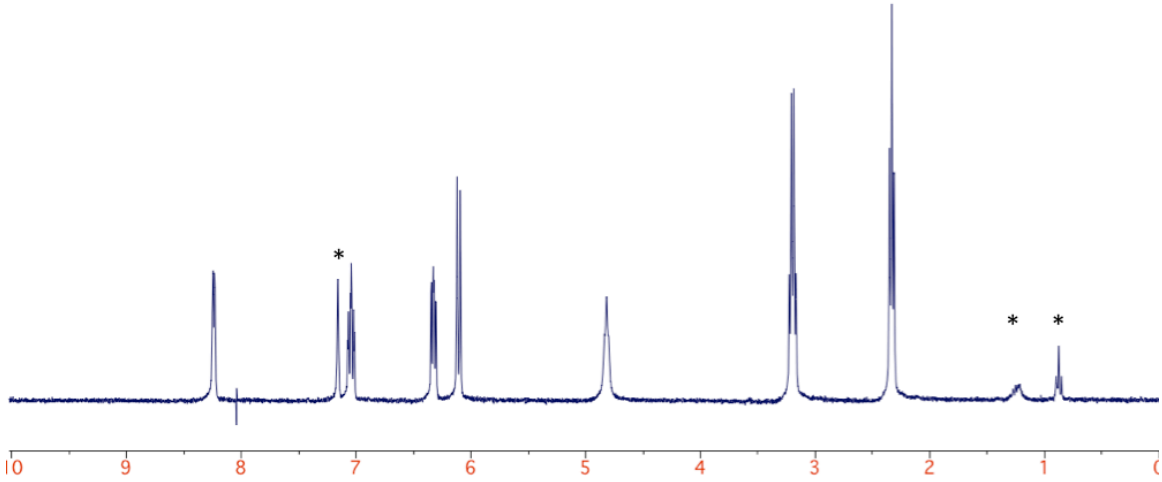

Figure A1.1. ^{1}H NMR spectrum (300 MHz, C_6D_6) of H_3py_3tren. Solvents denoted by asterisks.

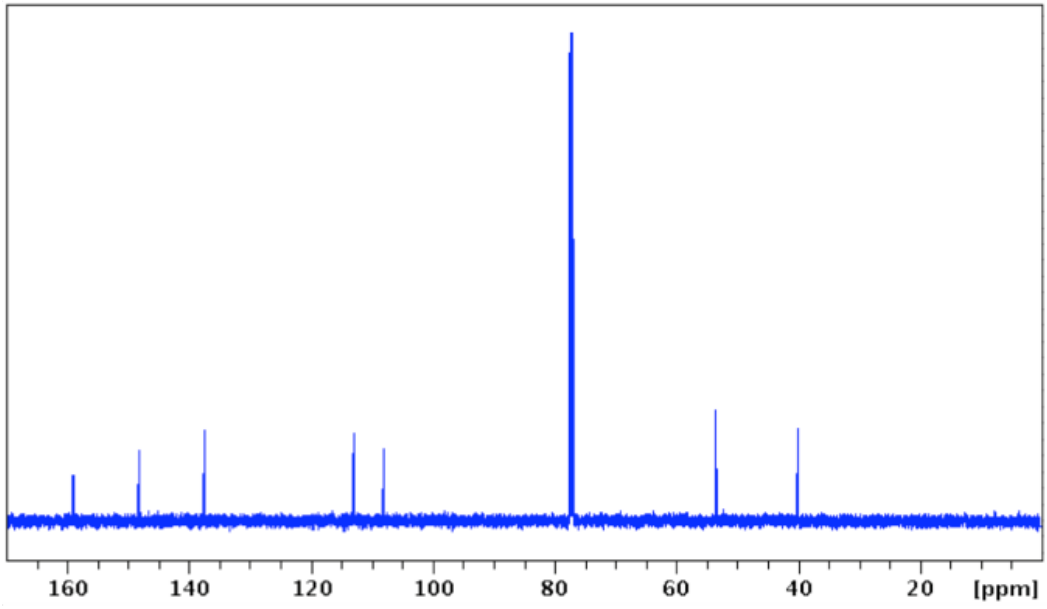

Figure A1.2. ^{13}C NMR spectrum (126 MHz, $CDCl_3$) of H_3py_3tren.

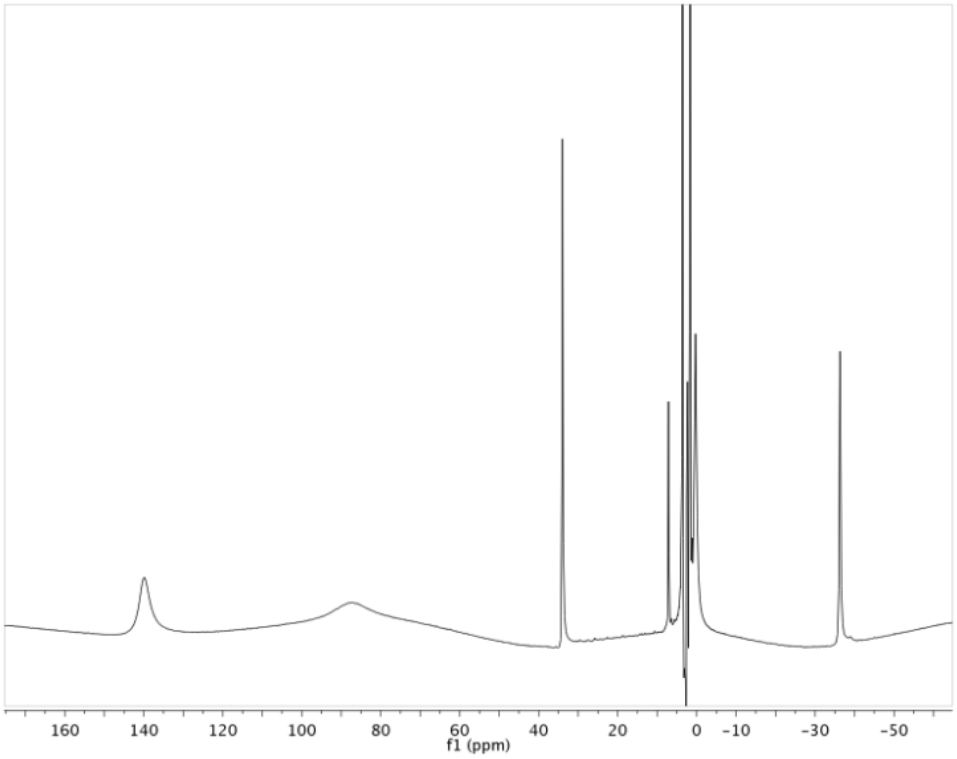

Figure A1.3. ^{1}H NMR spectrum (300 MHz, d_8-THF) of K[Co(py$_3$tren)].

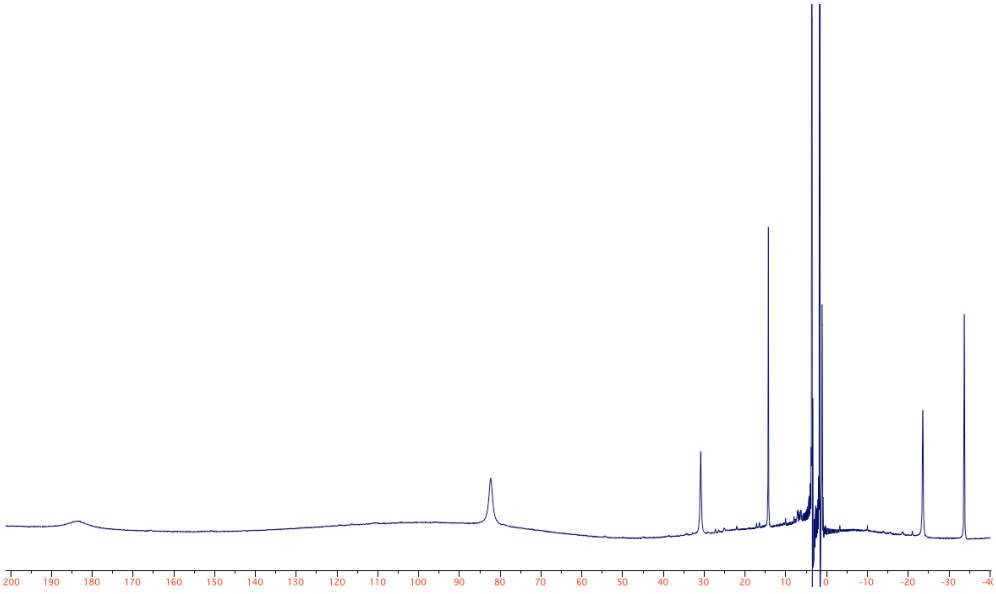

Figure A1.4. ^{1}H NMR spectrum (300 MHz, d_8-THF) of K[Fe(py$_3$tren)].

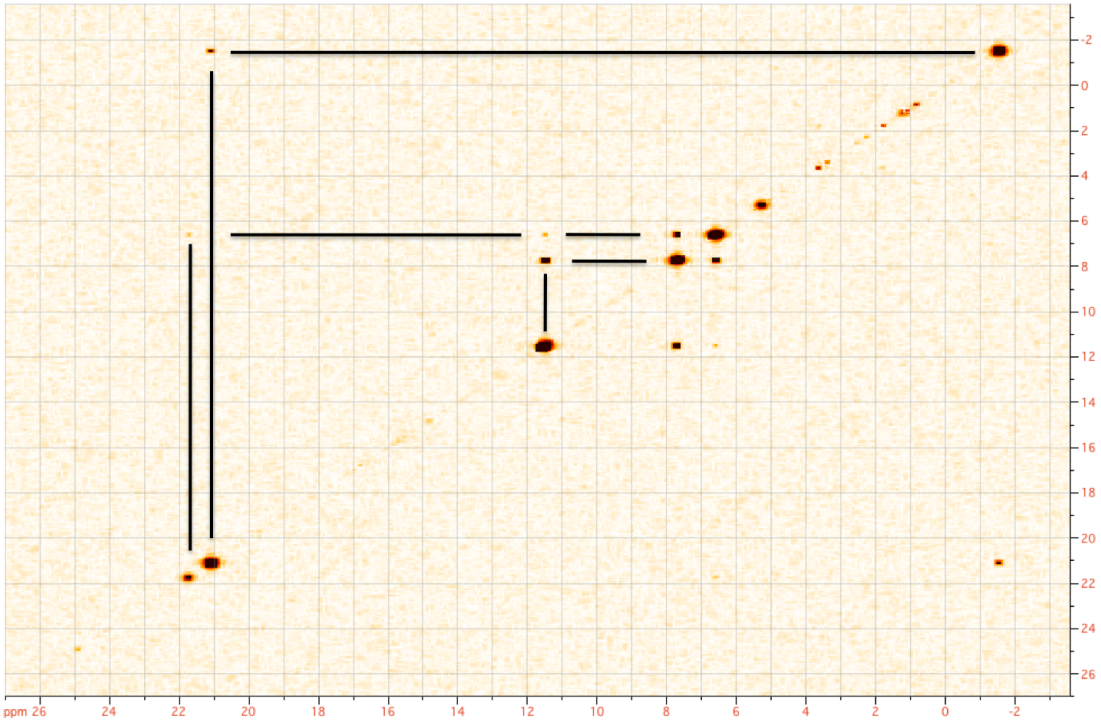

Figure A1.5. ^{1}H-^{1}H COSY NMR spectrum (300 MHz, CD_2Cl_2) of CoCoCl(py_3tren) **1**.

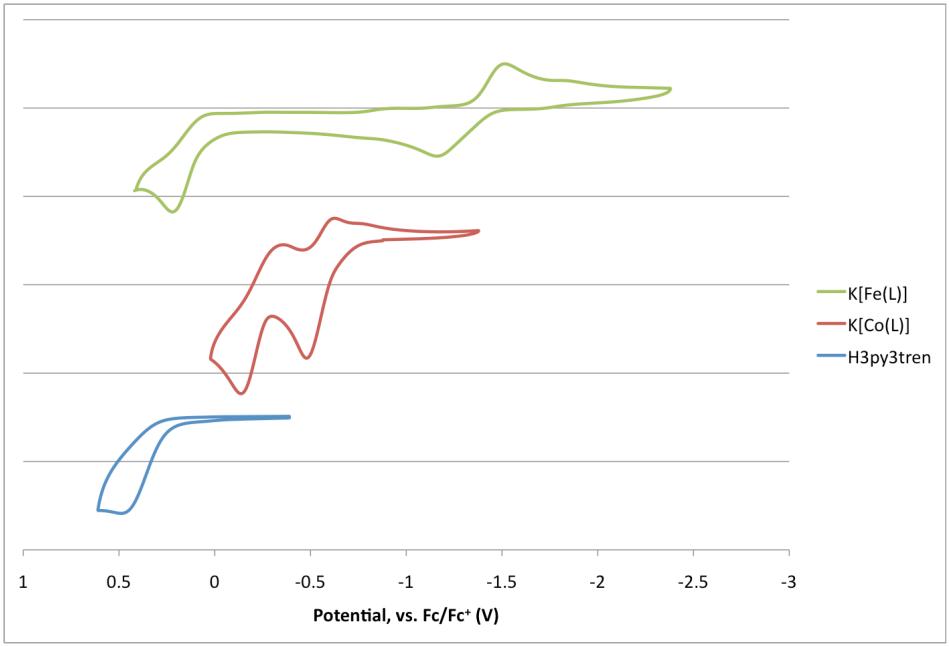

Figure A1.6. Cyclic voltammograms of (top) K[Fe(py_3tren)], (middle) K[Co(py_3tren)], and (bottom) H_3py_3tren. (300 MHz, d_8-THF) in 0.4 M [nBu_4N]PF_6/THF at 300 mV/s.

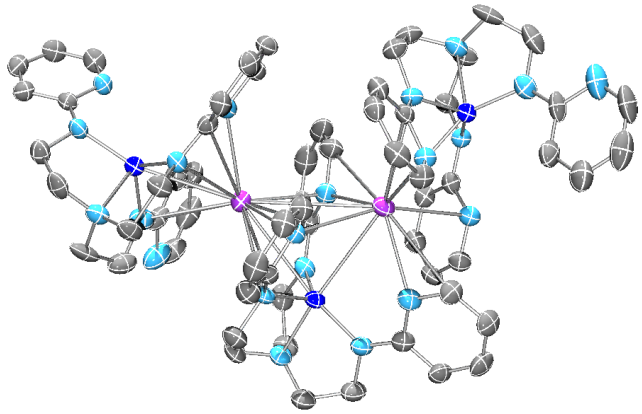

Figure A1.7. X-ray structure of K[Co(py$_3$tren)]. The molecule packs as a one-dimensional polymer. The asymmetric unit includes two independent molecules of K[Co(py$_3$tren)]; a third [Co(py$_3$tren)] anion is included to show how the polymer propagates.

Table A1.1. Crystallographic details for K[Co(py$_3$tren)].

	K[Co(py$_3$tren)]
chemical formula	$C_{21}H_{24}N_7CoK$
formula weight	472.50
crystal system	monoclinic
space group	$P2_1/c$
a (Å)	12.955(2)
b (Å)	16.210(3)
c (Å)	21.245(3)
α (deg)	90
β (deg)	106.123(2)
γ (deg)	90
V (Å^3)	4286.0(11)
Z	8
D_{calcd} (g cm^{-3})	1.465
l (Å), μ (mm^{-1})	0.71073, 1.018
T (K)	173(2)
θ range (deg)	1.60 to 26.37
reflns collected	18917
unique reflns	4634
data/restraints/parameters	4634 / 0 / 541
R_1, wR_2 ($I > 2\sigma(I)$)	0.0626, 0.1346

Table A1.2. Geometrical parameters, including bond lengths (Å) and angles (°) for K[Co(py$_3$tren)].[a]

	Molecule 1	Molecule 2
Co−N_{ap} (Å)	2.089(4)	2.089(4)
Co−N_{eq} (Å) [b]	1.955±0.010	1.954±0.014

[a] Estimated standard deviations (esd) are provided in parentheses. [b] M_1−N_{eq} bond lengths are reported as averages.

Table A1.3. Geometrical parameters, including bond lengths (Å) and angles (°) for complexes **2, 3,** and **5**, based on 30 keV data.[a]

	2	**3**	**5**
M_1−M_2 (Å)	2.49693(18)	2.5274(2)	2.5156(2)
r [b]	1.08	1.09	1.08
M_1−N_{ap} (Å)	2.0198(7)	2.0190(8)	2.0536(8)
M_1−N_{eq} (Å) [c]	1.9011±0.0031	1.9051±0.0053	1.9416±0.0067
M_2−Cl (Å)	2.3520(2)	2.3609(3)	2.3587(3)
M_2−N_{py} (Å) [c]	2.1073±0.0069	2.1624±0.0098	2.1768±0.0076
M_1−M_2−Cl (°)	177.407(8)	177.856(9)	177.154(9)

[a] Estimated standard deviations (esd) are provided in parentheses. [b] r = ratio of M_1−M_2 bond distance to the sum of M_1 and M_2 single-bond radii. [c] M_1−N_{eq} and M_2−N_{py} bond lengths are reported as averages.

Table A1.4. Crystallographic details from 30 keV anomalous scattering experiments for the MM'Cl(py_3tren) series, where MM' = CoFe **2**, CoMn **3**, and FeMn **5**.

	2	**3**	**5**
chemical formula	$C_{21}H_{24}N_7Co_{1.04}Fe_{0.96}Cl$	$C_{21}H_{24}N_7Co_{0.998}Mn_{1.002}Cl$	$C_{21}H_{24}N_7Fe_{0.995}Mn_{1.05}Cl$
formula weight	524.82	523.78	520.67
crystal system	monoclinic	monoclinic	monoclinic
space group	$P2_1/n$	$P2_1/n$	$P2_1/n$
a (Å)	9.2450(6)	9.3012(8)	9.3327(9)
b (Å)	12.5597(8)	12.4519(11)	12.4574(12)
c (Å)	18.4751(12)	18.5177(16)	18.4915(19)
α (deg)	90	90	90
β (deg)	98.7240(10)	98.632(2)	98.5268(15)
γ (deg)	90	90	90
V (Å^3)	2120.4(2)	2120.4(3)	2126.1(4)
Z	4	4	4
D_{calcd} (g cm^{-3})	1.644	1.641	1.627
l (Å), μ (mm^{-1})	0.71073, 1.617	0.41328, 0.302	0.41328, 0.279
T (K)	100(2)	100(2)	100(2)
θ range (deg)	1.934 to 24.353	1.902 to 24.670	1.520 to 24.525
reflns collected	17135	17761	17446
unique reflns	14038	14004	12304
data/restraints/parameters	14038 / 0 / 280	14004 / 0 / 280	12304 / 0 / 280
R_1, wR_2 ($I > 2\sigma(I)$)	0.0389, 0.1049	0.0355, 0.1140	0.0379, 0.0880

Table A1.5. CASSCF/CASPT2 Relative Spin State Energies

CoCoCl	**CASSCF (14/12) Relative Energies (kcal/mol)**	**CASPT2 Relative Energies (kcal/mol)**
singlet	0.00	0.00
triplet	0.81	2.00
quintet	2.43	5.55
septet	4.77	10.74
CoMnCl	CASSCF (12,12) Relative Energies (kcal/mol)	CASPT2 Relative Energies (kcal/mol)
singlet	77.0	72.0
triplet	0.00	0.00
quintet	1.14	2.47
septet	2.84	6.00
nonet	5.04	10.60
CoFeCl	CASSCF (13,12) Relative Energies (kcal/mol)	CASPT2 Relative Energies (kcal/mol)
doublet	0.00	0.00
quartet	0.99	2.26
sextet	2.63	5.80
octet	4.58	9.46
FeMnCl	CASSCF (11,12) Relative Energies (kcal/mol)	CASPT2 Relative Energies (kcal/mol)
doublet	0.00	0.00
quartet	0.71	1.66
sextet	1.94	4.27
octet	3.58	7.94
dectet	5.69	12.58
FeFeCl	CASSCF (12,12) Relative Energies (kcal/mol)	CASPT2 Relative Energies (kcal/mol)
singlet	0.00	0.00
triplet	0.36	4.35
quintet	2.39	4.32
septet	5.14	8.70
nonet	9.34	16.90
FeFeCl	CASSCF (12,15) Relative Energies (kcal/mol)	CASPT2 Relative Energies (kcal/mol)
septet	0.61	3.70
nonet	0.00	0.00
FeFeCl	RASSCF (12/20) Relative Energies (kcal/mol)	RASPT2 Relative Energies (kcal/mol)
singlet	0.00	N/A
septet	2.63 (0.00)	0.02
nonet	3.10 (0.47)	0.00

Table A1.6. Effective Bond Order and Weight of Main Configuration

	EBO	Weight of Main Configuration
FeFeCl septet	0.73	28%
CoCoCl singlet	0.22	19%
CoFeCl doublet	0.22	7.0%
CoMnCl triplet	0.22	6.5%
FeMnCl doublet	0.31	2.1%

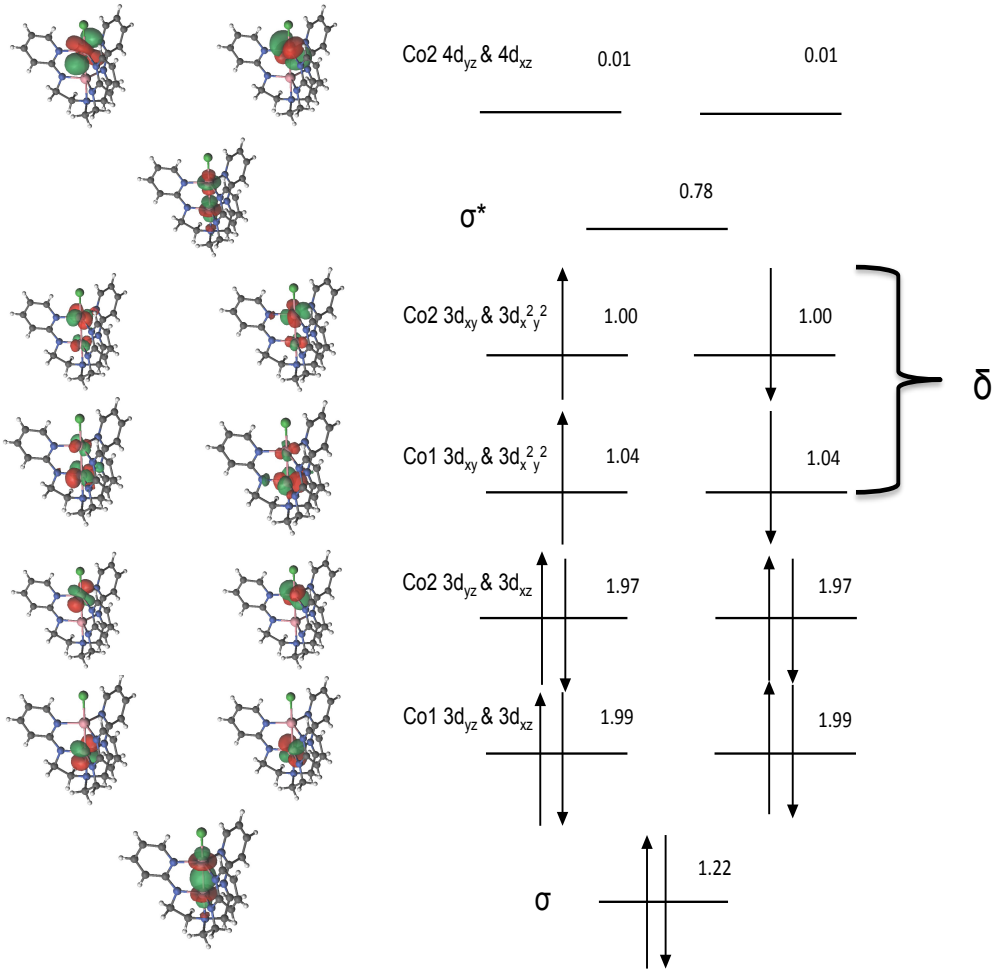

Figure A1.8. MO diagram for CoCoCl(py$_3$tren), with occupation numbers, showing the full active space.

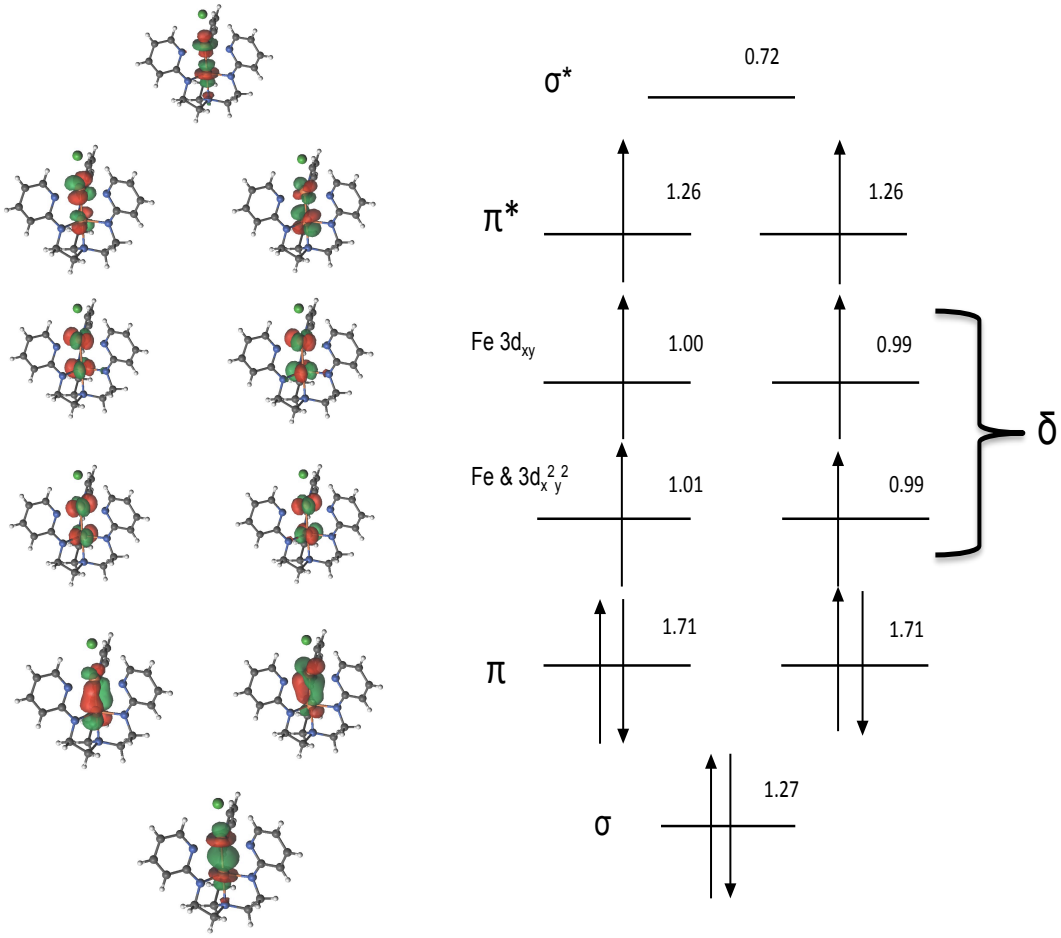

Figure A1.9. MO diagram for FeFeCl(py_3tren), with occupation numbers, showing the bottom half the active space, comprising 3*d* valence orbitals.

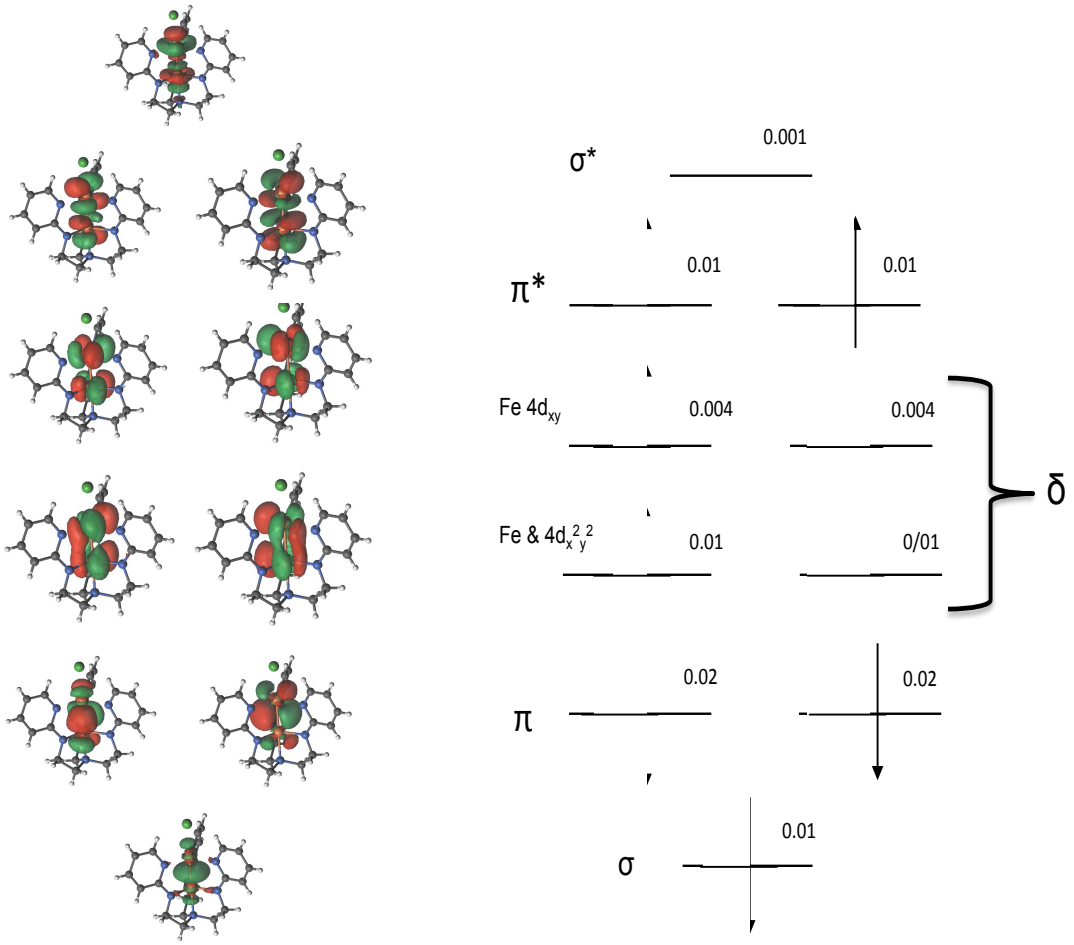

Figure A1.10. MO diagram for FeFeCl(py_3tren), with occupation numbers, showing the top half of the active space, comprising the correlating (and essentially unoccupied) 4*d* orbitals.

Table A1.7. Values and Total Energies (in a.u.) of the Considered High-Spin and Spin-Broken-Symmetry Solutions.

	PBE0	HSE	LC-ωPBE
CoCoCl			
HS	-4421.10598739646 (12.02)	-4421.28705547 (12.02)	-4421.79456035 (12.01)
BS	-4421.1198733571 (2.87)	-4421.30163682 (2.86)	-4421.80998972 (2.86)
CoFeCl			
HS	-4302.09152006 (15.79)	-4302.23975166 (15.79)	-4302.74007632 (15.78)
BS	-4302.10299312 (3.61)	-4302.25329967 (3.60)	-4302.75692961 (3.61)
CoMnCl			
HS	-4189.41541256 (20.02)	-4189.56481805 (20.02)	-4190.0616556 (20.01)
BS	-4189.42989109 (4.86)	-4189.57980209 (4.86)	-4190.07762632 (4.87)
FeMnCl			
HS	-4070.35204413 (24.78)	-4070.50336987 (24.78)	-4070.99278683 (24.77)
BS	-4070.36870057 (4.59)	-4070.52058816 (4.58)	-4071.01094875 (4.60)

Appendix 2: Supporting Information Figures for Chapter 3

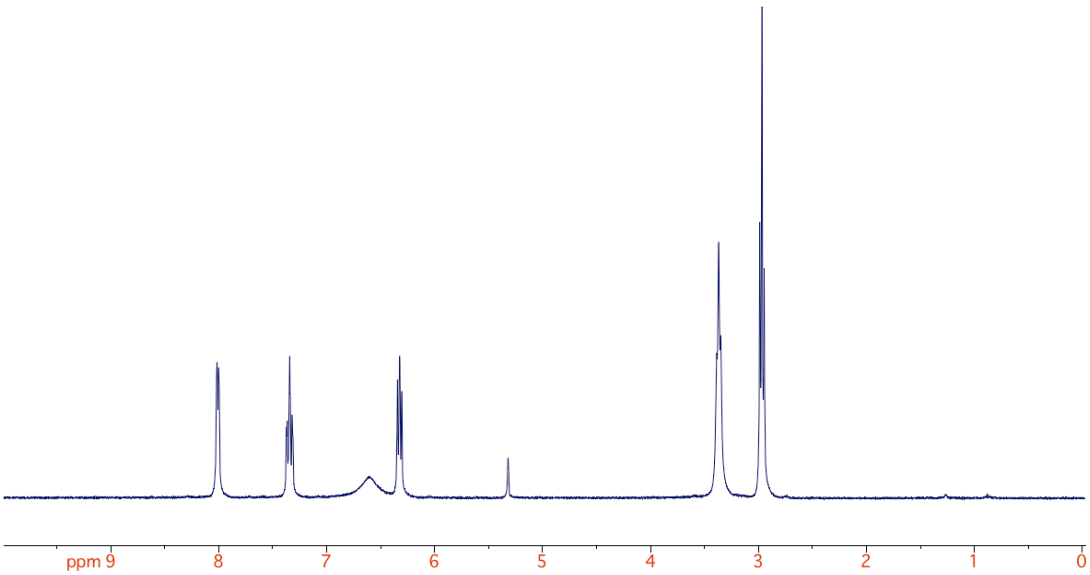

Figure A2.1. ^{1}H NMR spectrum of Al(py$_3$tren) in CD_2Cl_2.

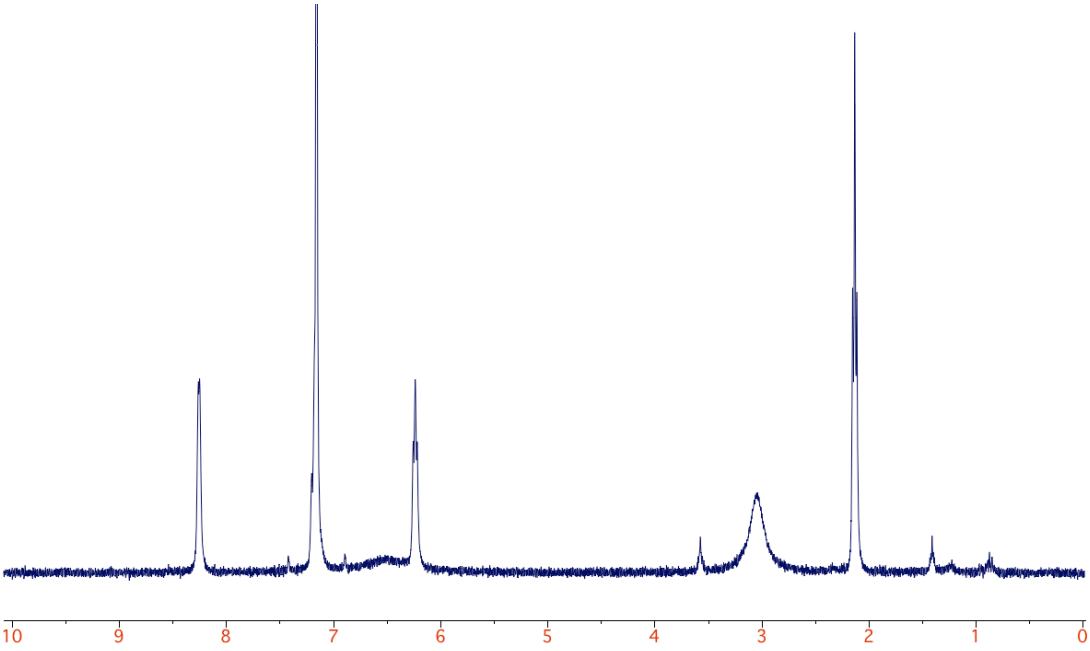

Figure A2.2. ^{1}H NMR spectrum of Al(py$_3$tren) in C_6D_6.

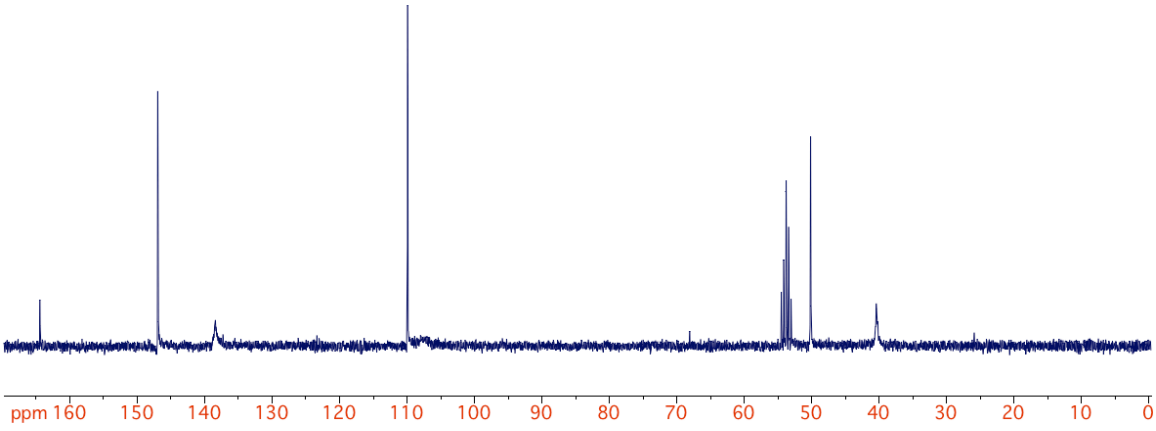

Figure A2.3. $^{13}C\{^{1}H\}$ NMR spectrum of Al(py_3tren) in CD_2Cl_2.

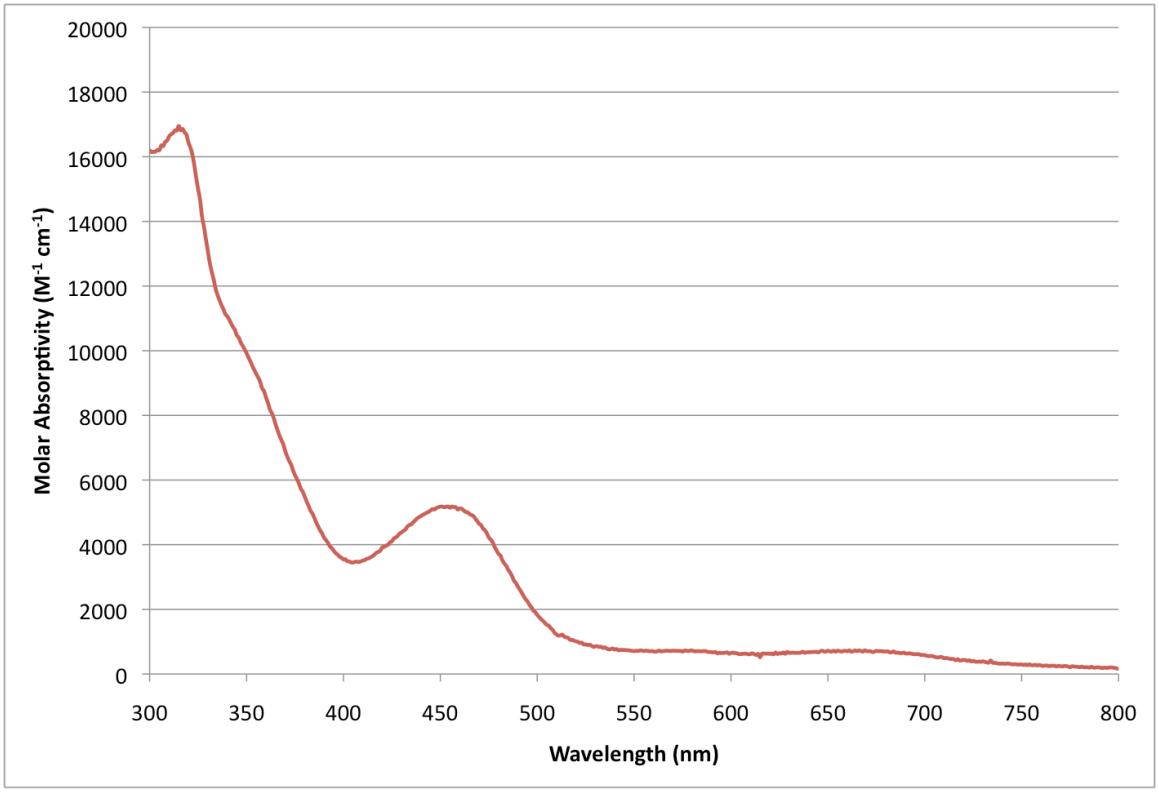

Figure A2.4. UV-Vis spectrum of CoCoBr(py_3tren) **1** in CH_2Cl_2.

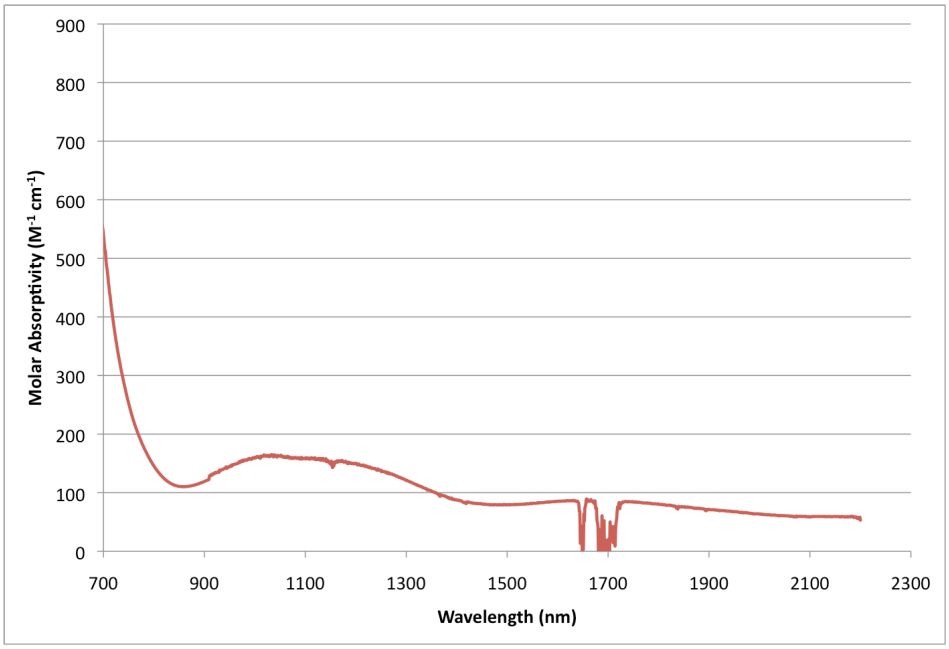

Figure A2.5. Vis-NIR spectrum of CoCoBr(py$_3$tren) **1** in CH_2Cl_2.

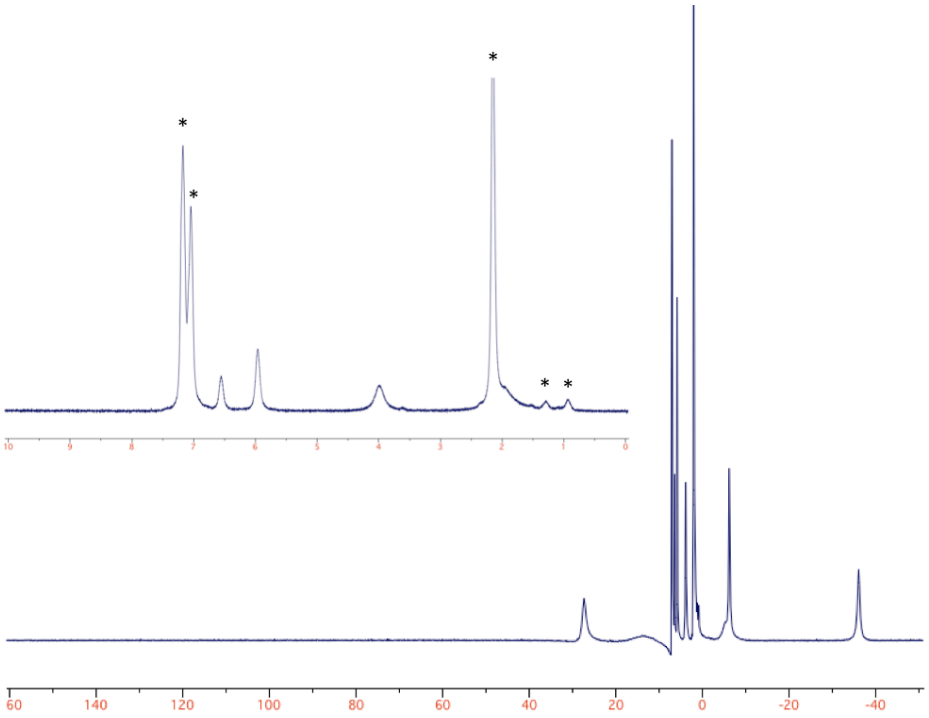

Figure A2.6. Room temperature ^{1}H NMR spectrum of paramagnetic CoCo(Bn)(py$_3$tren) **2** in d_8-toluene. Inset: Diamagnetic region of the ^{1}H NMR spectrum of CoCo(Bn)(py$_3$tren) **2** in d_8-toluene. Asterisks represent solvent peaks.

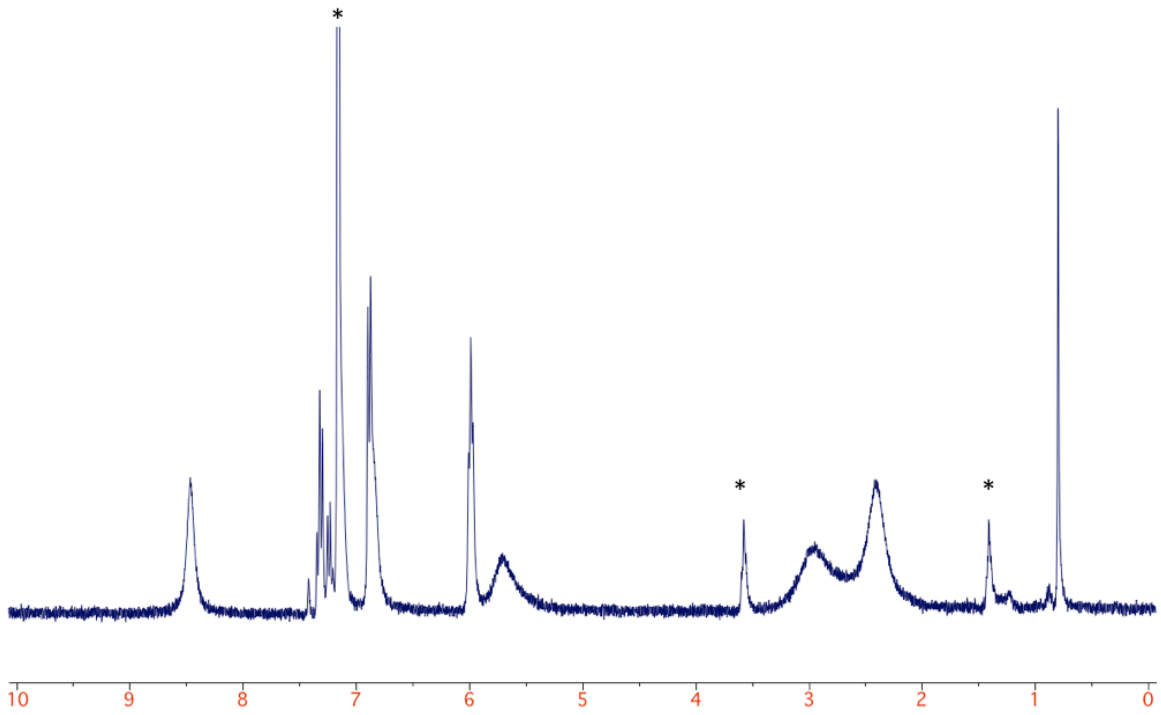

Figure A2.7. ^{1}H NMR spectrum of AlCo(Bn)(py$_3$tren) **4** in C_6D_6. Solvents are denoted with asterisks.

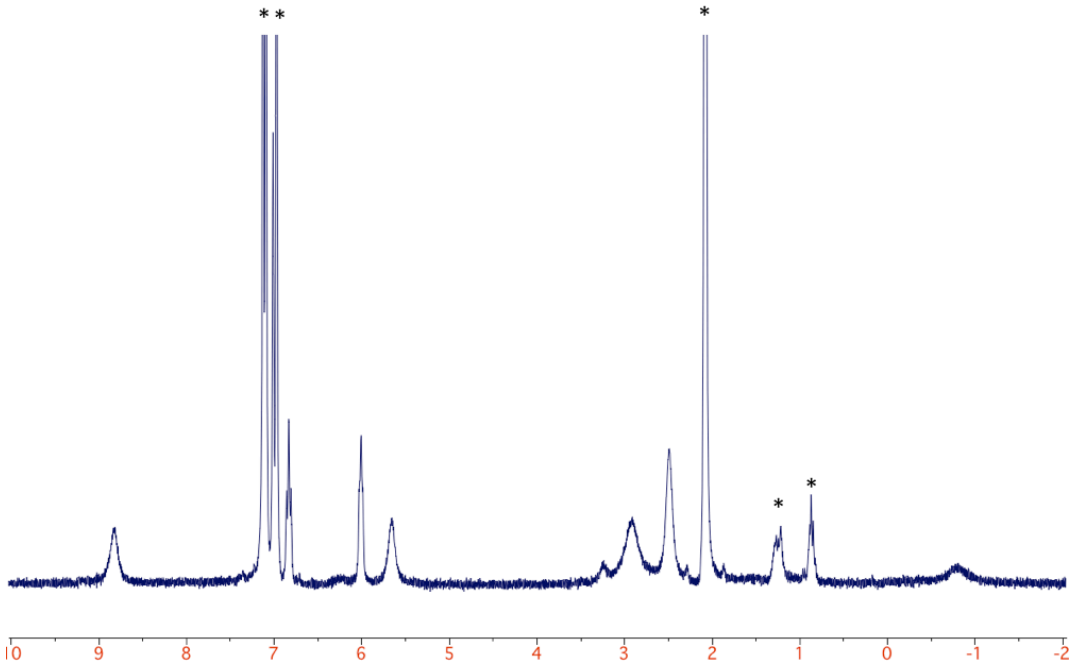

Figure A2.8. ^{1}H NMR spectrum of AlCo(Me)(py$_3$tren) **5** in d_8-toluene. Solvents are denoted with asterisks.

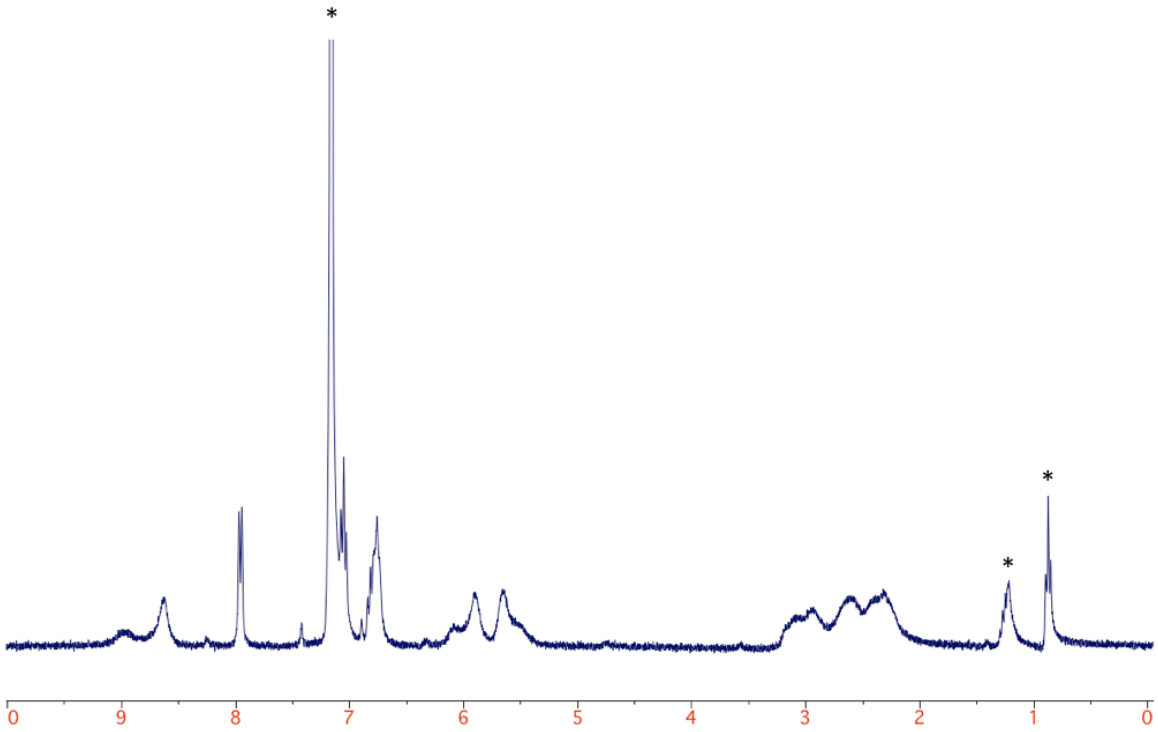

Figure A2.9. ^{1}H NMR spectrum of AlCo(Ph)(py$_3$tren) **6** in C_6D_6. Solvents are denoted with asterisks.

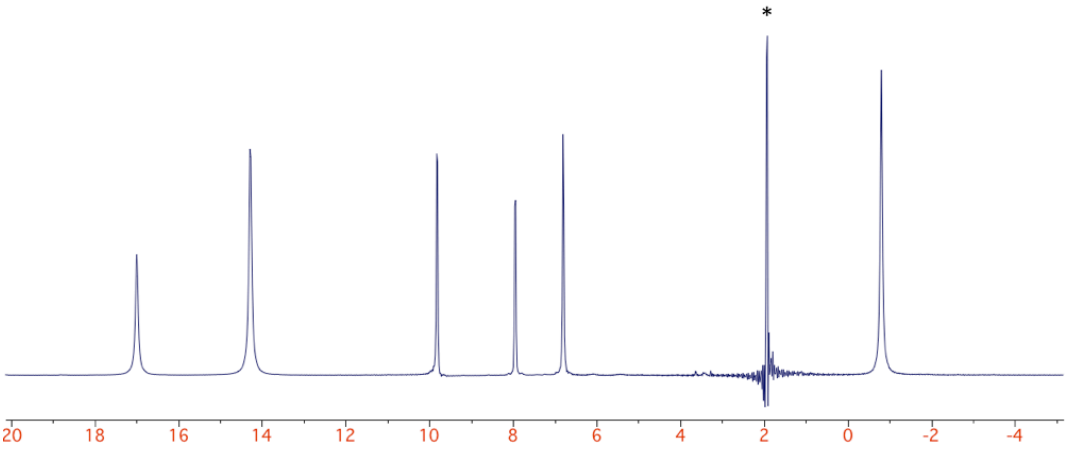

Figure A2.10. ^{1}H NMR spectrum of paramagnetic CoCo(PF_6)(py$_3$tren) **7** in CD_3CN. The asterisk marks CD_3CN.

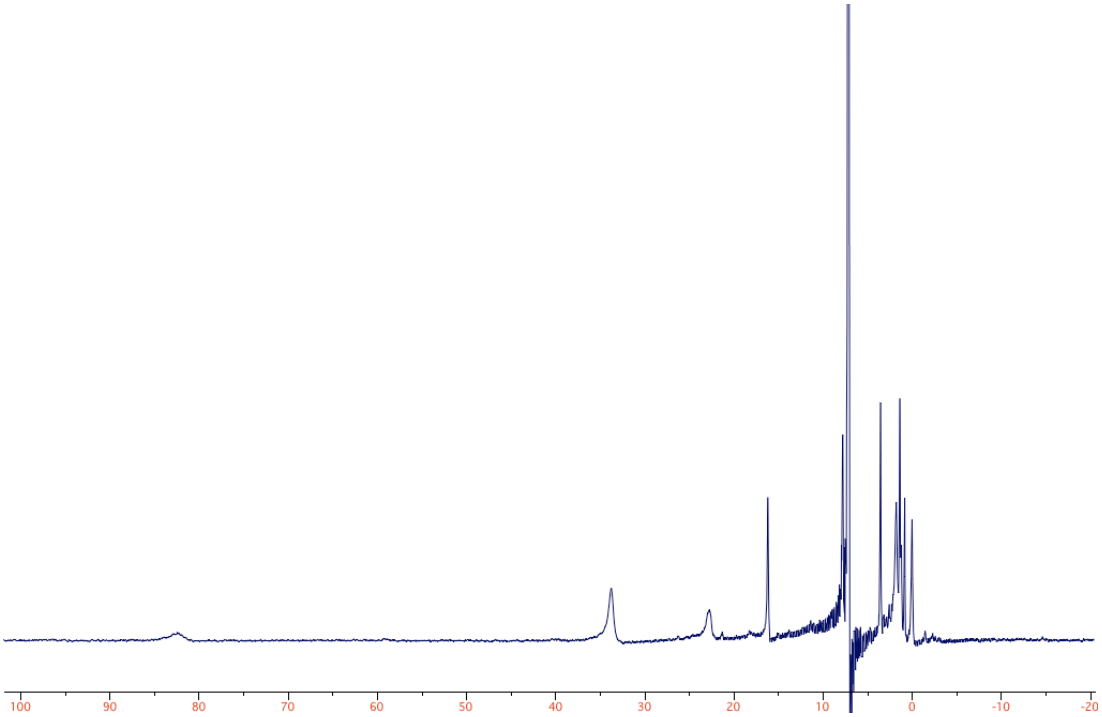

Figure A2.11. ^{1}H NMR spectrum of paramagnetic CoCo(py$_3$tren) in C_6D_6.

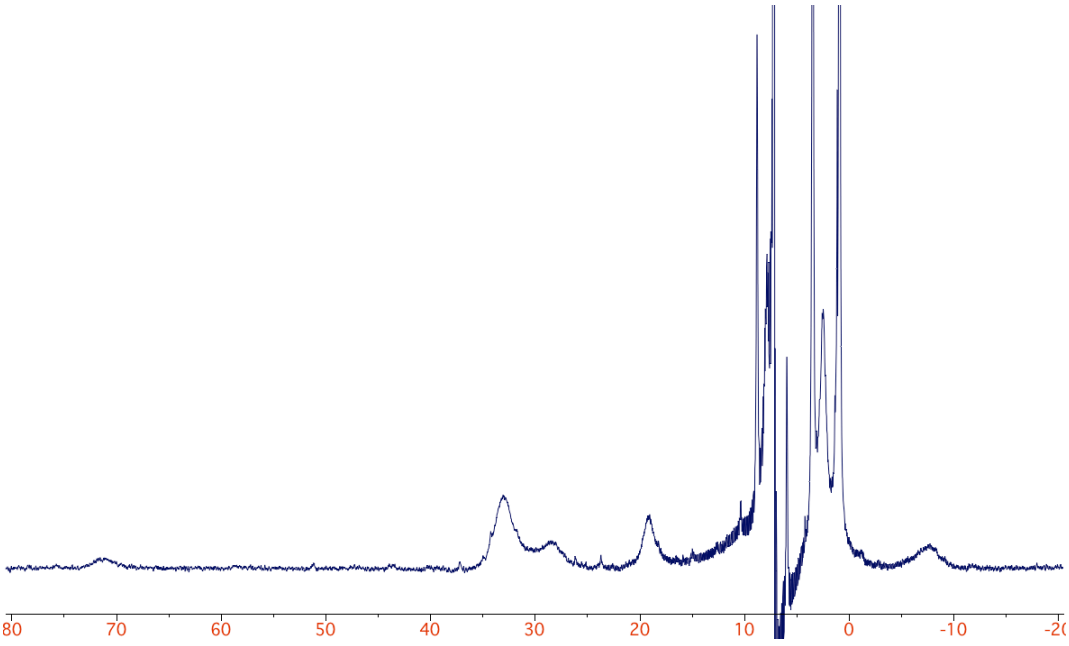

Figure A2.12. ^{1}H NMR spectrum of crystallized paramagnetic CoCo(TEMPO)(py$_3$tren) **9** in C_6D_6.

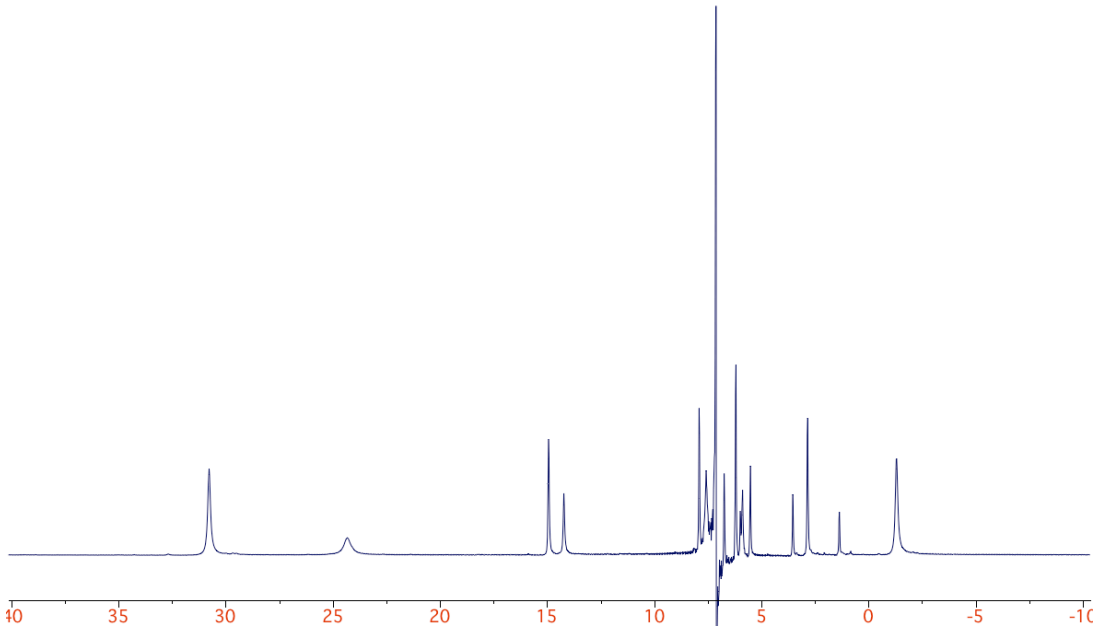

Figure A2.13. ^{1}H NMR spectrum of paramagnetic CoCo(OCPh$_2$Bn)(py$_3$tren) **10** from the independent synthesis in C_6D_6.

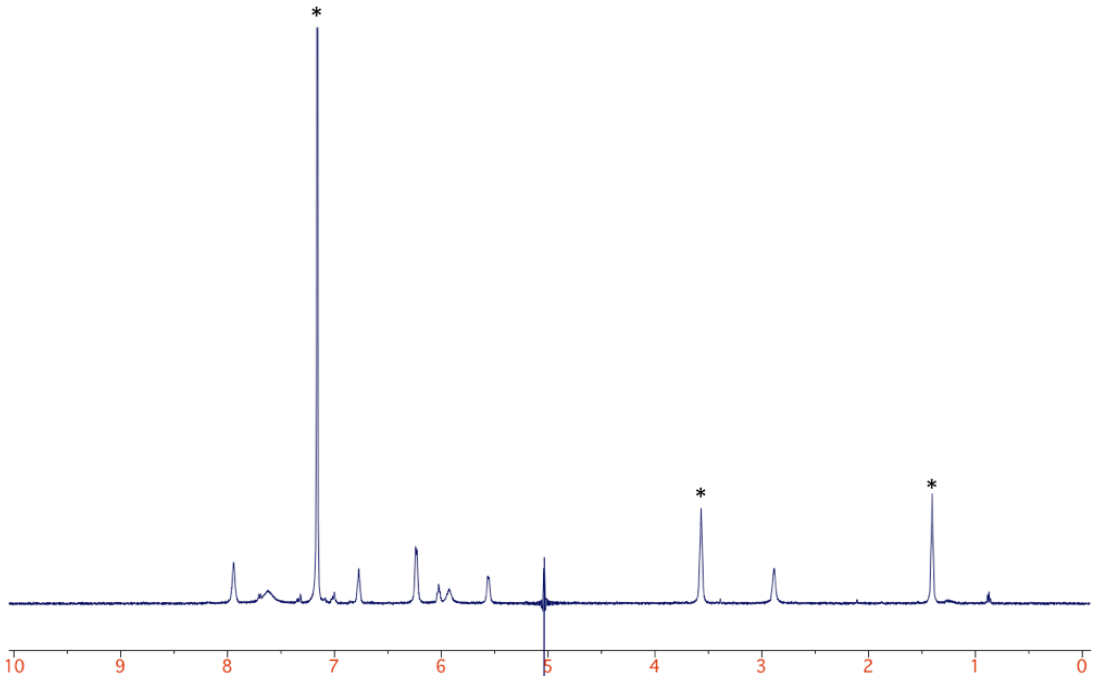

Figure A2.14. Diamagnetic region of the ^{1}H NMR spectrum of CoCo(OCPh$_2$Bn)(py$_3$tren) **10** in C_6D_6. Solvents marked with asterisks.

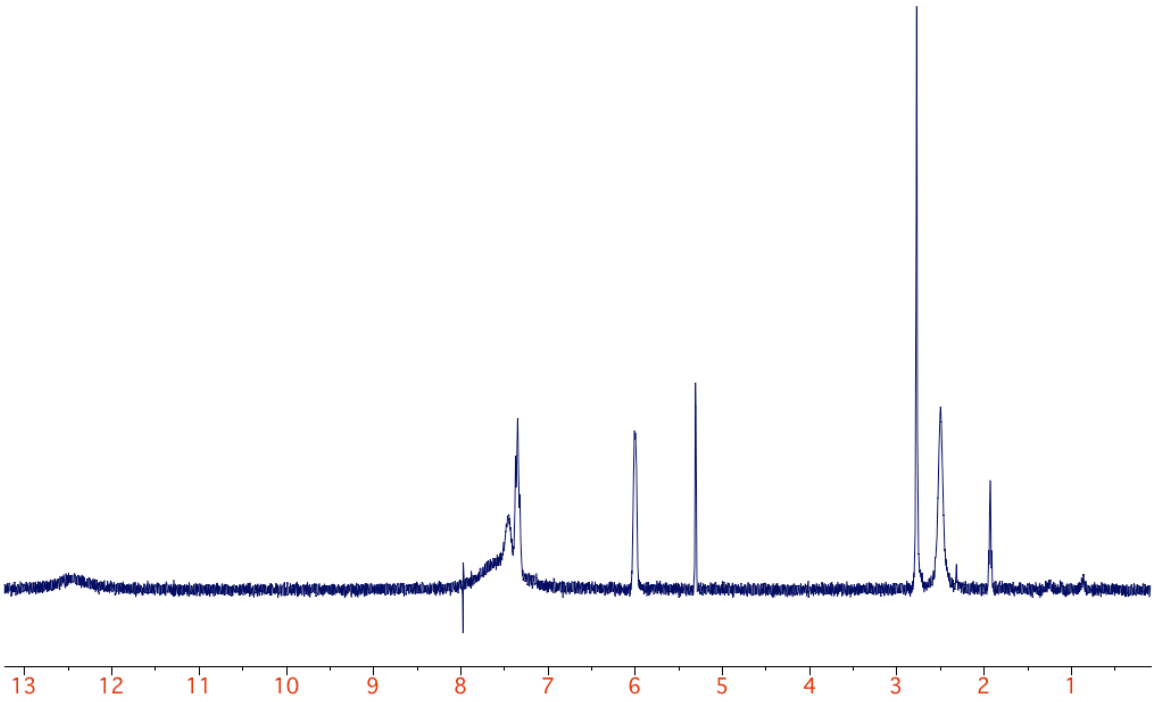

Figure A2.15. Diamagnetic ^{1}H NMR spectrum of CoCo(Su)(py$_3$tren) **11** in CD_2Cl_2.

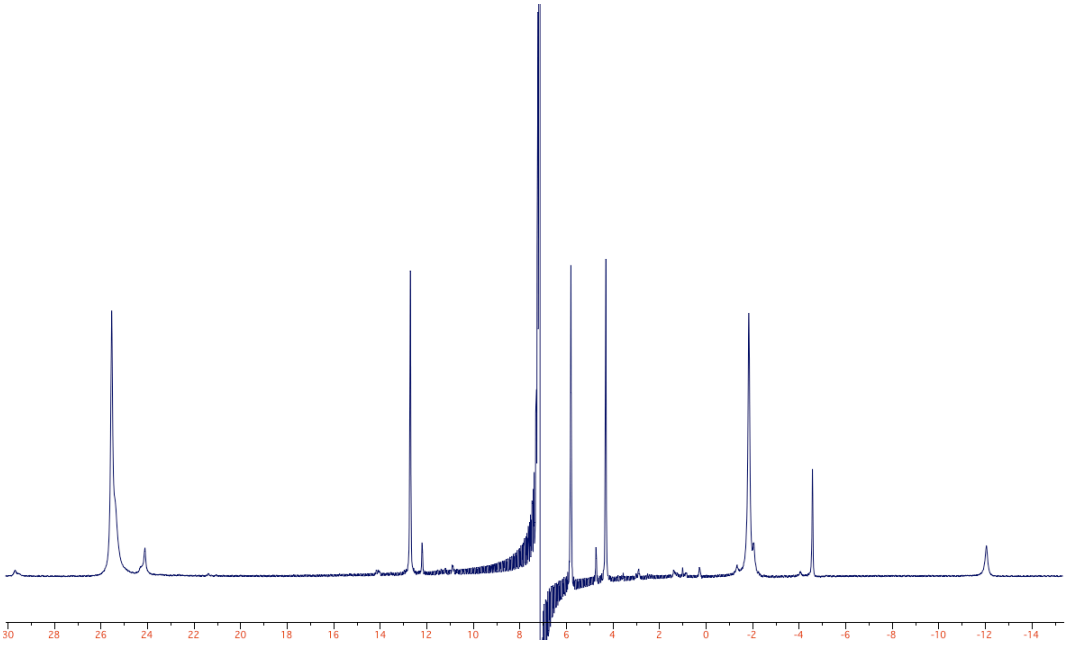

Figure A2.16. ^{1}H NMR spectrum of paramagnetic CoCo(OC(Me)=CH$_2$)(py$_3$tren) **12** from the independent synthesis in C_6D_6. A small impurity is present.

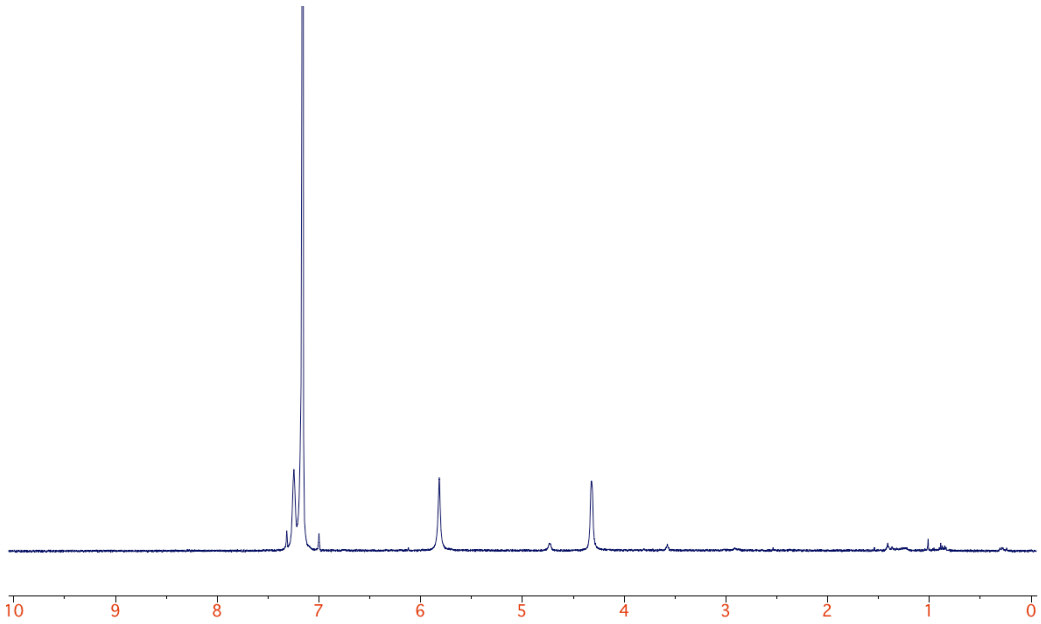

Figure A2.17. Diamagnetic region of the ^{1}H NMR spectrum of CoCo(OC(Me)=CH_2)(py_3tren) **12** from the independent synthesis in C_6D_6. A small impurity is present.

Reactivity Data

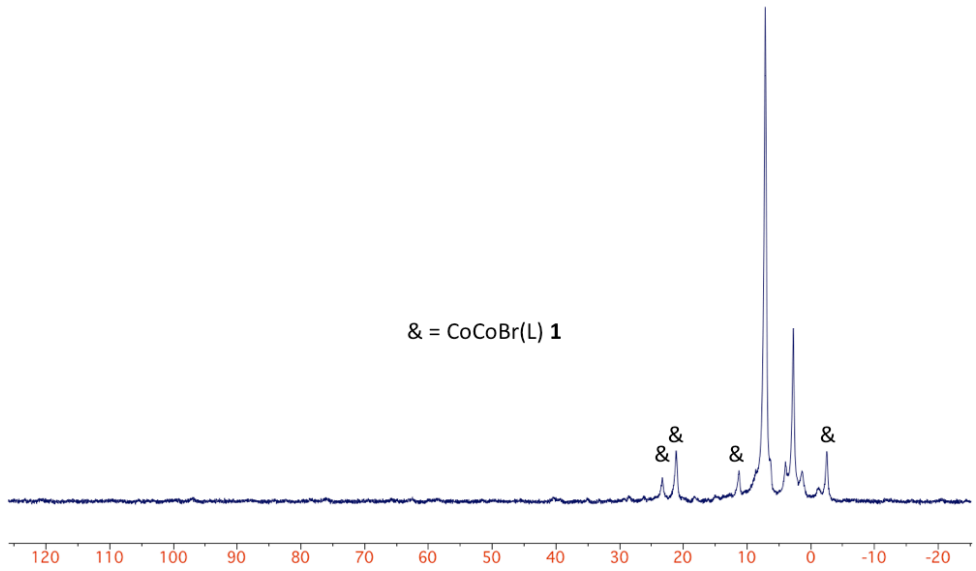

Figure A2.18. *In situ* paramagnetically shifted ^{1}H NMR spectrum of the reaction of benzyl bromide with CoCo(Bn)(py_3tren) **2** in C_6D_6.

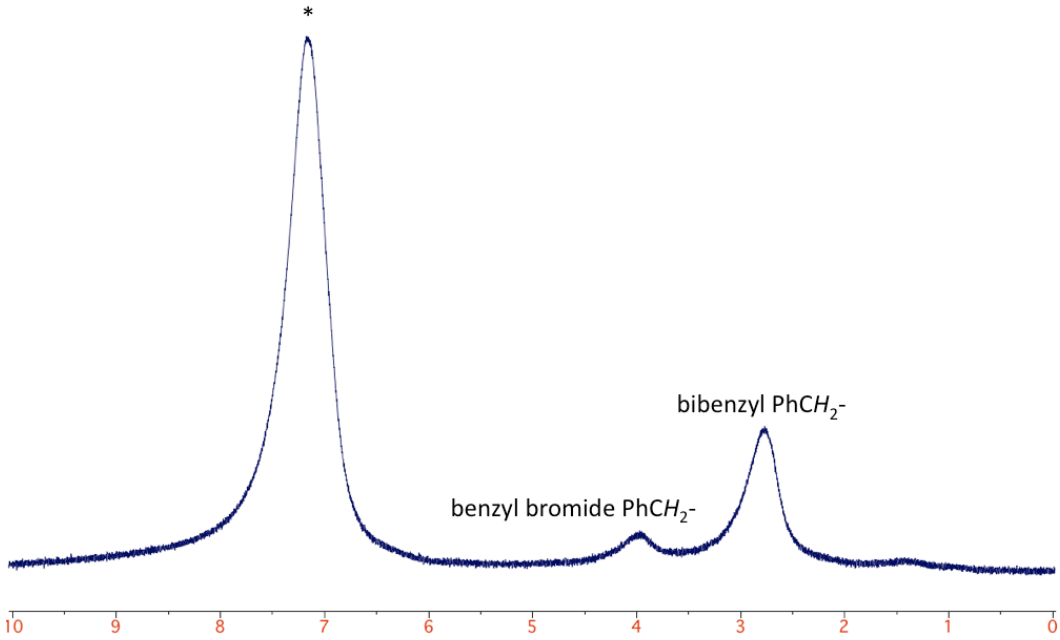

Figure A2.19. *In situ* diamagnetic region of the ^{1}H NMR spectrum of the reaction of benzyl bromide with CoCo(Bn)(py$_3$tren) **2** in C_6D_6.

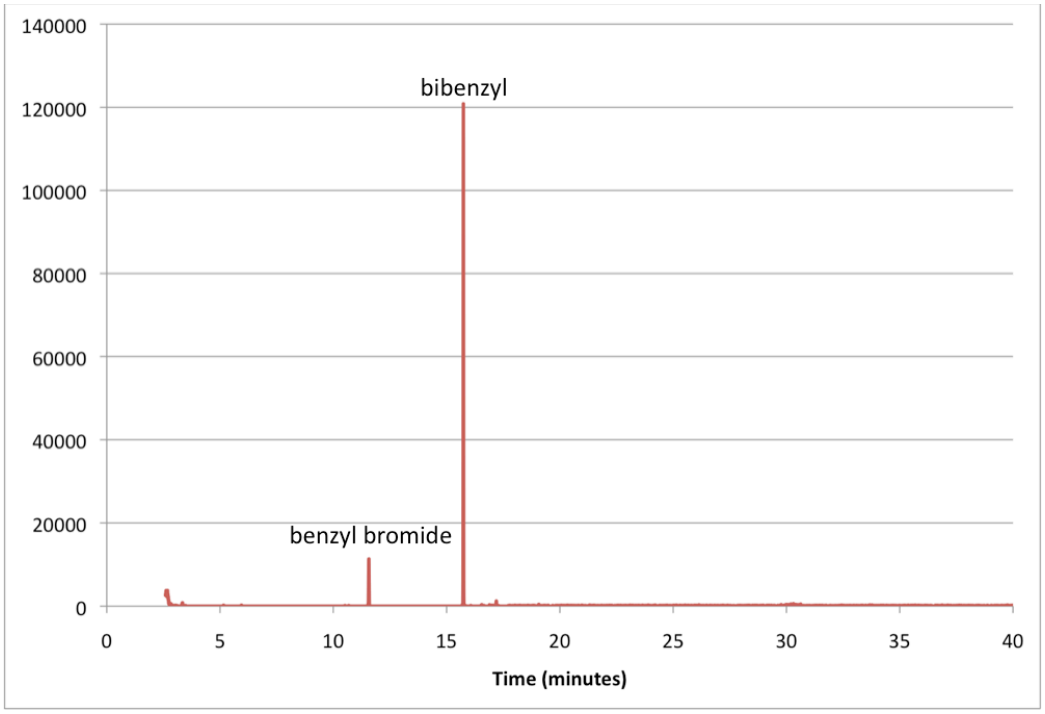

Figure A2.20. GC-MS data of the reaction of benzyl bromide with CoCo(Bn)(py$_3$tren) **2** in C_6D_6.

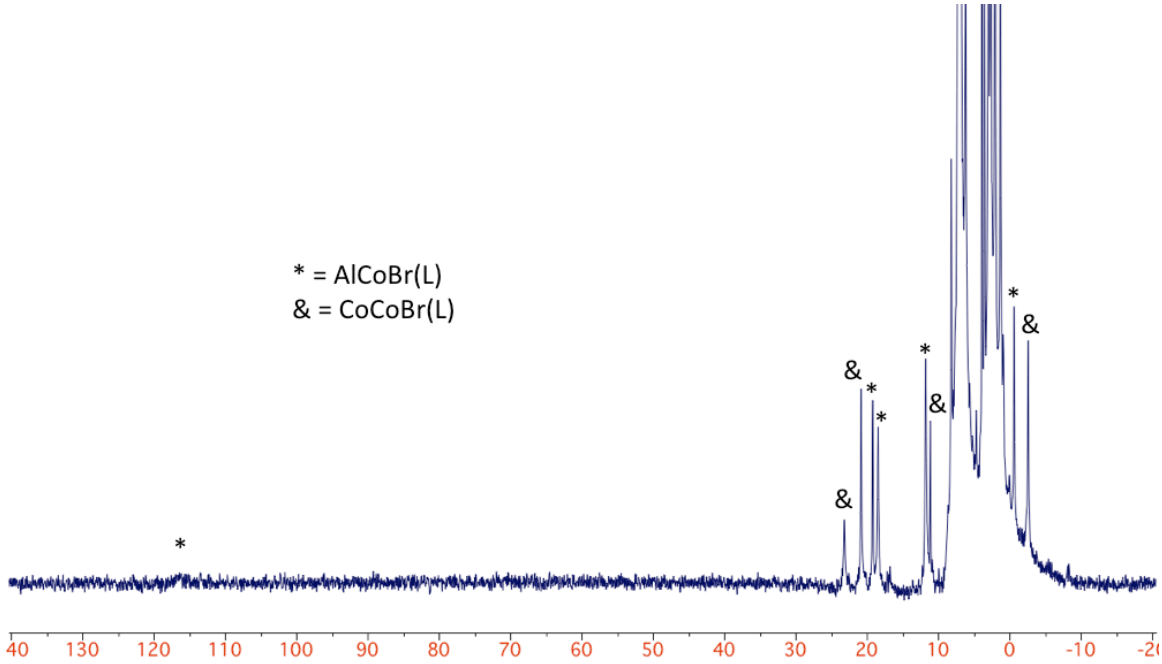

Figure A2.21. *In situ* paramagnetically shifted ^{1}H NMR of the reaction of benzyl bromide with AlCo(Bn)(py$_3$tren) **4** in C_6D_6.

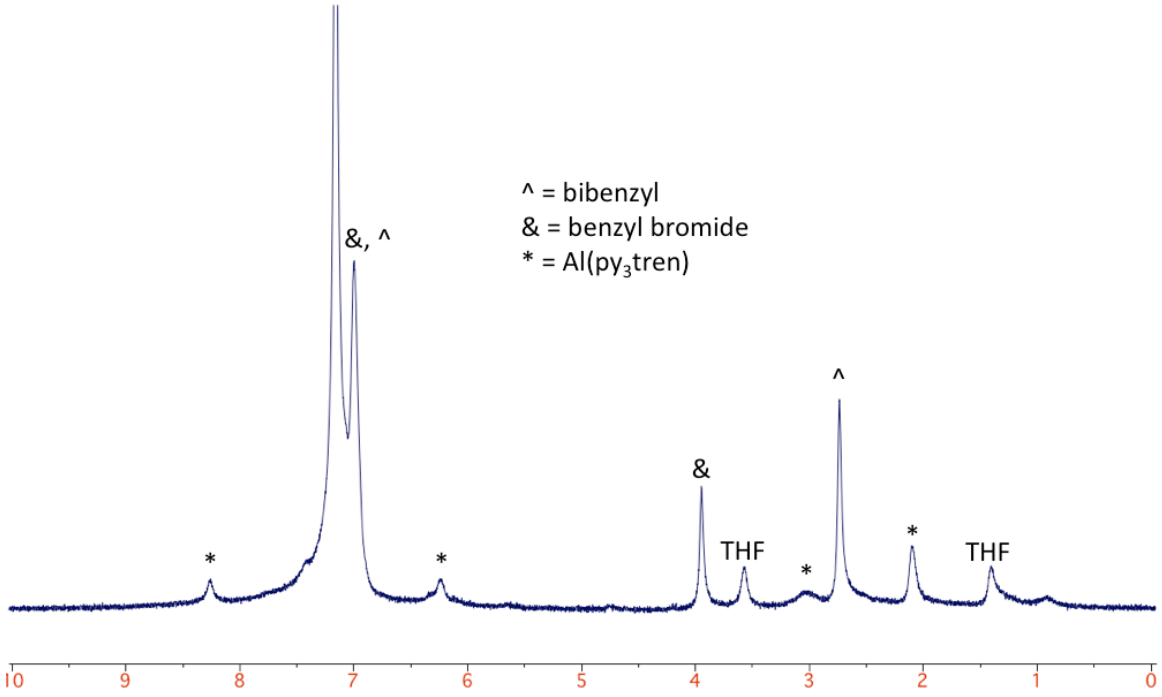

Figure A2.22. *In situ* diamagnetic region of the ^{1}H NMR spectrum of the reaction of benzyl bromide with AlCo(Bn)(py$_3$tren) **4** in C_6D_6.

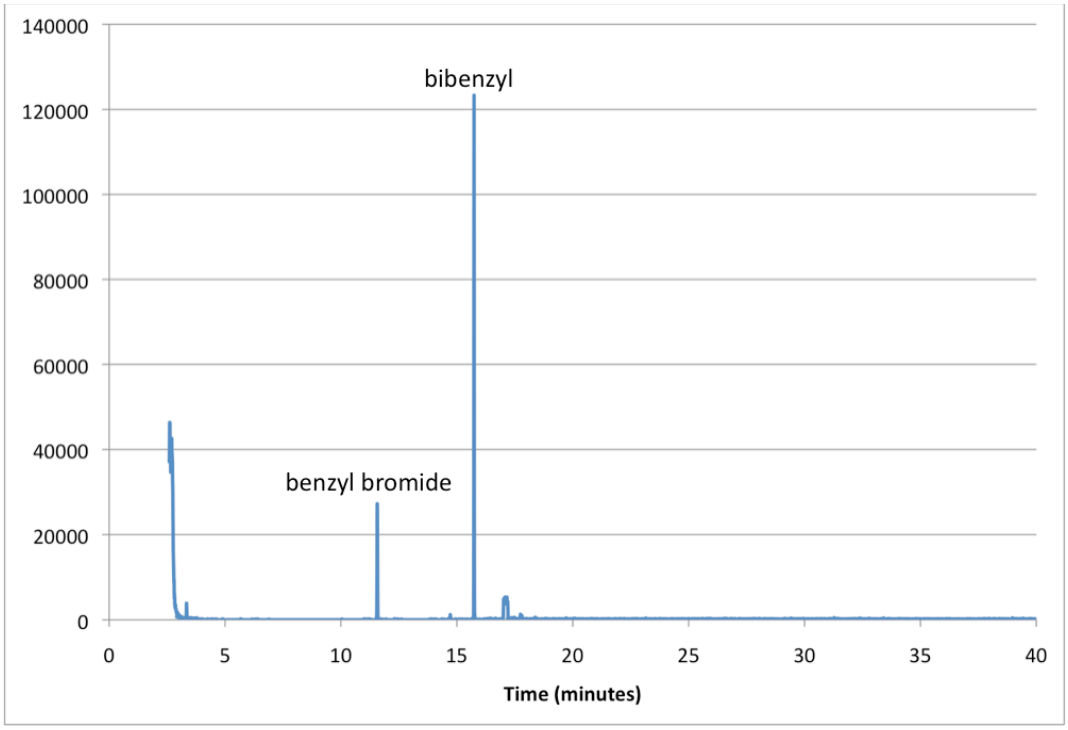

Figure A2.23. GC-MS data of the reaction of benzyl bromide with AlCo(Bn)(py_3tren) **4** in C_6D_6.

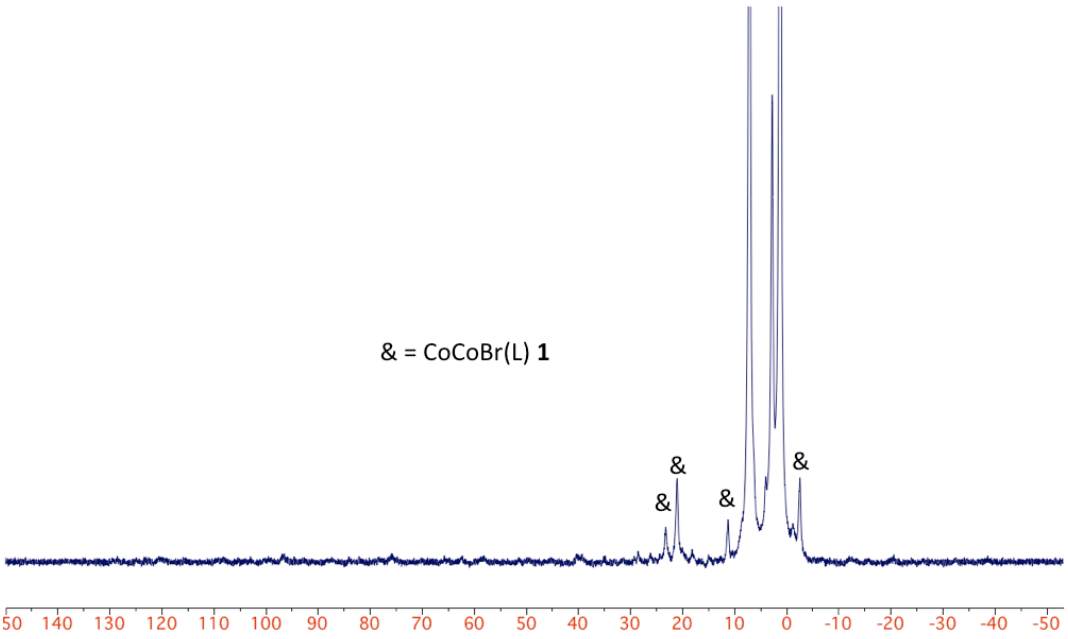

Figure A2.24. *In situ* paramagnetically shifted ^{1}H NMR spectrum of the reaction of 4-*tert*-butylbenzyl bromide with CoCo(Bn)(py_3tren) **2** in C_6D_6.

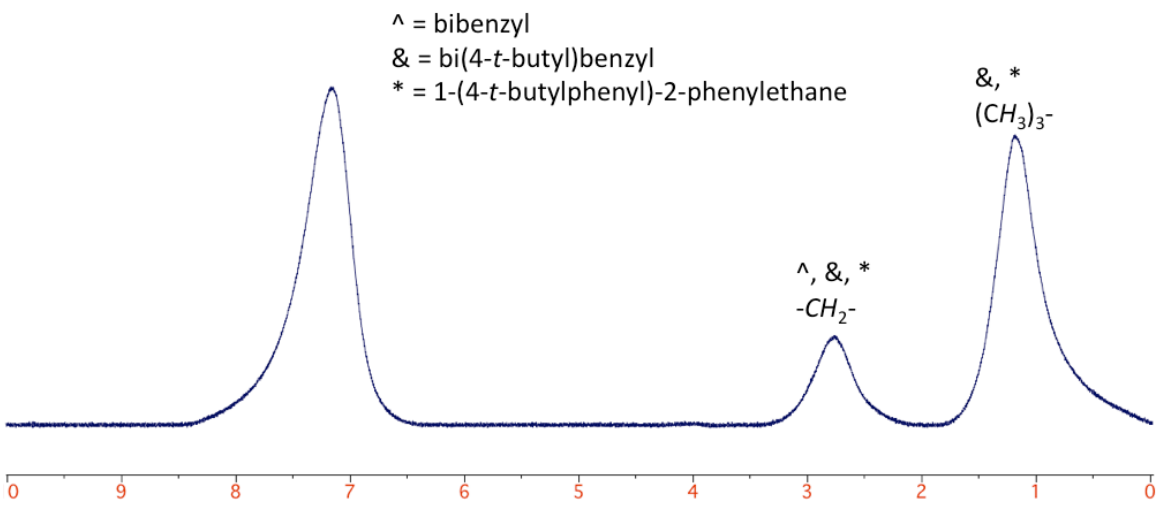

Figure A2.25. *In situ* diamagnetic region of the ^{1}H NMR spectrum of the reaction of 4-*tert*-butylbenzyl bromide with CoCo(Bn)(py$_3$tren) **2** in C_6D_6.

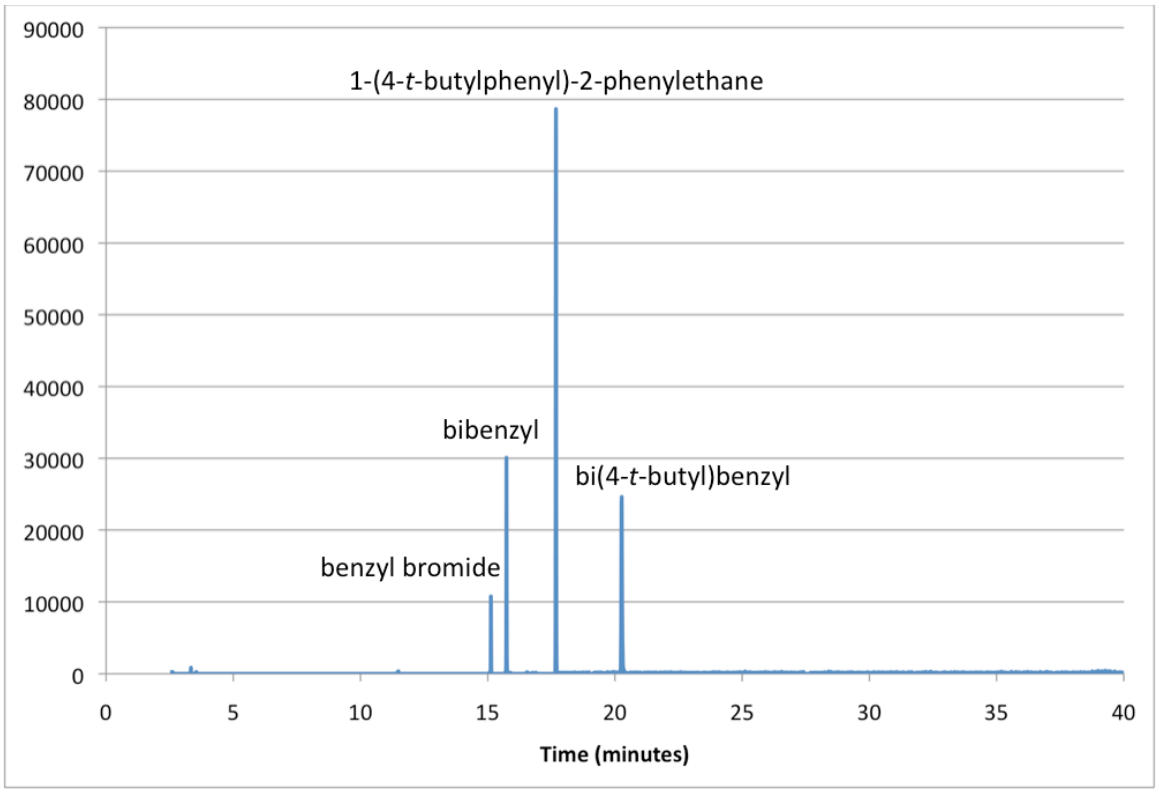

Figure A2.26. GC-MS data of the reaction of 4-(*tert*-butyl)benzyl bromide with CoCo(Bn)(py$_3$tren) **2** in C_6D_6.

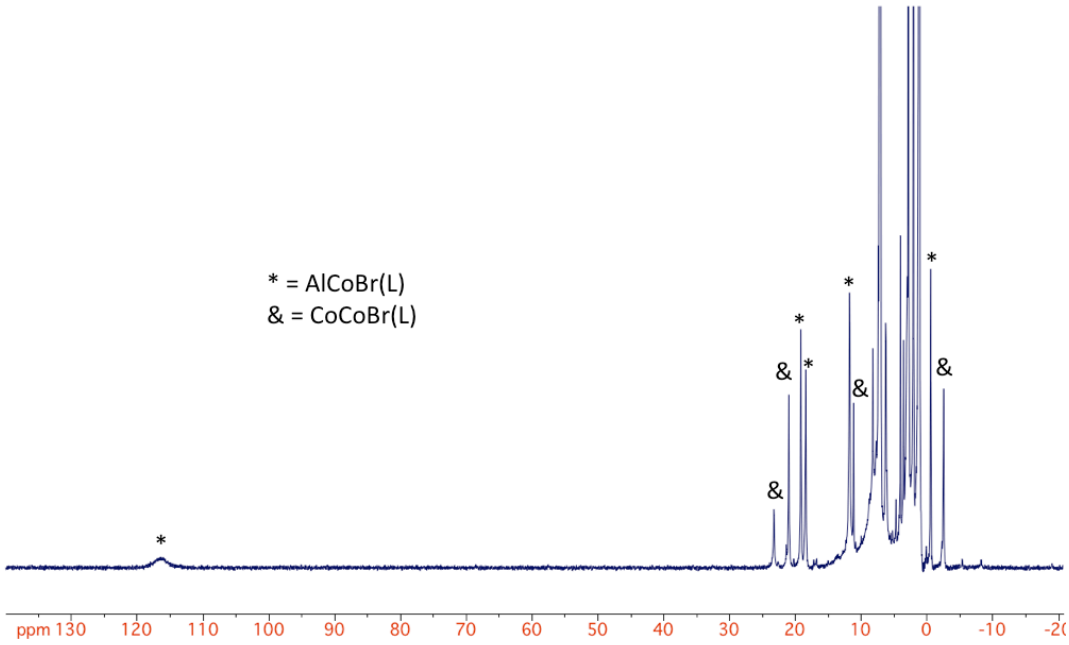

Figure A2.27. *In situ* paramagnetically shifted ^{1}H NMR spectrum of the reaction of 4-(*tert*-butyl)benzyl bromide with AlCo(Bn)(py$_3$tren) **4** in C_6D_6.

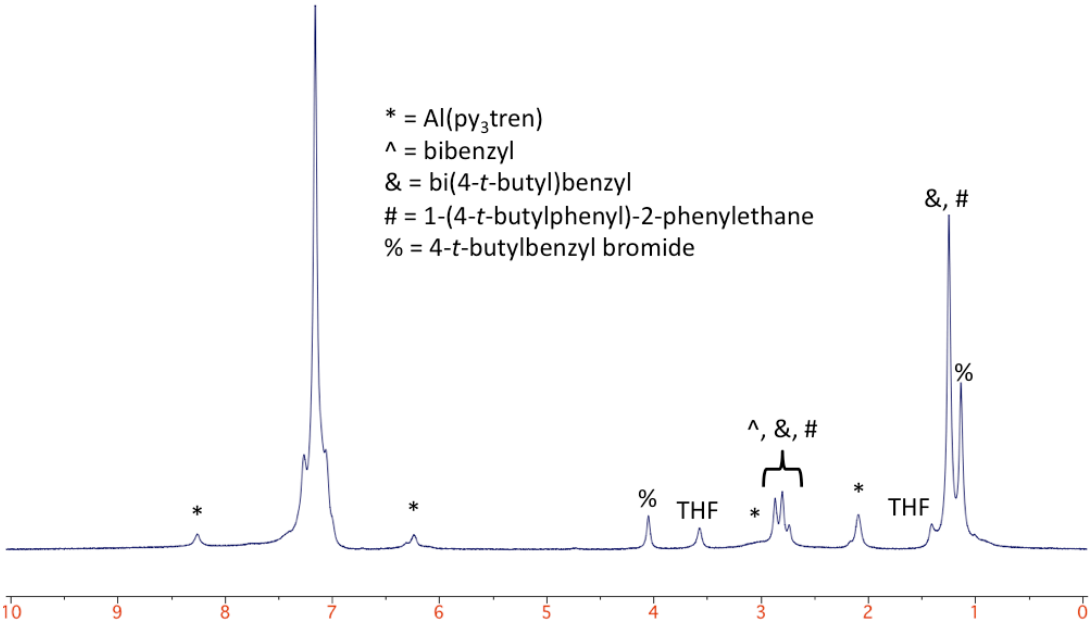

Figure A2.28. *In situ* diamagnetic region of the ^{1}H NMR spectrum of the reaction of 4-(*tert*-butyl)benzyl bromide with AlCo(Bn)(py$_3$tren) **4** in C_6D_6.

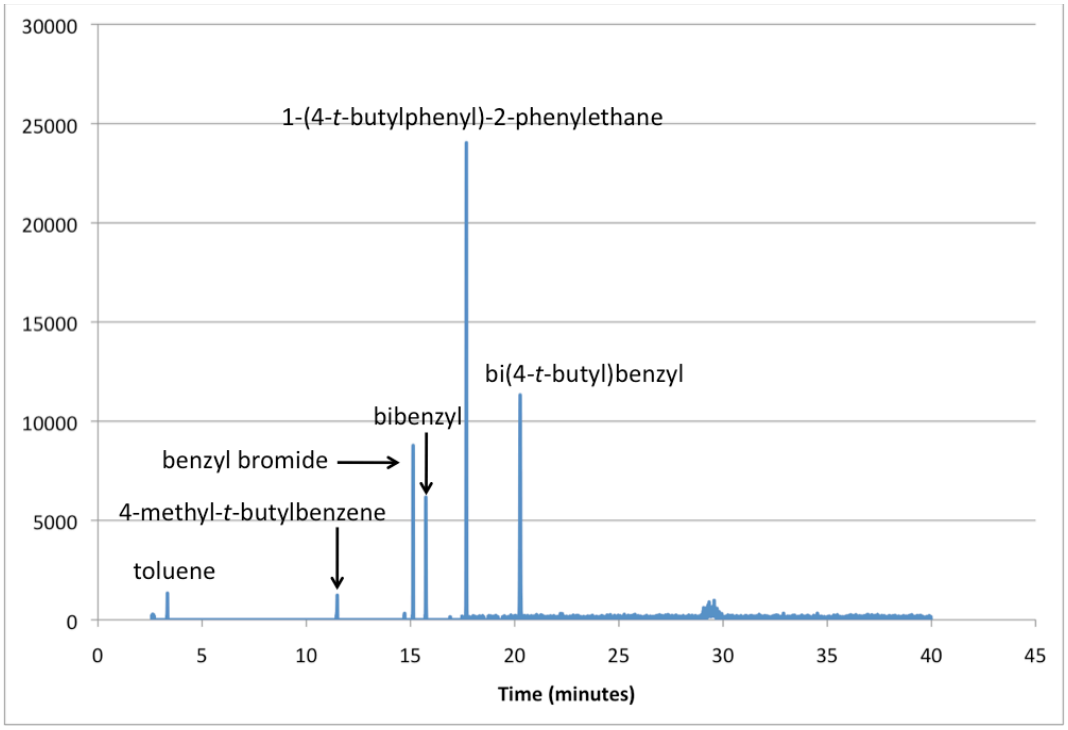

Figure A2.29. GC-MS data of the reaction of 4-(*tert*-butyl)benzyl bromide with AlCo(Bn)(py_3tren) **4** in C_6D_6.

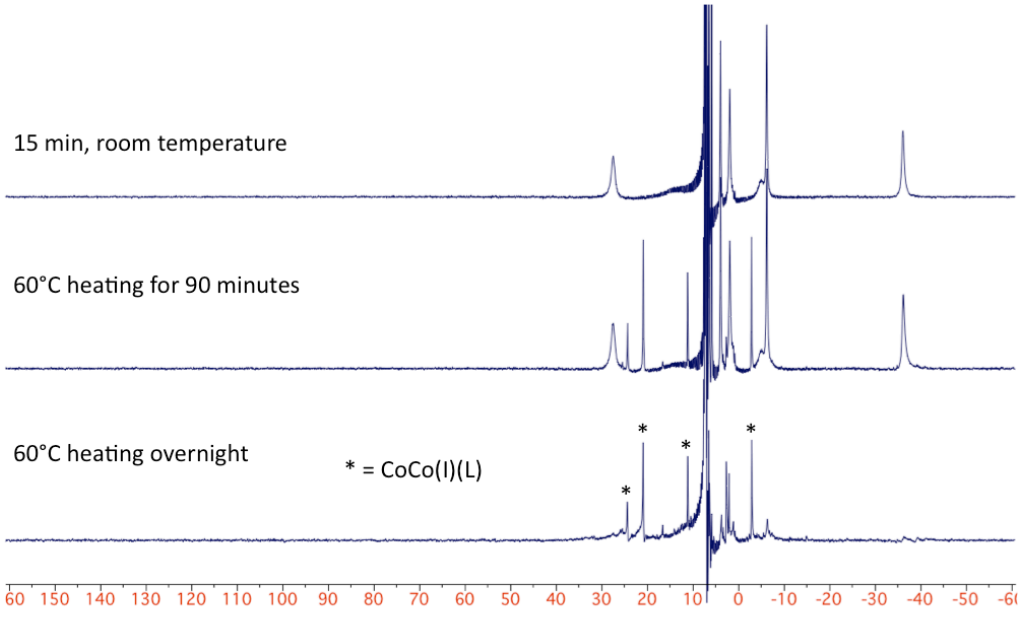

Figure A2.30. Time course of the *in situ* paramagnetically shifted ^{1}H NMR spectra of the reaction of iodobenzene with CoCo(Bn)(py_3tren) **2** in C_6D_6.

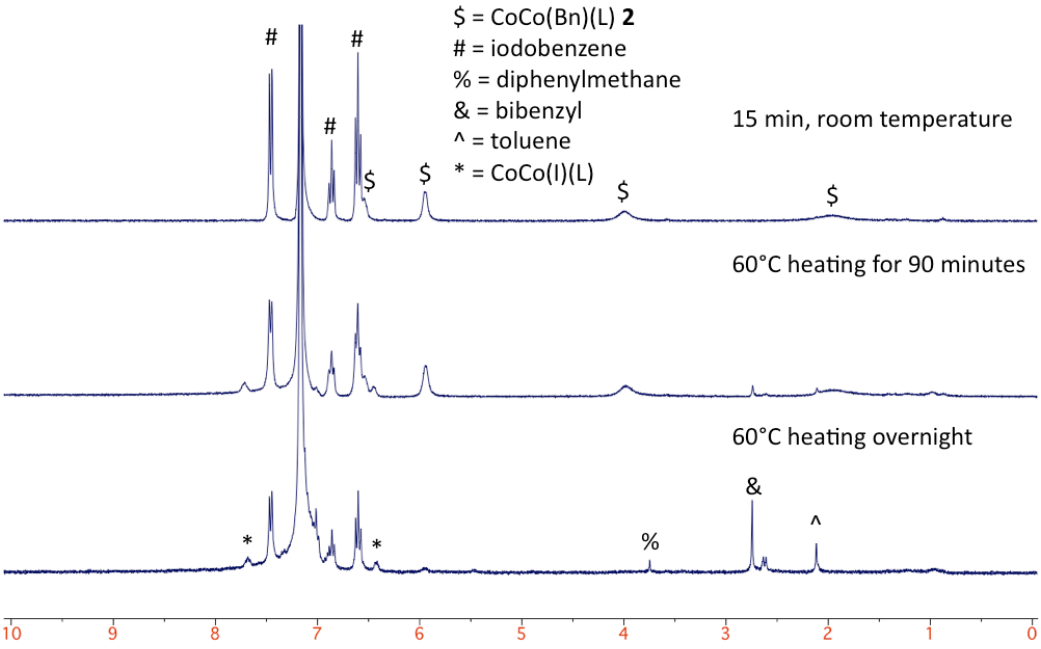

Figure A2.31. Time course of the *in situ* diamagnetic region of the ^{1}H NMR spectra of the reaction of iodobenzene with CoCo(Bn)(py$_3$tren) **2** in C_6D_6.

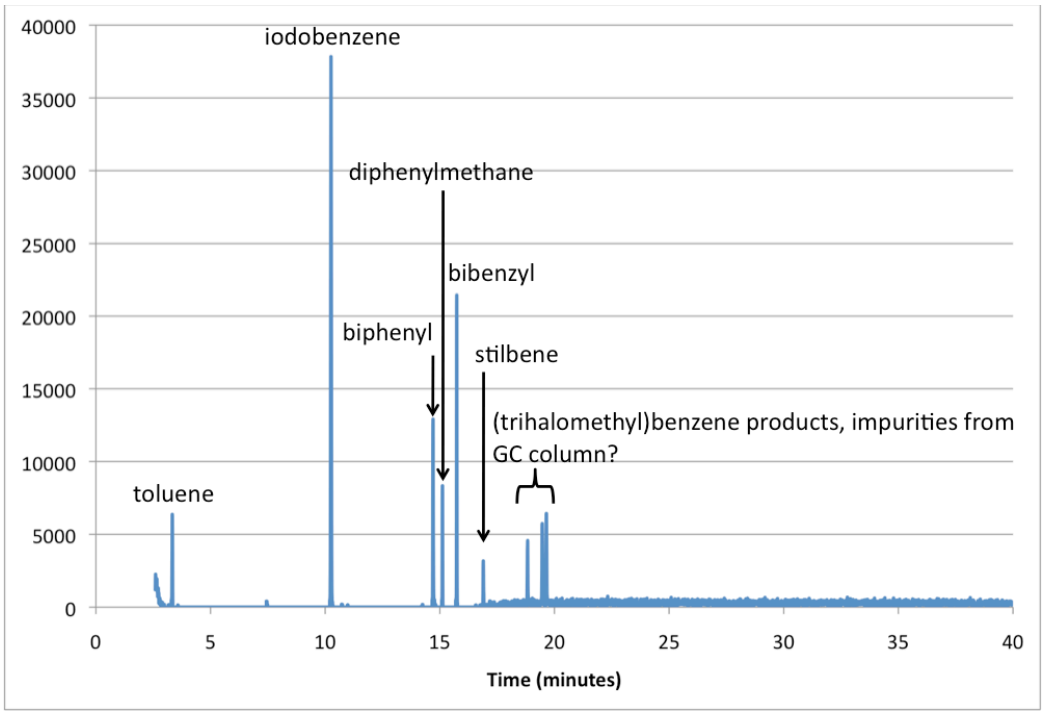

Figure A2.32. GC-MS data of the reaction of iodobenzene with CoCo(Bn)(py$_3$tren) **2** in C_6D_6.

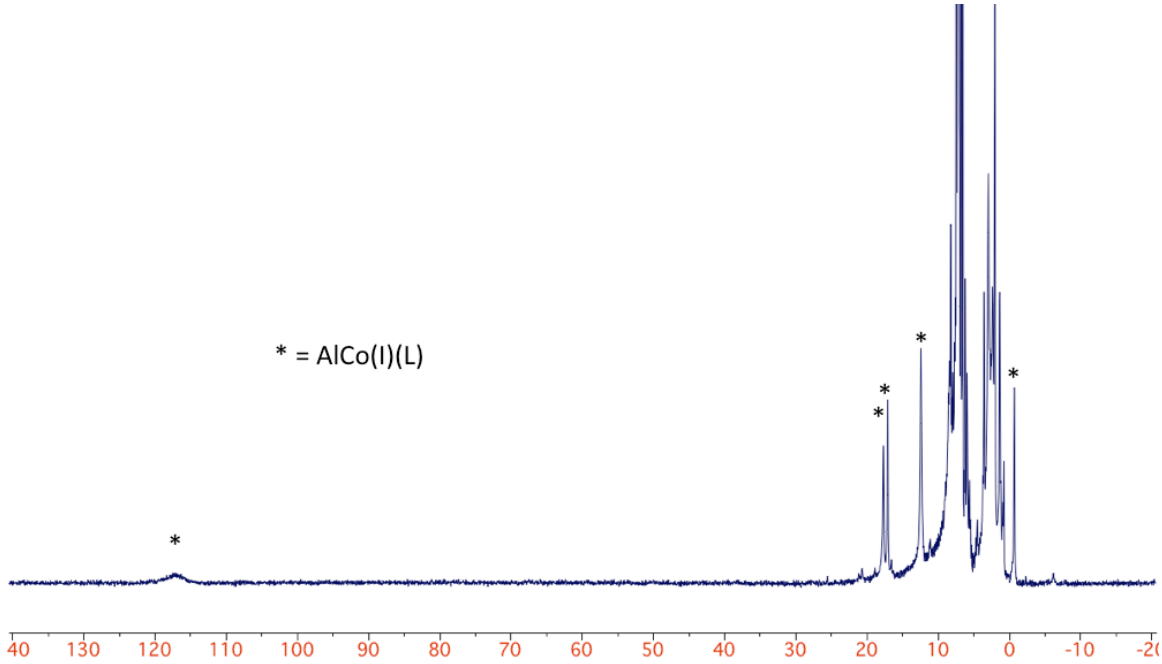

Figure A2.33. *In situ* paramagnetically shifted ^{1}H NMR spectrum of the reaction of iodobenzene with AlCo(Bn)(py$_3$tren) **4** in C_6D_6.

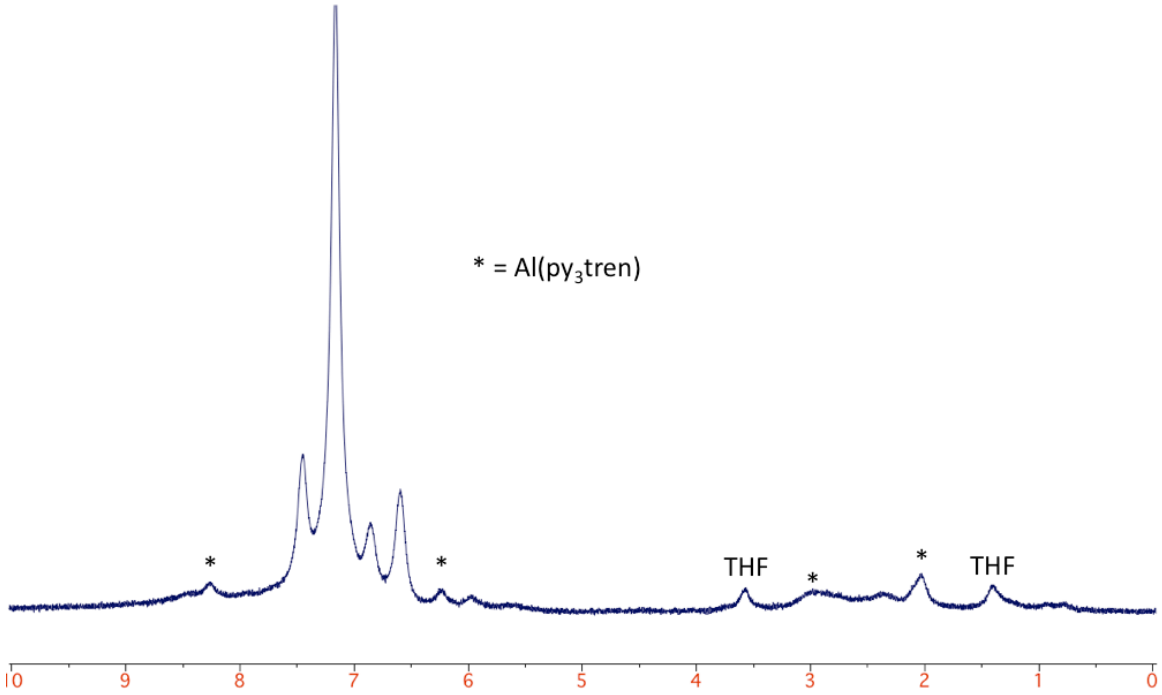

Figure A2.34. *In situ* diamagnetic region of the ^{1}H NMR spectrum of the reaction of iodobenzene with AlCo(Bn)(py$_3$tren) **4** in C_6D_6.

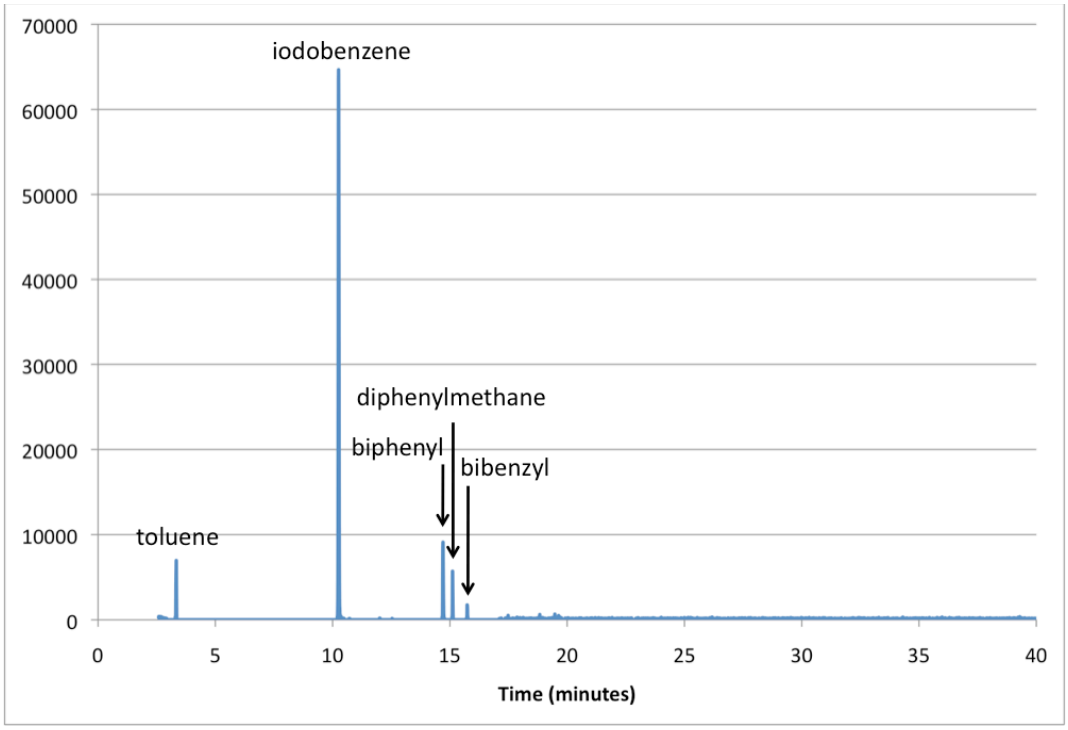

Figure A2.35. GC-MS data of the reaction of iodobenzene with AlCo(Bn)(py$_3$tren) **4** in C_6D_6.

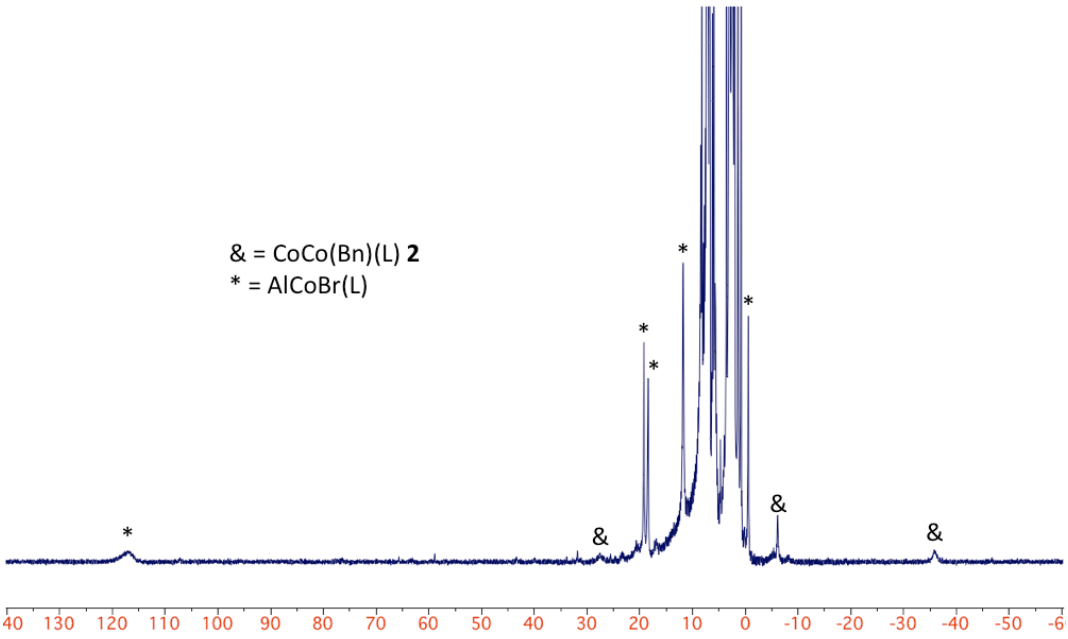

Figure A2.36. *In situ* paramagnetically shifted ^{1}H NMR spectrum of the reaction of bromobenzene with AlCo(Bn)(py$_3$tren) **4** in C_6D_6.

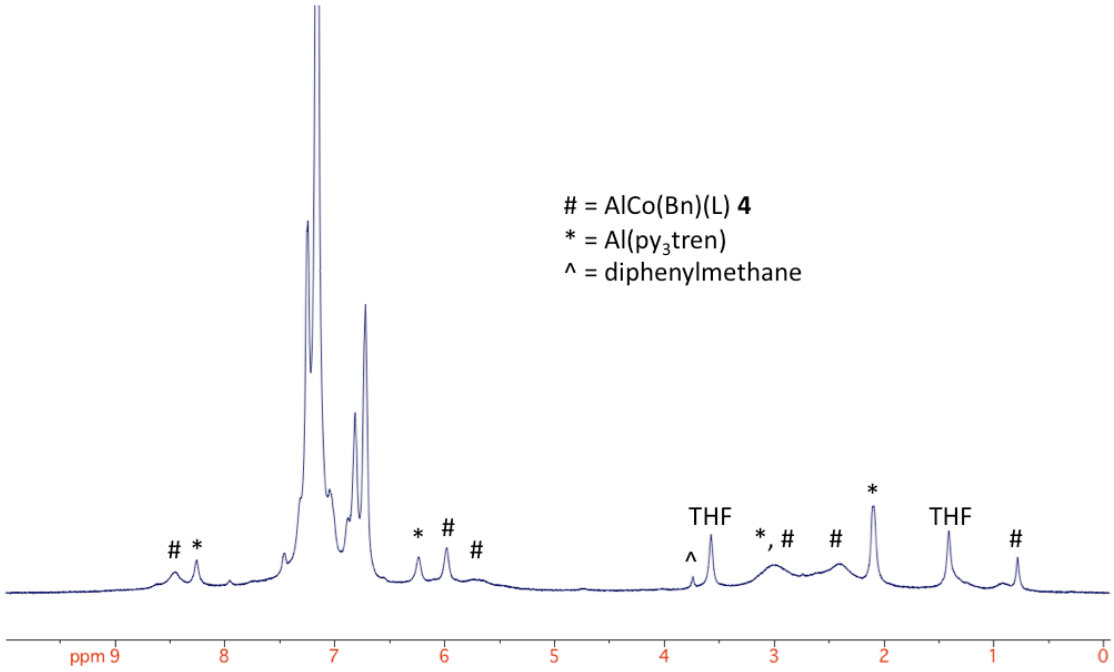

Figure A2.37. *In situ* diamagnetic region of the ^{1}H NMR spectrum of the reaction of bromobenzene with AlCo(Bn)(py$_3$tren) **4** in C_6D_6.

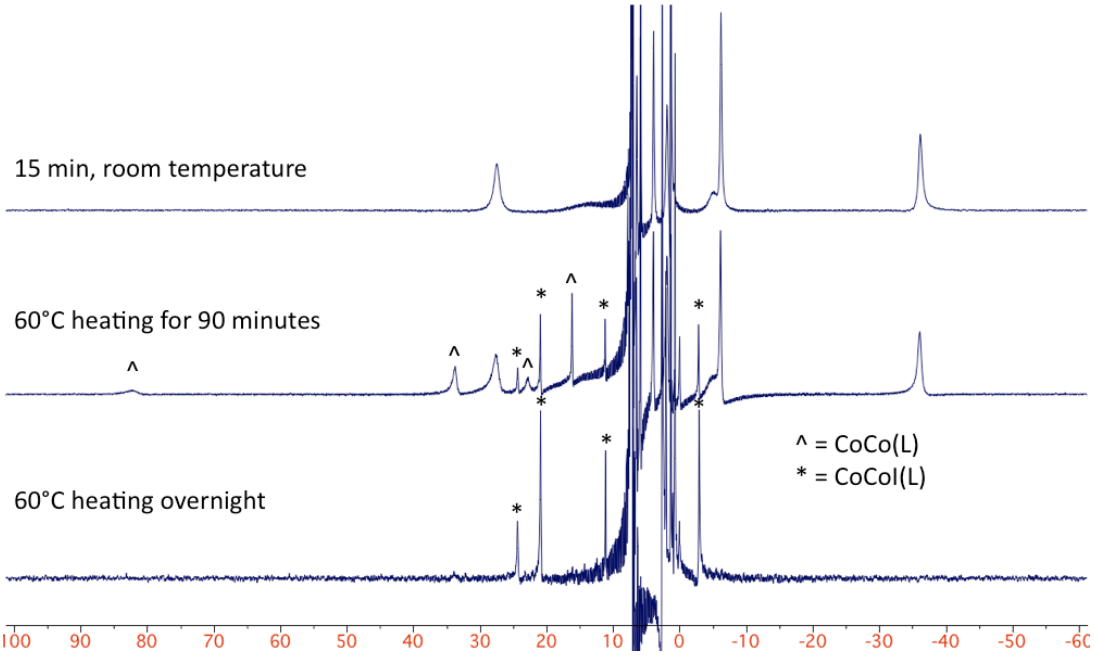

Figure A2.38. Time course of the *in situ* paramagnetically shifted ^{1}H NMR spectra of the reaction of iodomethane with CoCo(Bn)(py$_3$tren) **2** in C_6D_6.

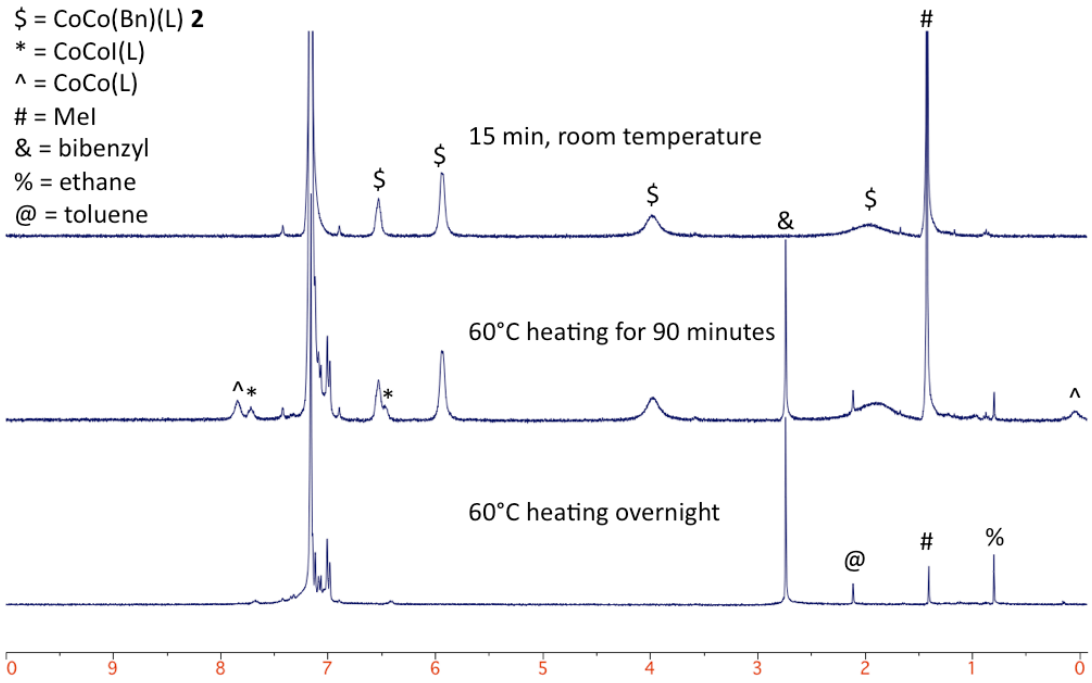

Figure A2.39. Time course of the *in situ* diamagnetic region of the ^{1}H NMR spectra of the reaction of iodomethane with CoCo(Bn)(L) **2** in C_6D_6.

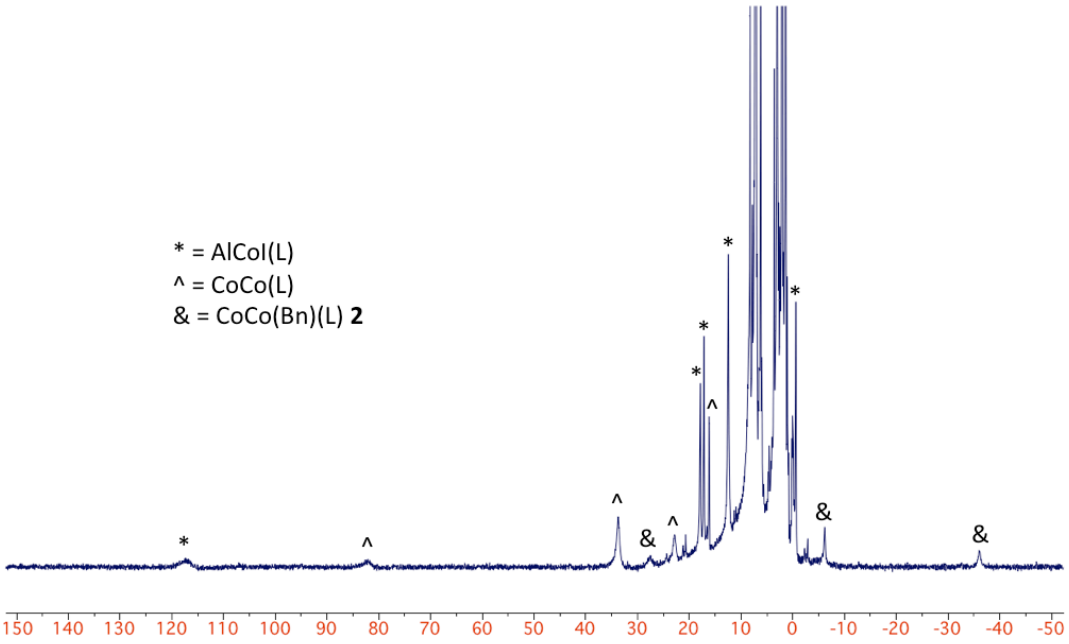

Figure A2.40. *In situ* paramagnetically shifted ^{1}H NMR spectrum of the reaction of iodomethane with AlCo(Bn)(L) **4** in C_6D_6.

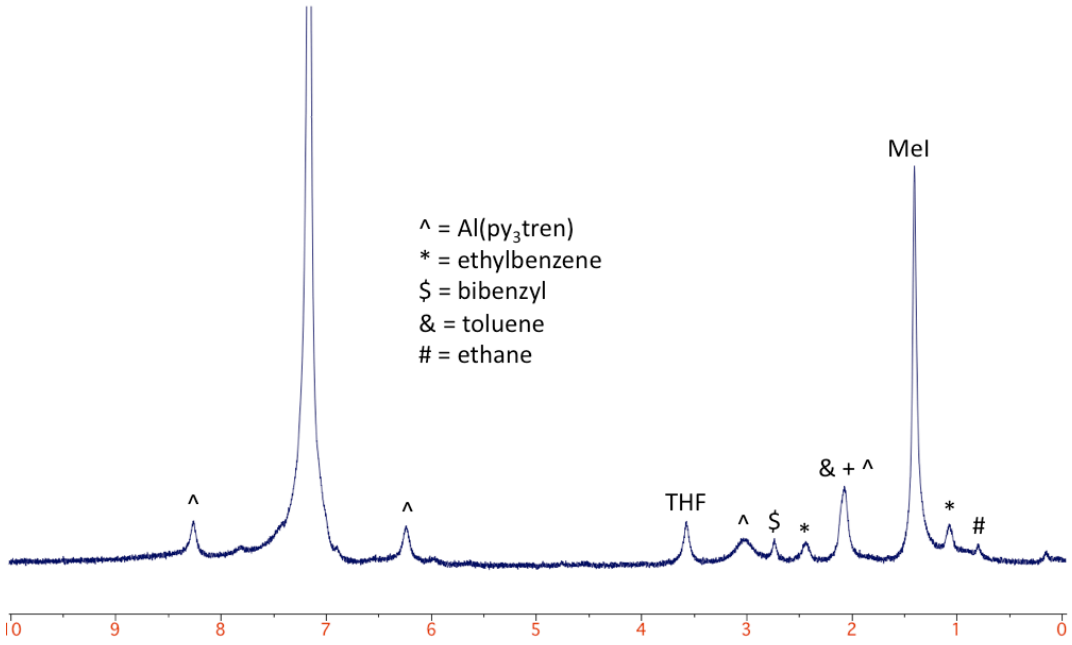

Figure A2.41. *In situ* diamagnetic region of the ^{1}H NMR spectrum of the reaction of iodomethane with AlCo(Bn)(L) **4** in C_6D_6.

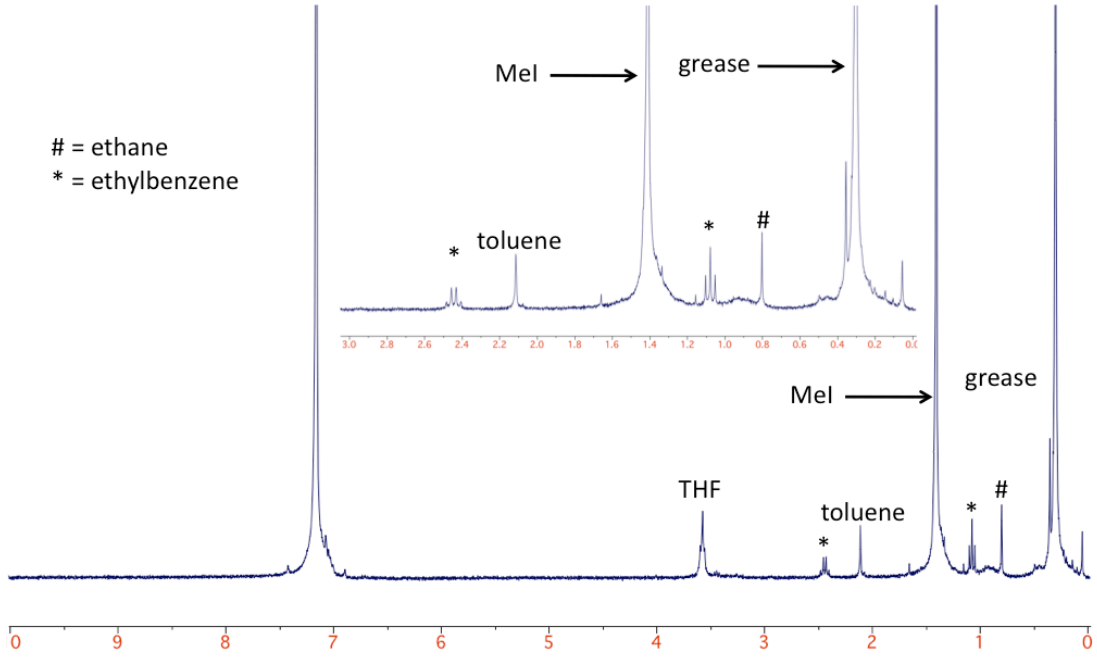

Figure A2.42. Diamagnetic region of the ^{1}H NMR spectrum of the volatiles from the reaction of iodomethane with AlCo(Bn)(L) **4** in C_6D_6.

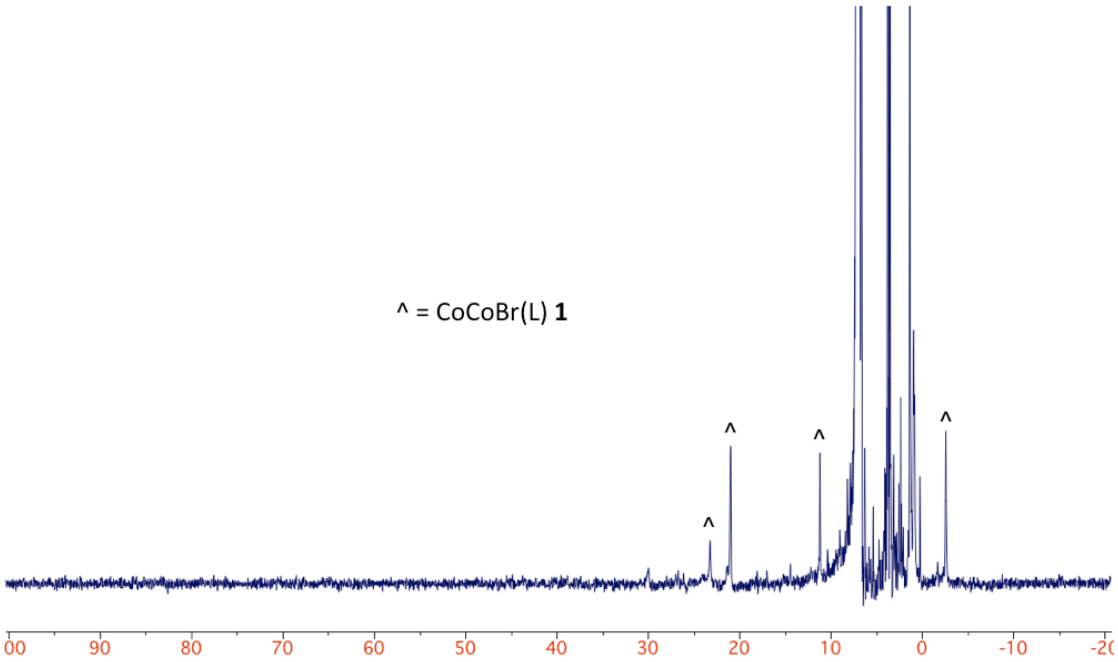

Figure A2.43. Paramagnetically shifted ^{1}H NMR spectrum of the reaction of Ph_3CBr with CoCo(Bn)(py_3tren) **2** in C_6D_6.

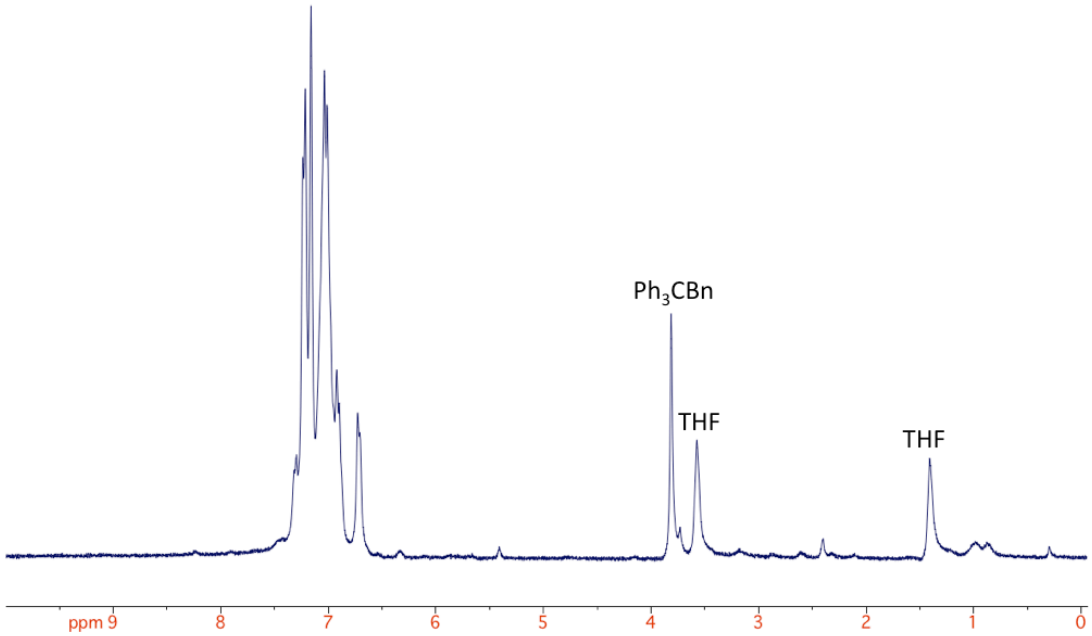

Figure A2.44. Diamagnetic region of the ^{1}H NMR spectrum of the reaction of Ph_3CBr with CoCo(Bn)(py_3tren) **2** in C_6D_6.

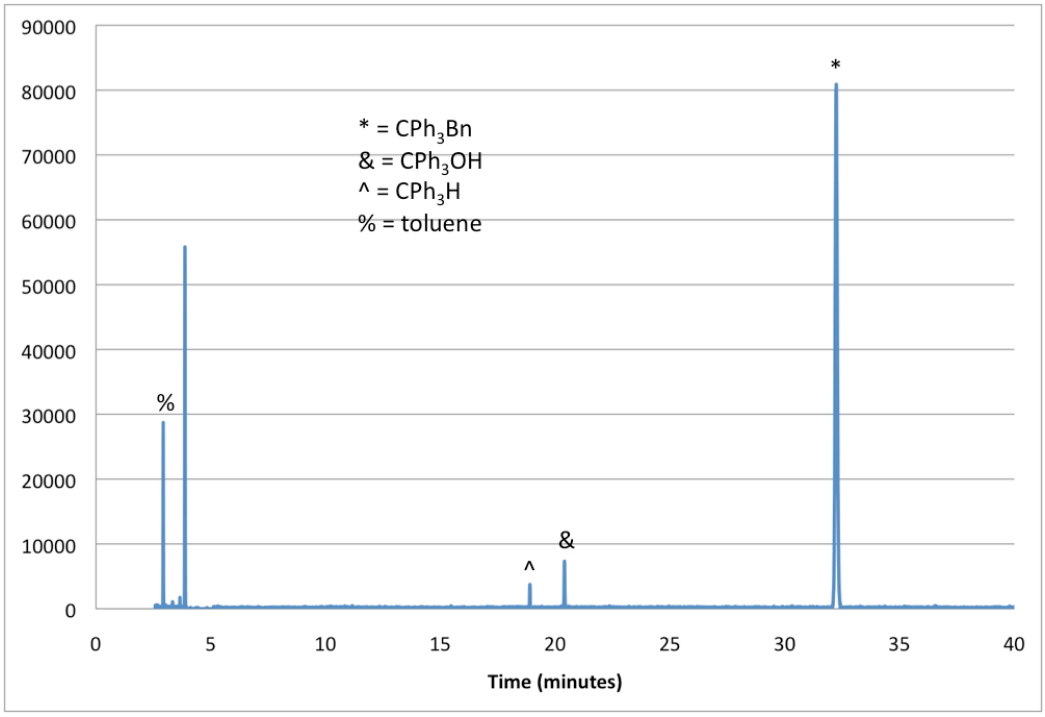

Figure A2.45. GC-MS data of the reaction of trityl bromide with CoCo(Bn)(L) **2** in THF.

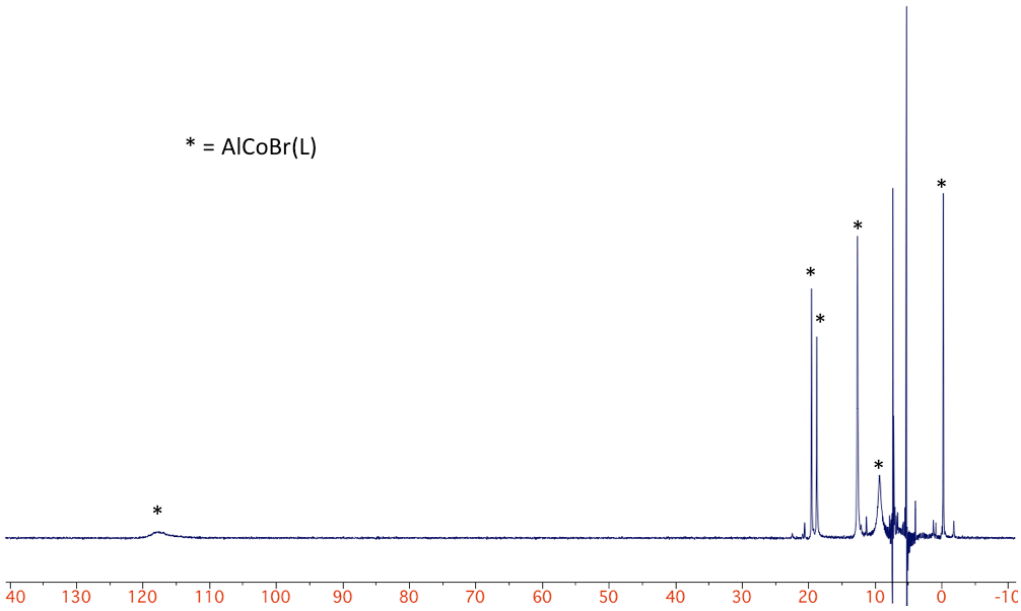

Figure A2.46. Paramagnetically shifted ^{1}H NMR spectrum of the reaction of Ph_3CBr with AlCo(Bn)(L) **4** in CD_2Cl_2.

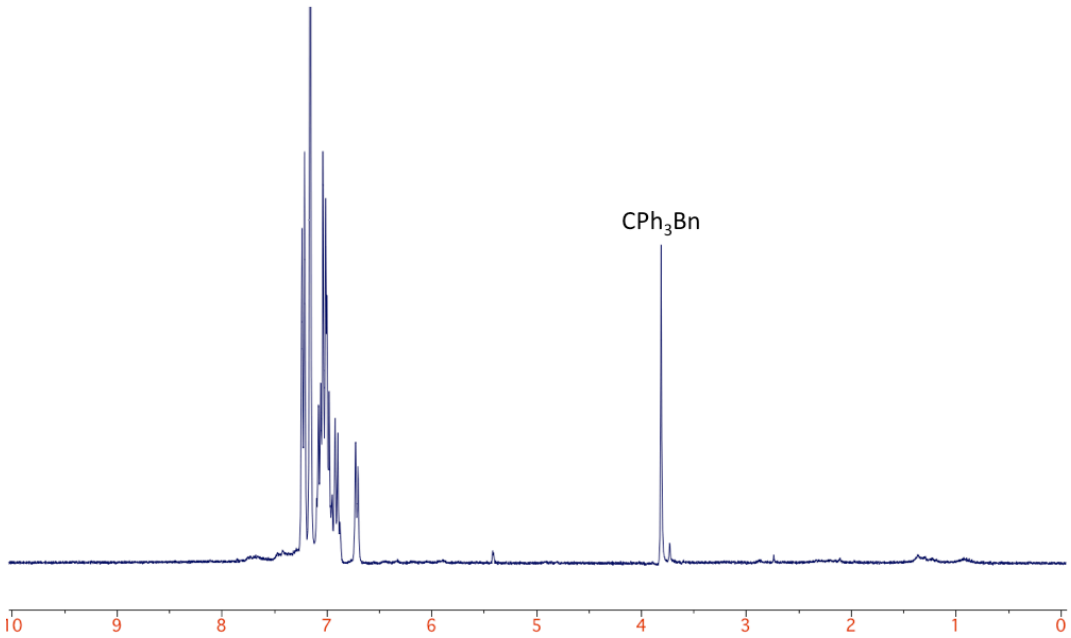

Figure A2.47. Diamagnetic region of the ^{1}H NMR spectrum of the reaction of Ph_3CBr with AlCo(Bn)(L) **4** in C_6D_6.

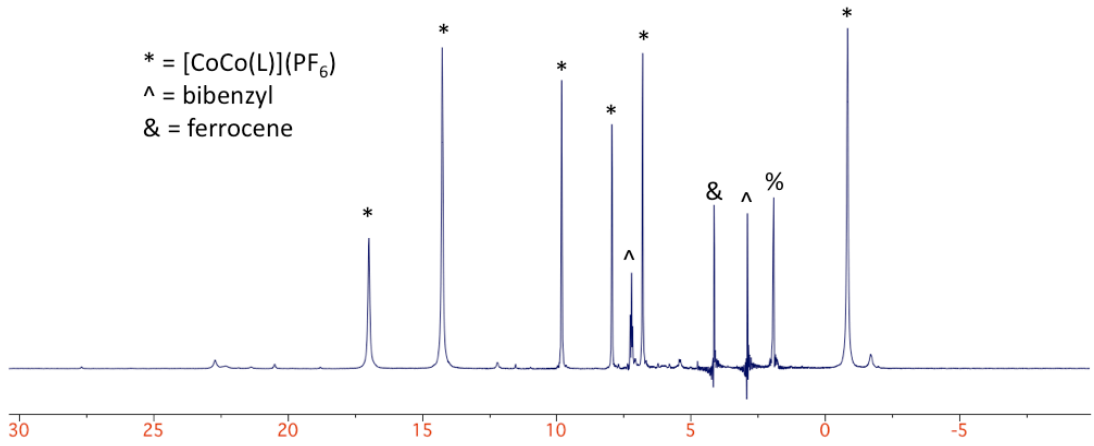

Figure A2.48. Paramagnetically shifted ^{1}H NMR spectrum of the reaction of $FcPF_6$ with CoCo(Bn)(L) **2** in CD_3CN. % denotes acetonitrile.

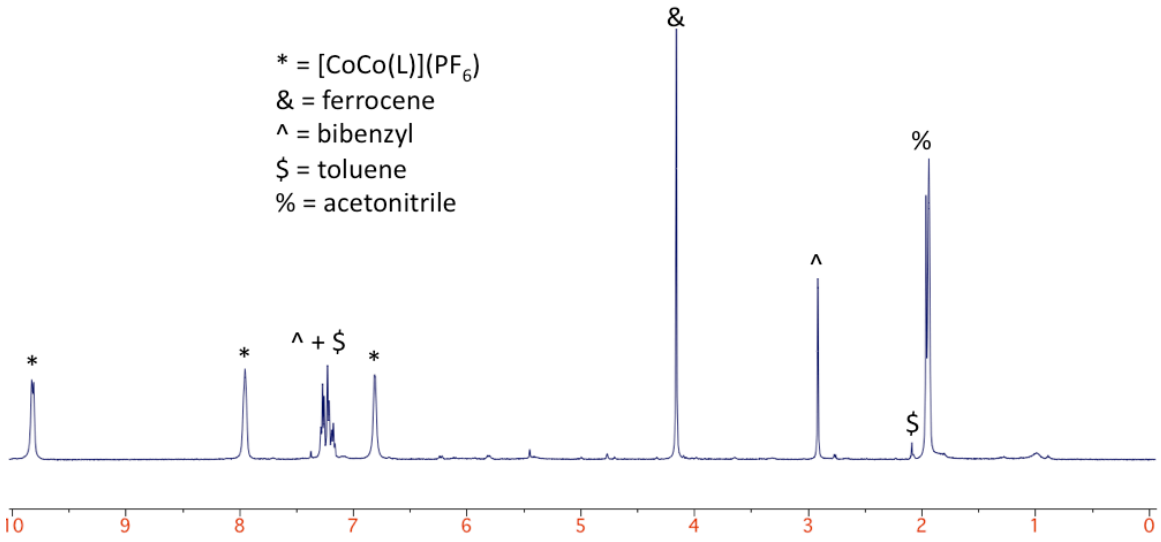

Figure A2.49. Diamagnetic region of the ^{1}H NMR spectrum of the reaction of $FcPF_6$ with CoCo(Bn)(L) **2** in CD_3CN.

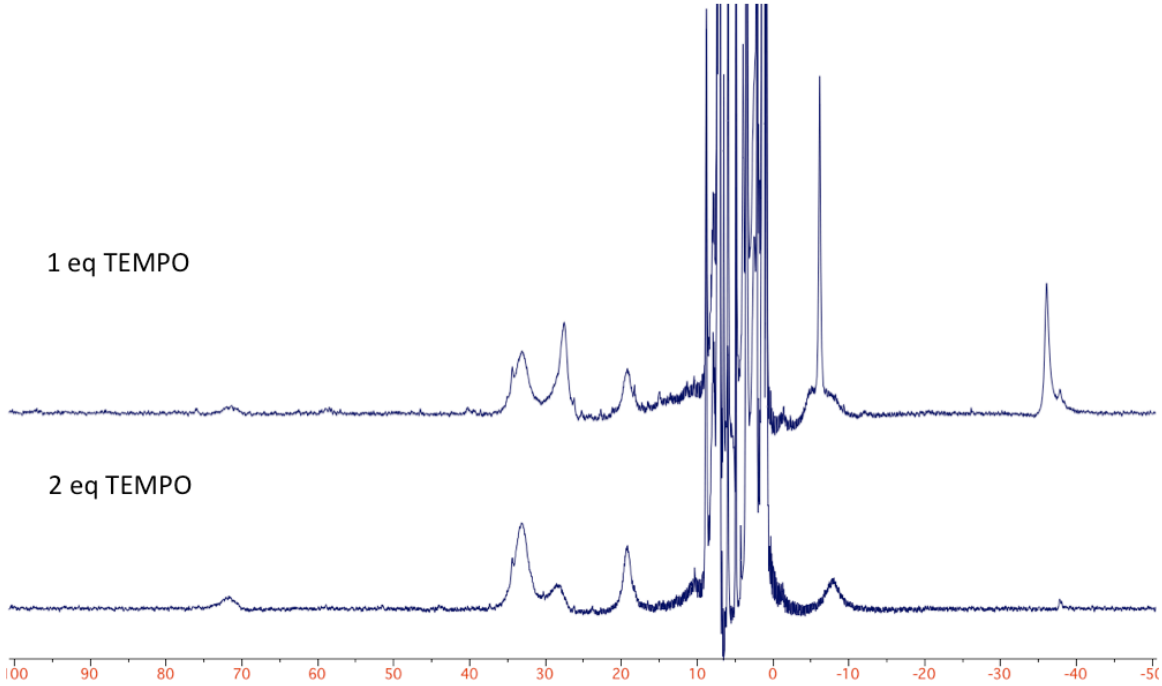

Figure A2.50. Paramagnetically shifted ^{1}H NMR spectra of the reactions of (top) 1 eq and (bottom) 2 eq TEMPO with CoCo(Bn)(py_3tren) **2** in C_6D_6.

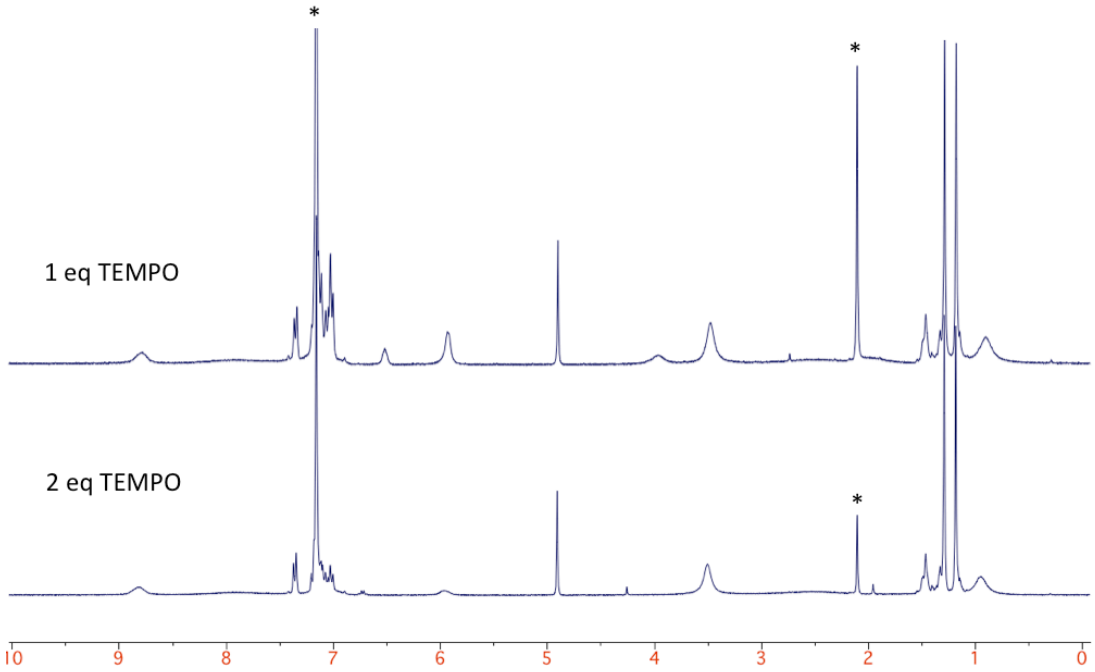

Figure A2.51. Diamagnetic region of the ^{1}H NMR spectra of the reactions of (top) 1 eq and (bottom) 2 eq TEMPO with CoCo(Bn)(py_3tren) **2** in C_6D_6. Solvents marked with asterisks.

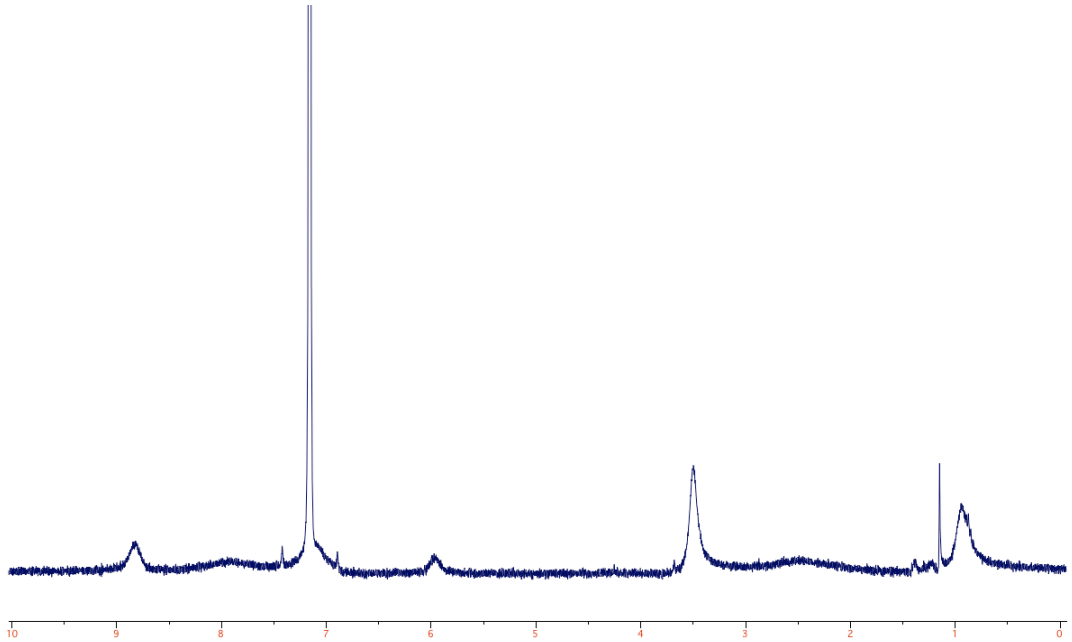

Figure A2.52. Diamagnetic region of the ^{1}H NMR spectrum of crystallized CoCo(TEMPO)(py_3tren) **9** in C_6D_6.

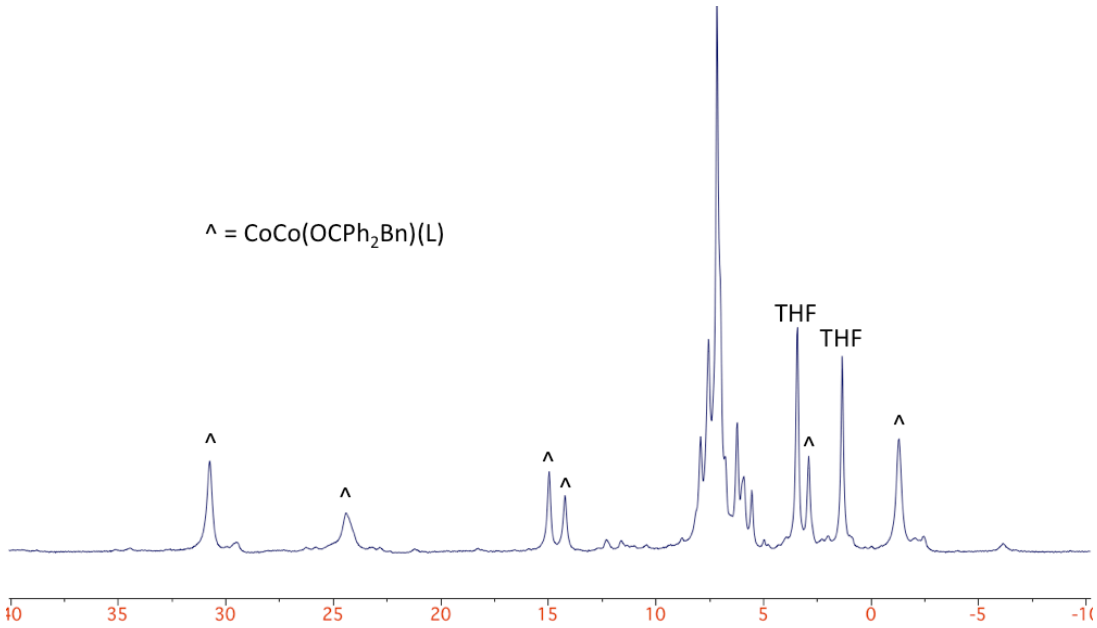

Figure A2.53. Paramagnetically shifted ^{1}H NMR spectrum of CoCo(OCPh$_2$Bn)(L) **10** from the addition of benzophenone to **2** with heating overnight in THF; NMR taken in C_6D_6.

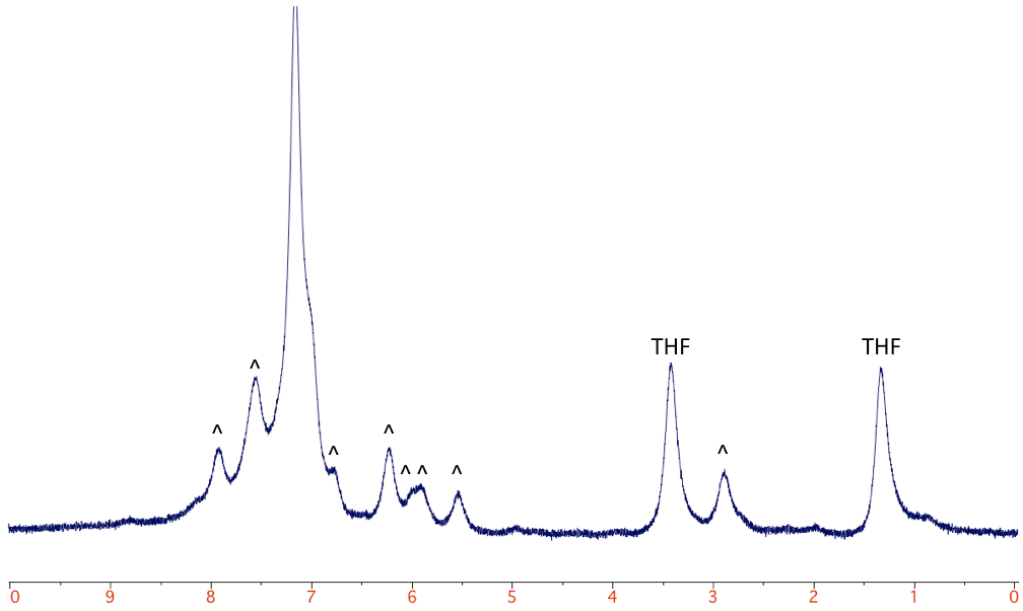

Figure A2.54. Diamagnetic region of the ^{1}H NMR spectrum of CoCo(OCPh$_2$Bn)(L) **10** from the addition of benzophenone to **2** with heating overnight in THF; NMR taken in C_6D_6. Solvents denoted with asterisks.

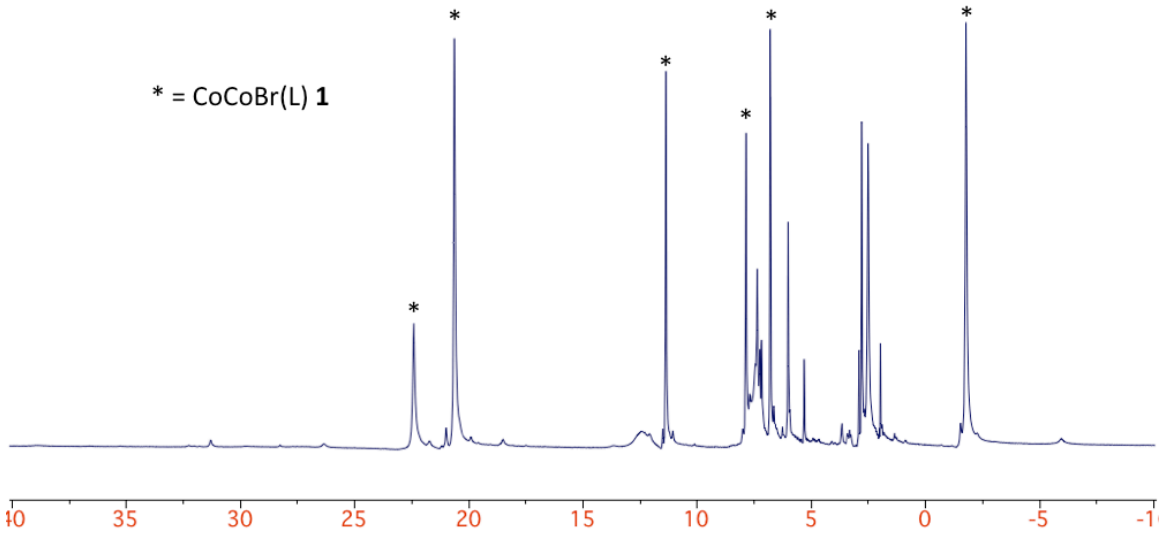

Figure A2.55. Paramagnetically shifted ^{1}H NMR spectrum of the reaction of NBS with **2** in CD_2Cl_2.

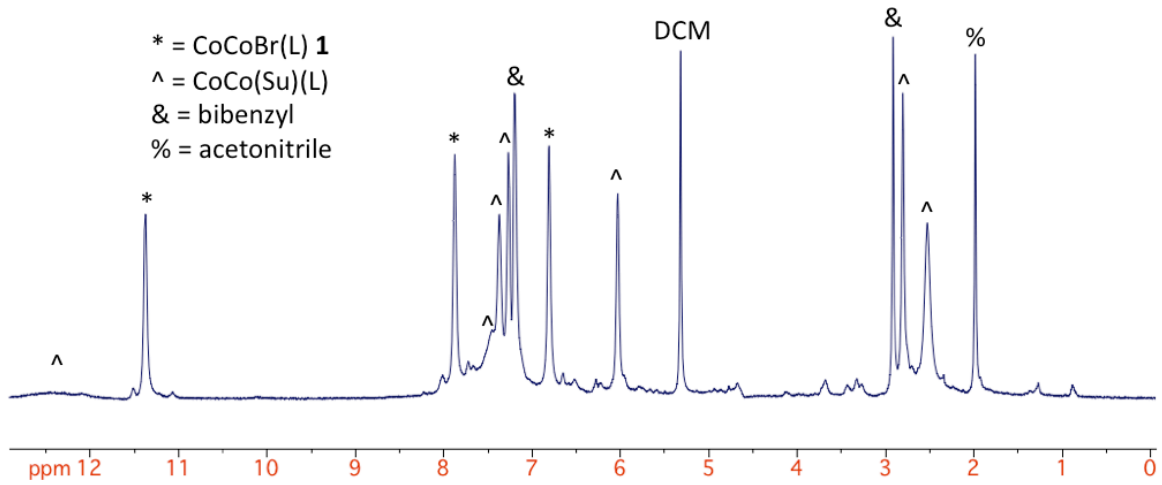

Figure A2.56. Diamagnetic region of the ^{1}H NMR spectrum of the reaction of NBS with **2** in CD_2Cl_2.

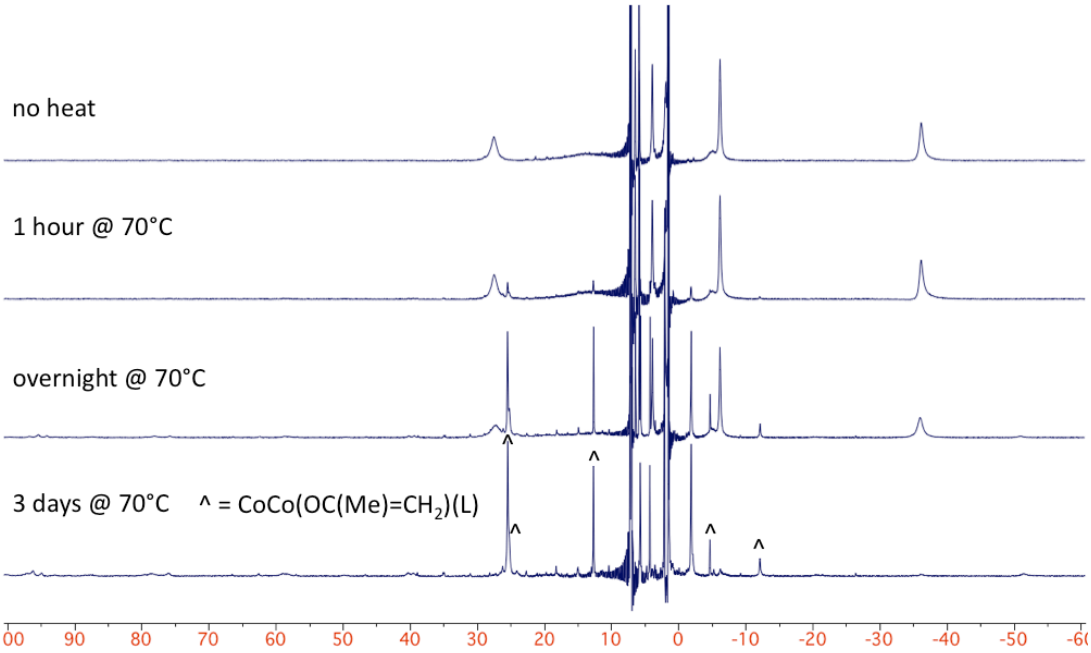

Figure A2.57. Paramagnetically shifted ^{1}H NMR spectra of the reaction of acetone with CoCo(Bn)(L) **2** in C_6D_6.

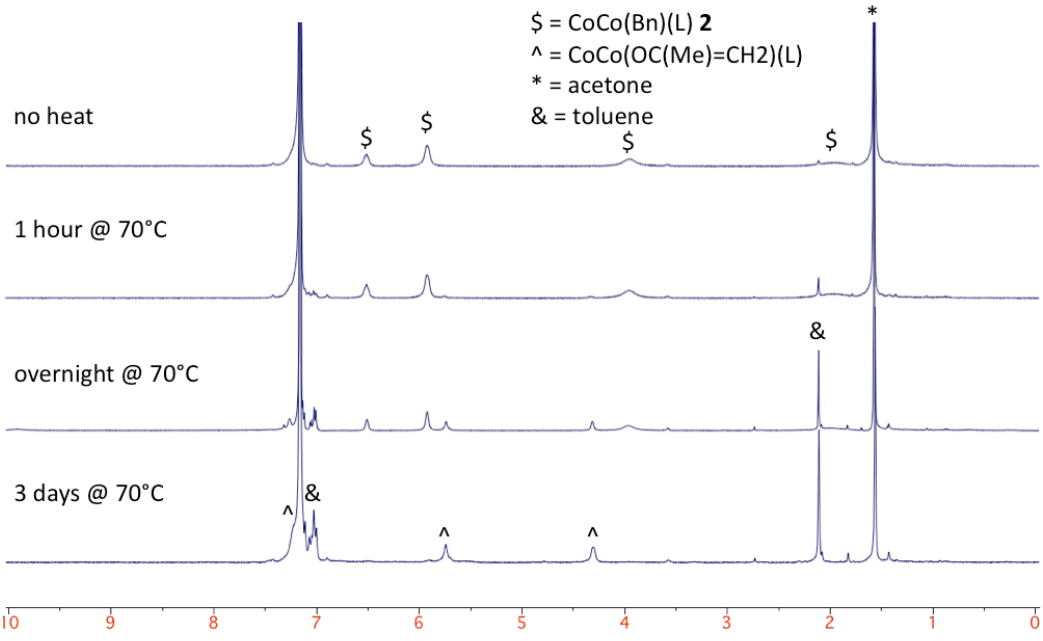

Figure A2.58. Diamagnetic region of the ^{1}H NMR spectra of the reaction of acetone with **2** in C_6D_6.

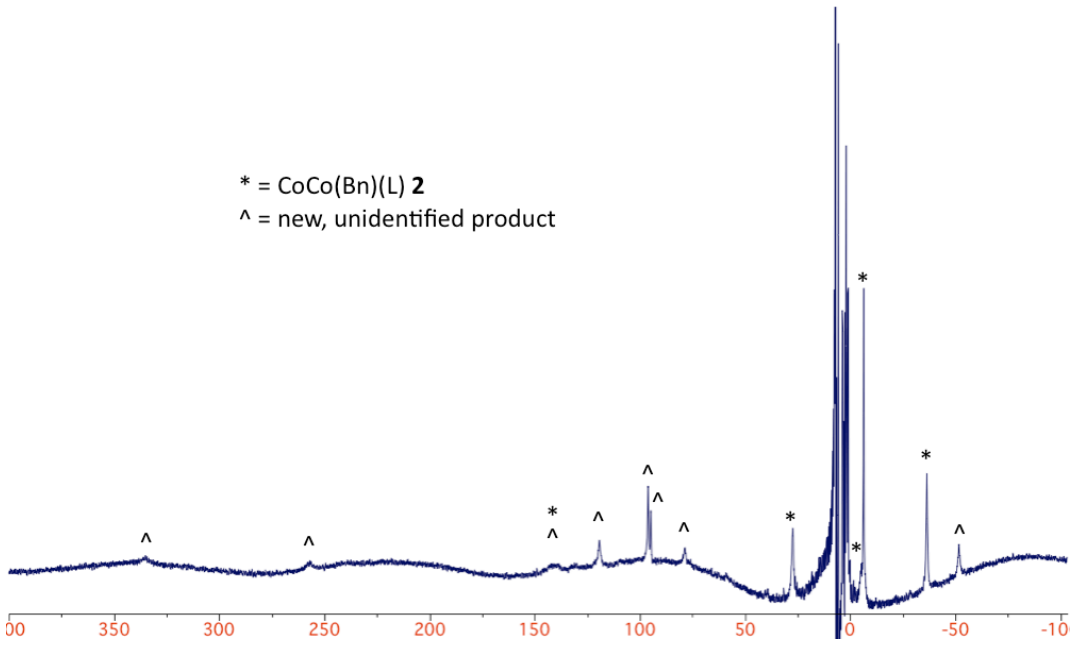

Figure A2.59. Paramagnetically shifted ^{1}H NMR spectrum from heating CoCo(Bn)(L) **2** for several days at 80°C in C_6D_6.

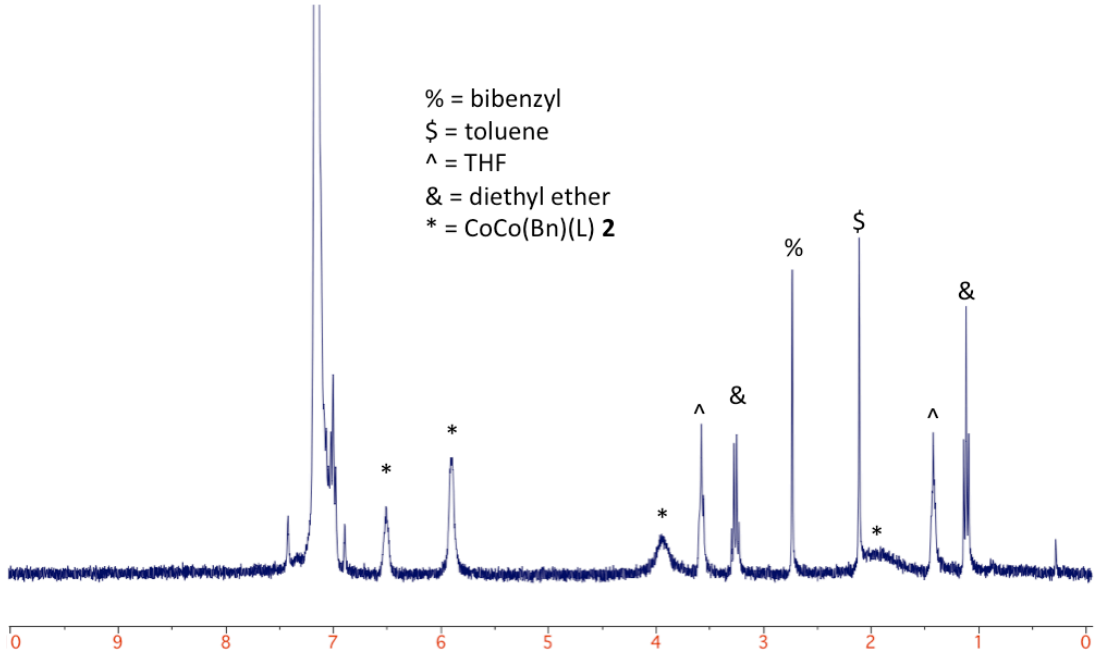

Figure A2.60. Diamagnetic region of the ^{1}H NMR spectrum from heating CoCo(Bn)(L) **2** for several days at 80°C in C_6D_6.

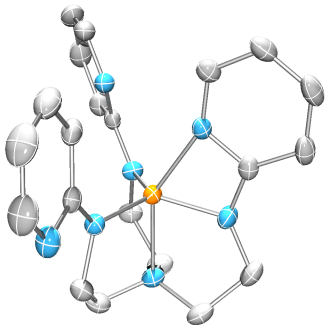

Figure A2.61. Solid-state structure of Al(py_3tren). Thermal ellipsoids are shown at 50% probability.

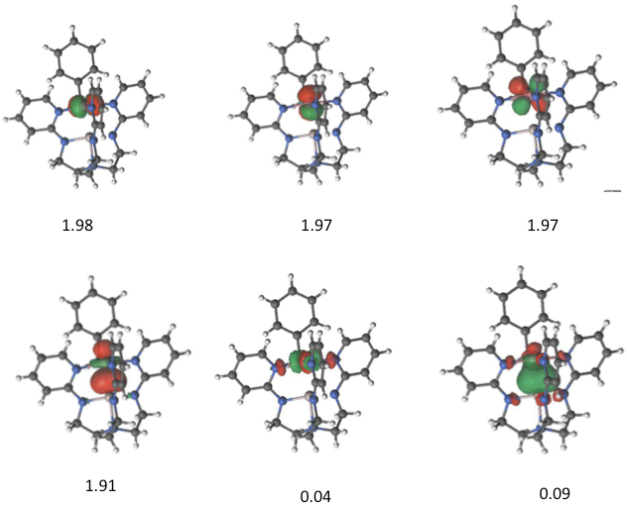

Figure A2.62. CASSCF orbitals of AlCo(Bn) **4** with an active space of (8,10) for the singlet state.

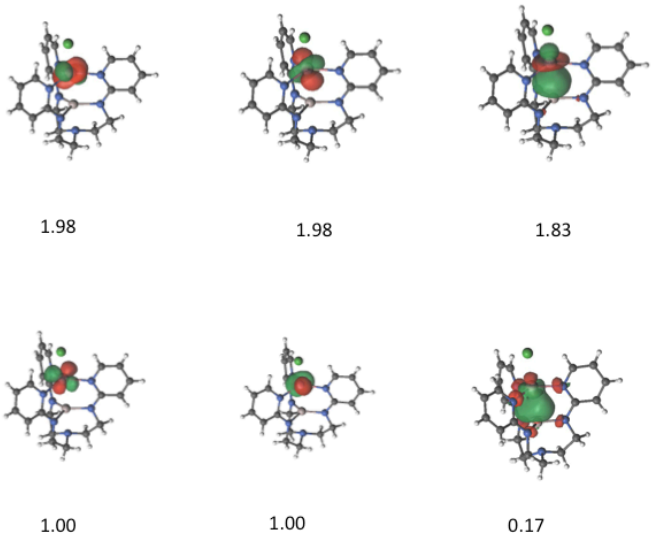

Figure A2.63. CASSCF orbitals of AlCoCl **3** with an active space of (8,10) for the triplet state.

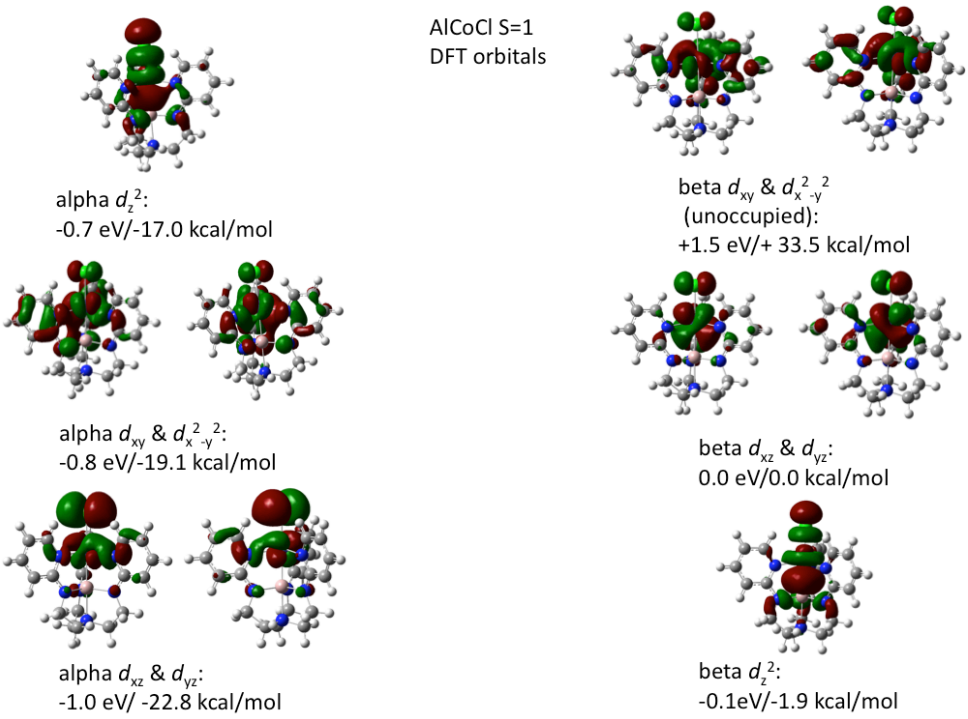

Figure A2.64. DFT orbitals of AlCoCl **3**.

Table A2.1. DFT orbital energies for the $S = 1$ state of AlCoCl(L) **3**.

Orbital	Relative Energy (eV)	Relative Energy (kcal/mol)
virtual beta d_{x2-y2}	+1.455	+33.559
virtual beta d_{xy}	+1.455	+33.547
beta d_{xz}/d_{yz}	0	0
beta d_{z2}	-0.082	-1.899
alpha d_{z2}	-0.737	-16.993
alpha d_{xy}	-0.827	-19.064
alpha d_{x2-y2}	-0.827	-19.070
alpha d_{xz}	-0.988	-22.791
alpha d_{yz}	-0.989	-22.810

Table A2.2. Relative energies[a] of the $S = 0$ and $S = 1$ states of AlCoCl(L) **3**.

	CASSCF	CASPT2	PBE single point[b]
$S = 0$	39.6	40.0	13.6
$S = 1$	0.0	0.0	0.0

[a] All energies in kcal/mol. [b] Computed using the crystal structure geometry.

Appendix 3: Supporting Information Figures for Chapter 4

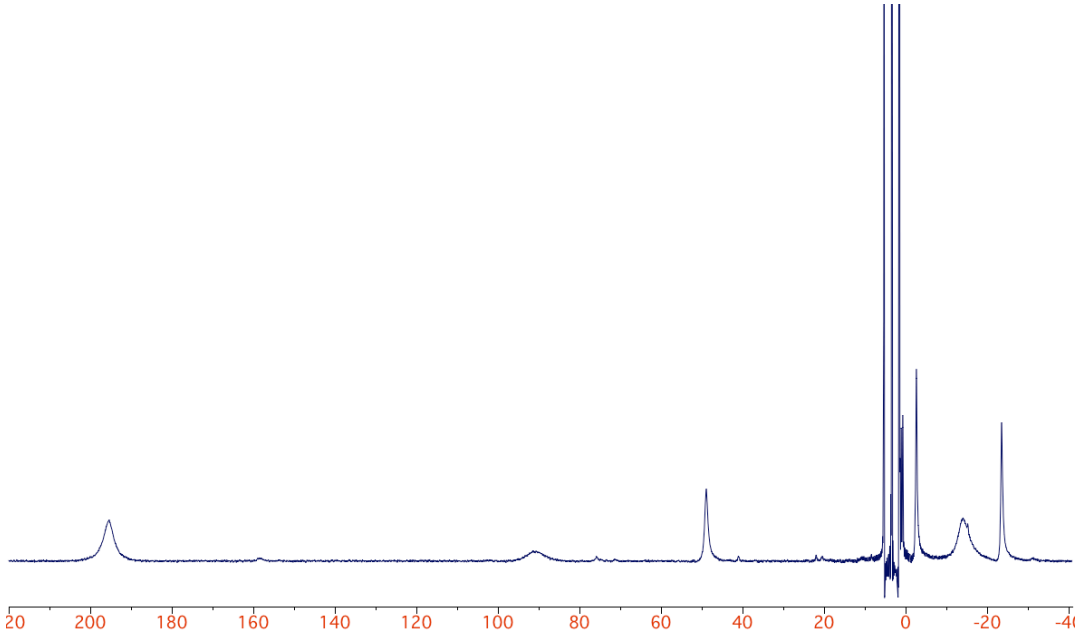

Figure A3.1. Paramagnetically shifted ^{1}H NMR spectrum of FeFe(OTf)(py$_3$tren) **1** in d_8-THF.

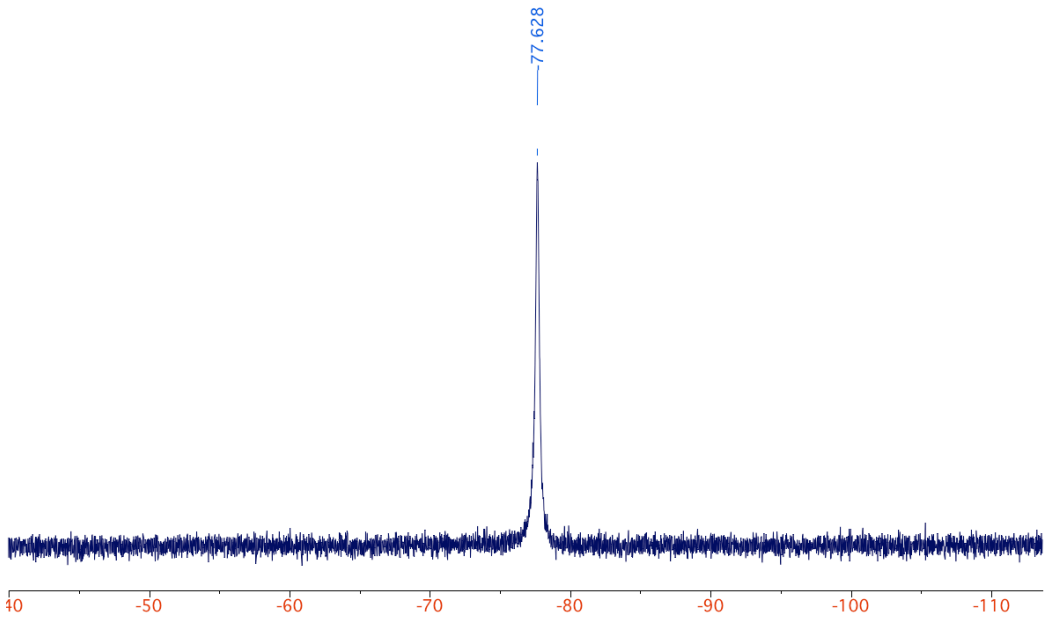

Figure A3.2. ^{19}F NMR spectrum of FeFe(OTf)(py$_3$tren) **1** in CD_3CN.

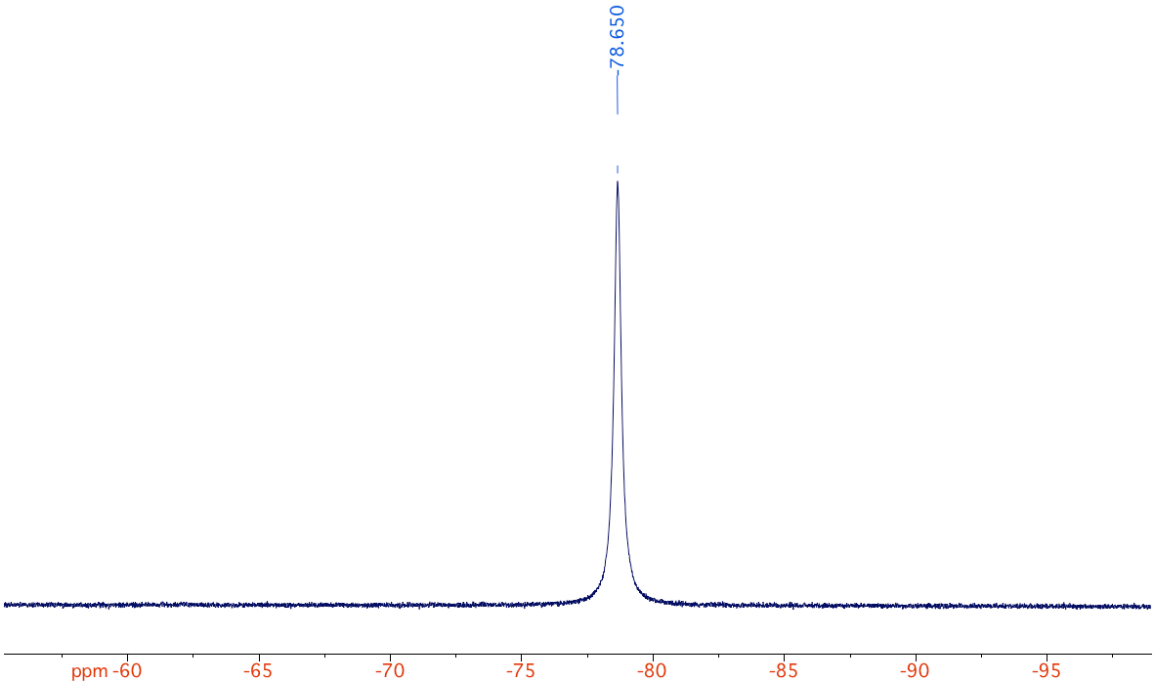

Figure A3.3. ^{19}F NMR spectrum of $[(FeFe(\mu_3\text{-}O)(py_3tren))_3][OTf]_2$ **2** in CD_3CN.

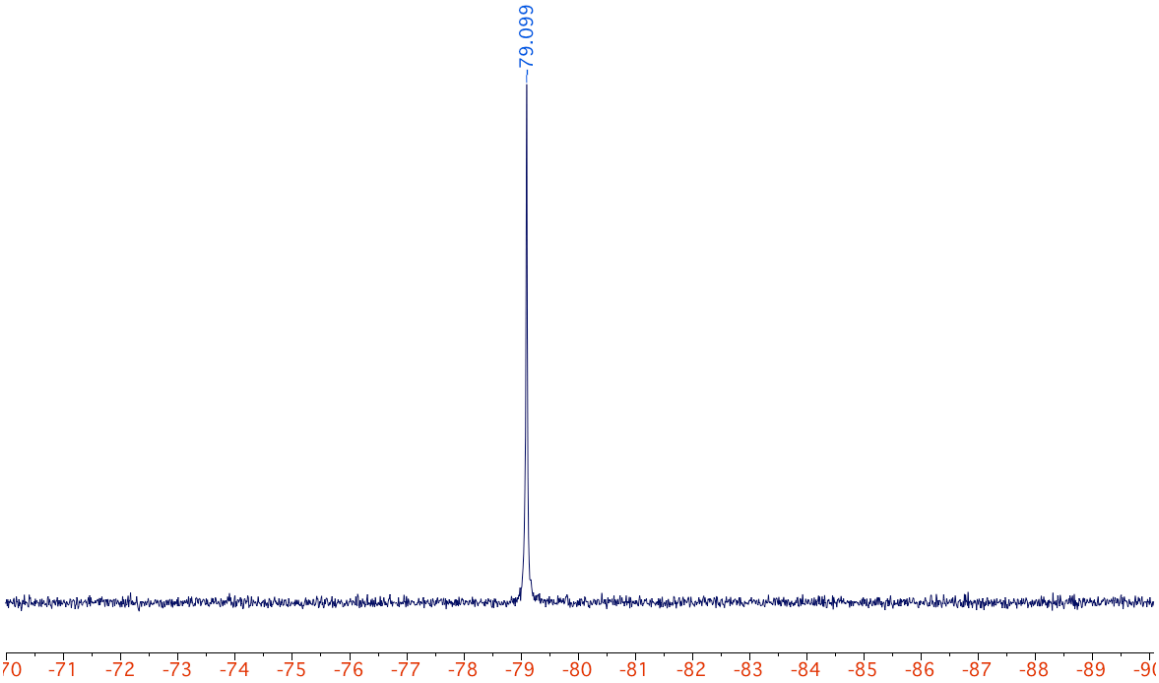

Figure A3.4. ^{19}F NMR spectrum of $[(FeFe(\mu_3\text{-}O)(py_3tren))_3][OTf]$ **4** in CD_2Cl_2.

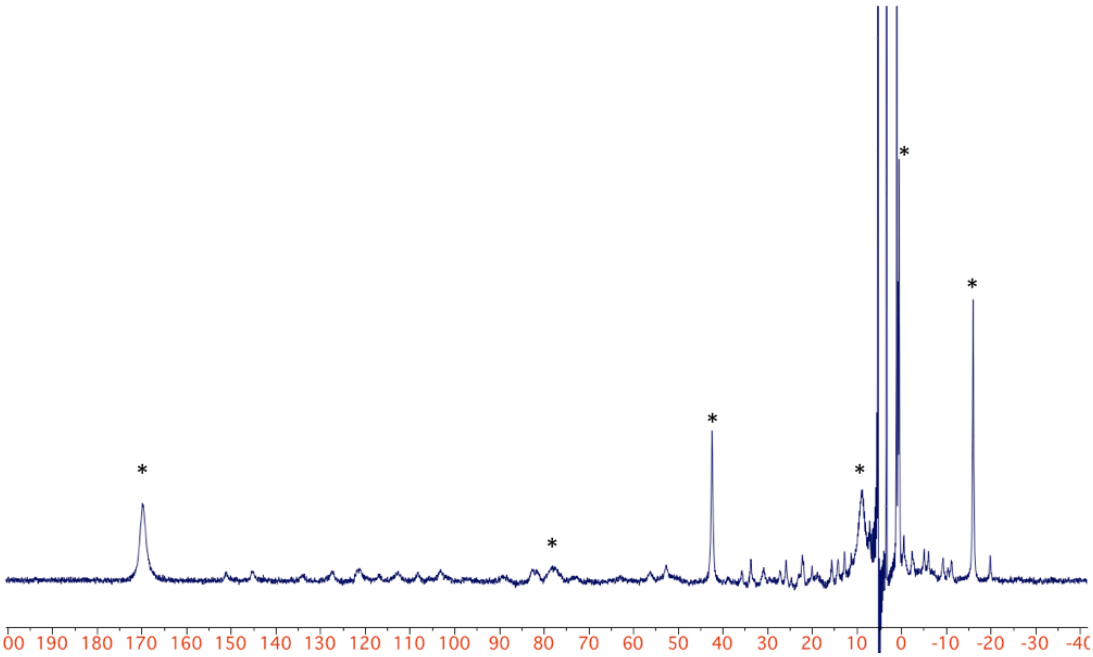

Figure A3.5. Paramagnetically shifted ^{1}H NMR spectrum of a mixture of [(FeFe(py$_3$tren))$_2$(μ_4-O)] **7** and FeFeCl(py$_3$tren) in CD_2Cl_2. Asterisks denote FeFeCl(py$_3$tren).

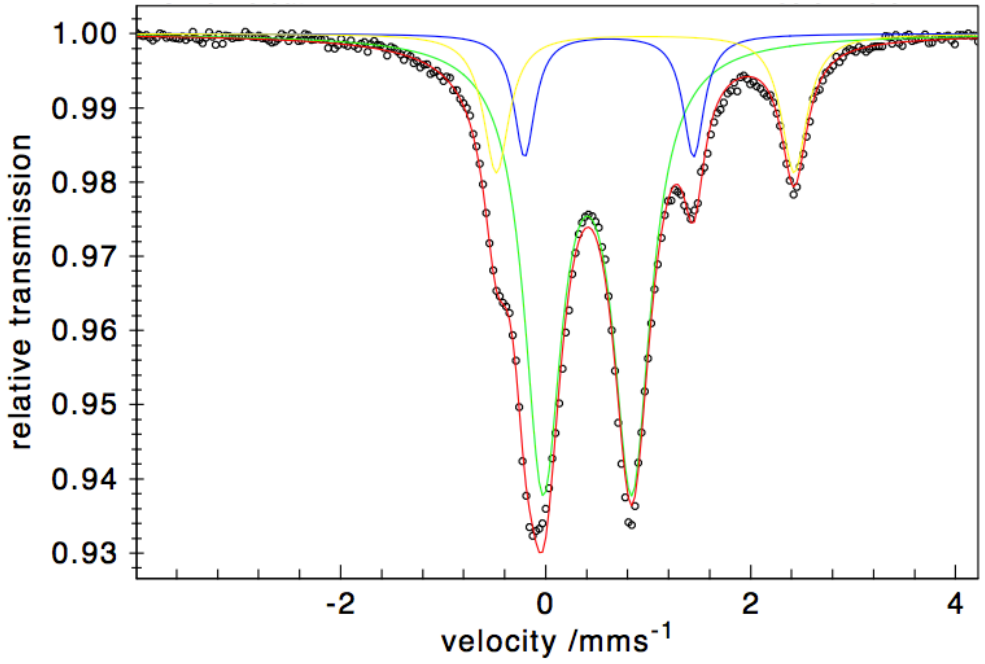

Figure A3.6. Mössbauer spectrum of **4** recorded at 160 K.

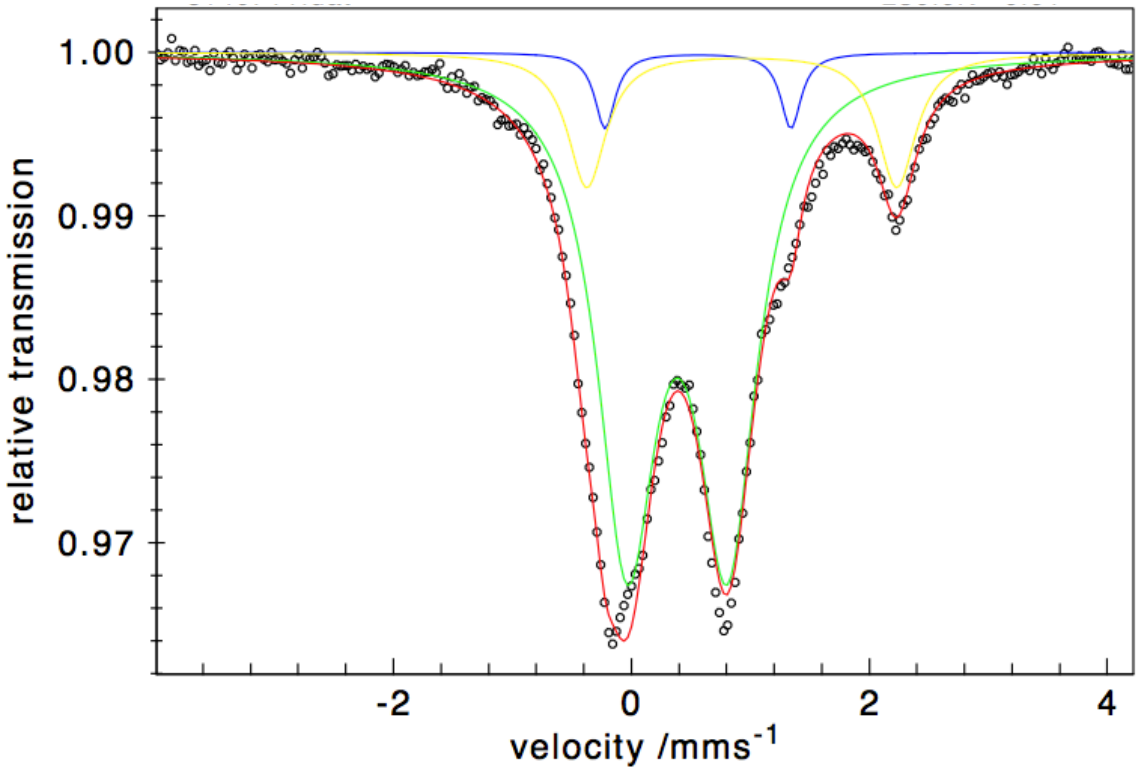

Figure A3.7. Mössbauer spectrum of **4** recorded at 230 K.

The isomer shifts, quadrupole splittings, and integrations for each doublet of moncation **4** at each temperature are tabulated in Table A3.1. The decrease in isomer shifts, quadrupole splittings, and intensities of the individual subspectra with increasing temperature is typical.[246] The doublet with δ = 0.67 mm s^{-1} exhibits a lower Debye temperature than the others, so its intensity fades more with increasing temperature than the others; moreover, Fe(III) usually gives a higher recoil fraction than Fe(II).[210,246]

Table A3.1. Variable temperature Mössbauer parameters of **4**.

Compound, charge	Isomer shift (δ, mm s^{-1})	Quadrupole splitting ($\lvert\Delta E_Q\rvert$, mm s^{-1})	Intensity (%)
80 K	0.43 0.67 1.01	0.88 1.75 3.10	67 17 17
160 K	0.41 0.62 0.97	0.87 1.65 2.91	73 12 16
230 K	0.39 0.56 0.93	0.84 1.56 2.60	81 5 15

Appendix 4: Supporting Information Figures for Chapter 5

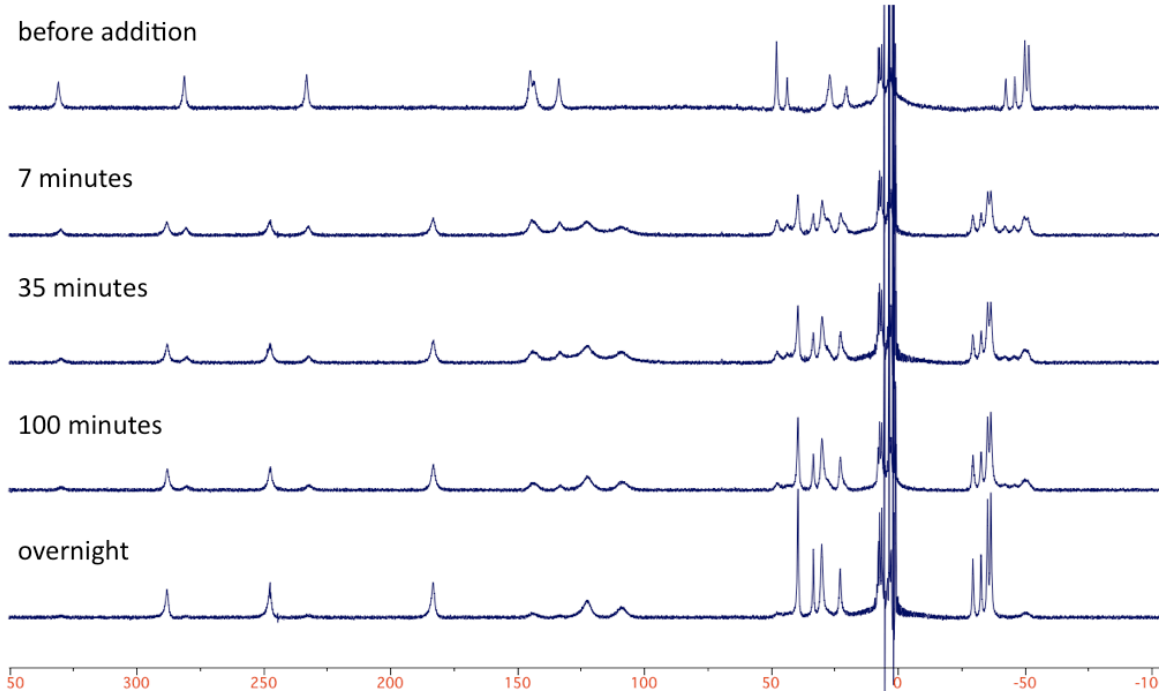

Figure A4.1. Time course of the paramagnetically shifted ^{1}H NMR spectra of the reaction of an atmosphere of O_2 with **3** in CD_3CN.

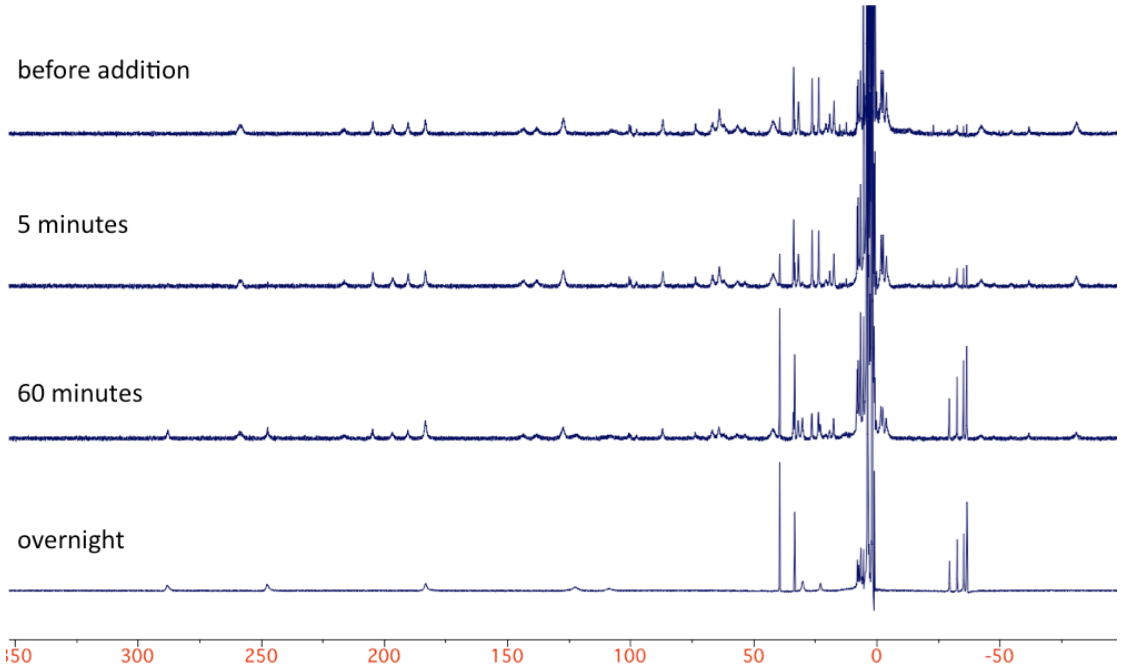

Figure A4.2. Time course of the paramagnetically shifted ^{1}H NMR spectra of the reaction of an atmosphere of O_2 with **6** in CD_3CN.

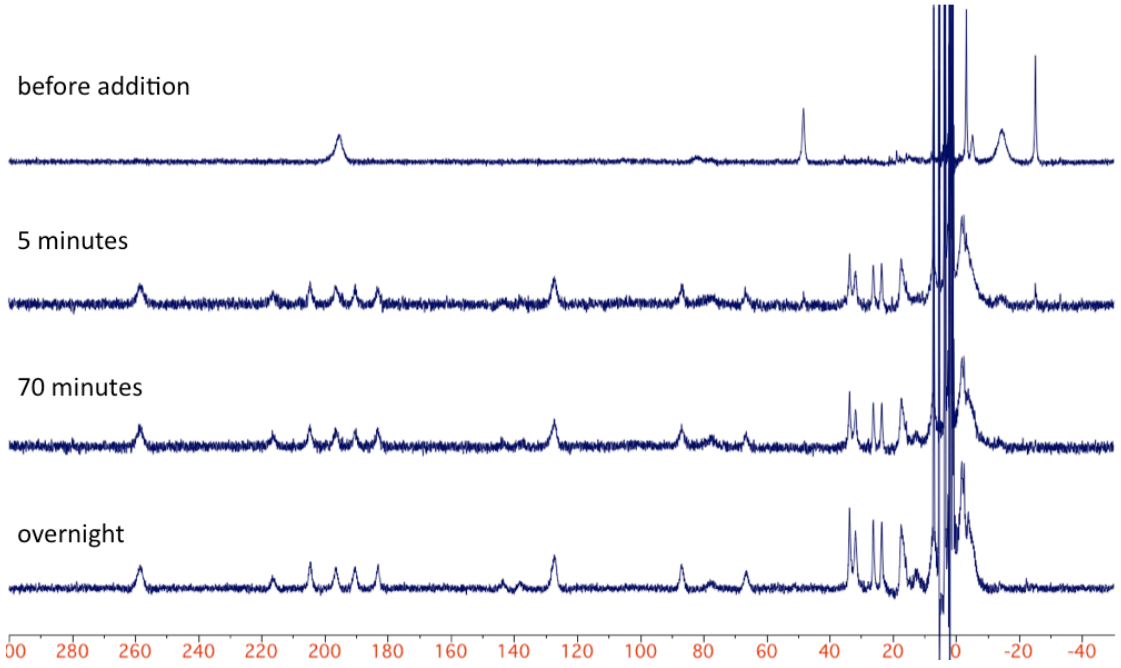

Figure A4.3. Time course of the paramagnetically shifted ^{1}H NMR spectra of the reaction of a half equivalent of O_2 with **1** in CD_3CN.

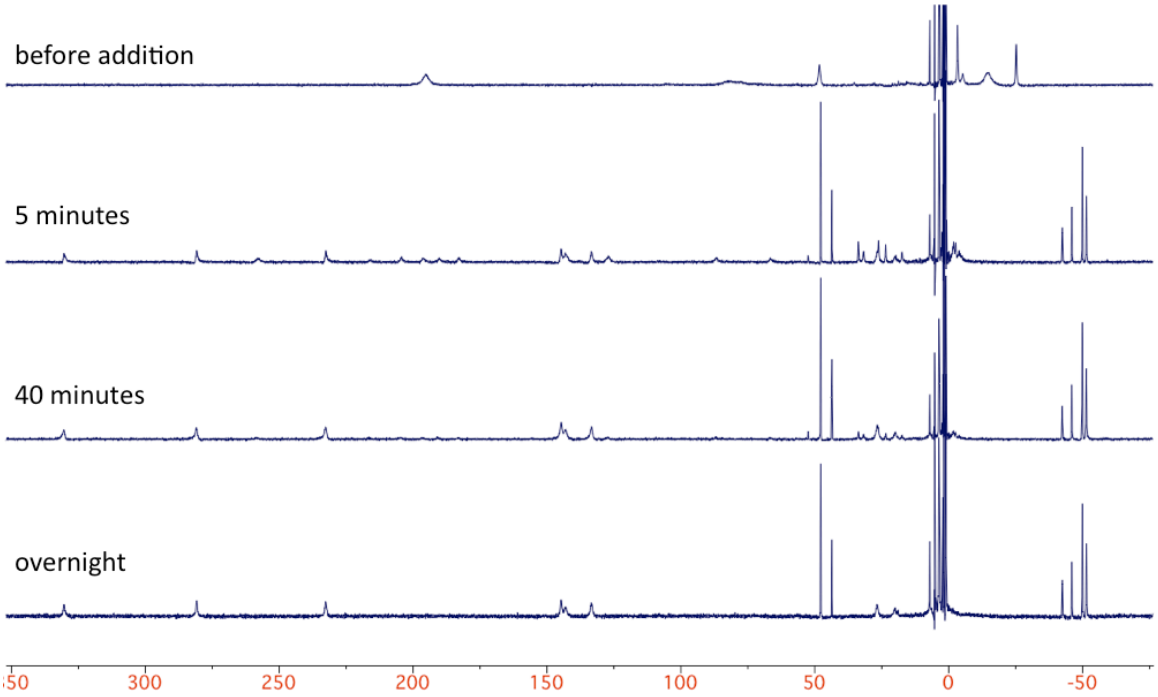

Figure A4.4. Time course of the paramagnetically shifted ^{1}H NMR spectra of the reaction of one equivalent of O_2 with **1** in CD_3CN.